CRANFIELD UNIVERSITY

Edmon Chehura

In-Line Fibre-Optic Laser Doppler Velocimeter using Bragg Grating Interferometric Filters as Frequency to Intensity Transducers

SCHOOL OF MECHANICAL ENGINEERING

PhD Thesis

CRANFIELD UNIVERSITY

SCHOOL OF MECHANICAL ENGINEERING

Centre for Photonics and Optical Engineering

PhD THESIS

Academic Year 2002

Edmon Chehura

In-Line Fibre-Optic Laser Doppler Velocimeter using Bragg Grating Interferometric Filters as Frequency to Intensity Transducers

Supervisor: Professor Ralph P Tatam

June 2002

This thesis is submitted in partial fulfilment of the requirements for the degree of Doctor of Philisophy

Acknowledgement

I would like to acknowledge an Overseas Research Scholarship Award (ORS) from the Committee of Vice Chancellors (UK) for sponsoring my studies. Thanks are due to Cranfield University for a student bursary that catered for my financial needs. This project won one of the two bursary awards in UK from the Bristol Industrial and Research Associates Ltd (BIRAL Ltd) and many thanks to the company for sponsoring my trip to the SPIE conference in USA. I would like to thank the Institute of Physics for providing me with travel bursaries that helped me attend conferences. My special thanks go to Prof. Ralph Tatam (my supervisor) for his most needed help and ideas and to Dr. S. James for his support. Many thanks to Dr. C-C Ye for his help with the Bragg grating fabrications, S. Staines for his ingenuity and technical constructions, Dr. H. D. Ford for her constructive ideas and Dr. D. Nobes for lending me some of his equipment. Thanks are due also to many people for their direct or indirect help during my studies particularly the present and past members of the Optical Sensors Group.

"The Lord is my Shepherd; I have everything I need." **Psalms 23**

ABSTRACT

Three dimensional complex flows particularly those of turbomachinery present challenges to current measurement technology in terms of restricted optical access, measurement accuracy for the on-axis velocity component, the need to resolve flow turbulence and measurement difficulty from close to surface or intra-channel measurements in rotating machinery.

A novel non-intrusive in-line fibre-optic laser Doppler velocimeter is presented specifically for the measurement of the on-axis component of velocity. The measurement principle is based on a Doppler frequency to intensity transducer in the form of a fibre-optic Bragg grating based Fabry-Perot interferometric filter. The filters were fabricated at 514.5 nm but in principle any desired wavelength may be used thus permitting any laser wavelength source to be used. Filters with appropriate features were designed with the aid of the theoretical models based on the coupled mode theory and transfer matrix approach.

The argon-ion laser emission wavelength was locked to a corresponding Doppler broadened absorption line of molecular iodine vapour while the Fabry-Perot interferometer phase was controlled in an independent feedback system using digital lock-in amplifiers. The optical frequency was stabilized to within 10 MHz for at least one hour while the phase was controlled to an equivalent of (within) ± 3 MHz in frequency. Both feedback loops utilized custom designed PID electronic circuit controllers. The bandwidth of the filter was tunable by up to 400 MHz, with a resolution of between 0.2 ms^{-1} and 1 ms^{-1}, and a sensitivity range of between 0.5 $[GHz]^{-1}$ and 1.7 $[GHz]^{-1}$. In this technique the filter was tuned to the optical wavelength, rather than tuning the laser wavelength to match the filter. The finished instrument was applied to the measurement of the on-axis component of velocity, of a rotating disc, over an available range of up to ± 42 ms^{-1}, limited only by the maximum velocity of the disc. The detection system was reconfigured for low velocity measurements at twice the sensitivity over a velocity range of ± 7 ms^{-1}. This technique demonstrates a unique contribution to fluid dynamics for the measurement of the traditionally difficult in-line component of velocity.

Contents

CHAPTER 1

Introduction

Optical experimental techniques to measure fluid velocity have over the years become wide and varied. Laser Doppler velocimetry (LDV) commonly known by the name Laser Doppler anemometry (LDA) is the earliest discovered technique that exploits the Doppler effect on light. The Doppler effect is well known effect in acoustics, which was first discovered by a German Physicist, Christian Doppler in 1842. It is this discovery and Einstein's Special Theory of Relativity (1905) that showed a similar effect on light together with the invention of the laser in 1960 that triggered laser anemometry.

The Doppler effect refers to the shift in frequency that occurs whenever there is relative motion between the source, receiver, propagating medium, or intervening scatterer. The principle of laser Doppler anemometry is based on a moving scatterer in the illuminated fluid with the laser and observer considered stationary relative to each other. A scatterer moving towards the observer scatters light at a frequency higher than that of the source (blue shift) while that moving away scatters lower frequency (red shift). This aspect forms an important part of the anemometer as it allows the direction of the measured velocity to be discriminated. The change in pitch of sound commonly experienced with fast moving trains, aircraft or racing cars is an example of the Doppler effect.

The Doppler shift in frequency has found wide applications that range from a simple police speed radar, atmospheric wind velocity measurements, measurements in respiratory systems and arterial flows [1], to complicated fluid dynamic measurements [2, 3].

The first exploitation of the Doppler shift in laser anemometry was implemented by Yeh and Cummins in 1964 [4] and this was possible because light scattered in a given direction exhibits a well-defined Doppler shift. Since then research and development

has continued to improve the experimental configurations and measurement techniques most of which were focussed on laboratory fluid flows. Today laser Doppler velocimetry has developed into a mature tool that is capable of applications in complex 3D and turbulent flows in windtunnels and turbomachinery [5, 6, 7]. Turbomachinery is particularly more challenging with flows being internal and quite often consisting of rotating machinery e.g. compressor and turbo fan flows that pose difficulty in terms of access and measurement techniques. Accurate experimental velocity data is required for design purposes to improve the system's efficiency, fuel economy as well as to ensure conformity to environmental friendly standards. Modern computer technology has advanced the theoretical simulation of complex flows to a level that supersedes experimental data and hence the increased demand to match the theory and provide validation data. The reliability of these simulations commonly known as computational fluid dynamic codes (CFD) depends on validation with accurate experimental data in order to be accepted. The search for the best experimental configuration is therefore an ongoing process to keep up with the increasing industrial sophistication.

Optical techniques have developed significantly in recent years partly due to the availability of new fibre-optical and electronic components and the increased demand on measurement accuracy [2]. These techniques offer fast response, have immunity to environmental perturbations, are non-intrusive to the measurement volume and are suitable for applications where direct probing of the flow is prohibitive such as measurements in high temperature or aggressive fluids or gases.

There is increasing demand to measure all three velocity components in order to fully characterise fluid flow phenomena for various applications that include turbomachinery design and the validation of increasingly sophisticated computational fluid dynamics codes. While transverse velocity components have been measured successfully using dual scatter configurations in laser Doppler velocimetry (LDV) and laser two-focus (L2F) anemometry, the on-axis component has remained elusive to measurement with sufficient accuracy [8]. Figure 1.1 is an illustration of the 3D components of velocity. The transverse or in-plane components are those which lie in the x-y plane while the on-axis component is along the optical axis of the probe head. Such lack of accuracy has

revealed deficiency in resolving flow turbulence. Measurement access to turbomachinery (internal) flows is limited which together with the difficulty in performing boundary layer measurements very close to walls or around blade tips/clearance is a major challenge.

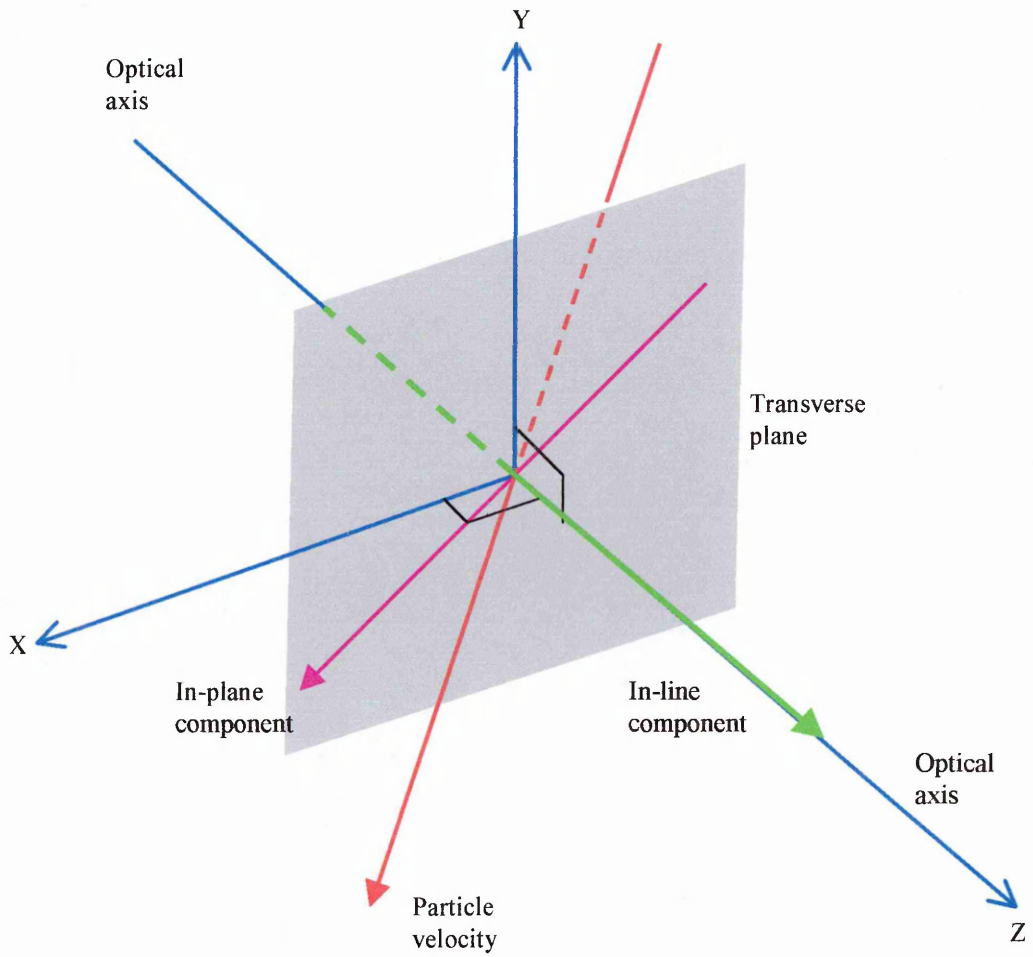

Figure 1.1: 3D components of velocity.

The principle of operation of point measurement techniques based on the Doppler frequency shift and time of flight measurements are described in Chapter 2. The implications of various experimental configurations with regards to measurement sensitivity and accuracy are considered. Also presented is the principle behind the production of the Doppler shift and the need to seed the flow with particles whose properties are also considered with more detail provided in Appendix A and C respectively.

Chapter 3 is a review that details previous efforts to measure the in-line velocity component with better accuracy using various optical techniques that were intended for inclusion in 3D instruments. The evolution of such efforts and their short comings are presented with the chapter gradually setting the scene for the scope of this thesis. The experimental configuration to obtain three component measurements providing equal resolution is to employ a system that directly measures orthogonal components. Such a system requires at least two orthogonal entrance ports (i.e. two probe heads) to the measurement volume. This configuration becomes inapplicable particularly in turbomachinery where optical access is limited and is usually restricted to a single window. Commercial systems therefore usually involve the use of 2 Doppler difference channels on a single probe head for non-orthogonal components of velocity [7, 9, 10]. The disadvantage of the configuration is that the small angle between the measured components introduces a large uncertainty in the on-axis component. More suited to the direct measurement of the in-line velocity component is the reference beam technique which is however, restricted to velocities of a few tens of ms^{-1} but is characterised by poor signal to noise ratio apart from being notorious in alignment difficulty (non fibre systems). Interferometric devices employing confocal Fabry-Perot or Michelson interferometers have been successfully used for direct measurement of high in-line velocity components [11] thereby complimenting the reference beam technique. Their measurement of low velocities is hampered by their susceptibility to environmental disturbances such as vibrations. The chapter also discusses the measurement of the on-axis component of velocity by planar-based techniques.

Recent developments in laser anemometry have increasingly shifted towards the use of optical fibre systems with the optical fibres mainly used as transmission medium and in some cases to perform signal conditioning. Chapter 4 will introduce and discuss in-fibre Bragg grating technology upon which the sensing properties of the new velocimeter presented in this thesis are derived. Various Bragg-grating based filters are proposed as candidates for flow velocity sensing as frequency to intensity transducers. It is perceived that optical-fibre devices are capable of replacing high bandwidth electronic processors, Bragg cells for directional discrimination (in LDV), atomic/molecular filters

(in Planar Doppler Velocimetry) and other components. Fibre-optic filters apart from being compatible with fibre systems can be fabricated at any wavelength and are wavelength tuneable, which makes them suitable for use with a laser of any wavelength emission. The laser does not have to be tuneable provided the emission is single frequency and highly stable. The design and inclusion of these devices in the new velocimeter is a novel application that brings unique attributes to flow velocity measurement e.g. the ability to tune the measurement velocity range, sensitivity and resolution among many advantages.

The fibre-optic filters were required to have narrow frequency bandwidths ranging from a few MHz to about 3 GHz so as to cover velocities encountered in windtunnel and turbomachinery (velocities up to about 2 000 ms^{-1} at 1.5 MHz/ms^{-1}). The filter transfer function was needed to have steep slopes, linear gradient, and high visibility for high velocity sensitivity, linear frequency to intensity transduction, and high signal to noise ratio respectively. Narrow frequency bandwidths of the filter provide high velocity resolutions. Theoretical models have been developed to investigate and characterise the suitability of numerous filter candidates for Doppler frequency discrimination. Chapter 5 describes the modelling techniques and presents some of the results while the programming code in Fortran 90 is in Appendix B. Filters that were investigated include end-pumped gratings, Moiré gratings, distributed feedback gratings, Michelson interferometer gratings and Fabry-Perot interferometers. The influence of strain and temperature to the filter transmission function was included in the models. The study reveals the flexibility in tailoring such filters to specific flow conditions.

The laser Doppler velocimeter featured in this thesis is comprised of various optical and fibre-optical and electronic components whose performances are of importance to the overall performance of the instrument. Some of the key system components are introduced and discussed in Chapter 6. The chapter includes the calibration and alignment of certain components e.g. the laser frequency to voltage coefficient and the LDV probe head alignment.

The details of the experimental fabrication of the end-pumped grating filters and Fabry-Perot interferometers are presented in Chapter 7. Also presented are experimental methods used to read the narrow frequency bandwidths which were of the order of 100 MHz to 800 MHz. The chapter experimentally shows the ability to tune the shape of the transfer function of the filter by the application of strain.

Bragg-grating based filters exhibit high sensitivities to strain, temperature and vibration and are often used as sensors for these quantities [12]. The deployment of such devices in an environment where these quantities vary with time will therefore cause signal drift that will affect the performance of the velocimeter. Chapter 8 describes two experimental techniques that were adopted to actively control and compensate for these effects in closed-loop feedback format. The laser wavelength stabilisation loop was based on locking the wavelength to a Doppler-broadened absorption line of molecular iodine vapour and a stability of about 10 MHz was achieved over a time period of about 2 hours a high improvement over the previously recorded 600 MHz. An independent system was set up to stabilise the phase of the fibre-optic Fabry-Perot filter based on the phase detection using digital lock-in amplifiers and the result was a frequency stability of < 5 MHz. Details on the proportional-integral-derivative (PID) electronic circuit controller designs that were used in both control loops are separately presented in Appendix D and Appendix E.

Chapter 9 is an assembly of the finished in-line fibre optic laser Doppler velocimeter using a Fabry-Perot filter as Doppler-frequency to intensity transducer and is presented in 3 different configurations. The experimental procedure and results are given for laboratory experiments using a rotating perspex disc. The velocity range measured by the system was 85 ms^{-1} and the velocimeter resolution was 0.2 ms^{-1}. Conclusions and further work on the velocimetry system are given in Chapter 10.

References

[1] L. Yuan-Hsiang, C. Yan-Yu, H. Yuan, L. Yi-Lin and J. Gwo-Jen, "*Design and development of laser Doppler velocimetry based on DSP technique for blood flow measurement*", Proceedings of SPIE, vol. 4082, pp. 198-207, 2000.

[2] C. Tropea, "*Laser Doppler anemometry: recent developments and future challenges*", Measurement Science and Technology, 6, pp. 605-619, 1995.

[3] G. L. Morrison, G. B. Tatterson and M. W. Long, "*A 3-D Laser Velocimeter Investigation of Turbulent, Incompressible Flow in an Axisymmtric Sudden Expansion*", AIAA 25th Aerospace Sciences Meeting, AIAA-87-0119, pp. 1-10, Reno, 1987.

[4] Y. Yeh and H. Z. Cummins, "*Localised fluid flow measurements with He-Ne laser spectrometer*", Appl. Phys. Lett., vol. 4, pp.176-178, 1964.

[5] M. Stieglmeier and C. Tropea, "*A miniaturised, mobile laser-Doppler anemometer*", Applied Optics, 31, pp. 4096-205, 1992.

[6] Chr. Resagk, U. Schellenberger, J. Grabow, C. Tropea and M. Stieglmeier, "*Two component LDA using optical multiplexing*", Measurement Science and Technology, 6, 674-81, 1995.

[7] G. L. Morrison, M. C. Johnson, D. H. Swan, and R. E. DE Otte Jr, "*Advantages of orthogonal and non-orthogonal 3D LDA systems*", Proceedings of 5th International Symposium on Applications of Laser Techniques to Fluid Mechanics, paper 25.2, Lisbon, 1990.

[8] J. F. Meyers, "*The elusive third component*", International Symposium on Laser Anemometry, ASME, pp. 247-254, 1985.

[9] L. Dancy, "*A review of three-component laser Doppler anemometer*", Journal of Optical Sensors, vol. 2, no. 6, pp. 437-469, 1987.

[10] P. K. Snyder, K. L. Orloff, and M. S. Reinath, "*Reduction of flow measurement uncertainties in laser velocimeters with nonorthogonal channels*", AIAA Journal, vol. 22, no. 8, pp. 1115-1123, 1984.

[11] Y-J. Rao, "*In-fibre Bragg grating sensors*", Meas. Sci. Technol. 8, pp 355-375, 1997.

[12] R. G. Seasholtz and L. J. Goldman, "*Combined fringe and Fabry-Perot laser anemometer for three component velocity measurements in turbine stator cascade facility*", NASA Technical Memorandum 87322, 1986.

CHAPTER 2

Principles of Laser Velocimetry

2.1 Introduction

Laser velocimetry has become the single most powerful tool for non-intrusive measurements of fluid velocity with a wide range of techniques all triggered by the original experiments first conceived by Yeh and Cummins [1]. Conventional instruments for velocity measurement such as hot wire and film anemometers, pitot and pitot-static probes are still widely used but their act of measurement introduces inaccuracies as their physical deployment in the measurement volume location disturbs the flow [2]. Optical techniques being non-contact to the flow have brought the potential to eventually replace these intrusive instruments.

The optically based measurement instruments use lasers to provide light beams for interrogating the flow. The flows are usually seeded with carefully chosen micron-sized scattering particles for molecules themselves only provide weak scattering. These particles are chosen such that they are able to follow the follow while providing enough scattered light. It is the scattered light that is encoded with the required velocity information. The encoding is usually in the form of the Doppler frequency shift of the scattered light or time of flight measurement of the particle.

The laser frequencies used are of the order of 10^{14} Hz, which is far beyond the bandwidth of any detector. Furthermore the Doppler frequency shift obtained can be a few MHz or less e.g. 3 MHz for a velocity of about 1 ms^{-1}, which is about 1 part in $2x10^{8}$ of the laser frequency and such resolutions in frequency are difficult to achieve even with high resolution optical spectrometers. This chapter discusses various methods used to extract this Doppler shift. Also discussed are the time of flight measurements

and light scattering by small micron-sized particles. A computer model of the properties of light scattered by small particles is presented in Appendix B.

2.2 The Doppler Frequency Shift

The concept of the Doppler shift in frequency of electromagnetic radiation is well established and it takes place whenever there is relative motion between the source, observer, and intervening medium. Laser Doppler velocimetry considers the source and observer to be stationary relative to each other and the Doppler shift is caused by a moving particle in the medium. This interaction is illustrated in Figure 2.1 but the derivation of the equation is given in Appendix A.

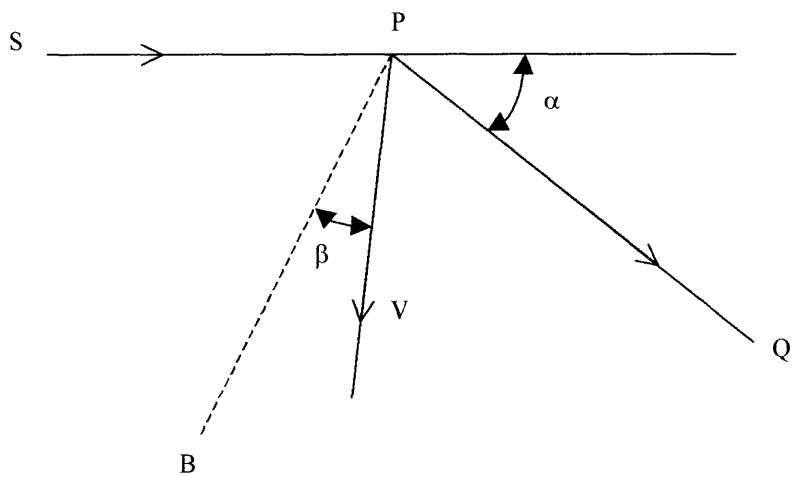

Figure 2. 1: The Doppler shift from scattered light.

S – source, Q – observation direction, P – particle,
Bisector of angle SPQ, V – measured velocity component.

The Doppler shift from the scattered light is given by (Appendix A)

$$\frac{\Delta\nu}{\nu} = \frac{2V}{c} \cdot \cos\beta \cdot \sin\left(\frac{\alpha}{2}\right) \qquad (2.1)$$

where ν, $\Delta\nu$, and c are respectively the laser frequency, Doppler frequency shift and speed of light in vacuum while α and β are as defined in the Figure 2.1. Equation (2.1)

shows that the Doppler shift depends on the bisector of the scattering angle and the component of the particle velocity in the direction of the scattering vector.

2.3 Measurement Sensitivity and Geometry

The Doppler shift equation (2.1) may be rewritten in vector form as

$$\Delta\nu = \frac{\nu_0}{c}\left(\hat{o} - \hat{i}\right)\cdot\overline{V} \qquad (2.2)$$

where $\hat{o}$ and $\hat{i}$ are unit vectors in the observation and illumination directions respectively and all other parameters are as defined in section 2.2 above. It was shown that the quantity in brackets represents the direction of the measured component, which is along the bisector of the incident and observation directions. The measurement sensitivity of a velocimeter for a given geometry may be defined by the frequency change per unit velocity, which is a constant quantity (Figure 2.2).

$$Sensitivity = \frac{\Delta\nu}{\left|\overline{V}\right|} = \frac{\nu_0}{c}\left(\hat{o} - \hat{i}\right)\cdot\hat{V} \qquad (2.3)$$

This equation shows that the sensitivity can be increased by reducing the angle Ω between the measured component and the flow vector and is a maximum when they are perfectly aligned with each other (Figure 2.2). The sensitivity can be further improved by increasing the length of the resultant vector in the measured component. This means that an ideal maximum sensitivity would occur if the laser and receiver were in the same position (i.e. $\Phi = 180^0$) so that the scattered light travels directly back along the laser beam with the flow either towards or directly away from the laser and receiver. Such a measurement geometry is however not practically feasible.

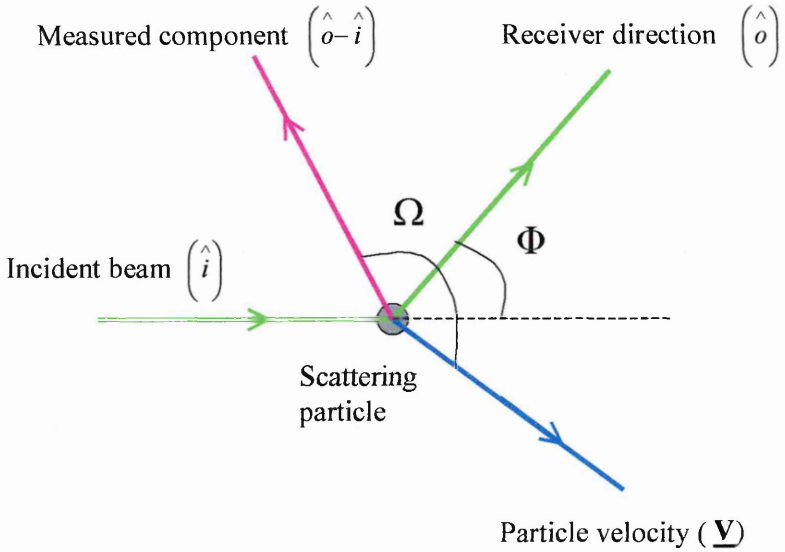

Figure 2. 2: Measurement geometry of the Doppler shift.

2.4 Laser Doppler Velocimetry

Laser Doppler Velocimetry consists of three fundamental experimental configurations all of which rely on the beating of two light-beams to extract the Doppler frequency [3]. Two beams of similar frequency are interfered together to produce a beat signal that is well within the bandwidth of the detector. The technique relies heavily on the coherent property of lasers to create an interference pattern when the beams are intersected. The interference may be modelled as containing fringes. The production of the Doppler-beat signal is briefly discussed here.

Consider the intersecting beams to have electric fields E_a and E_b that may be expressed at time, t by

$$E_a = E_{a0}\cos(2\pi\nu_a t + \phi_a) \qquad (2.4)$$

$$E_b = E_{b0}\cos(2\pi\nu_b t + \phi_b) \qquad (2.5)$$

where E_{a0} and E_{b0} are field amplitudes, ν_a and ν_b are the optical frequencies, and ϕ_a and ϕ_b are arbitrary phases. When the two fields are mixed together, the output, $I(t)$ of the detector (non-linear) is proportional to the square of the sum of the electric fields. The expansion of the expression shows that $I(t)$ has several components, the dc term which is proportional to the total intensity, a sum frequency $(\nu_a+\nu_b)$ term, a beat frequency $(\nu_a-\nu_b)$ term, and harmonic terms. The frequencies of the sum-frequency term and harmonic terms are too high for the signal to be registered by the detector thus the detected signal simplifies to

$$I(t) = B\left(\tfrac{1}{2}(I_a + I_b) + \sqrt{(I_a I_b)} \cdot \cos\left(2\pi(\nu_a - \nu_b)t + (\phi_a - \phi_b)\right)\right) \qquad (2.6)$$

where B is a constant and I_a and I_b are the intensities of the two beams.

While the beat frequency term provides the magnitude of the velocity the direction of the flow can however not be obtained from this term as it is a scalar quantity and thus additional components would have to be introduced for this purpose.

2.4.1 Reference Beam Configuration

The reference beam technique involves heterodyning the scattered light beam with a reference beam at the original laser frequency at the surface of a square law detector to give a beat frequency that is equal to the Doppler shift (Figure 2.3). The beat frequency is equal to the difference in frequency of the two beams of light. It can be observed by applying equation (2.6) to the reference beam system that an amplification effect is obtained by increasing the intensity of the reference beam, I_b if the Doppler shifted intensity, I_a is weak. However there is a fundamental limit to the signal to noise ratio obtainable by this amplification [2], the limit that is given by

$$SNR_{\max} = \frac{\eta \cdot I_a}{h\nu \cdot \Delta f} \qquad (2.7)$$

where SNR_{max} is the maximum signal to noise ratio, η is the quantum efficiency of the detector, Δf is the passband frequency of the detector, and h is Plank's constant. The coherence requirement [4] for optical beating means that the SNR will be small when compared to Doppler difference technique (Section 2.4.2) since the aperture size will have to be limited [5]. The aperture is limited in size to keep the wavefronts of the signal and reference beams in phase over the area of the photodetector.

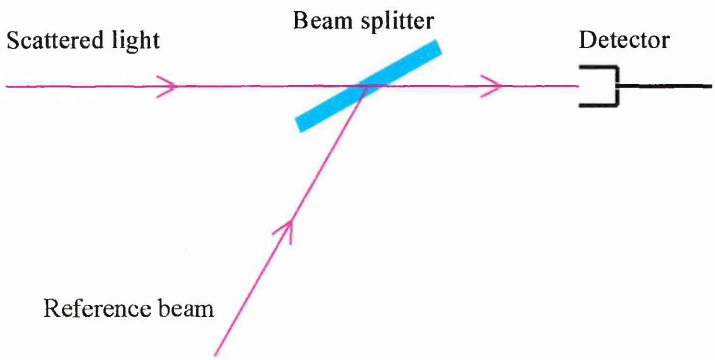

Figure 2. 3: Heterodyning in the Reference beam system.

The measurement volume is required to be as small as possible (e.g. 24 x 24 x 500 μm for a system developed at Cranfield University [6] so that a strong scattered signal that is coherent (in phase) with the reference beam is obtained. The measured component of velocity is along the bisector of the illumination and the collected scattered signal directions and it is possible to configure the system such that it is predominantly sensitive to the on-axis velocity component.

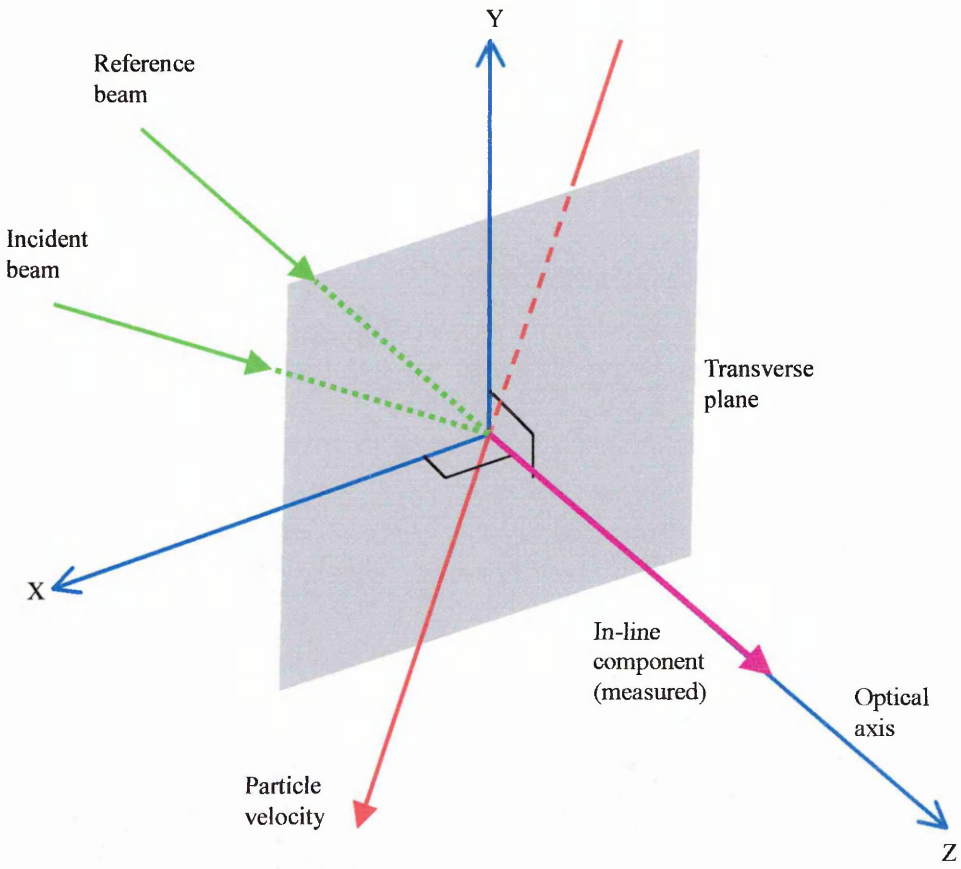

Figure 2.4: On-axis component of velocity measured by the Reference beam technique.

2.4.2 Doppler Difference Configuration

The Doppler Difference technique combines two coherent beams of light with equal intensity (from different directions) at a common focal point in the flow (thus defining the measurement volume) [7]. The scattered light is detected in a third direction. The interference creates fringes such that a particle traversing the volume scatters light at the rate at which it cuts through the bright fringes. Here the frequency measured is the difference in the Doppler shift of the two beams. The measured frequency shift is proportional to the fringe spacing and the component of velocity perpendicular to the fringes (Figure 2.5) [8].

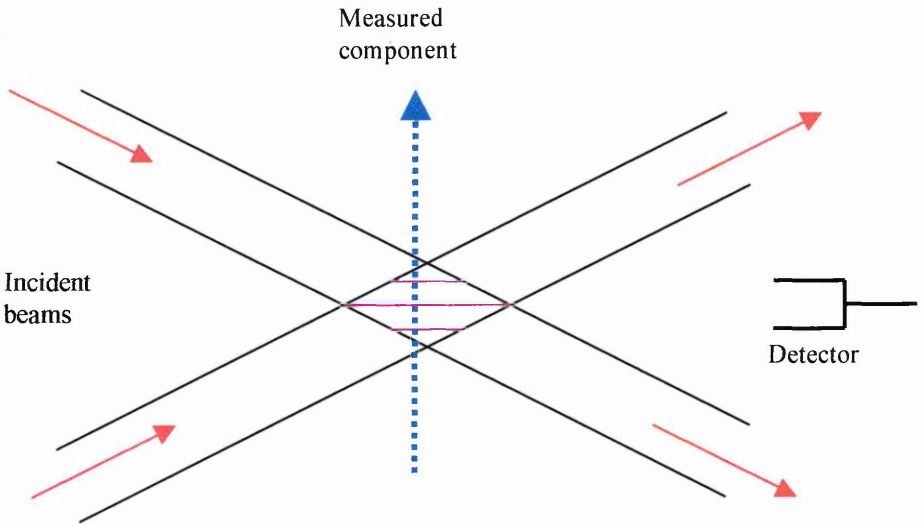

Figure 2. 5: Doppler difference configuration.

If equation (2.6) is applied to the Doppler difference system it shows that the maximum fringe visibility, V_s is given by:

$$V_s = \frac{\sqrt{(I_a I_b)}}{I_a + I_b} \qquad (2.8)$$

The Doppler frequency shift, $\Delta\nu$ is given by

$$\Delta\nu = \frac{2V}{\lambda} \cdot \sin\left(\frac{\alpha}{2}\right) \qquad (2.9)$$

where V is the particle velocity and α is the angle between the two illuminating beams. This equation shows that the shift in frequency is independent of the receiving direction and thus light may be collected over a wide aperture resulting in improved signal to noise ratio. Figure 2.6 illustrates the in-plane components of velocity that are measured by the Doppler difference technique.

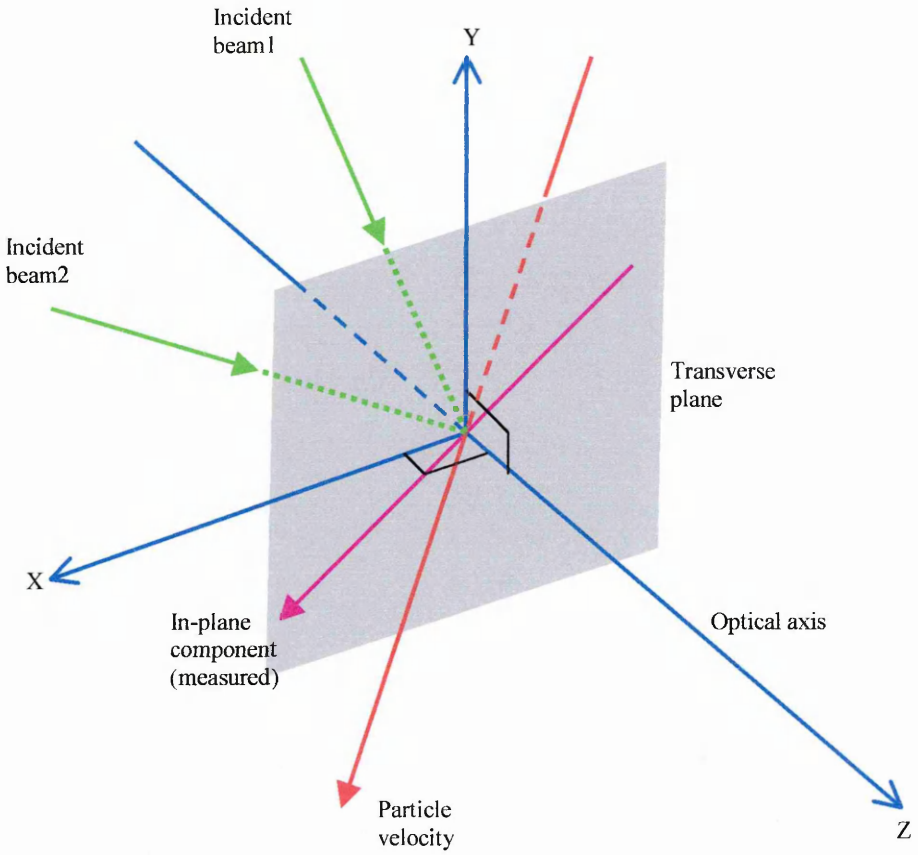

Figure 2. 6: Components of velocity (in-plane) measured by the Doppler difference technique.

The three-dimensional intensity distribution of the measurement volume reveals that the spatial frequency is dependent on the *z*-position due to curvature of the interference fringes caused by the tilted beams at the intersection (Figure 2.7). The error is however usually insignificant particularly as the number of fringes becomes large [9].

Significant errors occur when the beam waists are displaced from the focal plane as this results in gradients between the interference planes (Figure 2.8). The effect of this is to impress a false acceleration on a particle crossing the fringes at constant velocity. Thus precise beam overlap is mandatory and it is also desirable to have well focused beams at the point of overlap so as to enhance fringe intensity.

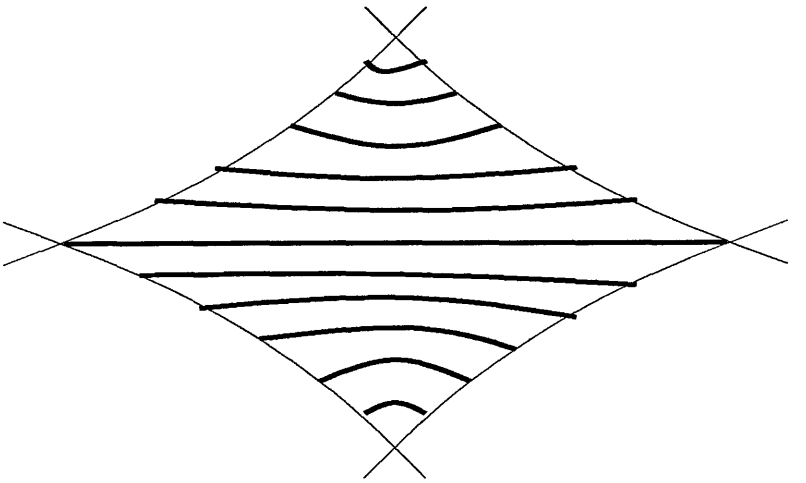

Figure 2. 7: Curvature of the interference fringes [9].

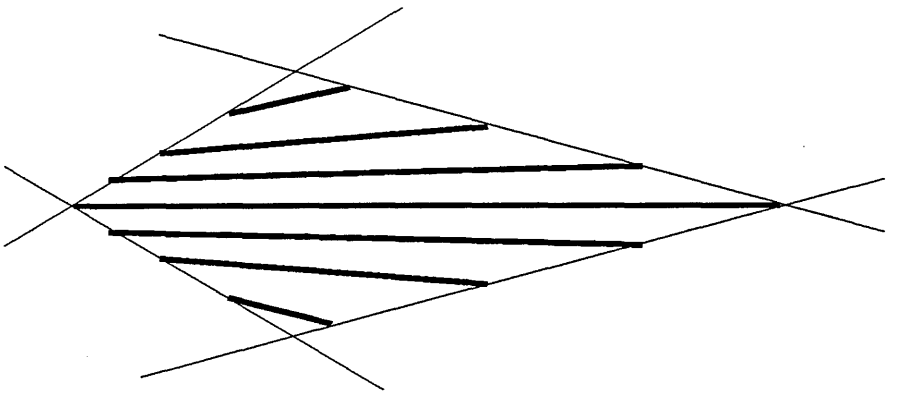

Figure 2. 8: from beam waists displaced from the focal plane [9].

It may also be inferred that the basic accuracy of the Doppler frequency measurement is determined by the number of fringes in the measurement volume for this determines the maximum number of cycles in the scattered signal from a traversing particle.
A third LDV configuration closely associated with the Doppler Difference technique is the dual scatter configuration [3] that consists of one illuminating beam and mixes two beams scattered in different directions. This technique is however difficult to implement due to the requirement of separate apertures for each beam and spatial coherence of the beams.

It is clear therefore that the success of an LDV experiment depends on critical alignment among other factors.

2.4.3 Direction Discrimination

The LDV beat frequency is the difference of two frequencies and it is not possible to differentiate between the two (in terms of size) and consequently the change in sign of the velocity can not be known. While this may not be a problem with one-dimensional flows, complex flows demand the ability to resolve the flow direction.

The most popular technique in LDV is to introduce a finite shift in frequency of one beam so as to pre-bias the zero velocity. The reference beam system uses a shift in the reference beam while one beam is usually shifted in frequency for the Doppler difference system. Frequency shifting makes it possible to measure the zero velocity. The introduced shift is however required to have a magnitude greater than the maximum Doppler shift in the flow to avoid unambiguous relation between velocity and signal frequency.

The most common method in LDV for frequency shifting is to pass the beam through an acousto-optic cell (Bragg cell) although second harmonic generation and electro-optic cells can be used [2]. If the angle between the beam and the generated acoustic waves satisfies the Bragg condition then reflections from successive acoustic wave fronts reinforce. The frequency shift of the diffracted beam is equal to the frequency of the sound wave generated by the Bragg cell [10]. Frequency shifts of up to about 1 GHz (corresponding to 312 ms^{-1} for the reference beam technique) are possible and thus the limitation to the maximum measurable Doppler shifts and hence the velocity is normally due to the electronic processor (31.2 ms^{-1} for 100 MHz processor, a reduction by a factor of 10).

2.5 Filter Based Doppler Velocimetry

It is desirable to have a velocimeter system that combines direct frequency measurement and automatic directional discrimination while retaining a simple experimental arrangement. Such a system was first realised by Komine et al [11] in which a molecular absorption line of iodine vapour was used as a frequency filter. The principle

of operation is based on the vapour's frequency-dependent absorption of the laser beam, which results in the transmission being a function of frequency (Figure 2.9). Fluctuations in the optical emission frequency are therefore detected as intensity fluctuations. This transduction from frequency to intensity would be linear if the absorption line edge is linear.

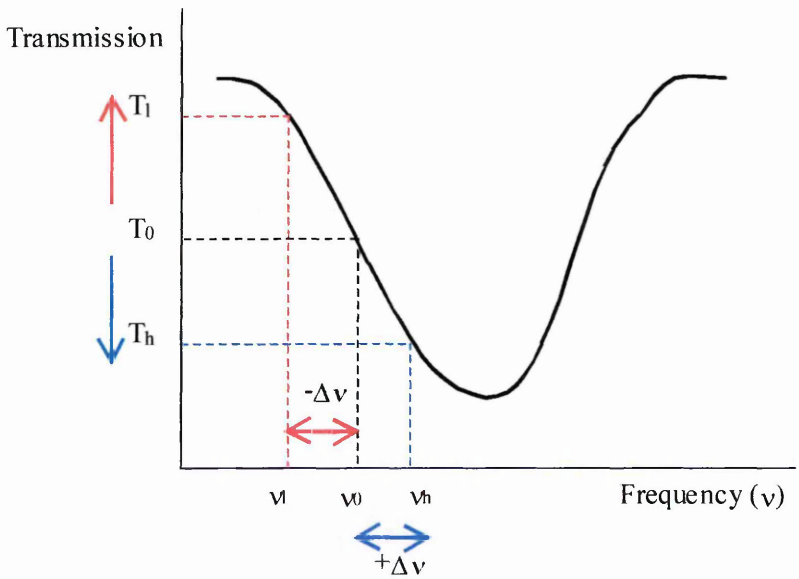

Figure 2. 9: Measurement of the Doppler frequency and direction of flow by the iodine absorption line.

The normal practice is to tune the laser frequency, ν_0 to the edge of the absorption line so that it corresponds to 50% attenuation in the transmission. This becomes the reference measurement point from which reversal in flow direction can be obtained. If a Doppler frequency shift, $+\Delta\nu$ occurs above the laser frequency, ν_0 then a decrease in transmission, T_h is recorded while a negative Doppler shift, $-\Delta\nu$ increases the transmission to T_l (Figure 2.9) for a laser frequency that is tuned to the left edge of the transfer function. It is required that the transfer function be accurately known prior to the velocity measurement and should be reproducible during or after the experiment for this provides the calibration curve. Absorption models or curve fitting may be used to smooth the calibration curve by superimposing the two and thus provide accurate frequency discrimination particularly when the edge of the absorption line is not linear [12].

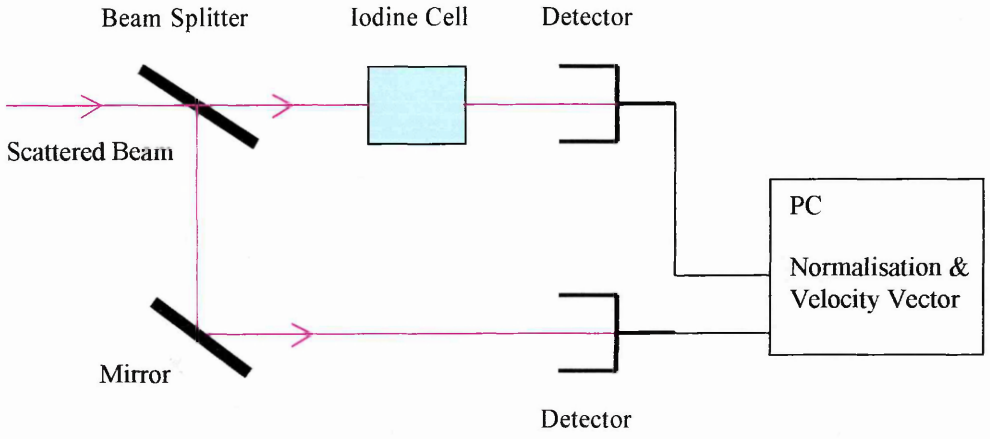

Figure 2. 10: Iodine filter based Doppler velocimeter.

The scattered beam from the measurement volume is passed through the iodine cell to the photodetector that measures its intensity. An optical referencing system is however required since the measurement of intensity fluctuations means that any changes to intensity due to e.g. laser output power changes can impress false Doppler shifts. A beam splitter is therefore used before the iodine cell to provide an unfiltered reference beam to another photodetector and this is divided into the filtered signal, a process known as normalisation that removes intensity variations imposed by factors other than the Doppler shift [11, 13-15].

It can be shown that the Doppler frequency shift is related to particle velocity by the same equation (2.1) or (2.2) above, which is derived from the scattering diagram Figure 2.1. This equation is reproduced here as equation (2.10).

$$\Delta\nu = \nu_0\left(\hat{o} - \hat{i}\right)\cdot\frac{\underline{V}}{c} \qquad (2.10)$$

where $\Delta\nu$ is the Doppler frequency shift, ν_0 is the laser frequency, $\underline{V}$ is the particle velocity and c is the velocity of light in vacuum while $\hat{o}$ and $\hat{i}$ are respectively the observer and incident unit directional vectors. It was already shown in section 2.2 that the measured component of velocity is along a bisector of the incident beam and receiver direction.

The shape of the transmission profile is influenced by the amount of vapour contained in the cell, its temperature and pressure among other things. For example the transmission function of the ALF is given by the equation [12]

$$T = \frac{I}{I_0} = \exp\left[-\Gamma \cdot \exp\left[-\left(\frac{\nu_d}{\delta}\right)^2\right]\right] \qquad (2.11)$$

where I_0 is the incident light intensity, I is the transmitted intensity, Γ is the absorption constant at resonance, ν_d is the frequency shift from the molecular resonance frequency, and δ is the thermal linewidth. The number of molecules along the beam path is related to the absorbed energy in terms of Beer-Lambert law that is expressed by

$$\frac{I}{I_0} = \exp(-\alpha L) \qquad (2.12)$$

where L is the length of the cell and α is the absorption coefficient that depends on the light frequency and on the molecular or atomic concentration of the absorbing medium. Typical cell dimensions are 80 – 100 mm in length for a cell operated around ambient temperature while cells of 40 – 50 mm in length have been applied with temperatures in the range 40 – 50 ^{0}C [12]. It is usual practice to keep these operating temperatures below 113 ^{0}C, the triple point of iodine so as to take advantage of the solid – vapour sublimation process.

It is clear from the above discussion that the iodine cell is a key component whose performance determines the accuracy of the velocimeter. Two modes of operation of the iodine cell are in common use. The saturated mode will have both solid and vapour iodine in equilibrium with each other. Temperature control for this type of cell is very critical as it controls both the vapour temperature and pressure. One design is based on a one body cell, which is however prone to vapour condensation on the windows. This problem is overcome when a cell consisting of a main body holding the vapour and side arm housing solid iodine is used. Temperature and vapour pressure control are therefore separated from each other with temperature control being applied to the main body

while vapour pressure is controlled by the temperature of the side arm. The main body temperature control is not critical (0.1 ^{0}C stability is sufficient) while the side arm temperature is very critical (0.01 ^{0}C is required) [12, 17]. The second mode of the iodine cell implementation is referred to as the unsaturated or starved cell. The temperature control of this type of cell is much more relaxed with control to within 0.1 ^{0}C being normally sufficient. The requirement is that the entire solid be vapourised above a certain minimum temperature in-order to maintain a constant gas density [16]. A more detail description and illustration of the cell structure is given in Chapter 6.

The iodine absorption linewidth is attributed to collisional, Doppler and hyperfine broadening. Collisional broadening depends on the vapour pressure of iodine and Doppler broadening is a function of temperature while hyperfine broadening is related to the hyperfine components and is not temperature dependent. This means that limited linewidth tuning is possible with Doppler broadening affecting the slope of the transfer function and therefore the sensitivity of velocity measurements [18-20]. Collisional broadening would increase the linewidth at the expense of lowering the slope thus increasing the velocity measurement range while decreasing the sensitivity. This has been implemented by the addition of a buffer gas such as nitrogen [21-23].

Limitations to the use of the iodine filter include the inability to achieve 0 – 100 % absorption which limits the velocity measurement range. Also the edges of the transfer function are not steep enough to resolve velocities less than about 1 ms^{-1} [20]. Furthermore the edges of the absorption line are not linear and this degrades the velocimeter sensitivity near the extremes of the range. The iodine ALF is also limited to those lasers whose wavelength of emission apart from being tuneable are matched to particular absorption lines.

2.6 Time of Flight

The time of flight configuration commonly known as laser-2-focus (L2F) or laser transit anemometry (LTA) provides an alternative method to the measurement of particle

velocity in fluids [24, 25]. Its principle is a simple idea based on the measurement of the fundamental physical quantities, namely the time taken to traverse a known displacement in-order to deduce the particle velocity. The configuration of the system consists of two separated, parallel, and highly focused laser beams forming a "light gate" of known width (Figure 2.11).

The beam diameter determines the system signal to noise ratio and is required to be small and constant. The beams narrowest diameter is typically 10 μm and the separation of the axes of the two beams is about 0.2 to 0.4 mm [26], which limits the spatial resolution achievable by the system. A particle moving along the focal plane produces two successive pulses of scattered light that are detected by 2 photomultiplier tube detectors.

One detector is aligned with one beam at its focal point and detects the start signal while the other detects the stop signal from the other beam. The time between the start and stop pulses is used to calculate the velocity, V by the equation

$$V = \frac{d}{t} \qquad (2.13)$$

where d is the distance separating the two beams of light and t is the time of transit. The velocity or component of velocity measured is perpendicular to the optical axis. The plane of the beams is therefore required to be parallel to the flow direction for the double pulse to be obtained. The signal processing is required to reject false double pulses that originate from 2 different particles crossing the same laser beam. The ratio of the beam diameter to beam separation (typically 10:350) in the probe volume determines an angle interval where particles might move in different directions but still intercept both beams and contribute to the time of flight data. The Gaussian beam intensity distribution will however cause particles passing through both focal points to generate higher signal amplitude than those crossing at the peripheral section.

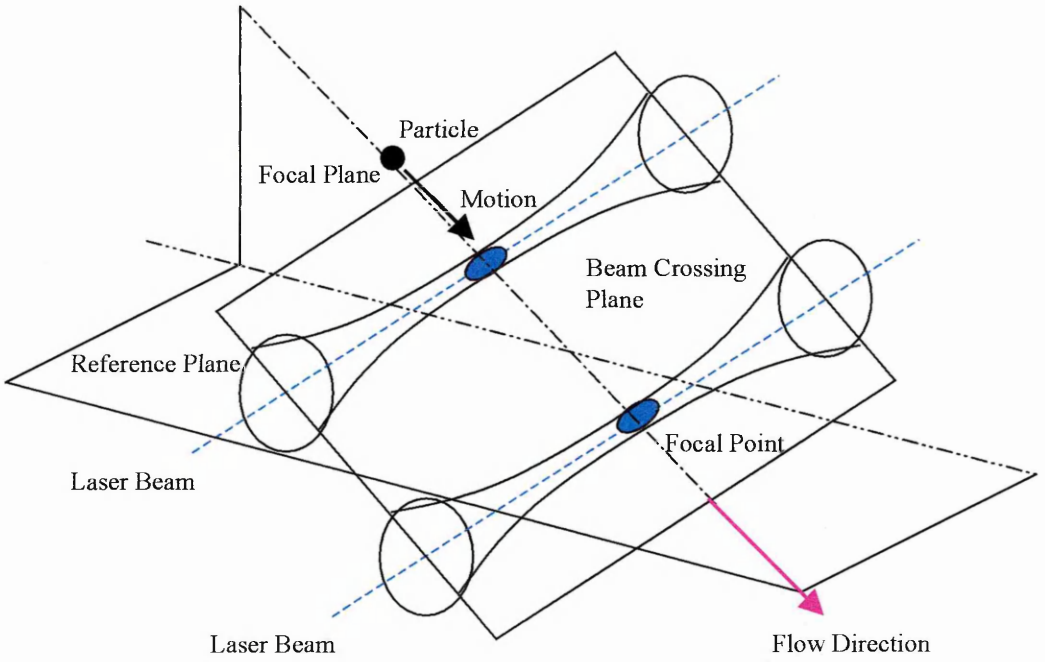

Figure 2. 11: L2F beam geometry and measurement principle.

One important advantage of the system is its significant signal to noise ratio, which is due to the fact that all the light power focused in the probe volume, contributes to the useful signal. L2F is however unable to measure high turbulence intensities and unfavourably long measuring times at high turbulence intensities (>10%) are unavoidable. The problem is partly due to a reduced probability of successful dual beam transit at high flow turbulence. The probe volume has since been redesigned by transforming the 2 small round spots (focal points) to 2 elongated dashes in-order to improve the measurement time through an increase in the length of the measurement volume [26].

Figure 2.12 is an illustration of the velocity components that are measured by the L2F velocimeter. It shows that such components always lie on the plane (transverse) perpendicular to the optical axis.

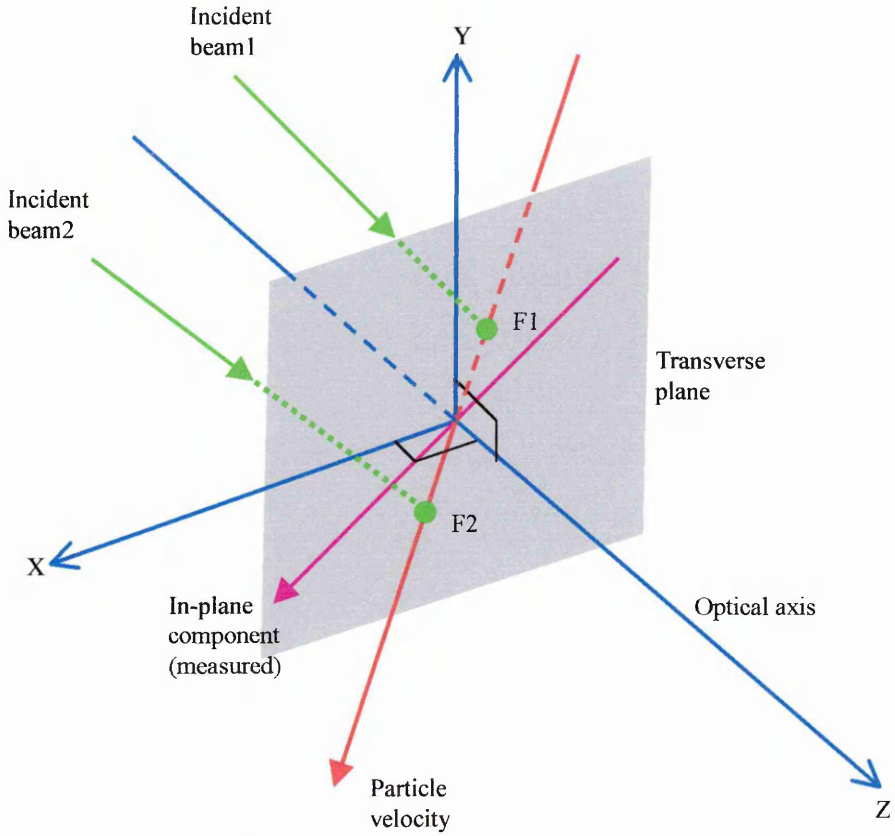

Figure 2. 12: Components of velocity measured by L2F velocimeter.

The measurement of 3D velocity components with this technique is not as straight forward as the one component system. These measurements would require another L2F channel at an angle to the first channel so that a component of velocity along the optical axis can now be measured. Such an angle can not however be made smaller than 30^0 otherwise the system resolution is seriously degraded and consequently single headed systems of this nature are not encouraged.

A rather complicated 3D L2F design consists of 2 beam pairs of different colour defining two L2F channels that cross each other to form the probe volume at their intersection (Figure 2.13) [26]. The system gives 3D velocities by taking measurements before and after rotation of the whole system.

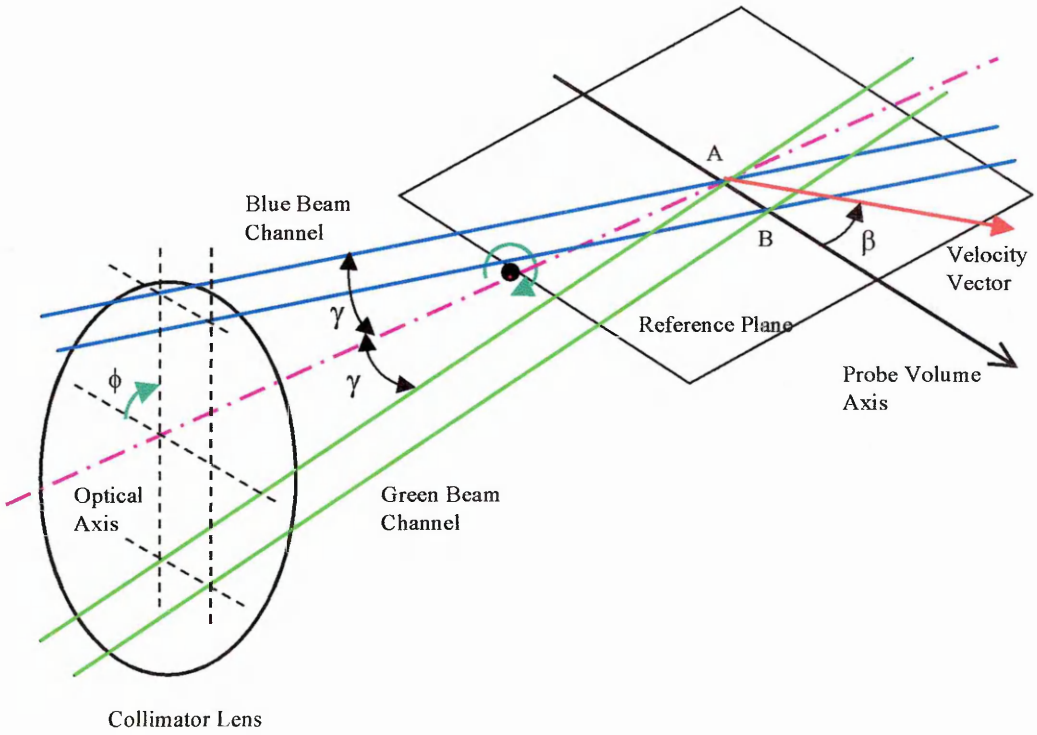

Figure 2. 13: 3D L2F system with crossed beam configuration [26].

Successful measurements can only be made when the velocity vector lies in the plane of one beam pair. The velocity vector is brought to this plane by rotating the whole system about the optical axis. A similar rotation is performed in-order to measure the flow angle, β but this time the velocity vector is made to lie in the reference plane, which is defined by the optical axis and the line joining the focal points.

An axial displacement between the start and stop beams of a 2D-multicolour L2F system (Figure 2.14) can be introduced to form an alternative 3D-velocimeter configuration [27]. The stop beam focus is displaced from that of the start beam by an angular displacement, γ. The effective probe volume length is thus reduced as shown and only flow particles within this volume will make successful dual beam transits. Two sets of measurements will have to be taken one after a rotation of the beams` plane through 180^0 and one before a rotation. The axial beam displacement gives the system sensitivity to the on-axis velocity component, which can then be measured after the rotation.

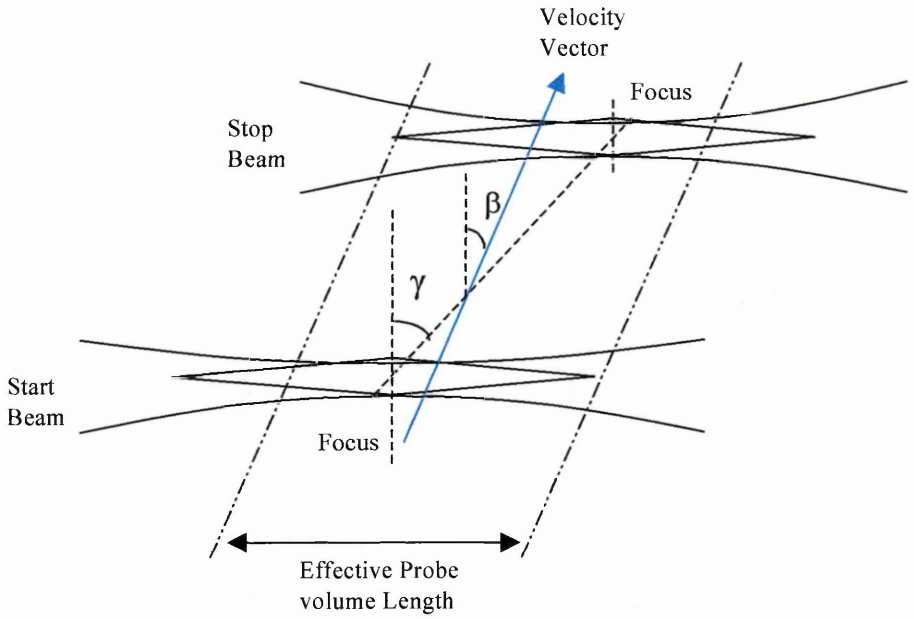

Figure 2. 14: 3D L2F system with axial beam displacement configuration [26].

2.7 Light Scattering by Particles

Laser velocimetry systems use laser beams for interrogating the flow and a suitable means of scattering the light out of the flow to the detector is therefore required. Fluid molecules would be ideal for this purpose because of their small size and therefore their ability to faithfully follow the flow but are usually too small to provide appreciable scattering. Some suitable particles may be naturally present in liquids but not often the case with gases. The general practice is therefore to artificially add specially chosen particles (seeding particles) in-order to enhance scattering efficiency and hence the signal to noise ratio at the detector. The size of the particle becomes one of the primary requirements as it determines its flow following behaviour as well as the amount of scattered light.

The study of complex flows is of major interest in laser velocimetry in-order to reveal structures such as flow mixing, re-circulation, shock waves, boundary layers, vorticity, and turbulence intensity in general and it becomes imperative that the particle should offer instantaneous response in such cases. Particles normally used have size comparable to the laser wavelength and are of the order of 1 μm in diameter, which fall

in a scattering regime that is well known as "Mie scattering" [28]. A sufficiently high particle number density is required in-order to continuously track the flow otherwise the time taken to accumulate data will be prohibitive.

Also important are the optical properties of the seeding particles particularly the refractive index. One important parameter is the size parameter, x defined by

$$x = \frac{2\pi m a}{\lambda} \qquad (2.14)$$

where a is particle radius, m the flow refractive index, and λ is the laser wavelength. This parameter defines three general scattering regimes, which are Rayleigh, Mie, and Geometrical scattering and are given by $x \leq 1$, $1 \leq x \leq 500$, and $x \geq 500$ respectively.

Solutions to Mie scattering problems are complex and analytical solutions exist only for spherical particles [28, 29]. A model was developed in Mathcad^{TM} and some results and the calculation procedure is given in Appendix C. The magnitude and angular distribution of light scattered from a particle depends on its size, shape and refractive index. The results show that the scattering varies with angle in a complicated way and is different for the two-othorgonal polarisations of light. Generally the scattering in the forward direction has a strong maximum compared to a weak maximum in the backward direction and the ratio of the two is usually in the range 100-1000. Side scatter shows a minimum, which is generally in the angular range of 100-140^0. The model results are important in several ways for it enables the choice of suitable seeding particle properties as well as the detector distance from the flow and its angular positioning. Figure 2.15 is an example of the directional dependence of scattered light on the incident polarisation.

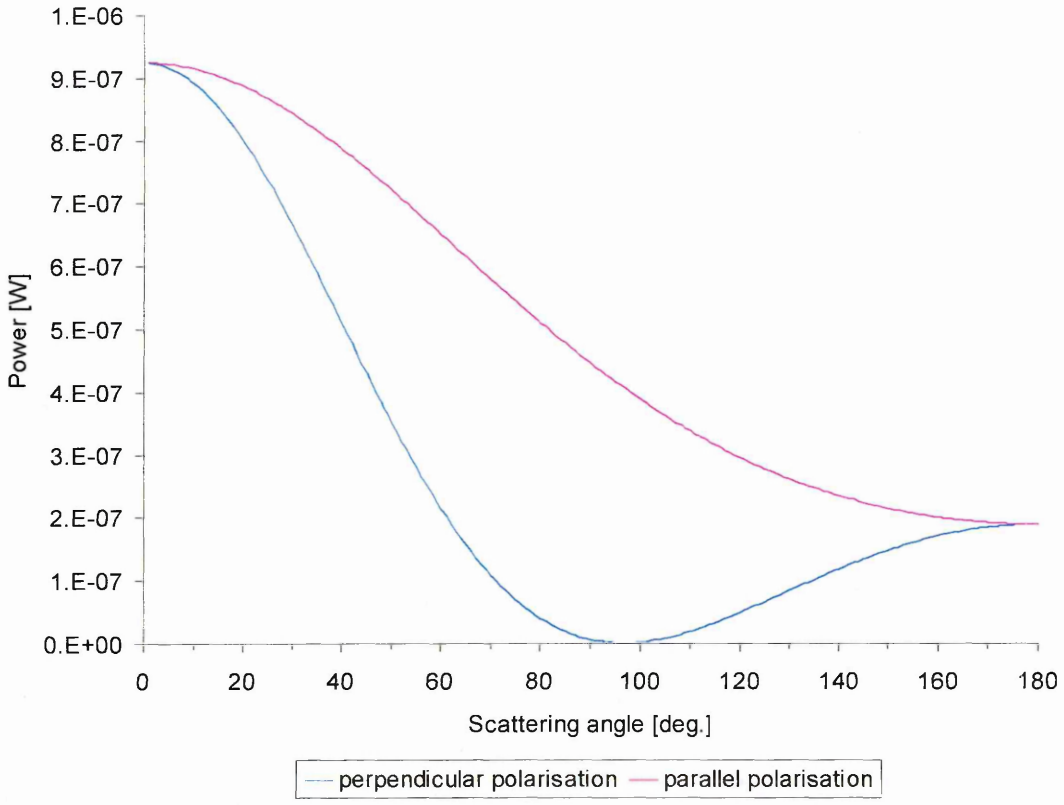

Figure 2. 15: Scattered power for a particle of 0.2 μm diameter of refractive index 1.5 that is illuminated with light of 514.5 nm wavelength (Appendix C).

2.8 Summary

Two main velocity encoding schemes namely the Doppler shift and time-of-flight have been described. Methods for measuring the Doppler shift frequency via heterodyne techniques to produce a beat signal or direct measurement using an absorption line filter were presented. The operating principles including limitations of the most important non-intrusive point measurement schemes LDV, L2F and molecular filter based laser Doppler velocimetry were introduced and some comparison results are given in Table 2.1. More about the performance of these and interferometric velocimeters are discussed in Chapter 3. Since a laser beam is used in all these systems to interrogate the flow the scattering from seeding particles was discussed but a detailed approach is given in Appendix C.

Technique	*Advantages/Principles*	*Disadvantages*
Reference beam	- heterodyne technique - measures directly the "in-line" component of velocity - makes time averaged measurements	- poor SNR - high beat frequency limits velocity range to ~ 30 ms^{-1} (100 MHz - P) - difficult to align (bulk) - long measurement volume ~ 500 μm - uses Bragg cell for direction measurement
Doppler difference	- heterodyne technique - high SNR and no alignment problem - time averaged measurements - measures "in-plane" velocity components	- uses Bragg cell for directional discrimination - electronic processors limit velocity range - inaccurate for "in-line" component
Filter based	- uses atomic absorption line for direct frequency measurement - measures the "in-line" component of velocity - automatic directional discrimination	- velocity range limited by filter frequency bandwidth to ~ 300 ms^{-1} - slope of filter transfer function limits velocity resolution to ~ 1-2 ms^{-1}
L2F	- time of flight measurement and has high SNR - measures "in-plane" velocity components - directional discrimination from pulse arrivals - no limited velocity range	- inaccurate for "in-line" component - limited to low turbulence intensity , 30 %

Table 2.1: Summary of the techniques. P-processor.

References

[1] Y. Yeh and H. Z. Cummins, "*Localised fluid flow measurements with an He-Ne laser spectrometer*", Applied Physics Letters, vol. 4, no. 10, pp. 176-178, 1964.

[2] T. Durrani and C. Greated, "*Laser systems in flow measurement*", Plenum Press, New York, 1997.

[3] F. Durst, A. Melling, and J. H. Whitelaw, "*Principles and practices of laser Doppler Anemometry*", 2nd Edition, 1981.

[4] E. Siegman, "*The antenna properties of optical heterodyne receivers*", Proceedings of the IEEE, vol. 5, no. 10, pp. 1350-1356, 1966.

[5] J. F. Meyers, "*The elusive third component*", International Symposium on Laser Anemometry, ASME, pp. 247-254, 1985.

[6] S. W. James, R. P. Tatam and R. L. Elder, "*Design considerations for three dimensional fibre optic laser Doppler velocimeter for turbomachinery applications*", Review Scientific Instruments, vol. 8, pp. 3241-3246, 1997.

[7] L. E. Drain, "*The Laser Doppler Technique*", John Wiley and Sons, 1980.

[8] D. Egan, "*In-Line Fibre Optic Laser Doppler Velocimetry for Turbomachinery Applications*", PhD Thesis, 2000.

[9] L. Lading, G. Wigley, and P. Buchhave, "*Optical Diagnosis for Flow Processes*", Plenum Press, 1994.

[10] B. M. Watrasiewicz and M. J. Rudd, "*Laser Doppler Measurements*", Butterworths, 1976.

[11] H. Komine and S. J. Brosnan, "*Instantaneous three component Doppler global velocimetry*", Laser Anemometry, ASME 1, U.S. Patent No. 4, 919, 536.

[12] R. L. McKenzie, "*Planar Doppler Velocimetry for large scale wind tunnel applications*", AGARD FDP Symposium on Advanced Measurement Technology, Seattle, USA, 1997.

[13] T. J. Beutner, G. S. Elliott, G. W. Williams, H. D. Baust, J. Crafton and C. D. Carter, "*Forebody and leading edge vortex measurements using planar Doppler velocimetry*", Measurement Science and Technology, 12, pp. 378-394, 2001.

[14] J. Crafton, C. D. Carter and G. Elliott, "*Three-component phase-averaged velocity measurements of an optically perturbed supersonic jet using multi-*

component planar Doppler velocimetry", Measurement Science and Technology, 12, pp. 409-419, 2001.

[15] M. S. Reinath, "*Doppler global velocimeter development for large wind tunnels*", Measurement Science and Technology, 12, pp. 432-441, 2001.

[16] V. S. S. Chan, A. L. Heyes, D. I. Robinson, and J. T. Turner, "*Iodine absorption filters for Doppler global velocimetry*", Meas. Sci. Technol. 6, pp. 784-794, UK, 1995.

[17] T. J. Buetner and H. D. Baust, "*Recent developments in Doppler global velocimetry*", AGARD FDP Symposium on Advanced Aerodynamic Measurement Technology, Seattle, USA, 1997.

[18] I. Roehle, "*Three dimensional Doppler global velocimetry in the flow of a fuel spray nozzle and in the wake region of a car*", Flow Meas. Instrum., vol. 7, no. ¾, pp. 287-294, 1996.

[19] H. Komine, S. J. Brosnan, W. H. Long, and E. A. Stappaerts, "*Doppler Global Velocimetry–Development of a flight research instrumentation system for applications to non-intrusive measurements of the flow field*", NASA Contractor Report 191490, 1994.

[20] R. L. McKenzie, "*Measurement capabilities of planar Doppler velocimetry using pulsed lasers*", Applied Optics, vol. 35, no. 6, 1996.

[21] P. S. Clancy and M. Samimy, "*Multicomponent velocimetry in high speed flows using Planar Doppler Velocimetry*", Paper AIAA 97-0497, 35th Aerospace sciences meeting & exhibit, Reno, NV, 1997.

[22] P. S. Clancy, M. Samimy, and W. R. Erskine, "*Planar Doppler Velocimetry: Three component velocimetry in supersonic jets*", Paper AIAA 98-0506, 36th Aerospace sciences meeting & exhibit, Reno, NV, 1998.

[23] G. S. Elliot, M. Samimy, and S. A. Arnette, "*Details of molecular filter based velocimetry technique*", Paper AIAA 94-0490, 32nd Aerospace sciences meeting & exhibit, Reno, NV, 1994.

[24] I. Trebinjac, A. Vouillarmet and I. Claudin, "*Refinements of a L2F anemometry technique for inter-blade flow field investigations*", Proceedings of the 16th International Congress on Instrumentation in Aerospace Simulation Facilities, pp. 54.1-54.6, Ohio, 1995.

[25] X. Ottavy, I. Trebinjac and A. Vouillarmet, "*Treatment of L2F anemometer measurement volume distortions created by curved windows for turbomachinery applications*", Measurement Science and Technology, 9, pp. 1511-1521, 1998.

[26] R. Schodl, "*Laser Transit Velocimetry*", Lecture Series 1991-05, pp. 1-195, 1991.

[27] R. Schodl and W. Forster, "*A multi colour fibre optic laser two focus velocimeter for 3-dimensional flow analysis*", AIAA-88-3034, July 1988.

[28] H. C. van de Hurst, "*Light scattering by small particles*", John Wiley and Sons, 1957.

[29] R. J. Martin, "*Full-field Doppler Anemometry*", MPhil Thesis, Cranfield University, UK, 1993.

CHAPTER 3

Review of In-Line Laser Doppler Techniques

3.1 Introduction

The principles of measurement of the techniques described in this chapter were discussed in Chapter 2 along with the measurement coordinate system. The definitions and relations between the "in-plane" and "in-line" components of velocity are described by Figure 1.1 in Chapter 1. The velocity components that are measured by each technique have also been discussed in Chapter 2. This chapter reviews the developments of the laser techniques particularly for the measurement of the in-line component of velocity and included are the advantages and disadvantages they carry.

3.2 Laser Doppler Velocimetry

LDV measurement of three velocity components usually implies a compromise in the accuracy of measurement of one component. The in-plane components have been measured with about equal precision while the on-axis component has been dubbed an "elusive component" [1] due to very low precision in its measurement. High power laser sources are required since LDV images light scattered by individual particles and their scattering efficiency is low.

3.2.1 Reference Beam Configuration

The reference beam technique was the first to exploit the Doppler shift in scattered laser light to measure fluid velocities and was first conceived by Yeh and Cummins in 1964 [2]. They discovered that the spectral linewidth of laser light passed through a water cell seeded with polystyrene particles was spectrally broadened, which was an effect due to

the Doppler shift in frequency caused by particles moving with the flow. The principle of the technique is to mix together at the photomultiplier tube detector, a reference laser beam with a beam scattered off the particles in the measurement volume (Figure 3.1). Both laser beams are derived from the same source. Later variations of this technique included heterodyning unscattered light through the flow with scattered light from the same measurement volume along the reference beam direction, a technique that eased alignment problems [3].

Apart from its ability to provide a direct measure of the on-axis velocity component, the technique suffers from several limitations. These include poor signal to noise ratio due to the constraints of the coherence requirement [4] that requires use of a small collection aperture, the need for precise wave front alignment, and a limited velocity range due to high signal beat frequency. The technique is hampered by background flare from solid surfaces and also the measured frequency shift is dependent on the direction of viewing.

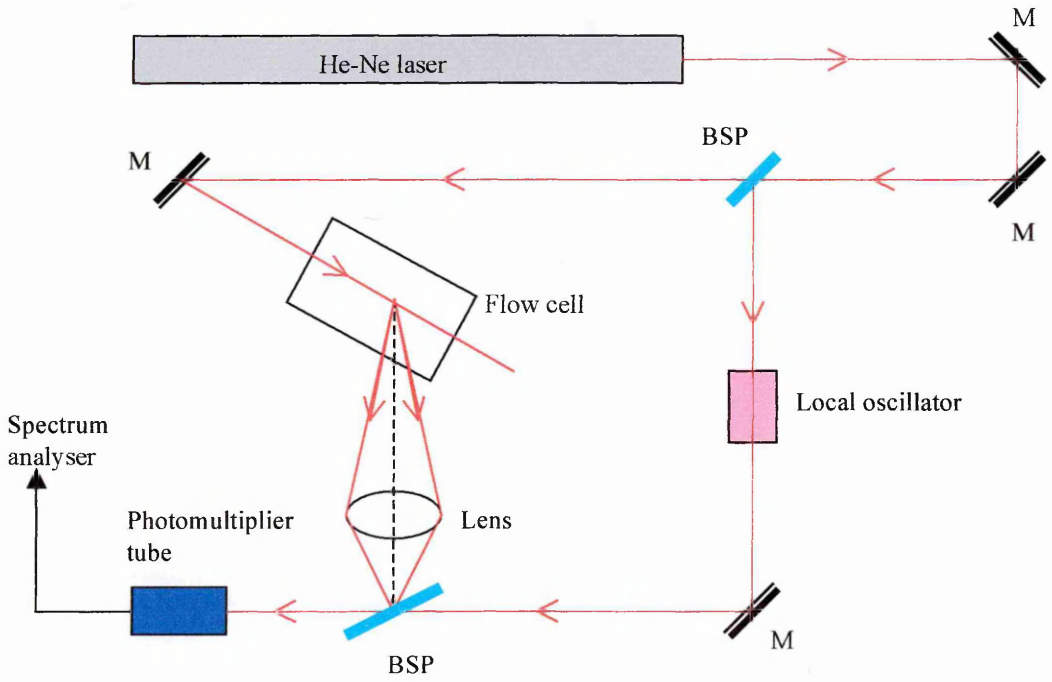

Figure 3. 1: Reference Beam Laser Doppler Velocimeter [2].

BSP- beam splitter, and M – Mirror.

These problems continue to prompt further research and development. The use of guiding properties of optical fibres and their small sized core diameters has significantly improved alignment problems and flare rejection in optical fibre systems [5-10]. Other issues pertaining to component size and cost have been addressed and these include the replacement of bulk gas lasers with diode lasers and the introduction of semiconductor detectors, the result being a miniaturised (portable) instrument.

The first 3D system was based around a reference beam technique [11] (Figure 3.2).

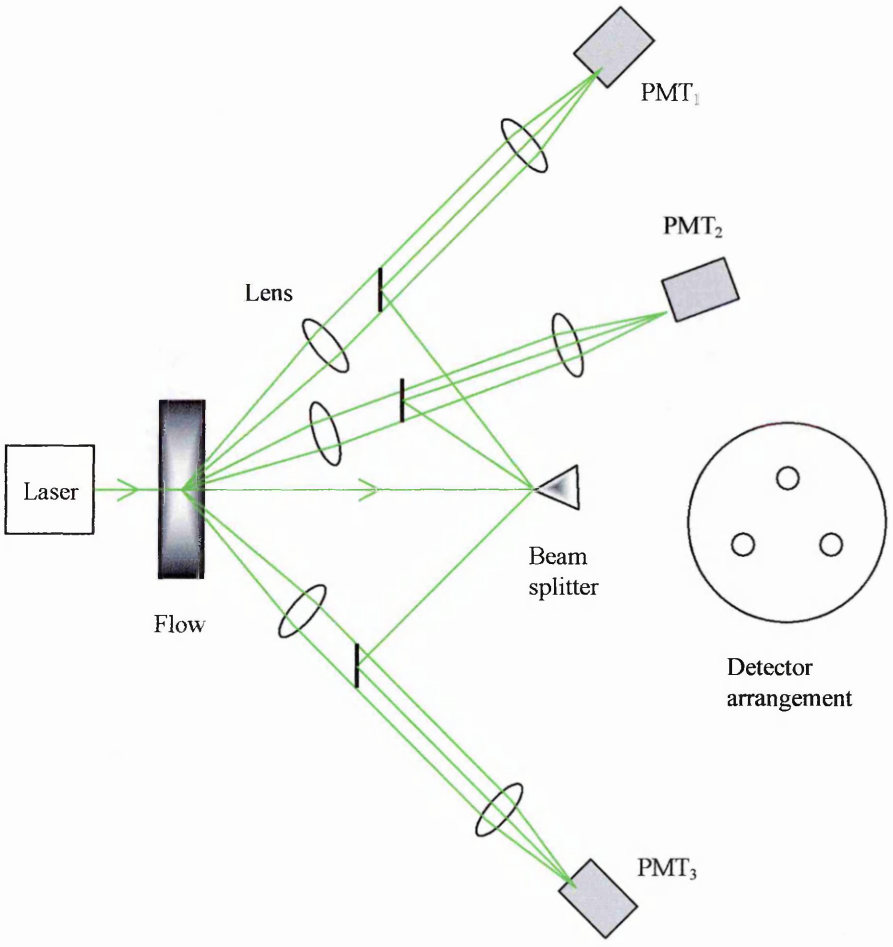

Figure 3. 2: The first 3D Reference beam system [11].
PMT – Photomultiplier tube.

It consisted of one illumination direction and three non-coplanar viewing directions that were off-axis at 120^0 to each other in forward scatter. A tetrahedral prism was used to split the beam into three reference beams, one for each photomultiplier tube detector.

The system was difficult to implement due to alignment problems, poor signal to noise ratio caused by the small solid angle that was used for light collection, and large shot noise associated with the high beam power ratio. The approach produced large coordinate transformation errors when transforming from a non-orthogonal to an orthogonal system and was therefore unsuitable for 3D measurements which prompted further research into alternative configurations.

3.2.2 Doppler Difference Configuration

The Doppler difference technique is an extension of the reference beam system and is mainly designed to improve on its signal to noise ratio. Two strong, approximately equal intensity beams are mixed and brought to a focus at the measurement control volume where they interfere (Figure 3.3).

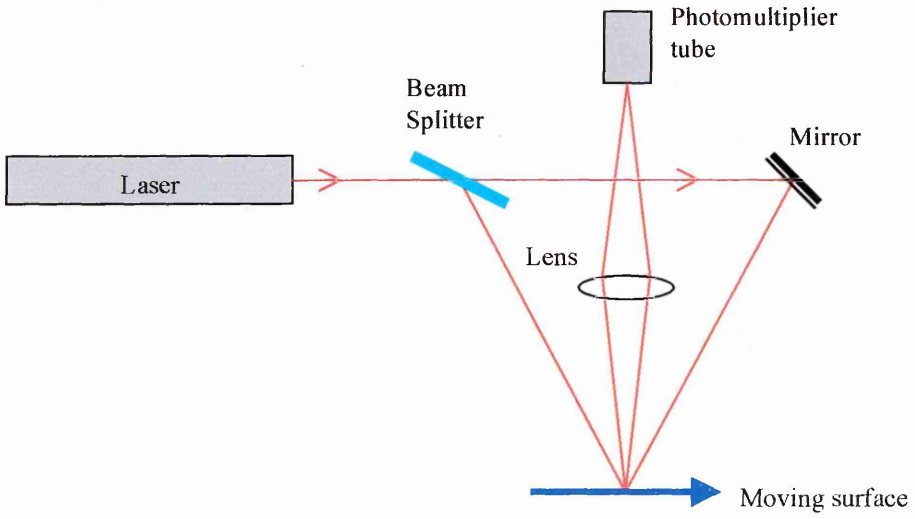

Figure 3. 3: Doppler Difference technique in back scatter mode [12].

The interference pattern is often modelled as consisting of interference fringes such that a particle crossing these fringes scatters light of high and low intensity at a rate proportional to its velocity (equation 3.1).

$$\nu = \frac{2V\cos\beta\sin\left(\alpha/2\right)}{\lambda} \qquad (3.1)$$

The frequency modulation (Doppler shift) is ν for a particle moving with velocity V at an angle β normal to the fringe planes where α is the angle between the illumination beams. The measured Doppler frequency is independent of viewing angle and wide collection apertures are possible without any degradation in the signal to noise ratio [12, 7].

The frequency range of the technique is adjusted by varying the illumination beam geometry, independently of the direction of observation. A wide range of variations of this technique has been developed. The technique, although a significant development over the reference beam, cannot however make direct measurements of the on-axis velocity component where a single entrance port to the flow is available. The technique measures velocity components that are transverse (orthogonal) to the optical axis. At least two Doppler Difference channels each measuring one component inclined at an acute angle to each other is required (on one probe head) for 2D measurements with the third component obtained by a rotation of one channel for a flow whose access is restricted to only one entrance port [13]. The inclined channels give the instrument its sensitivity to the on-axis component of velocity but the transformation from a non-orthogonal to an orthogonal system imposes accuracy penalty. Three orthogonal channels [Figure 3.4] would directly measure the on-axis and the two transverse components of velocity [13-15]. The figure shows 3 Doppler difference channels (blue, green and purple) all crossed orthogonally at a common measurement volume. A common lens focuses the crossed green and purple channels. Three photomultiplier tube detectors each for a different channel are used for signal detection.

Most suited to 3D measurements is the combined 2-component Doppler Difference and 1-component Reference beam arrangement [16, 17]. However the reference beam is hindered by its poor spatial resolution (due to long measurement volume although a slight off axis collection may be used), and is very sensitive to light scattered from wind tunnel walls and windows apart from the limitations discussed above. Commercial

systems are therefore based on 3 Doppler Difference systems that are inclined to each other by some small angles.

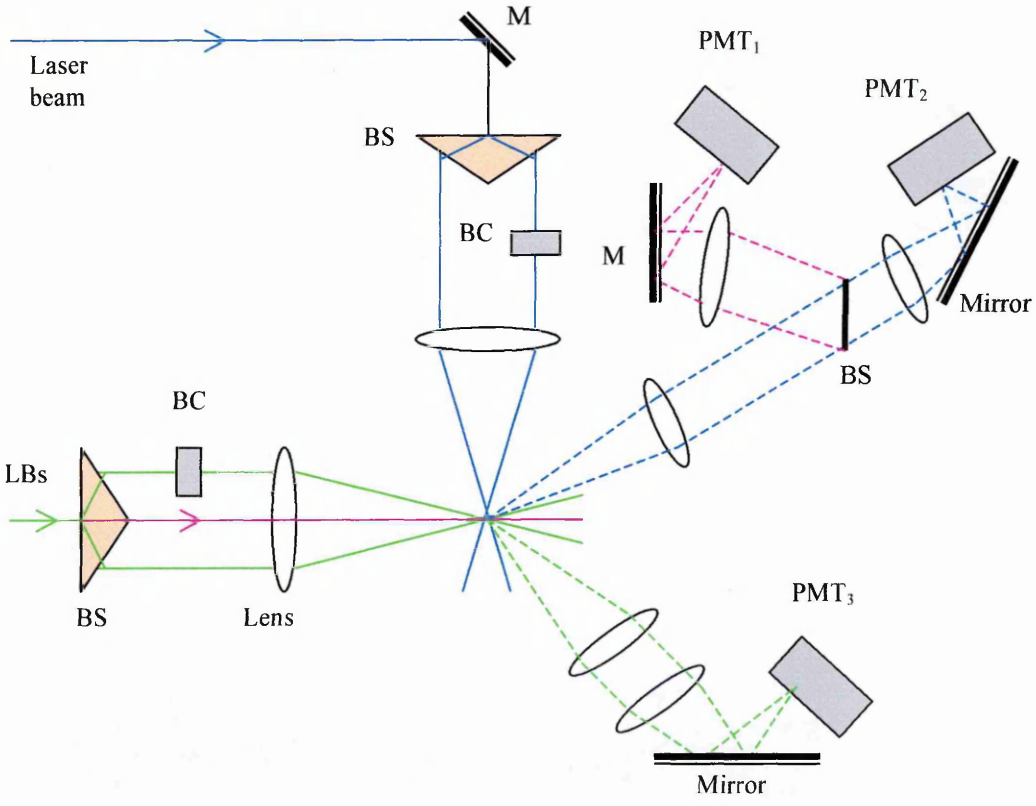

Figure 3. 4: 3D Orthogonal crossed Doppler difference channels [15].

LBs – 2 laser beams, BS – beam splitter, M – mirror, BC – Bragg cell, PMT – photomultiplier.

The most commonly used is the 3D Doppler Difference system for multicomponent velocity measurements. A direct accurate measure of the three components has been done with three orthogonal Doppler Difference channels from three-probe heads. However many optical applications such as turbomachinery and aerospace combustors have limited access typically one window and this favours systems that use a single probe head. A single probe head consisting of 3 Doppler Difference channels or alternatively 2 probe heads [Figure 3.5] often used with the channels at a small coupling angle typically 20^0 – 30^0 [18]. Such small coupling angles cause large uncertainties in the on-axis component. This further confirms the elusiveness of the third (on-axis) component of velocity to accurate measurements and hence the need for continued research to come up with an accurate 3D velocimeter.

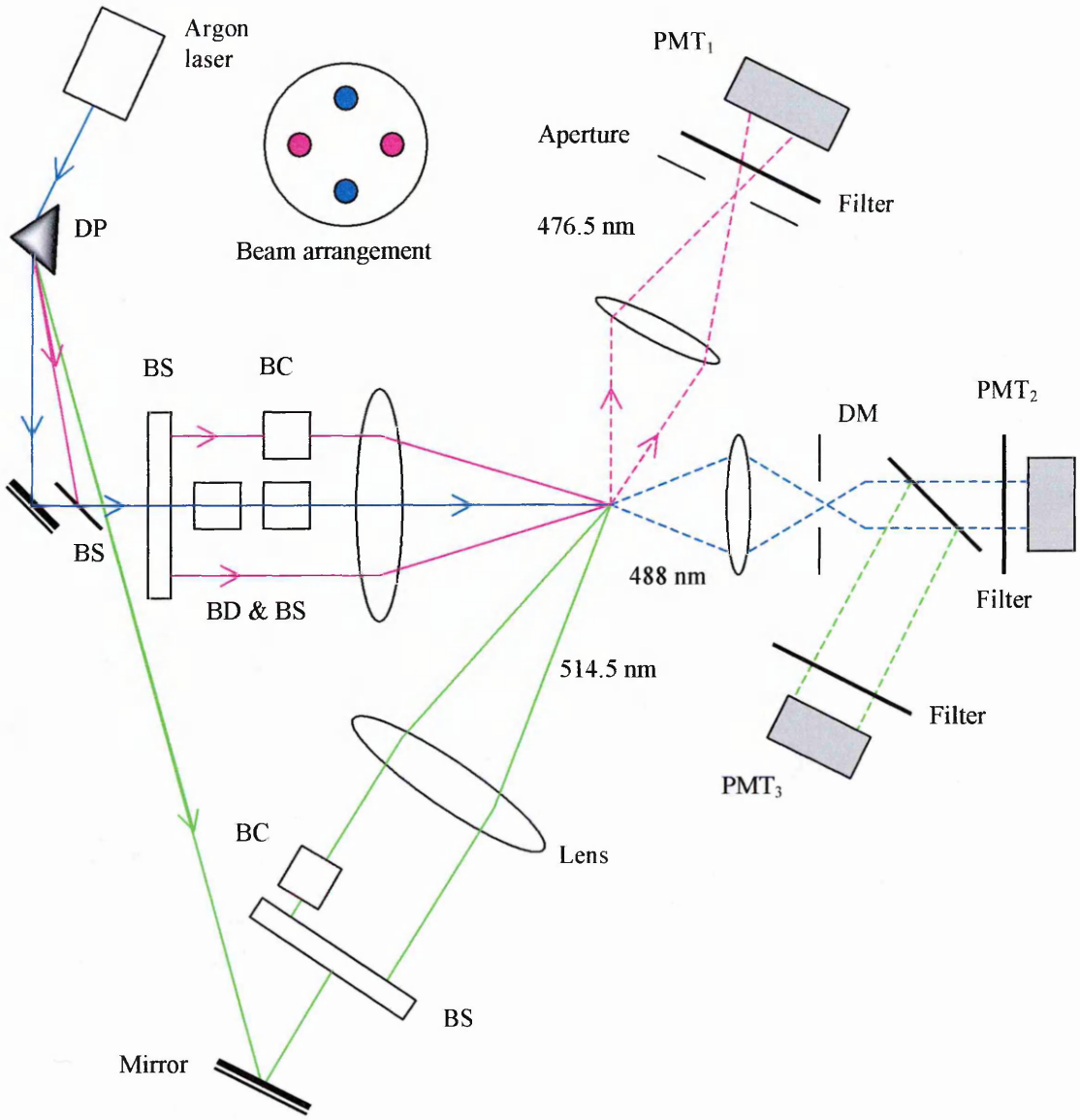

Figure 3. 5: 3D Doppler difference colour separated velocimeter [18].

DP – dispersion prism, BS – beam splitter, DM – dichroic mirror,
PMT – photomultiplier tube, BD – beam dispersion.

3.3 Laser-Two-Focus Velocimetry

Laser-Two-Focus (L2F) velocimetry is a well-established technique in laser velocimetry that was first conceived in 1968 [19], about four years after the discovery of LDV. L2F has significant signal to noise ratio as all scattered light from the tightly focussed beams contribute to the signal and this makes it ideal for probing high speed, narrow blade channel and boundary layer flows. The technique is however unsuitable for high

turbulence intensities (restricted to less than 30%) as the probability of a successful dual beam transit reduces [20].

A "light gate" is produced by highly focussing two parallel light beams into the flow region. The velocity is then obtained from the time of flight of a particle passing through both the light beams along the focal plane. Measurements were made inside rotating blade channels by periodically switching the laser beam using a light chopper (Figure 3.6) [21]. A minimum distance from a scattering surface is typically 1 mm. An important parameter in L2F is the beam diameter (typically 10 μm) to beam separation ratio (typically 10/350), which determines the probability of successful interception of both beams.

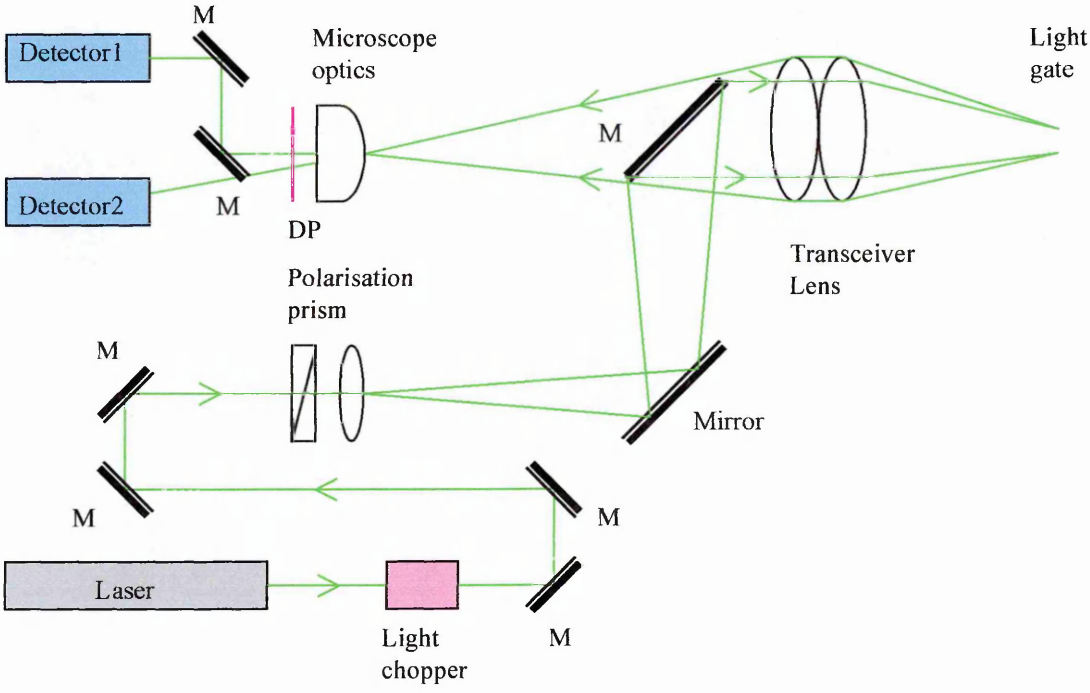

Figure 3. 6: Schematic of the L2F Velocimeter [20].

The principle of the L2F technique is to measure the velocity component along the axis joining the two beams and thus perpendicular to the optical axis. This means that at least two orthogonal L2F optical heads will have to be installed in order to perform a direct measurement of the on-axis component of velocity, which may not be compatible with restricted access flows. Practical commercial systems however exists that use two

inclined channels from which the three velocity components are calculated. Single optical head configurations have also been implemented either utilising a multicolour crossed-beam technique or an axial probe-volume displacement technique [21] (see Chapter 2). Spatial resolution for L2F is poor being typically 0.2 to 0.4 mm.

3.4 Interferometer based Velocimetry

3.4.1 Fabry-Perot Interferometer

This technique performs direct measurements of the on-axis component of velocity while imposing no upper frequency limit. However the measurement of low velocities is made difficult by the high stability requirements of the laser frequency and the need to have extremely high resolution. The light gathering power of the interferometer is not limited by the antenna theorem although this advantage tends to be offset by its relatively low transmission. When used in its scanning mode, the mirror separation of the interferometer is continuously changed thereby providing a variable-frequency narrowband filter that limits observation to those particles whose Doppler shifted frequency coincides with the interferometer transmission frequency.

One such technique employed a plate Fabry-Perot (FP) interferometer scanned through one free spectral range (FSR) that was used to measure velocity in two-phase flow [22]. The results did not agree with theory especially in the low velocity regime. Jackson and Paul [23] developed a more stable confocal FP that measured Doppler frequency shifts in excess of 300 MHz, well beyond the limit of the reference beam LDV (Figure 3.7).

The FSR of the FP interferometer was 2 GHz with a resolution of 7.5 MHz and finesse of 300. Comparisons of the results with measurements taken by a Pitot tube were in good agreement and the accuracy was found to be better than 0.5 %. The determination of direction of velocity is unambiguous and the system is not limited by the shot noise of the local oscillator unlike the reference beam LDV. The workers proposed that the velocity range could be extended downwards by decreasing the FSR of the Fabry-Perot [24]. It was suggested that the cavity length of the confocal Fabry-Perot (CFP) be made

equal to half the cavity length of the laser, a condition that would superimpose all laser modes thereby eliminating the need to have the fundamental transverse electromagnet (TEM_{001}) mode. They demonstrated theoretically that a laser velocimeter incorporating such a CFP and operated in backscatter mode could measure velocities down to 0.25 ms^{-1}.

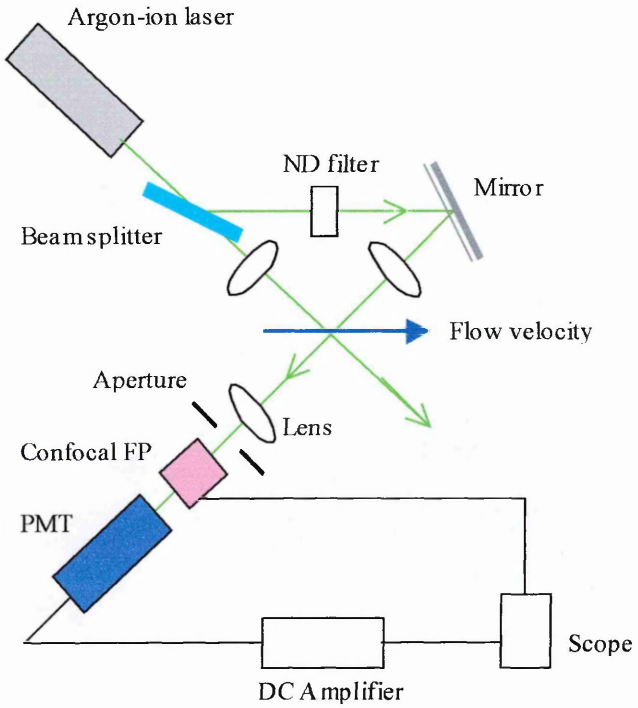

Figure 3. 7: Symmetric optical arrangement of the scanning Fabry-Perot interferometer showing the velocity vector to which the instrument is sensitive [22].
ND – neutral density filter, PMT – photomultiplier tube.

Further developments to the CFP laser velocimetry were implemented [25] but this time the CFP was used in its static mode in order to perform instantaneous supersonic velocity measurements (Figure 3.8).

Theoretical studies were carried out to design an aperture that was able to transform the well-known non-linear dispersion of the CFP into a linear relationship between its transmission intensity and the Doppler frequency shift of the scattered light. The time response of their instrument was 1 μs, which is essentially the product of the transit time of the light inside the FP, and the finesse. Instrument accuracy therefore depends on

finesse, aperture design, and alignment of the aperture with the FP ring system. It was further proposed that if the aperture was omitted and the FP was resonantly driven then the instrument response time could be improved to 0.1 μs or less. This idea was derived from a similar application originally conceived nearly 10 years earlier [26] but using a plate FP that was more unstable.

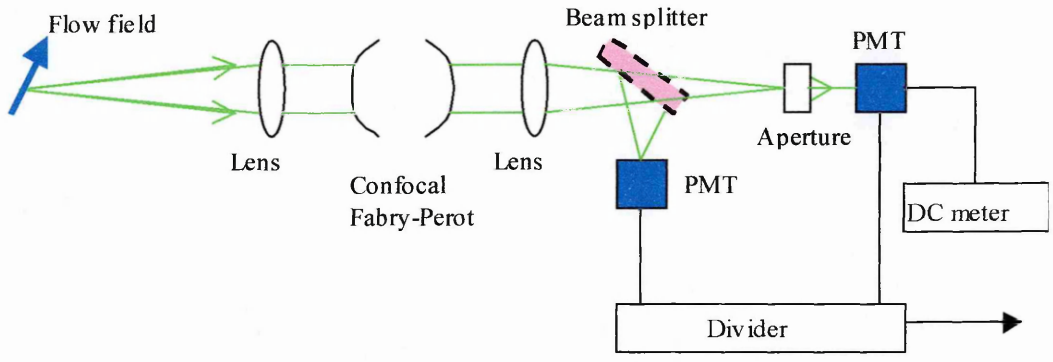

Figure 3. 8: Static Fabry-Perot system for the measurement of unsteady flow fields with high turbulence intensity [24].

PMT – photomultiplier tube.

Later to follow [27] was a comprehensive application of both the scanning and static CFP for velocity measurements in a wide variety of experimental situations including flows with interacting shock fronts, turbulence, and large velocity gradients in a windtunnel and free jet. The technique did not require seed particles because dust and naturally condensing water particles provided enough signals, which demonstrates the high sensitivity of the system. Comprehensive electronic control techniques and a digital memory system were adopted to minimise the effects due to laser frequency fluctuations and non-linearity in the CFP piezoelectric drive. The spatial resolution and response to turbulence of the system were experimental measured.

A laser anemometer based on a confocal FP interferometer was developed to measure a small on-axis velocity component in a turbomachinery flow with a large transverse component [28] (Figure 3.9).

A Bragg cell generated a reference signal at a known offset frequency from that of the laser and this was used for the frequency calibration of the velocimeter. A data acquisition and processing technique that was adopted enabled the storage of data in histogram format with each histogram constituting 256 bins for a single sweep of the FP interferometer. Data processing by the computer could be done in one of the two modes. In the first mode a histogram was generated from either a single sweep of the FP or from multiple sequential sweeps added bin-by-bin.

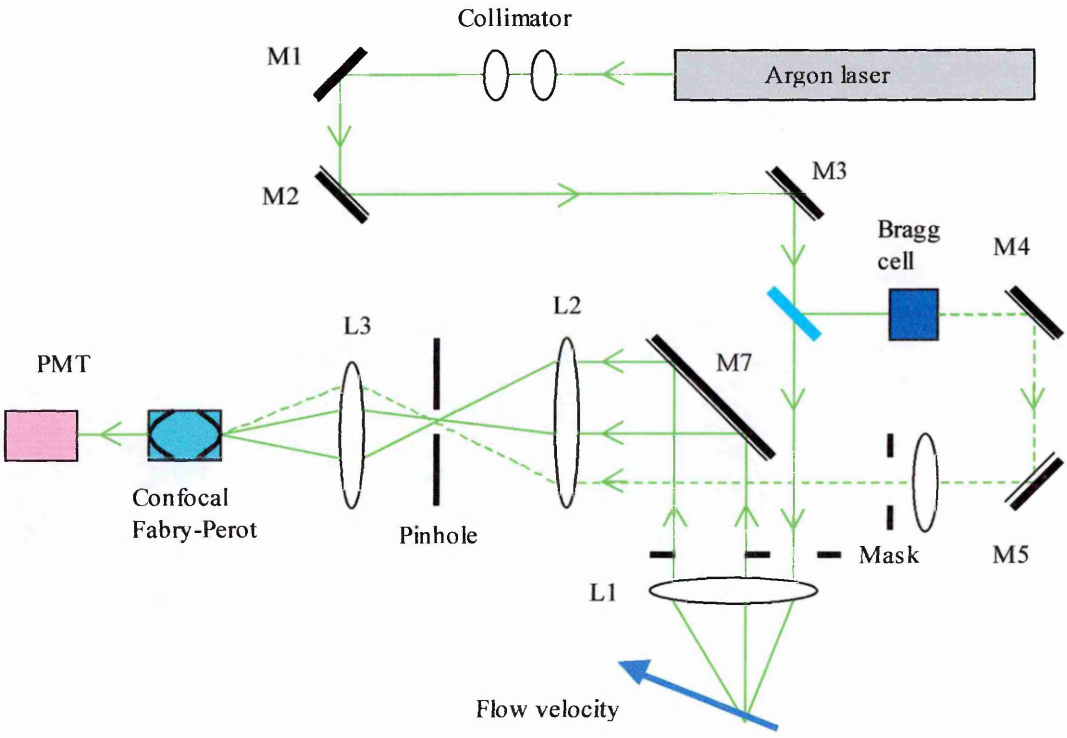

Figure 3. 9: Optical configuration for measuring small optical-axis velocity component with a static confocal Fabry-Perot interferometer [27].

PMT – photomultiplier tube, M – mirror, L – lens.

In the second mode two histograms were generated where one corresponded to data taken during even number sweeps and the other corresponded to data taken during odd number sweeps. This was useful, as the flow could be seeded during even number sweeps only. The difference between corresponding counts from the two histograms therefore represented the spectrum of only light scattered from the seed particles. This operation was required to attenuate light scattered from surfaces near the probe volume thus allowing measurements close to surfaces to be made.

The use of the Bragg cell also permitted a laser frequency-drift compensation scheme to be implemented. The peak of the Bragg cell spectral line was locked to a particular bin in the histogram by comparing the sum of the counts in two ranges consisting of an equal number of bins on each side of the reference bin. The computer then generated an analogue voltage that was used to adjust the offset voltage of the ramp generator (applied to the FP) to maintain an equal number of counts in each range. The anemometer was able to measure turbulence intensities of about 2.5 % in both a subsonic free jet flow and in a full annular cascade of 36 turbine stator vanes. The instrument was however unable to take measurements closer than about 7 mm from the hub due to increased amount of unshifted light from surfaces. The authors adopted a similar backscatter configuration employing the confocal FP interferometer to measure three components of velocity [29]. They discovered that the measurement accuracy of the transverse components of velocity was poor but quite good for the on-axis component.

In their next 3D measurements they incorporated a dual-scatter LDV for the measurement of the transverse components while the confocal FP measured the on-axis velocity component in an annular turbine stator cascade facility [30] (Figure 3.10). The passband of the FP was scanned over a frequency range that included the laser frequency, the Doppler shifted frequency of light scattered from the seed particles, and the Bragg shifted reference frequency. The system did not require a large window for optical access. The FP measurements could be made to 3 mm of the hub but not any closer and the on-axis velocity fluctuations were about 7 % of the magnitude of velocity.

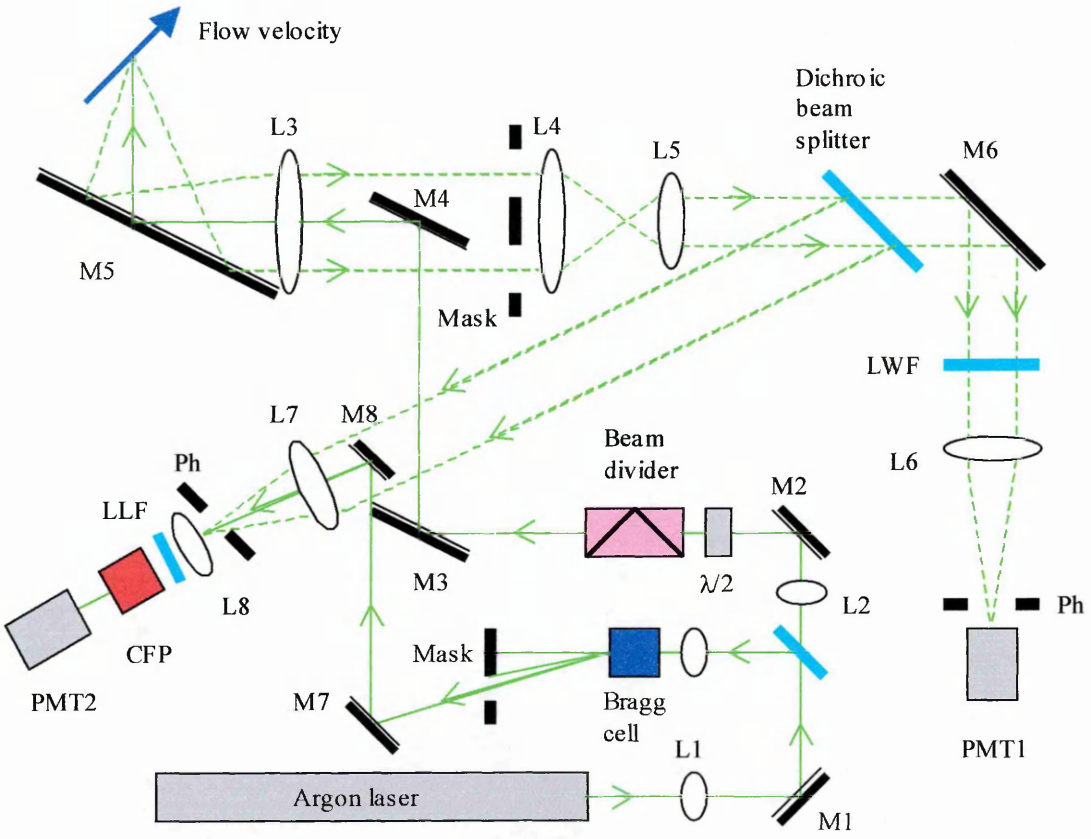

Figure 3. 10: Optical configuration for the measurement of on-axis velocity component in an annular turbine stator cascade facility [29].

PMT – photomultiplier tube, L – lens, M – mirror,
CFP – confocal Fabry-Perot, Ph – pinhole.

3.4.2: Michelson Interferometer

Another approach to spectrometric velocity measurements was later applied in the form of a phase-stabilised Michelson interferometer. The technique could however not replace the FP interferometer as it also tended to suffer from vibrations and was therefore limited to higher velocities [31].

The phase-stabilised Michelson interferometer generates a continuous electrical signal following proportionally and with a microsecond time resolution the Doppler changes in the laser light wavelength such that a real-time velocity recording is achieved [31]. The velocity range of the technique has no upper limit but its ability to resolve low velocities is however limited mainly by laser wavelength fluctuations.

The argon-ion laser wavelength was stabilised by controlling one cavity mirror that was mounted on a piezoelectric element. Part of the original laser beam was directed through an etalon, which acted as a reference Michelson interferometer (that had a large optical path difference) using a folded light path between two mirrors (not shown in Figure 3.11). This phase-stabilisation system applied to the reference Michelson interferometer was similar to that of the spectrometer. Laser wavelength fluctuations are reported to have been reduced by a factor of ten. The system achieved a velocity resolution of 0.1 ms^{-1}.

The system was however still liable to drift due to thermal effects that change the optical path difference of the Michelson interferometer whereas thermal dilatation of the laser cavity changes the wavelength. The problem was overcome by sending part of the original collimated laser beam into the spectrometric Michelson interferometer from the top side (not shown in Figure 3.11) to set up yet another phase-stabilisation system.

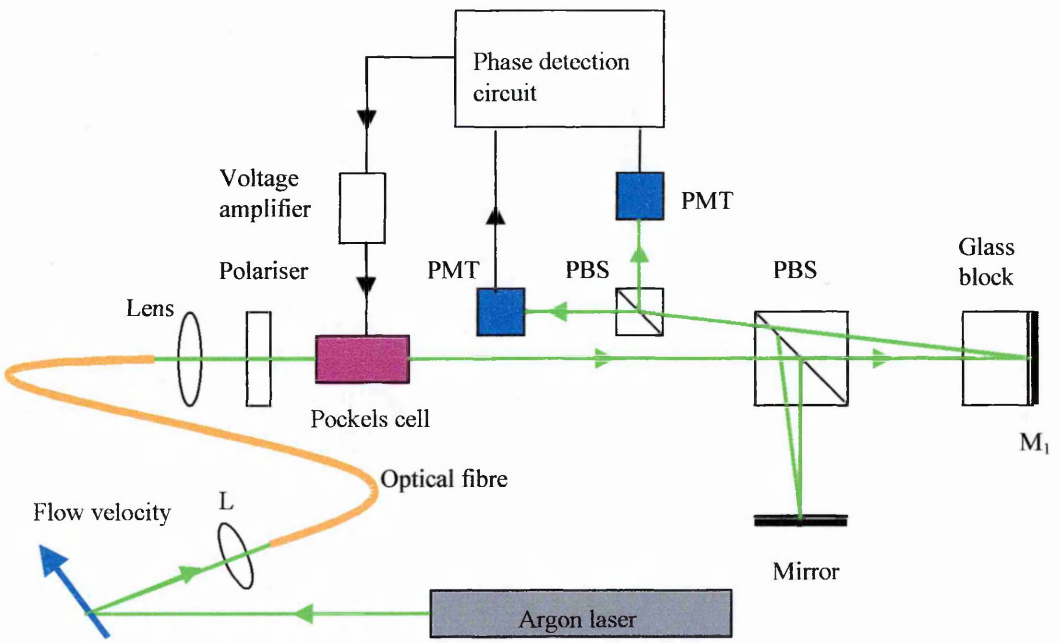

Figure 3. 11: On-axis component configuration using Michelson spectrometer [31].
L – lens, PMT – photomultiplier, PBS – polarising beam splitter, M – mirror.

The resulting beams in the interferometer have opposite polarisation to that of the scattered light beams. The beams leave the interferometer to the top where an additional

polarising beam splitter and two photomultiplier tubes are placed (not shown in the Figure 3.11). A phase stabilising circuit was used to either control the piezoelectric mounted interferometer mirror or one of the laser cavity mirrors. No further information was given concerning the stability margin that the workers achieved with this system.

The glass block in Figure 3.11 is used to generate an optical path difference in the interferometer that leads to the required wavelength sensitivity.

3.5 Point Filter-Based Laser Doppler Velocimetry

The technique employs a molecular or atomic absorption line usually in the form of an iodine vapour cell to perform direct frequency discrimination (Chapter 2). Hoffenberg and Sullivan implemented the first of this technique [32] following the original idea first conceived by Komine [33] in a related planar measurement system known as Doppler global velocimetry (DGV) or planar Doppler velocimetry (PDV).

The filter-based point system provides a continuous analogue velocity signal from which the temporal nature of the flow such as turbulence can be deduced. The instrument was used to study the flow of a turbulent jet seeded with smoke particles (Figure 3.12).

The argon-ion laser beam is focused into a region of the flow thereby defining the measurement volume. Scattered light from the measurement volume is collected by a lens and passed through a non-polarising beam splitter that splits it into two equal signals. Two photomultiplier tubes (PMT) are used to detect the signals and one PMT views through an iodine vapour cell that transduces Doppler frequency shifts into intensity change (Chapter 2). The iodine cell was used in its optically thick regime to provide an absorption line with a steep edge for high sensitivity to velocity (Figure 3.13).

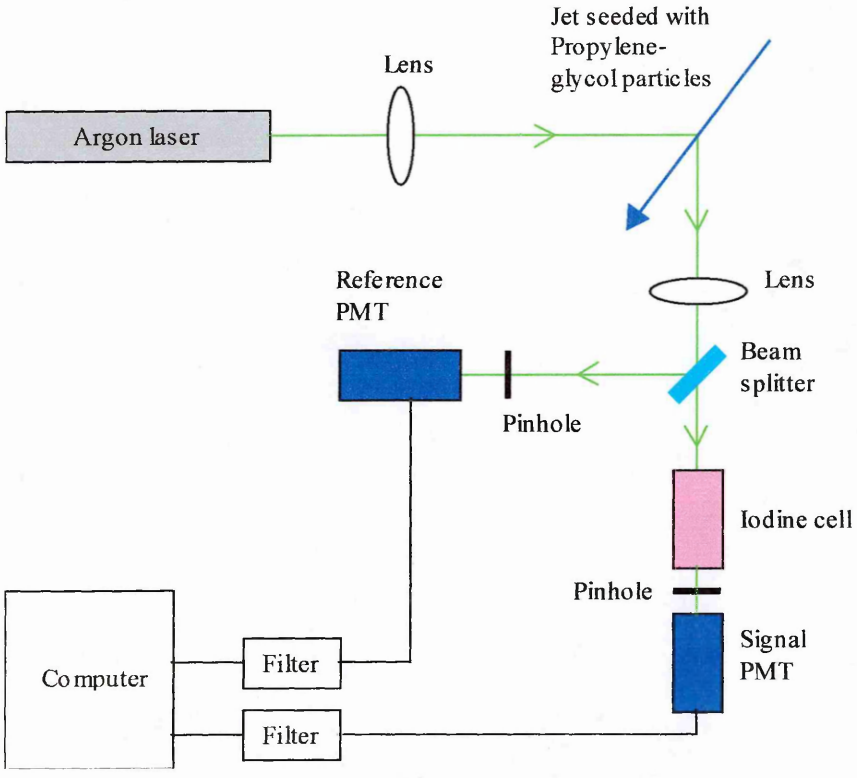

Figure 3. 12: Layout of the Filter-Based Laser Doppler Velocimetry system for on-axis component measurement [31].

PMT – photomultiplier tube.

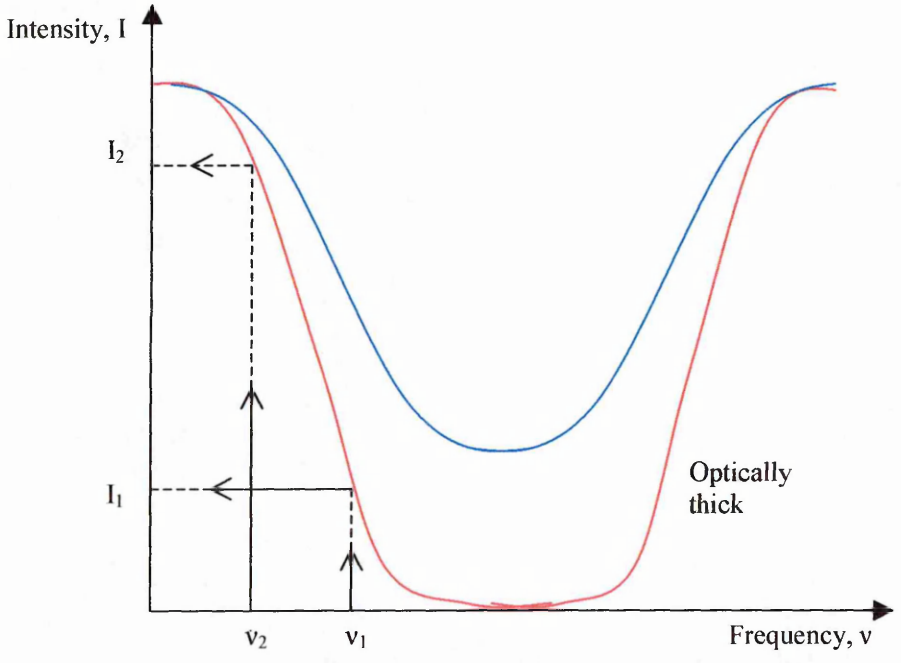

Figure 3. 13: Iodine transfer function. I_1 and I_2 – transmitted intensity corresponds to laser frequency ν_1 and ν_2 respectively.

A ratio of the two PMT signals is calibrated to give the required velocity. Pinholes were used in front of the detectors to ensure that they both observed the same region of the flow. The presented results were in good agreement with independent measurements from LDV experiments. The workers did not take account of drift in the laser frequency and as a result their results for the axial jet were up to 25 % error in the velocity range of less than 100 ms^{-1} when compared to LDV data. It was then recommended that future work should include some form of laser frequency compensation either by direct control or monitor.

The idea was later implemented by Roehle and Schodl [34] who set up a point filter-based laser Doppler velocimeter system to investigate the feasibility and accuracy achievable by a full field version of the technique (Figure 3.14).

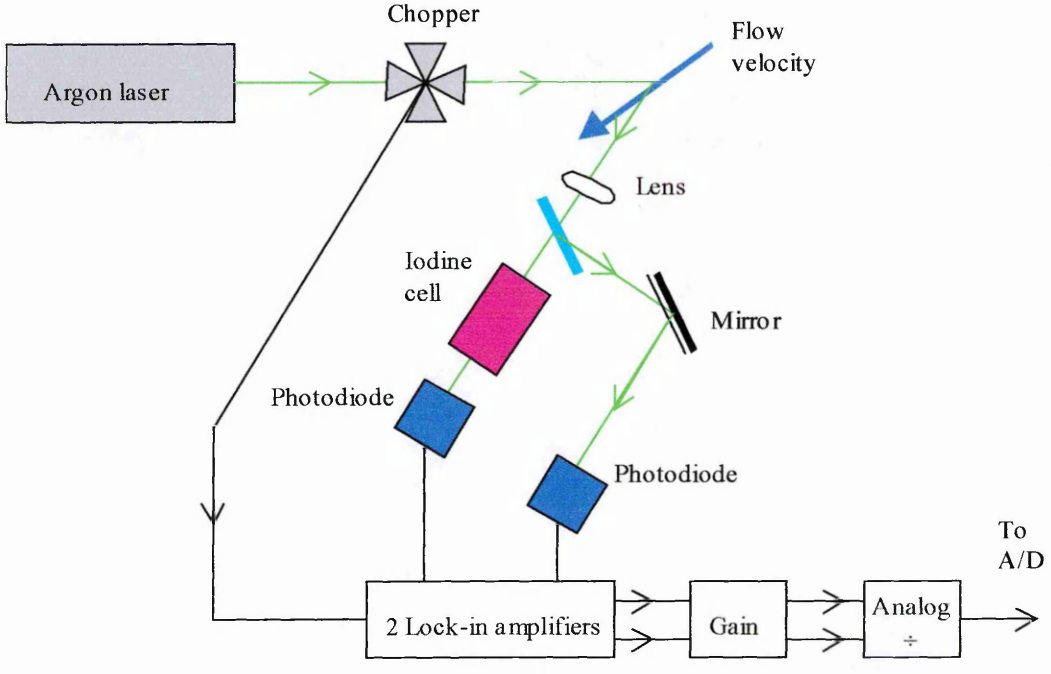

Figure 3. 14: On-axis component configuration with suppressed detection of background light [33].

A/D – analogue to digital converter.

In their system they under took to actively control the laser frequency to an impressive stability of ± 1 MHz. Spatial filtering was also applied but this time with one pinhole in

front of the beam splitter to define a common measurement point for the two detectors. The laser beam directed to the flow was effectively pulsed using an optical chopper; a measure that was aimed at suppressing daylight influences but could not reject light scattered by walls and windows. Photodiode detectors were used for the filtered and reference signals and two lock-in amplifiers then amplified the signals in phase with the chopper frequency. The resulting signals were sent to an analogue divider circuit to calculate a ratio of the filtered to the reference signal and then sampled with an A/D converter.

The results were compared to measurements from laser-two-focus (L2F) experiments (believed to have a measurement error of less than 0.5 %) and a relative measurement error of $\pm$ 3 ms^{-1} was obtained in the measurement range of 40 to 130 ms^{-1}. An absolute and systematic error of $\pm$ 3 ms^{-1} suggested that their technique should be useful for high-speed applications.

McKenzie [35] used a pulsed, injection seeded, frequency doubled Nd: YAG laser in a point based system to measure the velocity of a rotating disc (Figure 3.15). An optical fibre that is ten times longer than the fibre used to collect the reference light from the laser to the same photodiode detector collects light scattered from the measurement volume. Thus signals occurring simultaneously at the source were detected at different times by the same detector. The signals were sent to a 10 ns integrator, which then gave 12-bit digital outputs proportional to the energy of each reference and signal pulse. McKenzie`s impressive $\pm$ 2 ms^{-1} maximum error for velocities on the rotating disc demonstrated that the laser frequency monitoring scheme he used was equally effective. This error was primarily attributed to the fundamental digital uncertainty of $\pm$ 1 count for a 12-bit A/D board.

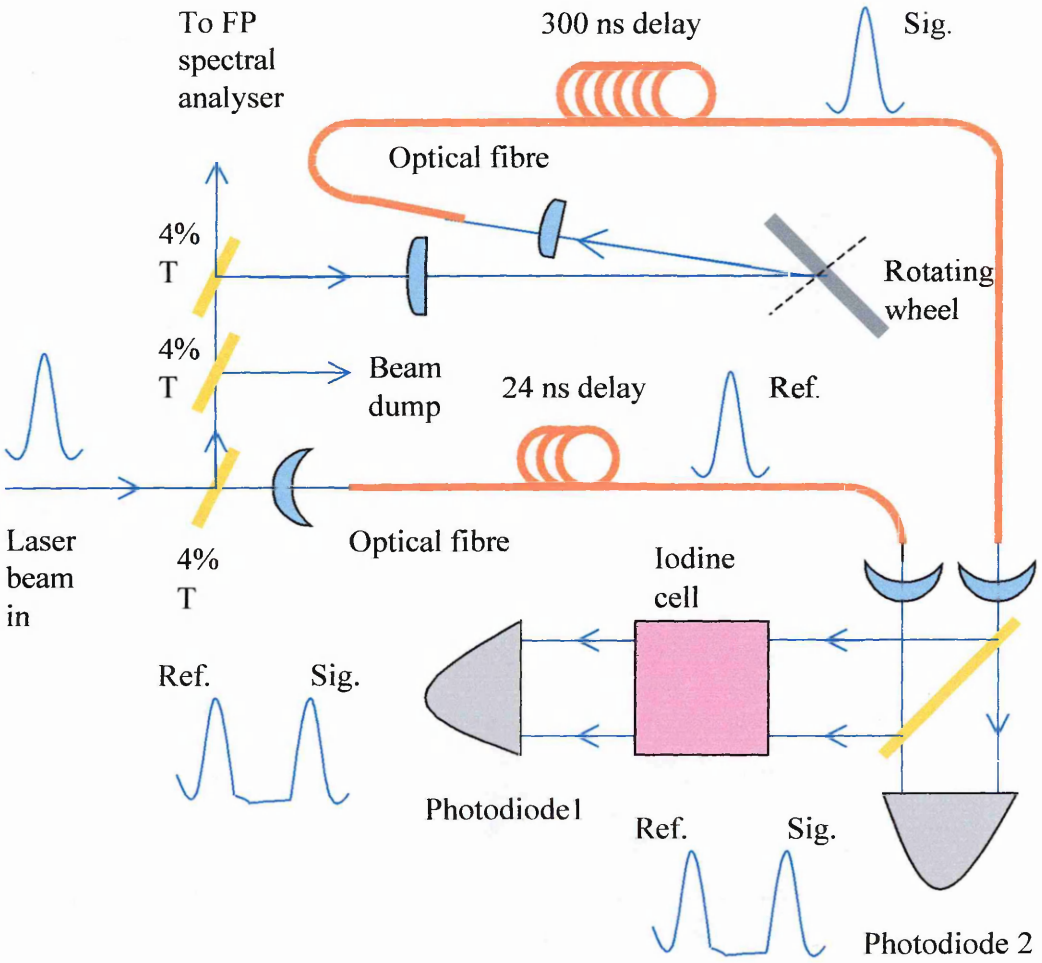

Figure 3. 15: Optical configuration for the measurement of the velocity of a rotating wheel [34].

FP – Fabry-Perot

Kuhlman et al [36] set up a two-component point filter-based laser Doppler velocimeter that resolved velocities in two orthogonal directions. The optical system described is very similar to that first applied by Hoffenberg and Sullivan [32] but uses photodiode detectors. The authors undertook to monitor the laser frequency by monitoring the transmission of a small portion of the laser beam (at the original frequency) through a reference iodine cell. Any relative shift in the laser frequency (as measured by the reference iodine cell) was subtracted from the frequency change calculated by the velocity measuring components.

The performance and accuracy of the velocimeter was investigated by measuring the velocity of a rotating wheel and fully developed turbulent pipe flow. The accuracy based on the rotating wheel velocity results was evaluated as ± 1 % of full scale while linearity was of the order of 0.5 % of the measured velocity range (57 ms^{-1}). This measurement accuracy proved to be considerably better than those documented by other researchers. The improvement was primarily attributed to a better calibration scheme for the iodine cell that was adopted from the previous work of Meyers and Komine [37] that include the cell structure, oven and temperature controllers. The calibration was accomplished through a continuous scan of the mode structure of the argon-ion laser by mechanically altering the tilt of the etalon through about 10-20 mode hops over a 20-30 second period. It was observed that the reference cell was unable to consistently determine the zero velocity and thus measurements prior to and after the actual data acquisition had to be taken. A zero velocity drift of ± 1.5 ms^{-1} over 30 minutes was detected and was attributed to drift in the cell stem temperature.

Naylor [38] also describes an extended report of the researchers' work, which included an analysis of the extent to which the viewing angle variations affected the velocity data. This group at West Virginia University has carried-out extensive work on both point and planar velocimetry and at least 4 MSc and PhD theses have been published on point Doppler velocimetry alone between 1997 and 1999, a period of only 3 years. The two-component point Doppler velocimeter was later used to measure flow over a NACA 0012 airfoil at 0^0 angle of attack at a velocity of 21 ms^{-1} [39]. The probe beam was not focussed so a relatively large sample volume of 2 mm diameter was produced. The rms velocities, when compared to the hot wire measurements, were found to be within 0.5 to 0.7 ms^{-1} while mean velocities agreed to 3 ms^{-1}. Efforts to quantify the instrument response to turbulence continued with the measurement in a uniform circular jet of 1-inch diameter and exit velocity of 60 ms^{-1} [40]. Vapour limited (Chapter 2) cells were adopted and the previously observed offset velocity was eliminated and any remaining errors in the measurements were linked to the degree of accuracy of the cell calibration. The system was able to resolve flow turbulence as low as 1.7 % and was said to approach the sensitivity achievable by a laser velocimetry using a counter processor. Recently the group improved on the accuracy of their own point Doppler

velocimeter by using vapour-limited iodine cells that are not sensitive to temperature variation [41]. The laser beam focussing was also improved and smaller pinholes defined a much smaller measurement volume, a measure that resulted in improved rms (root mean square) values of velocity.

The system response to resolve flow turbulence was investigated by making measurements in a uniform circular jet flow, annular jet, and a swirling jet. The measurement repeatability is reported to be within 1-2 ms^{-1} for the mean velocity, and within 1 ms^{-1} for the rms velocity results. Independent measurements carried-out with a hot wire compared reasonably well to within 2-4 ms^{-1} for the exit profiles of mean axial velocity, but was consistently 20-30 % higher for the rms velocity everywhere but at the exit of the standard jet. It was thought that the spatial averaging effect in the velocimetry system, the technique used to calculate rms values, and possible reduction of turbulence level by the smoke seeding particles could be the cause. An investigation of the A/D board used for data acquisition proved that it responsible for a rms noise of about 2 % of the exit mean velocity. The authors conclude by suggesting that a future improvement to their instrument signal-to-noise ratio would require large area avalanche photodiodes and a better A/D board.

Crafton et al [42] describes a point filter-based laser Doppler velocimetry in which the diode laser frequency is actively controlled by locking it to a reference Caesium Faraday-cell. The cell consists of a magnetooptic atomic vapour placed in an axial magnetic field between a pair of crossed polarisers. The slope and frequency range of the transmission edge of the Faraday cell can be tuned by adjusting the temperature, magnetic field strength, and polariser angle of the Faraday cell. Measurement results are reported from a rotating disc and seeded turbulent jet. An accuracy of 0.5 ms^{-1} for the seeded jet and a rms noise level of 0.05 ms^{-1} on the surface of a spinning disc were obtained. A low frequency noise in the system was linked to the use of two separate cells (instead of single cell) and the integrator circuit. It was suggested that one cell be used for both frequency control and velocity measurements, and use of digital techniques for the servo. The frequency response of the system was set by the 1-second

time constant of the lock-in amplifier. A distributed feedback reflector diode laser with a power output of 150 mW and operating at a wavelength of 852 nm was used.

A recent publication for 3-dimensional gas turbine measurements describes a hybrid system consisting of a two-component L2F velocimeter for transverse components and the use of an iodine vapour cell in a point Doppler velocimeter configuration for on-axis component of velocity [43].

3.6 Other Techniques: Planar Velocimetry

3.6.1 Particle Image Velocimetry

The development of Particle Image Velocimetry (PIV) was the first truly planar velocity measurement technique and has been used on a wide variety of applications (ranging from very low laminar velocity flow to supersonic flows) to obtain velocity measurements across a planar field of view [44, 47]. The basic principle of operation involves illuminating flow particles with two laser pulses and obtaining a double exposure image [Figure 3.16]. When the camera shutter is fully opened the particles are illuminated twice during a short time period by a thin laser sheet. The displacement between the two images and the time interval defined by the laser pulses provides the velocity vector.

The limitation of the classical PIV technique is that it is only capable of recording the projection of the velocity vector into the plane of the laser light sheet. The out-of-plane velocity component is lost while the true in-plane components are affected by a parallax (perspective) error, which is unrecoverable. Also, sharp focus for the image is obtained at the expense of a varied magnification across the image plane.

Long focal length lenses are normally used to keep the projection error small by imaging the flow from a large distance [48, 44]. This exercise will only improve the accuracy of the in-plane components but the out-of-plane component remains unmeasured.

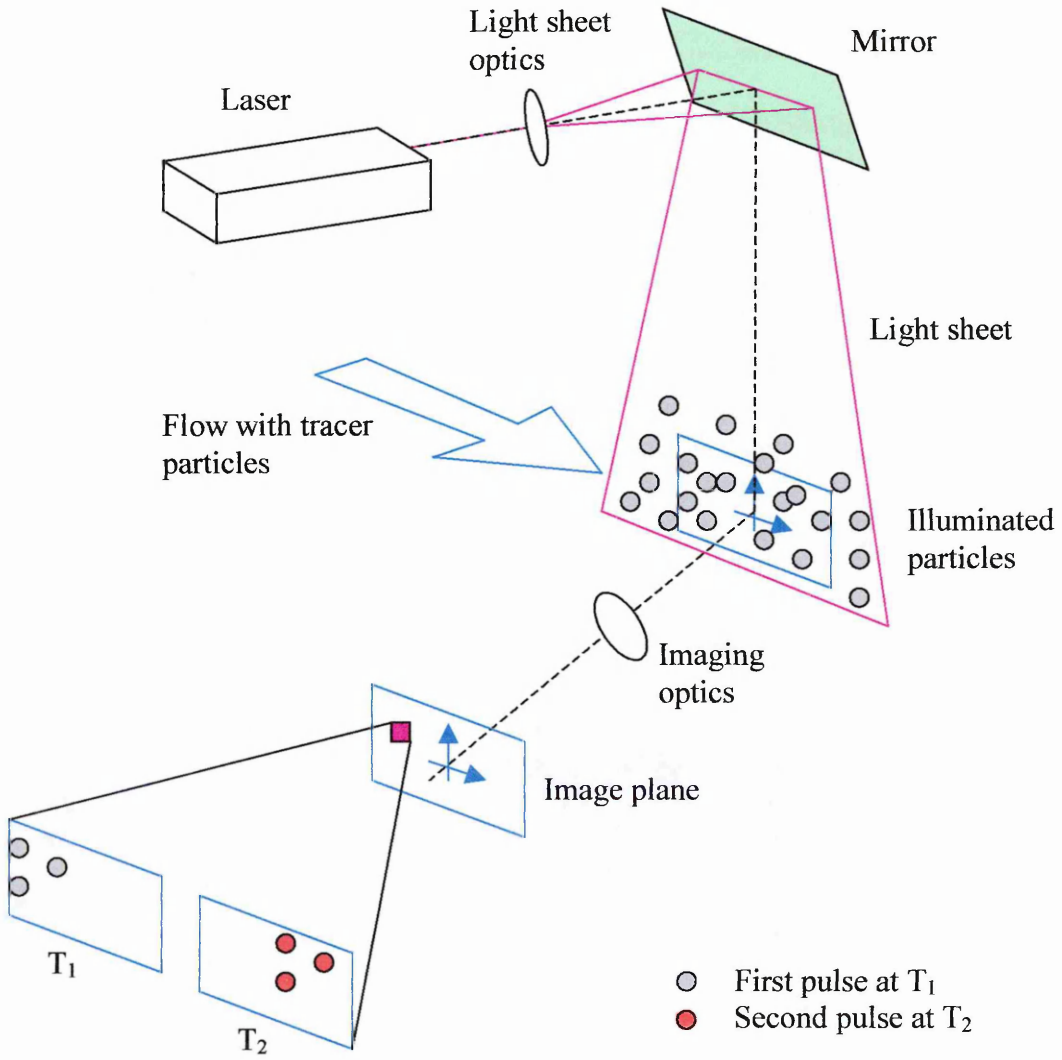

Figure 3. 16: Experimental set up for the measurement of the transverse velocity components by PIV [46].

Complete 3D measurements will require the measurement of out-of-plane velocity component in addition to the in-plane components. A number of approaches have been tried to measure this difficult component. One technique uses a second camera from a different viewing axis in a set up known as stereoscopic PIV recording [49, 45]. The accuracy in the on-axis component measurement increases when the angle between the two cameras approaches 90^0. The arrangement of the imaging lenses and cameras introduces perspective distortion and additional calibration for the magnification factor is required. The deterioration of the lens Modulation Transfer Function (MTF) towards

the edges reduces measurement accuracy and a good MTF at small f-numbers (f#<4) is mandatory.

The out-of-plane component of velocity can also be measured by expanding the laser light sheet into a thick slab to enable PIV measurements throughout a volume [49]. This method is capable of the highest measurement precision but is currently not suited to limited optical access experiments.

A dual-plane PIV technique for the measurement of the out-of-plane component requires an additional third illumination pulse and a slight out-of-plane displacement of the light sheet [49]. The precision of measurement is however dependent on many factors. The problem of high-speed recording of 3 images in succession is still to be addressed. For example, a typical image spacing of the order of 100 to 300 μm requires the time interval between laser pulses to be of the order of 1 μs for two component PIV using one camera [44]. The technique is therefore restricted to low speed flows. Also a large number of particle concentrations are required.
Among the shortcomings of the PIV technique are the requirements for the individual particles to be imaged, low light collection optics and considerable off-line processing time.

3.6.2 Doppler Global Velocimetry

Doppler Global Velocimetry (DGV) now commonly known as Planar Doppler Velocimetry (PDV) has attracted a lot of interest among researchers since its inception by Komine et al in 1990 [50]. DGV images Doppler shifted light that is scattered from particles entrained in the flow as they impinge upon a laser light sheet directed into the flow. A Charge Coupled Device camera (CCD) viewing through an optical filter collects the scattered light whose intensity is a representative of the velocity of particles across the field of view in the flow. The optical filter is usually in the form of a molecular iodine vapour enclosed in a glass cell (Figure 3.17).

The filter is required to have an absorption line (Figure 3.13) near the wavelength of the laser to be used. The flank of an absorption line provides a frequency dependent intensity transmission and thus Doppler shifts in frequency are directly measured by conversion to intensity level. The intensity images are processed to obtain velocity information across the region of the flow illuminated by the light sheet.

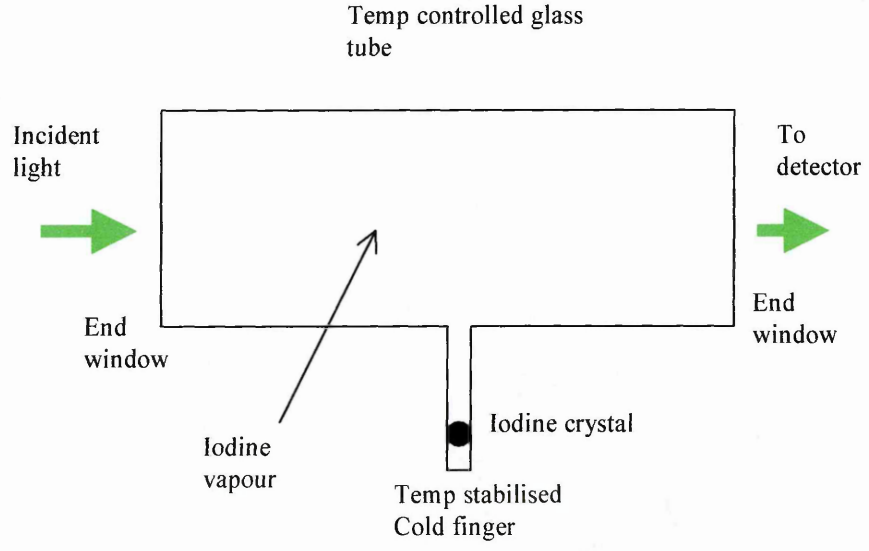

Figure 3. 17: Schematic of iodine cell.

A second CCD (reference) camera is used to collect light split off from the scattered light that is directed into the iodine cell (Figure 3.18). This reference signal is used to normalise the Doppler signal from the signal camera to remove intensity fluctuations whose origin is not the Doppler shift from the flow.

Three-dimensional unsteady flows may be measured using a single laser sheet and three pairs of synchronised CCD cameras mounted at different angles to simultaneously capture instantaneous velocity pictures [45-47]. Stable flows are normally measured by using a single pair of CCD cameras and three laser light sheets oriented in different directions but having a common measurement volume [53-55].

An opto-mechanical switch is used to select one laser light sheet at a time [54]. This method uses fewer cameras and is therefore less expensive while it is simpler and easier to calibrate in terms of intensity to frequency conversion. Its long integration time

allows the use of sparser seeding and speckle noise normally common with the pulsed laser technique is eliminated [54].

The two commonly used lasers for these measurements are the continuous wave (CW) argon-ion laser at 514.5 nm and a pulsed frequency doubled Nd: YAG laser at a wavelength of 532 nm. Steady flows are measured with the argon-ion laser [54] while the Nd: YAG laser is used for measurements in unsteady flows [56-60]. The pulsed laser typically with a pulse length of 10 ns effectively freezes the motion of the particles and thus provides velocity data at the pulse rate of the laser. The use of this laser provides more flexibility as both temporal and spatial averaging may be implemented [56-59]. The Gaussian beam intensity profile of the argon-ion laser coupled with seed density variations may result in large intensity gradients across the images, which could saturate the CCD cameras.

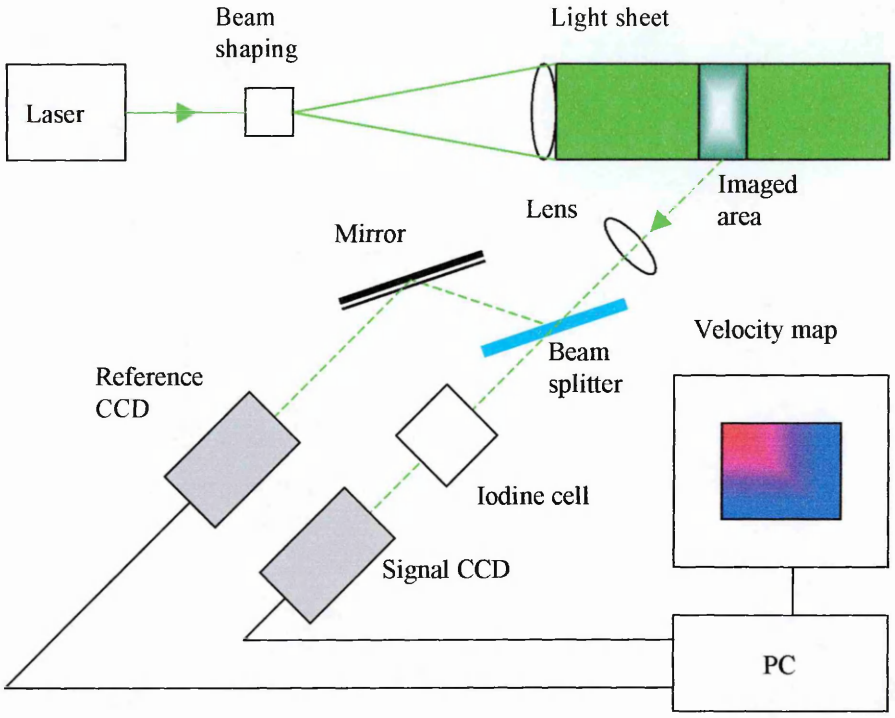

Figure 3. 18: One component DGV system using 2 CCD cameras [53].

The DGV system implementation is essentially the same for all groups actively involved in this research, the only difference being in the light collection optics. Two basic image acquisition techniques are currently employed. Emphasis on displaying real

time velocity images in continuously running wind tunnels favours the use of two separate CCD cameras for acquisition of one velocity component [61, 50]. The other technique utilises a single CCD camera and has been preferred for acquisition of absolute velocities [62-64, 57]. This method is however slow and reduces the spatial resolution by 50%. The author's laboratory is actively involved in Planar Doppler velocimerty research for turbomachinery applications [65]. Recent publications [66] include the use of fibre imaging bundles for instantaneous flow measurement [67].

A key element of a DGV receiver system is the iodine cell responsible for converting the Doppler frequency shifts into variations in intensity of the scattered light. The approximately linear part of the absorption profile has an operating frequency range of about 600 MHz [52]. The range maybe small if large velocity changes are encountered and various workers have treated this dynamic range problem. For example [68,69], the laser frequency was tuned to bottom of the absorption edge away from the nominal 50% point in order to measure high velocities of about 300 ms^{-1}, which would otherwise fall outside the dynamic range. Other researchers considered the addition of a buffer gas such as nitrogen to broaden the absorption line width and increase the frequency range [70, 71] and measurements were reportedly made in supersonic flow [72]. This pressure broadening of the absorption line is achieved at the expense of the sensitivity of the filter to velocity changes. Limited tuning is however available to the absorption line slope by application of controlled heating to the cell (Doppler broadening) to vary the slope and therefore the sensitivity of the velocimeter. The idea was used to develop a theoretical model for transmission optimisation of the filter [56].

DGV measurement systems consist of a number of components whose characteristics will interact to determine the final performance of the instrument. To date no DGV system has addressed the need for minimum resolved velocities or absolute errors as previous measurements have mainly focused on the demonstration of the capability of the system [60]. Since the technique relies on intensity measurements, there are various sources of error, which may lead to biases or random uncertainties in the velocity [73]. Intensity variations due to seed density and laser power variations may be accounted for by normalisation with the reference image. Among other effects contributing to errors

are the camera, polarisation sensitivities, angular dependence of the scattering intensity, and background light variation [74, 75]. Some of the DGV component errors often encountered are briefly discussed in Table 3.1.

The iodine cell has a minimum line width that leads to a velocity resolution of about 1 ms^{-1} and this renders DGV a relatively high velocity-measuring instrument. It can be concluded that the search for a flexible and high precision instrument to measure the difficult on-axis component of velocity for limited access flows at all velocity ranges has to go on.

DGV Component	*Error Source*	*Type of error*
CCD camera	Dark noise, read-out noise, non-linearity, and photon statistical noise.	Random
Laser light sheet	Frequency drifts, non-uniform content, and power fluctuation.	Fixed and random
Iodine molecular filter	Calibration errors, conversion factor errors, and purity.	Fixed
Image splitting	Flat-field image and sampling errors/image registration.	Fixed
Particle scattering	Speckle image noise	Random
Beam splitter	Non-polarising beam splitter often polarisation sensitive	Fixed
Multiple component measurement	Angle errors and Doppler shift registration.	Fixed

Table 3. 1: DGV component error [72]

3.7 Summary

This chapter has shown a lot of research interest in addressing flow velocity measurement accuracy for 3D application. The Doppler difference LDV and L2F velocimeter exist commercially and provide accurate 2D in-plane velocity components. However the measurement of 3D velocities buy these techniques have lacked sufficient accuracy particularly on the on-axis component because of transformation errors encountered when transforming from non-orthogonal to orthogonal components [1]. The reference beam LDV measures the on-axis component directly and could be useful in a hybrid system consisting of a 2D Doppler difference LDV or L2F velocimeter for the measurement of 3D components. However the reference beam technique suffers from several setbacks which include a limitation in the range of the measured velocity (~ 30 ms^{-1}) and a poor signal to noise ratio. Other techniques based on the use of atomic or molecular absorption filters have been used and were able to complement the reference beam by measuring higher velocities of up to 300 ms^{-1} but their measurement of low velocities was hindered by their poor resolution which is of the order of 1-2 ms^{-1}. The accuracy of this technique among other setbacks is primarily determined by the absorption filter.

Interferometric velocity measurement techniques have been set up to directly measure the on-axis component and these included the flat plate or the confocal Fabry-Perot and Michelson interferometers. Hybrid instruments using a 2D Doppler difference LDV (in-plane components) and one of these interferometers (on-axis component) were applied to 3D velocity measurements. The Interferometer techniques have in principle no upper limit on the magnitude of the measurable velocity but are prone to signal drift and vibrations thus limiting their ability to measure low velocities [27, 31].

It is interesting to note that the on-axis component has eluded other optical techniques particularly PIV where research efforts to solve the problem are in progress. Table 3.2 give a summary and comparison of some of the techniques that were discussed in this chapter with more comparisons given in Table 2.1 (Chapter 2).

Technique	*Application*	*Summary*
Reference beam - LDV	Low speed windtunnels	4 x 10^{-5} ms^{-1} resolution, ~ ± 15 ms^{-1} velocity range limited by electronic processor (usually 100/120 MHz), ~ 200 mm working distance, 50x50x500 μm typical measurement volume size [2,6,7,10]
Doppler difference-LDV	Turbomachinery & windtunnel	50x50x500 μm typical measurement volume, high signal to noise ratio
Atomic filter-based	Windtunnel & turbomachinery	1 – 2 ms^{-1} resolution, ~ 300 ms^{-1}, 70x70x350 μm typical measurement volume size [35]
L2F	Narrow blade channels, boundary layers, & windtunnels	High beam focus ~ 10 μm, 0.2 – 0.4 mm spatial resolution, < 30 % turbulent flow measurement, ~ 270 mm typical working distance, > 500 ms^{-1} velocity range [20,21]
Confocal FP interferometer	Turbomachinery high speed flow with high turbulence intensity	Direct measurement of "in-line" velocity component, significant signal gathering power but low signal transmission, unsuitable for low velocities because of vibration, requires very stable laser frequency, no upper limit to velocity range e.g. 2 x 10^{-1} ms^{-1}, 1 – 2 ms^{-1} resolution, 0.1 μs temporal resolution [25,27]
Michelson interferometer	2-phase flow, surface movements, shockwaves & turbulent flows	Direct measurement of "in-line" velocity component, susceptible to wavelength jitter, thermal drift and vibration, good for high velocities, 0.1 ms^{-1} resolution at best, 0.1 μs temporal resolution [31]

Table 3. 2: Summary of the properties of the optical flow measurement techniques.

References

[1] J. F. Meyers, "*The elusive third component*", International Symposium on Laser Anemometry, ASME, pp. 247-254, 1985.

[2] Y. Yeh and H. Z. Cummins, "*Localised fluid flow measurements with a He-Ne laser spectrometer*", Applied Physics Letters, vol. 4, no. 10, pp. 176-178, 1964.

[3] R. J. Goldstein and D. K. Kreid, "*Measurement of Laminar Flow Developed in a Square Duct Using a Laser Doppler Flowmeter*", Journal of Applied Mechanics, Item 34, Series E, No. 4, pp. 813-818, 1967.

[4] E. Siegman, "*The antenna properties of optical heterodyne receivers*", Proceedings of the IEEE, vol. 5, no. 10, pp. 1350-1356, 1966.

[5] D. A. Egan, "*In-line Fibre Optic Laser Doppler Velocimetry for Turbomachinery Applications*", Ph.D. Thesis, Cranfield University, 1998.

[6] G. D. Byrne, S. W. James, and R. P. Tatam, "*A Bragg grating based fibre optic reference beam laser Doppler anemometer*", Measurement Science and Technology vol. 12, pp. 909-913, 2001.

[7] R. A. Lockey, "*Optoelectronic time-division multiplexing for multicomponent laser Doppler Anemometry*", Ph.D. Thesis, Cranfield University, 1996.

[8] S. W. James, R. P. Tatam, and R. L. Elder, "*Design considerations for three dimensional fibre optic laser Doppler velocimeter for turbomachinery applications*", Review Scientific Instruments, vol. 8, pp. 3241-3246, 1997.

[9] D. A. Egan, S. W. James, and R. P. Tatam, "*On-axis laser Doppler velocimetry for turbomachinery applications using optical fiber techniques*", Proceedings of SPIE: Optical Technology in Fluid, Thermal, and Combustion Flow 111, vol. 3172, pp. 17-26, 1997.

[10] S. W. James, R. A. Lockey, D. Egan, and R. P. Tatam, "*Fibre optic based reference beam laser Doppler velocimetry*", Optics Communications, vol. 119, pp. 460-464, 1995.

[11] R. M. Huffaker, "*Laser Doppler detection systems for gas velocity measurement*", Applied Optics, vol. 9, no. 5, pp. 1026-1039, 1970.

[12] H. D. Vom Stein and H. J. Pfeifer, "*A Doppler difference method for velocity measurements*", Metrologia 5, no. 2, pp. 59-61, 1969.

[13] L. Dancey, "*A review of three-component laser Doppler anemometry*", Journal of Optical Sensors, vol. 2, no. 6, pp. 437-469, 1987.

[14] P. K. Snyder, K. L. Orloff, and M. S. Reinath, "*Reduction of Flow-Measurement Uncertainties in Laser Velocimeters with Nonorthogonal Channels*", AIAA Journal, vol. 22, no. 8, 1984.

[15] J. F. Meyers, and S. P. Wilkinson, "*A comparison of Turbulence Intensity Measurements using a Laser Velocimeter and Hot Wire in a Low Speed Jet Flow*", International Symposium on Applications of Laser-Doppler Anemometry to Fluid Mechanics, Lisbon, Portugal, 1982.

[16] M. M. Ross, "*Combined Differential and Reference Beam LDV for 3D Velocity Measurement*", Optics and Lasers in Engineering, vol. 27, pp. 587-619, 1997.

[17] K. L. Orloff and S. E. Logan, "*Confocal backscatter laser velocimeter with on-axis sensitivity*", Applied Optics, vol. 12, pp. 2477, 1973.

[18] W. J. Yanta, "*A three-dimensional laser Doppler velocimeter (LDV) for use in wind tunnels*", ICIASF Record, pp. 294, 1979.

[19] H. Thompson, "*A Tracer Particle Fluid Velocity Meter Incorporating a Laser*", Journal of Scientific Instruments (J. Phys. E.), Series 2, vol. 1, pp. 929-932, 1968.

[20] R. Schodl and W. Forster, "*A Multi Colour Fiber Optic Laser Two Focus Velocimeter for 3-Dimensional Flow Analysis*", AIAA/ASME/SAE/ASEE 24th Joint Propulsion Conference, Boston, Massachusetts, 1988.

[21] R. Schodl, "*Laser Transit Velocimetry*", Lecture Series 1991-05, Von Karmen Institute of Fluid Dynamics, pp. 1-95, 1991.

[22] R. N. James, W. R. Babcock, and H. S. Seifert, "*A laser-Doppler technique for the measurement of particle velocity*", AIAA Journal, vol. 6, no. 1, pp. 160-162, 1968.

[23] D. A. Jackson and D. M. Paul, "*Measurement of hypersonic velocities and turbulence by direct spectral analysis of Doppler shifted laser light*", Physics Letters, vol. 32A, no. 2, pp. 77-78, 1970.

[24] D. A. Jackson and D. M. Paul, "*Measurement of supersonic velocity and turbulence by laser anemometry*", Journal of Physics E, vol. 4, no. 3, pp. 173-177, 1971.

[25] D. M. Paul and D. A. Jackson, "*Rapid velocity sensor using a static confocal Fabry-Perot and a single frequency argon laser*", Journal of Physics E, vol. 4, pp. 170-172, 1971.

[26] J. Cooper and J. R. Grieg, Journal of Scientific Instruments, vol. 40, pp. 433-437, 1963.

[27] D. A. Jackson and P. L. Eggins, "*Supersonic velocity and turbulence measurements using a Fabry-Perot interferometer*", Applications of Non-Intrusive Instrumentation Fluid Flow Research, AGARD CP-193, pp. 6-1 – 6-13, 1976.

[28] R. G. Seasholtz and L. J. Goldman, "*Laser anemometer using a Fabry-Perot interferometer for measuring mean velocity and turbulence intensity along the optical axis in turbomachinery*", Engineering Applications of Laser Velocimetry, ASME, pp. 93-101, 1982.

[29] R. G. Seasholtz and L. J. Goldman, "*Three component velocity measurements using Fabry-Perot interferometer*", Second International Symposium on applications of Laser Anemometry to Fluid Mechanics, pp. 8.6 – 8.12, 1984.

[30] R. G. Seasholtz and L. J. Goldman, "*Combined fringe and Fabry-Perot laser anemometer for three component velocity measurements in turbine stator cascade facility*", NASA Technical Memorandum 87322, 1986.

[31] Smeets and A. George, "*Michelson Spectrometer for instantaneous Doppler velocity measurements*", Journal of Physics E: Scientific Instruments, vol. 14, 1981.

[32] R. Hoffenberg and J. P. Sullivan, "*Filtered particle scattering: Laser velocimetry using an iodine filter*", ASME-FED, vol. 161, Fluid Measurement and Instrumentation, pp. 135-138, 1993.

[33] Komine, U.S. Patent No. 4, 919, 536, pp. 1-16, 1990.

[34] Roehle and R. Schodl, "*Evaluation of the accuracy of the Doppler global technique*", Optical Methods and Data Processing in Heat and Fluid Flow, pp. 155-161, London, UK, 1994.

[35] R. L. McKenzie, "*Measurement Capabilities of Planar Doppler Velocimetry using Pulsed Lasers*", AIAA Paper 95-0297, 33rd Aerospace Sciences Meeting and Exhibit, Reno, NV, 1995

[36] Kuhlman, S. Naylor, K. James, and S. Ramanath, "*Accuracy Study of a 2-Component Point Doppler Velocimeter*", AIAA Paper 97-1916, 28th Fluid Dynamics Conference, Snowmass Village, CO, 1997.

[37] F. Meyers and H. Komine, "*Doppler Global Velocimetry: A new way to look at velocity*", 4th International Conference on Laser Anemometry, Advances and Applications, pp. 289-296, Cleveland, OH, 1991.

[38] S. M. Naylor, "*Development and Accuracy Determination of a Two-Component Doppler Global Velocimeter*", PhD Dissertation, West Virginia University, Morgantown, WV, 1998.

[39] M. Kuhlman and D. L. Webb, "*2-Component Point Doppler Velocimetry Measurements of Turbulent Flow over an Airfoil*", AIAA Paper 99-3517, 30th Fluid Dynamics Conference, Norfolk, VA, 1999.

[40] J. Kuhlman and P. Collins, "*Circular jet 2-component point Doppler Velocimetry velocity data*", AIAA Paper 2000-2296, 21st Aerodynamic Measurement Technology and Ground Testing Conference, Denver, CO, 2000.

[41] J. Kuhlman, Pat Collins, and Tom Scarberry, "*Two-component point Doppler velocimetry data in circular jets*", Measurement Science and Technology, vol. 12, pp. 395-408, 2001.

[42] J. Crafton, N. M. Messersmith, and J. P. Sullivan, "*Filtered Doppler Velocimetry: Development of a Point System*", AIAA Paper 98-0509, 36th Aerospace Sciences Meeting and Exhibit, Reno, NV, 1998.

[43] Roehle, G. Karpinski, and R. Schodl, "*3-component-Doppler laser-two-focus: a new kind of three component velocimeter*", ICIASF`99: 18th International conference on Instrumentation in Aerospace simulation facilities, pp. 13.1-13.9, Toulouse Cedex, 1999.

[44] Lourenco, A. Krothapalli, and C. A. Smith, "*Recent advances in particle image velocimetry*", AGARD FDP Symposium on Advanced Aerodynamic Measurement Technology, Seattle, USA, 1997.

[45] P. Wernet, "*PIV for Turbomachinery Applications*", SPIE vol. 3172, pp. 0277, 1997.

[46] J. W. Kooi, K. Pengel, M. Raphel, C. Willert, and J. Kompenhans, "*Applications of PIV in the large low speed facility of DNW*", AGARD FDP Symposium on Advanced Aerodynamic Measurement Technology, Seattle, USA, 1997.

[47] F. Coton, R. Galbraith, I. Grant, and D. Hurst, "*Analysis of complex flow fields by animation of PIV and high resolution unsteady pressure data*", AGARD FDP Symposium on Aerodynamic Measurement Technology, Seattle, USA, 1997.

[48] P. W. Bearman, J. K. Harvey, and J. N. Stewart, "*Development of PIV for two and three component velocity in large low speed wind tunnel*", AGARD FDP Symposium on Advanced Aerodynamic Measurement Technology, Seattle, USA, 1997.

[49] Raffel, C. Willert, and J. Compenhans, "*Particle Image Velocimetry*", Springer-Verlag Berlin Heidelberg, 1998.

[50] H. Komine, S. J. Brosnan, A. B. Litton, and E. A. Stappaerts, "*Real-Time Doppler Global Velocimetry*", Paper AIAA 91-0337, 29th Aerospace sciences meeting, 1991, Reno, Nevada.

[51] H. Komine and S. J. Brosnan, "*Instantaneous three component Doppler global velocimetry*", Laser Anemometry, ASME 1, U.S. Patent No. 4, 919, 536.

[52] H. Komine, S. J. Brosnan, W. H. Long, and E. A. Stappaerts, "*Doppler Global Velocimetry – Development of a flight research instrumentation system for applications to non-intrusive measurements of the flow filed*", NASA Contractor Report 191490, 1994.

[53] Roehle and R. Schodl, "*Applications of three dimensional Doppler global velocimetry to turbomachinery and wind tunnel flows*", Proc. 90th Symp. Of AGARD-PEP on Advanced non-intrusive Instrumentation for Propulsion Engines, Brussels, Belgium, 1997.

[54] Roehle, "*Three dimensional Doppler global velocimetry in the flow of a fuel spray nozzle and in the wake region of a car*", Flow Meas. Instrum. Vol. 7, No. ¾, pp. 287-294, 1996.

[55] Roehle, C. Willert, and R. Schodl, "*Recent applications of three dimensional Doppler global velocimetry in Turbomachinery*", Proceedings of International Symposium on Applications of Laser Techniques to Fluid Mechanics, Lisbon, 1998.

[56] R. L. McKenzie, "*Measurement capabilities of planar Doppler velocimetry using pulsed lasers*", Applied Optics, vol. 35, No. 6, 1996.

[57] R. L. McKenzie, "*Planar Doppler Velocimetry performance in low speed flows*", Paper AIAA 97-0498, 35th Aerospace sciences meeting and exhibit, Reno, NV.

[58] R. L. McKenzie, "*Planar Doppler Velocimetry for large scale wind tunnel applications*", AGARD FDP Symposium on Advanced Measurement Technology, Seattle, USA, 1997.

[59] J. W. Lee, J. F. Meyers, A. A. Cavone, and K. E. Suzuki, "*Doppler global velocimetry measurements of the vortical flow above an F/A-18*", Paper AIAA 930414, 31st Aerospace sciences meeting and exhibit, 1993.

[60] T. J. Buetner and H. D. Baust, "*Recent developments in Doppler global velocimetry*", AGARD FDP Symposium on Advanced Aerodynamic Measurement Technology, Seattle, USA, 1997.

[61] J. F. Meyers, "*Doppler global velocimetry The next generation*", Paper AIAA 92-3897, 17th Aerospace Ground Testing Conference, Nashville, TN.

[62] R. W. Ainsworth, S. J. Thorpe, and R. J. Manners, "*A new approach to flow field measurement – A review of Doppler Global Velocimetry Techniques*", Int. J. Heat and Fluid Flow 18, pp. 116-130, 1997.

[63] R. W. Ainsworth and S. J. Thorpe, "*The development of a Doppler global velocimeter for transonic turbine applications*", Presented at the International Gas Turbine and Aeroengine Congress and Exposition, The Hague, Netherlands, 1994.

[64] M. W. Smith and G. B. Northam, "*Applications of absorption filter planar Doppler velocimetry to sonic and supersonic jets*", Paper AIAA 95-0299, 33rd Aerospace sciences meeting and exhibit, Reno, NV, 1995.

[65] H. D. Ford, and R. P. Tatam, "*Development of extended field Doppler Velocimetry for Turbomachinery Applications*", Optics and Lasers in Engineering, vol. 27, pp. 675-696, 1997.

[66] H. D. Ford, D. S. Nobes, and R. P. Tatam, "*Acousto-optic frequency switching for single-camera planar Doppler Velocimetry*", Optical Diagnostics for Fluids, Solids and Combustion, Proc. SPIE, vol. 4448, pp. 272-282, San Diego, USA, 2001.

[67] D. S. Nobes, H. D. Ford, and R. P. Tatam, "*Instantaneous, two camera, three dimensional planar Doppler velocimetry using imaging fibre bundles*", Optical Diagnostics for Fluids, Solids and Combustion, Proc. SPIE, vol. 4448, pp. 283-294, San Diego, USA, 2001.

[68] J. F. Meyers, "*Development of Doppler global velocimetry as a flow diagnostic tool*", Meas. Sci. Technol. 6, pp. 769-783, UK, 1995.

[69] J. F. Meyers, "*Applications of Doppler global velocimetry to supersonic flows*", Paper AIAA 96-2188, 19th AIAA Advanced Measurement and Ground Testing Technology Conference, New Orleans, LA, 1996.

[70] S. Clancy and M. Samimy, "*Multicomponent velocimetry in high speed flows using Planar Doppler Velocimetry*", Paper AIAA 97-0497, 35th Aerospace science meeting and exhibit, Reno, NV, 1997.

[71] G. S. Elliot, M. Samimy, and S. A. Arnette, "*Details of molecular filter based velocimetry technique*", Paper AIAA 94-0490, 32nd Aerospace sciences meeting and exhibit, Reno, NV, 1994.

[72] S. Clancy, M. Samimy, and W. R, Erskine, "*Planar Doppler Velocimetry: Three component velocimetry in supersonic jets*", Paper AIAA 98-0506, 36th Aerospace and sciences meeting and exhibit, Reno, NV, 1998.

[73] J. F. Meyers, J. W. Lee and R. J. Schwartz, "*Characterisation of measurement error sources in Doppler global velocimetry*", Measurement Science and Technology, 12, pp. 357-368, 2001.

[74] G. L. Morrison and C. A. Gaharan Jr, "*Uncertainty estimates in DGV systems due to pixel location and velocity gradients*", Measurement Science and Technology, 12, pp. 369-377, 2001.

[75] M. W. Smith, "*The reduction of laser speckle noise in Planar Doppler Velocimetry Systems*", 20th AIAA Advanced Measurement and Ground Testing Technology Conference, Albuquerque, pp. 1-11, 1998.

CHAPTER 4

In-Fibre Bragg Grating Technology

4.1 Introduction

The ability of an in-fibre Bragg grating to provide frequency-dependent light transmission offers prospects of a high resolution narrow linewidth filter for laser Doppler velocimetry applications. This chapter will introduce some background on in-fibre Bragg grating technology and its current applications. Chapter 5 describes the theoretical models that were used to design the filters and the experimental work on filter fabrication is covered in Chapter 7. Among the desired characteristics of the filters for flow measurement applications is the need to have a transfer function that has a narrow bandwidth of up to about 3 GHz (for appreciable sensitivity to velocities encountered in windtunnels and turbomachinery), high linearity of the slope, high visibility (for a high signal to noise ratio) and be easily tuneable in wavelength. Required also is a compact and stable filter that could additionally be passively compensated for strain and temperature using chirp or athermalisation techniques as in fibre-optic telecommunications. Active stabilisation is also easier implemented on small-sized filters.

4.2 In-Fibre Bragg Grating

In-fibre Bragg gratings are formed as a result of a periodic modulation of the refractive index of the core of the optical fibre by illumination with two coherent beams of light. The illumination creates an interference pattern along the core of the fibre with index modulation occurring where the light density is high. If broadband wavelength light is passed through the fibre a narrow band reflected beam is obtained at the writing wavelength while all other wavelengths are transmitted unaffected (Figure 4.1). The

maximum reflectivity of the grating occurs when the phase matching condition known as the Bragg condition is satisfied.

$$p \cdot \lambda_B = 2 \cdot n_{eff} \cdot \Lambda \qquad (4.1)$$

Equation (4.1) [1] defines the Bragg condition in which p represents the order of interaction with $p = 1$ being the most efficient for mode coupling. The Bragg wavelength is defined by λ_B while n_{eff} and Λ respectively represent the effective refractive index of the mode and the grating period.

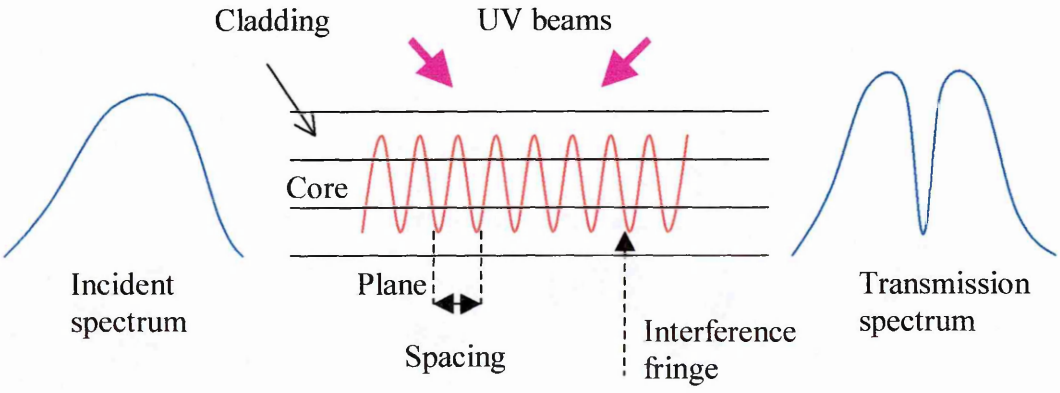

Figure 4. 1: The principle of an in-fibre Bragg grating technology.

Several theories have been proposed as possible causes of the photosensitive effect [2, 3]. However practical evidence tends to support the existence of a photobleaching phenomenon that is triggered by a single-photon absorption process in the UV or two-photon absorption in the visible radiation [4]. The photosensitivity lies predominantly with germanium-oxygen (GeO) defects associated with oxygen deficiencies in the chemical structure of the fibre. The GeO defect has an absorption band around 242 nm and this absorption results in ionisation that creates a GeE' centre (vacancy) and a free electron that is subsequently re-trapped.

4.2.1 Internally Fabricated Gratings

The phenomenon of the photosensitivity of Germania (G_eO_2) core-doped silica (SiO_2) fibres was first demonstrated by Hill et al [5]. Later work [6-8] explains the existence of the non-linear transmission in optical fibres (used for light transmission purposes) at modest blue/green intensity levels as severely affecting the operation of a fibre-optic laser Doppler velocimeter. It was shown that two intense contradirectionally propagating coherent beams in this type of fibre exhibited refractive index modulation along the axis of the fibre. The cause of the phenomenon has not been fully understood although experimental evidence seems to support the existence of a two-photon absorption process (TPA).

An intense single-longitudinal mode argon-ion laser-beam at either 488 nm or 514.5 nm illuminates a preferably single mode silica optical fibre core-doped with germanium (Figure 4.2). Writing intensities of at least 20 mW and up to about 250 mW have been commonly used on fibre lengths as short as 15 cm and as long as 1 m [9]. The fibre length is however limited by the coherence length of the argon-ion laser (~2.2 m).

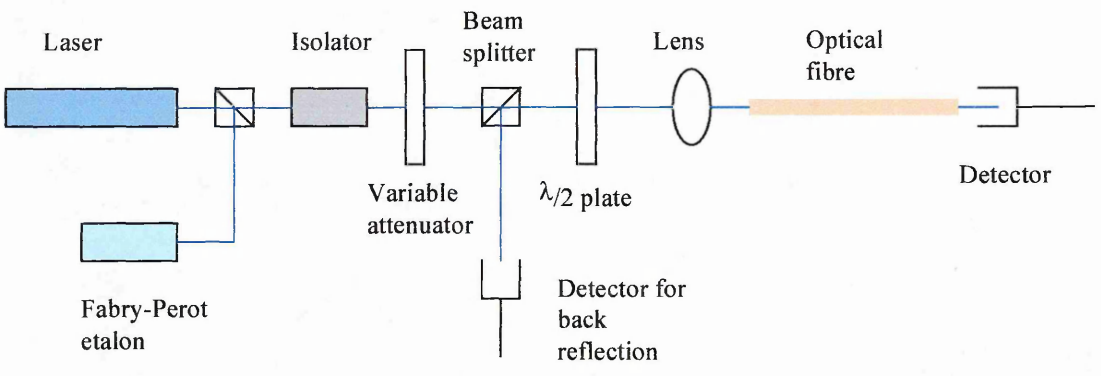

Figure 4. 2: Experimental configuration for internally written Bragg gratings.

The forward propagating mode suffers from approximately 4 % Fresnel reflections at the far end of the fibre and this constitutes a backward mode. The two oppositely propagating modes, under the right phase and intensity conditions, are coupled together. The interference from the two modes produces a standing wave that grows with time. This imposes a periodic perturbation to the refractive index of the fibre-core.

A very narrow linewidth interference filter is formed whose width depends on the length of the optical fibre as well as the writing intensity. The linewidth increases with the increase in writing intensity [10]. The growth of the filter is rapid due to distributed reflection arising from the periodical spatial modulation of the fibre refractive index. The filter growth is self-organising or sustaining in a "boot strap" process. Highly selective permanent interference filters have been reported fabricated with growth times up too about 30 minutes after which the modified index may saturate [11].

Figure 4.3 shows the typical transfer function from an end-pumped grating of length 10 cm and Bragg wavelength of 514.5 nm. The reflectivity is shown as 83 % for a refractive index modulation of 2.5×10^{-6}. The graph shows that the full width bandwidth is 0.002 nm corresponding to 2.3 GHz in frequency while the full width half maximum frequency bandwidth is 1.5 GHz. This result was generated from a computer model based on the transfer matrix approach which is described in Chapter 5 with the programming code given in Appendix B. A longer length of the optical fibre gives a narrower bandwidth e.g. 1 m length of fibre gives a bandwidth of about 100 MHz. The filtering properties are therefore controlled by varying the length of the grating. The bandwidth controls the velocity measurement range while the combination of bandwidth and the magnitude of reflectivity govern the resolution and sensitivity to velocity measurement. Figure 4.3 shows that the filter forms at the exact wavelength of fabrication i.e. 514.5 nm and this feature is desirable in-order to match the filter wavelength to the wavelength of the laser required for use in flow velocity measurement.

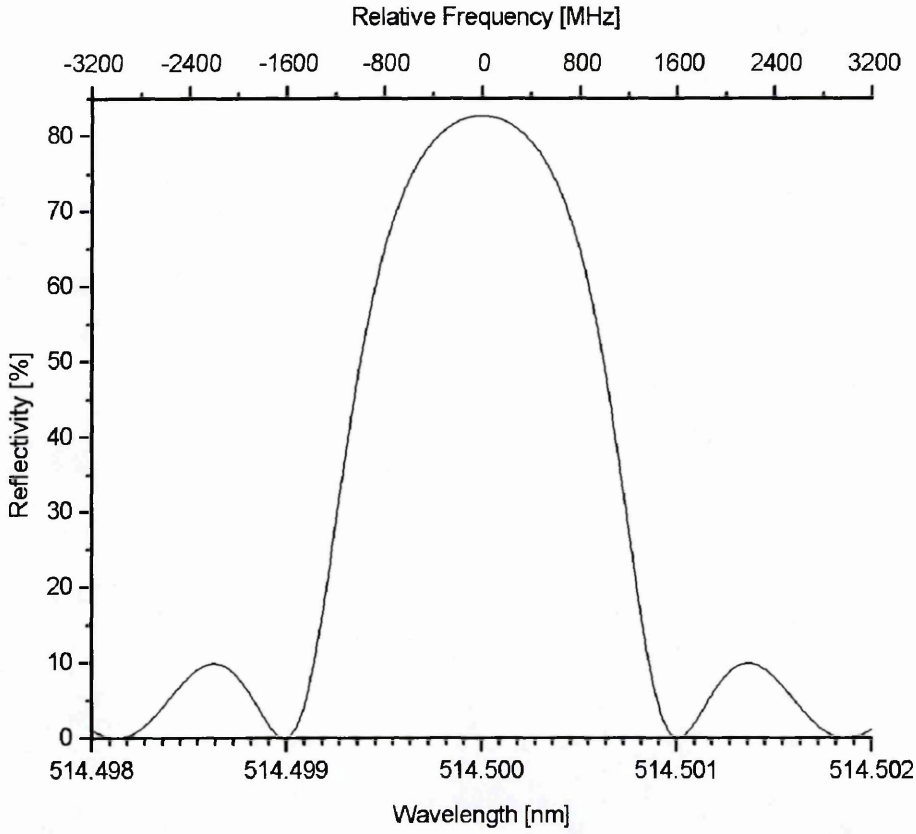

Figure 4. 3: Typical end-pumped grating transfer function of length 10 cm.

4.2.2 UV Fabricated Gratings

An important break through was the discovery of a more efficient and all-important grating fabrication scheme by the external illumination of the fibre core [12]. The principle (transverse two beam interferometer) involved direct side illumination of the fibre by a pair of intersecting linearly polarised coherent beams of UV light having equal intensity and parallel electric field vectors. This induces a one-photon absorption (OPA) process at 245 nm that triggers grating formation. The required power density for the writing process is achieved by focussing both beams to a narrow stripe on to the fibre (parallel to it) using cylindrical lenses in each arm of the interferometer. Interference takes place between parts of the beam with the same phase and intensity thereby creating a fringe pattern. The written fringe pattern is perpendicular to the fibre axis.

The absorption cross-section for OPA is around 5 orders of magnitude larger than for TPA process and consequently the writing intensity required for OPA is much less than for TPA e.g. typically 0.1 $\mu W/\mu m^2$ compared to 10-$mW/\mu m^2$ [13]. The UV gratings therefore require shorter fabrication times of about 5 minutes as compared to about 30 minutes for internal grating fabrication. Externally written UV gratings allow large index change over lengths of gratings of the order of a few mm. The angle between the two UV beams of light can be varied by rotational adjustments (and may include mirror displacements relative to each other and/or relative to the focus on the fibre) to a pair of mirrors, which gives flexibility in selecting the wavelength at which the grating can be written. This angle, θ (Figure 4.4) is related to the Bragg wavelength, λ_B by

$$\lambda_B = \frac{n_{eff} \cdot \lambda_{UV}}{n_{UV} \cdot \sin\theta} \qquad (4.2)$$

where n_{eff}, n_{UV} and λ_{UV} are the effective refractive index of the mode in the fibre, the refractive index of the fibre in the UV and the UV wavelength respectively.

It has been reported that the refractive index of an internally written Bragg reflector continues to change or grow during its use as a reflector [14], an effect not noticeable with the UV fabricated gratings. The lifetime of a Bragg grating filter is important for long term usage. It is the mechanical strength of the optical fibre and stability of the Bragg grating that govern this lifetime. Mechanical strength is degraded by the removal of the jacket when writing the grating and by the weakening of the fibre due to UV exposure. The stability of a grating is improved by thermally annealing the grating at a temperature higher than the operational temperature to avoid fast degradation of the reflectivity and wavelength drift [15]. This also stabilises the grating against the out diffusion of hydrogen if the fibre was hydrogen loaded.

The coherence length of the light source limits the length of the filter that can be achieved. This fabrication system is however prone to vibrations which could completely wash out the grating [16]. An alternative transverse holographic interferometric technique utilises a right-angled prism [Figure 4.5]. This configuration is

more stable compared to that of the first method and allows for extended exposure times [17]. The method requires a spatially coherent laser source.

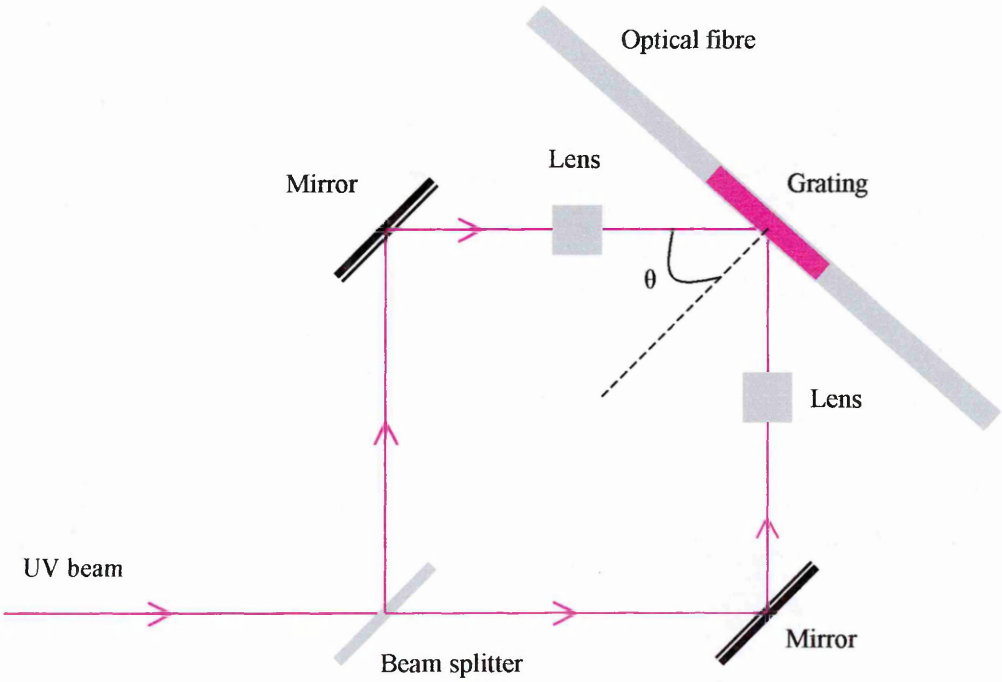

Figure 4. 4: Transverse two-beam interferometer for externally written Bragg gratings [12].

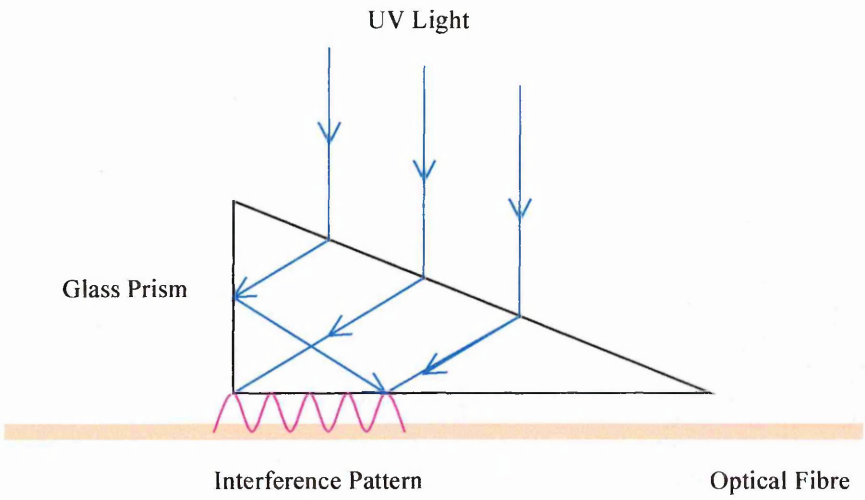

Figure 4. 5: Prism interferometer [17].

The techniques discussed so far may not be suitable for precise grating wavelength

definition due to the difficulty in setting the angles of interfering beams; a phase mask method is therefore usually preferred because it defines the wavelength at which the grating is to be written [18]. A phase mask is a relief grating etched in a silica plate and its principle of operation is based on the diffraction of an incident UV beam into several orders. The period of the phase mask grating is approximately the same as that of the Bragg grating to be written in the fibre. The technique is highly stable and many fabrication configurations are therefore available. The requirement for spatial and temporal coherence of the laser source is relaxed and the insensitivity of the system to translation allows for long gratings to be fabricated. A rectangular prism configuration uses the first order diffracted beams that are internally reflected to produce interference at the fibre [17].

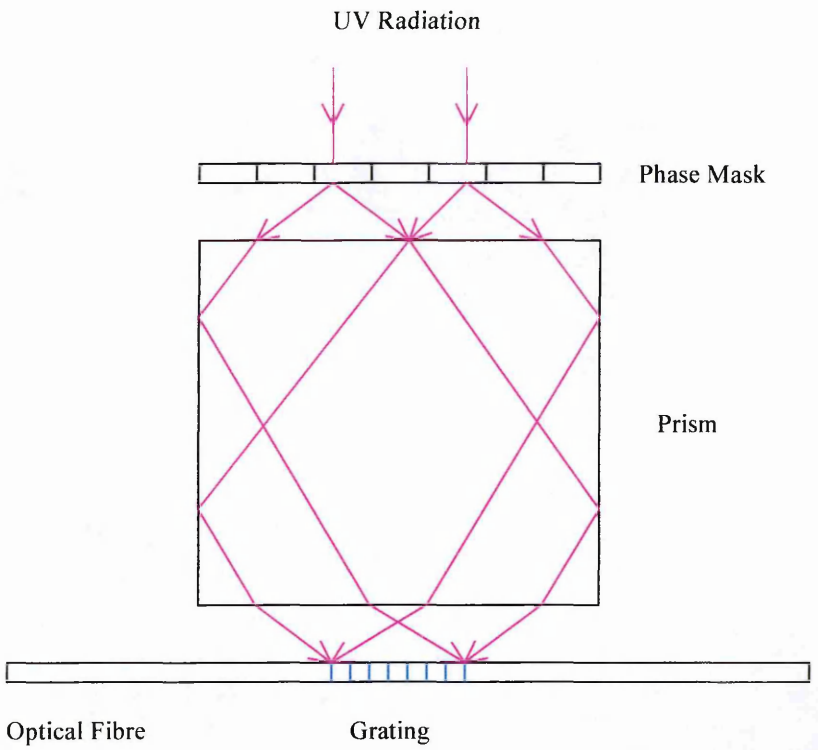

Figure 4. 6: Holographic writing technique using a phase mask and a prism [17]

The phase mask technique originally suffered from the disadvantage of requiring different masks for different Bragg wavelengths. This has however been overcome by the use of a magnifying lens before the phase mask in order to vary the Bragg

wavelength [19]. The magnifying lens magnifies the periodicity of the phase mask which is a requirement for varying the Bragg wavelength of the grating.

If high intensity UV laser beams (power density ≥ 30 MW/cm^2) are used in fabrication a surface damage may occur to the fibre core-cladding interface [17]. This condition is triggered by single photon absorption at 248 nm that excites electrons into the conduction band where they seed the formation of free electron plasma. The electron plasma then causes an abrupt surge in UV absorption that causes damage to the glass. High quality 100 % reflecting gratings can be formed in about 20 ns [13]. Gratings produced by this method are referred to as type II and are thermally very stable as they can withstand temperatures up to 800 ^{0}C [14]. Such gratings however suffer from extensive short wavelength out-of-band loss due to the coupling of the guided mode to the radiation field.

Bragg gratings whose pitch (period) or refractive index modulation is non-constant are referred to as chirped. The chirp, depending on its direction causes longer or shorter wavelengths to travel further into the grating before being reflected. Chirped gratings have been fabricated by varying the pitch along the grating length [20] such that the Bragg condition (Equation 4.1) varies continuously or quasi-continuously for different wavelengths along the length of the grating [Figure 4.7]. Such gratings provide wider bandwidth than uniform pitch gratings, which provides larger wavelength tuning range, useful for the work presented in this thesis.

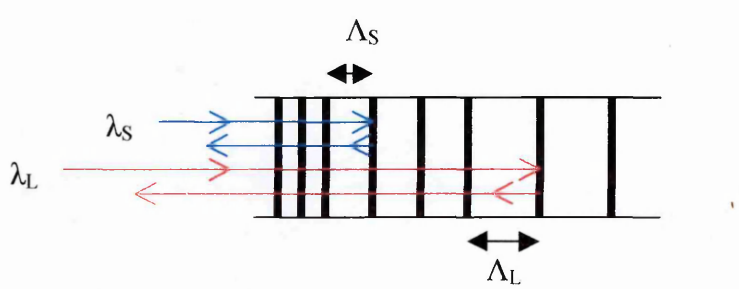

Figure 4.7: Chirped Bragg grating showing non-constant period.

Λ_s and Λ_L refer to the short and long periods respectively while λ_s and λ_L are the corresponding reflected short and long wavelengths.

The methods described by Figure 4.4 to Figure 4.6 can be used to write chirped gratings by positioning the fibre such that its axis is inclined at an angle to the fringes. An alternative method is to expose a bent fibre to a uniform period interference pattern which produces a variation in the effective period along the fibre axis [21]. A more flexible method is to form a chirped grating using the interference between dissimilar wavefronts by using cylindrical lenses in each arm of the original interferometer [22]. A piece-wise chirped grating may be produced by a stretch and write technique in which the fibre held under tension is subjected to a sequence of exposures via the uniform phase mask [23]. Tension is released between exposures. Tilting the fibre with respect to the uniform-pitch phase mask may also produce a linear chirp.

A refractive index modulation that varies linearly along the length of the fibre may be inscribed (producing a linearly chirped grating) by exposing a tapered fibre to a uniform period interference pattern [24].

Figure 4.8 shows a chirped Bragg grating transfer function superimposed to the transfer function of a normal (un-chirped) Bragg grating both at a Bragg wavelength of 514.5 nm. The two transfer functions were generated using the transfer matrix approach that is presented in Chapter 5. In both cases the grating length is 2 mm and the refractive index modulation is 1.2×10^{-4} corresponding to a reflectivity of 81 % for the normal grating. A chirp of 0.1 nm/mm was applied which resulted in a reduced reflectivity of 24 % and a full width bandwidth of about 0.7 nm. The full width bandwidth for the normal grating is about 0.1 nm which corresponds to approximately 113 GHz in frequency. This value is too large when compared to practical flow velocities that are encountered in windtunnels and turbomachinery where Doppler frequency shifts of only a few hundred MHz are produced. Thus UV-fabricated Bragg gratings are not suitable for use as frequency to intensity transducers for they will have negligible sensitivity to practical velocities.

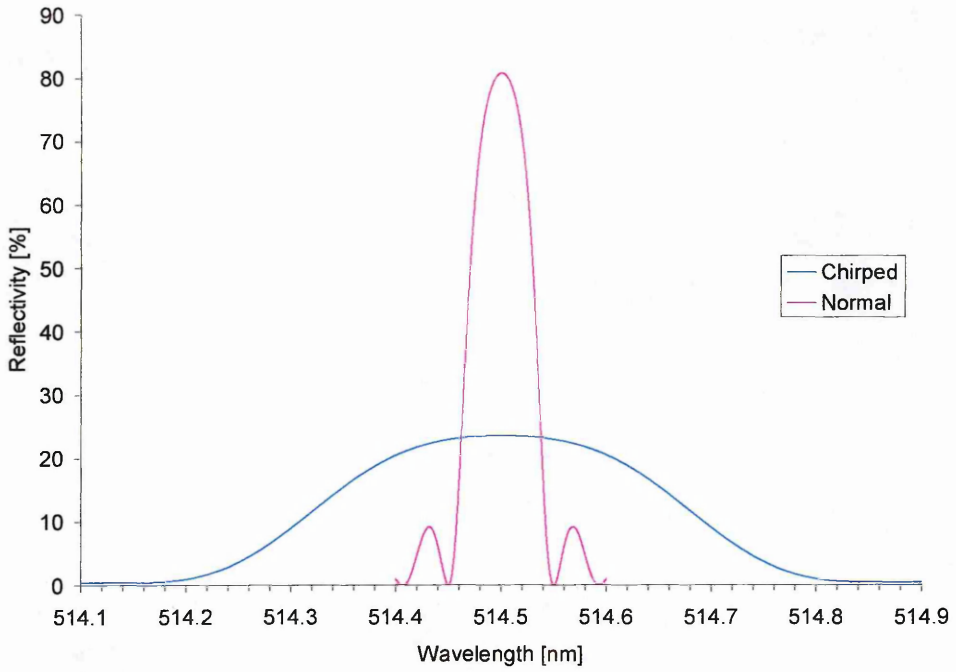

Figure 4. 8: Typical transfer functions of a normal and a chirped Bragg grating.

4.3 Optical Fibre Fabry-Perot Interferometer

An optical fibre Fabry-Perot is fabricated by writing two in-fibre Bragg gratings with similar centre wavelengths that are separated by some distance. The gratings are written by the side holographic techniques using ultraviolet (UV) laser radiation. The gratings constitute distributed mirrors whose reflectivity is wavelength dependent and are thus characterised by a narrow bandwidth. Light able to penetrate the stop-band of one grating is brought into resonance inside the cavity resulting in multiple band-pass peaks appearing in the stop-band. The Fabry-Perot unlike a Bragg grating is an interferometric device that works in transmission and is also used in reflection. The bulk Fabry-Perot filter and the Fabry-Perot formed by two dielectric coated fibre ends separated by some distance could be used but these will not be wavelength tuneable and will not provide the characteristic requirements described in Chapter 5 and 9.

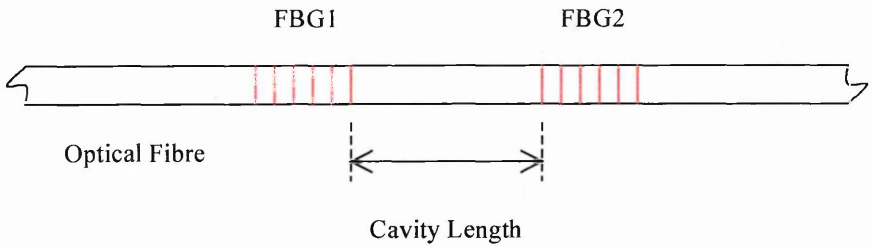

Figure 4. 9: Schematic of FP cavity structure.

The free spectral range (FSR) and finesse of the fibre-optic Fabry-Perot is not fixed but depends on several factors. These include the grating lengths, reflectivity and bandwidth, as well as the cavity length of the Fabry-Perot. Legoubin et al [25] showed that the FSR decreases from the centre of the transmission spectrum outward. Town *et al* [26] reported the fabrication of wide-band Fabry-Perot filters achieved by writing two chirped gratings displaced from each other by some distance. The gratings were chirped in the same direction to ensure a net dispersion of zero. The technique implemented was a dual-beam holographic exposure from dissimilar wavefronts. Oppositely chirped Bragg gratings have also been fabricated to form a Fabry-Perot cavity with a wide range of FSR useful for sensor applications [27].

Figure 4.10 is the typical transfer function of a Fabry-Perot filter simulated from the transfer matrix model described in Chapter 5. The filter consists of two Bragg gratings (at 514.5 nm centre wavelength) separated from each other by 6 cm. Each Bragg grating is 2 mm in length and has a reflectivity of about 30 % that corresponds to a refractive index modulation of 4.8×10^{-5}. The Bragg grating bandwidth is about 0.1 nm (full width) while the passband is only about 0.0005 nm (FWHM) with a free spectral range of 0.0015 nm. These FP values correspond to a passband frequency of about 550 MHz (FWHM), FSR of 1.65 GHz and a finesse of 3. Thus the FP transfer function is attractive for flow measurement application as its FSR can easily be varied. Higher finesse filters would offer higher resolution to velocity but the measurement velocity range is smaller. Low FSR filters are prone to environmental perturbations because of their large length and as a compromise it would be suitable to use smaller FSR.

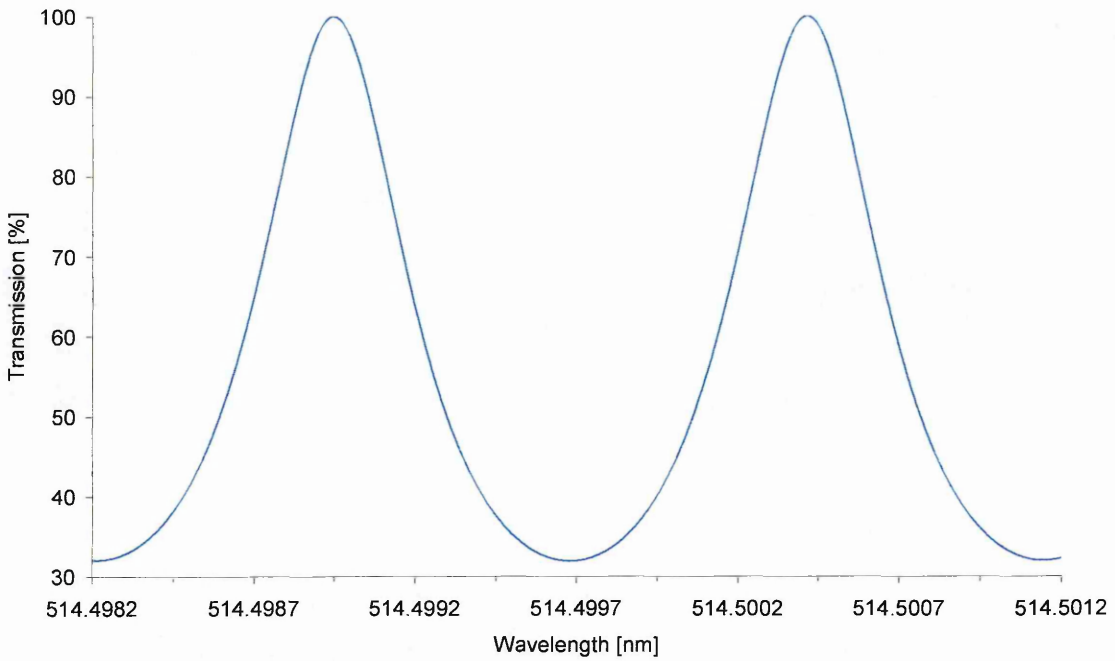

Figure 4. 10: A typical transfer-function of Fabry-Perot filter.

4.4 Phase-shifted Grating

A phase-shifted or distributed feedback (DFG) grating is a simple band-pass filter made by incorporating a phase step in the grating structure. The position and size of this phase determine the position and wavelength of the pass-band. The structure resembles a Fabry-Perot that has a cavity length of less than the wavelength of light. It produces a very narrow pass-band that has a Lorentzian type lineshape.

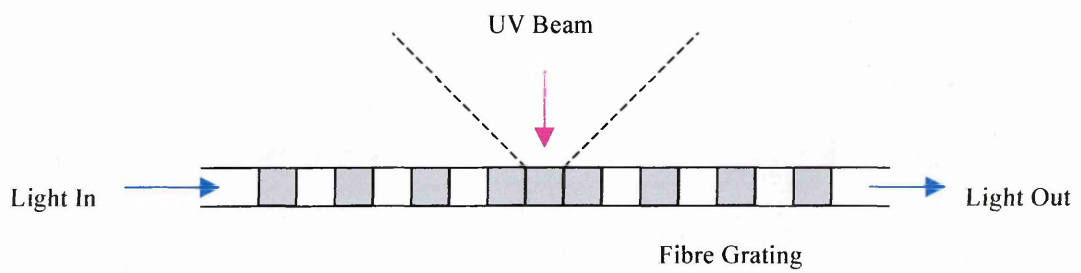

Figure 4. 11: Refractive index modulation of a distributed feedback grating showing UV post-treatment of half a grating period.

One method of fabrication involves a phase mask that consists of a phase shift in the middle, which is responsible for a single transmission window at the centre of the stop-band of the grating [28]. The technique is either to scan a frequency doubled argon-ion laser spot symmetrically along a phase mask in contact with a length of fibre or to use a two-beam interferometer focussed on the fibre. A grating written using a point-by-point technique may be post-treated by illuminating a small section using a laser beam that is focused to a small spot. The illumination raises the refractive index of that point thereby partially erasing the grating, the effect being to produce two gratings that are out of phase with each other. A π-phase shifted grating written by this technique produced a pass-band transmission of about 100 MHz in bandwidth [29].

A chirped grating written by the method of interference of dissimilar wavefronts can be post-treated by focussing an UV beam in the centre of the grating [30]. A wide lossless stopband could also be achieved by further writing two chirped gratings that overlap in the passband of the first. The bandwidth is dependent on the size of the laser spot. Post-treating of a grating is difficult particularly when the grating length is small and undesirable spurious broadband reflections have been reported. Similar results may be achieved by using a chirped phase-mask incorporating a phase step. An alternative technique involves blanking-off a small part of a chirped grating during grating fabrication thereby creating a phase shift in the structure. The bandwidth of the pass-band produced decreases with increasing reflectivity [31].

Phase-shifted Bragg gratings produced by the introduction of a single phase step in the grating structure produce a narrow transmission window but with a broad base resulting in a weak slope of the profile that is more triangular in shape [30]. The introduction of two or three phase shifts at well chosen locations within the grating structure resulted in a pass-band transmission that is more like rectangular in shape with a flat top and steep slopes [32]. The bandwidth of the pass-band however increases. For example two $\pi/2$ phase-shifts inserted into a short Bragg grating of length 4L (L=440 μm), at locations L and 3L by UV post-processing or using a phase mask produced a wider passband than a single $\pi/2$ phase-shift at the centre of Bragg grating of length L. Two such phase-shifts produced 86 % transmission peak of passband width 0.25 nm (in a stop band of 2.3 nm)

compared to a transmission of 64 % and passband width of 0.12 nm (in a stop band width of 2.6 nm) for a single $\pi/2$ phase-shift inserted at the centre of the grating. These results are confirmed by theoretical analysis that was implemented for two or three phase shifts [33].

The first reported experimental and theoretical analysis of multiple phase-shifts in optical fibre Bragg gratings demonstrated the ability to tailor bandpass filter spectral response in terms of such parameters as bandwidth, steepness, flatness and stopband depth [34]. The fabrication technique involved a phase-shifted phase-mask illuminated by an UV-beam. Sugden *et al* [35] carried-out experimental fabrication of bandpass filters by concatenating up to three chirped gratings in optical fibres using a holographic technique that involved dissimilar wavefronts. The technique is reported as causing tilted grating planes that induce coupling loss to radiation modes at the low wavelength side of the grating, a feature that increased with an increase in grating reflectivity.

Figure 4.12 is the transfer function of a DFG filter that was modelled from the transfer matrix method presented in Chapter 5. The graph shows a passband appearing in the stopband of the original normal Bragg grating. The filter of length 2 mm contains a π-phase shift in the middle of a normal Bragg grating with a centre wavelength of 514.5 nm. The characteristics of the transfer function are ideal for velocity measurement. It has linear slopes and the passband can be made narrow by varying the length of grating, reducing the strength of the grating and adjusting the location of the phase shift. A strong refractive index modulation of 1.4×10^{-4} was used to generate this figure thus a large passband of 0.07 nm (full width) was produced corresponding to about 78 GHz of frequency. The FWHM bandwidth is about 0.03 nm or 31 GHz while the filter transmission depth is 72 %. Passband widths of the order of 100 MHz (FWHM) are obtainable.

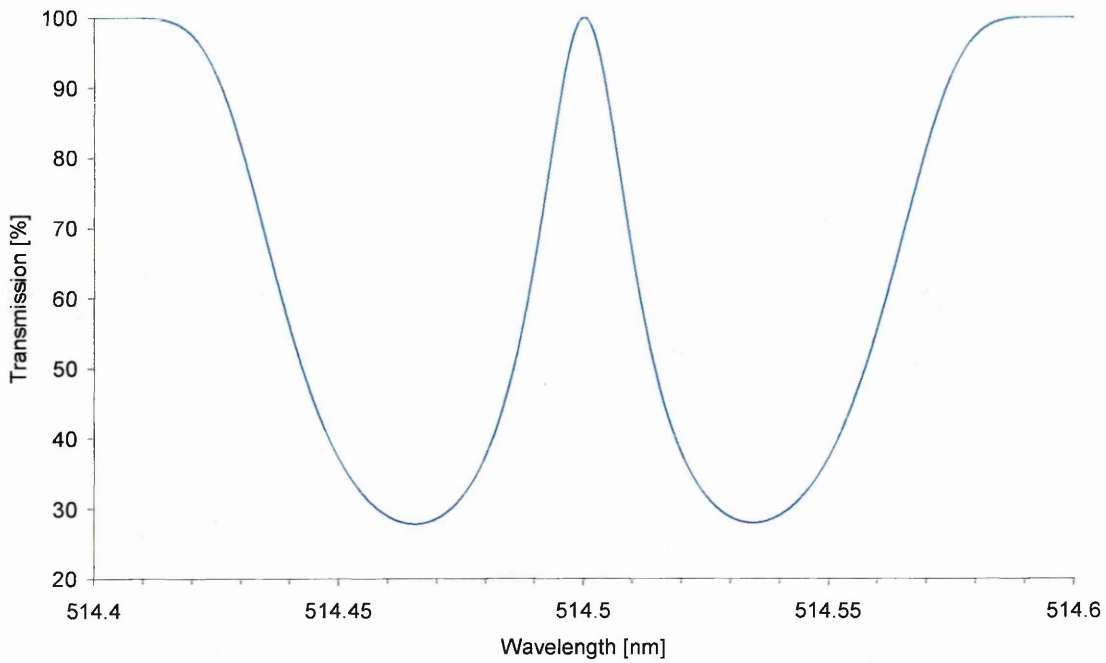

Figure 4. 12: A typical transfer-function of a DFG.

4.5 Moiré Grating

Two gratings with slightly different wavelengths are written at the same location in an optical fibre. The Moiré effect is the simultaneous existence of two such gratings having different periods such that the total UV dose used in the fabrication is not affected. The constant intensity distribution ensures that the induced change in the effective index of the mode remains constant along the grating length. A phase shift would appear since the two gratings will have a different phase response. An increase in the phase shift will cause more passbands to appear in the transmission of the grating structure.

The structure can be fabricated by writing one grating first before altering the beam angle to write the next at the same position. A similar technique involves writing one grating using a chirped phase-mask then stretching the fibre to fabricate the next grating with the same phase-mask. The chirp has the effect of flattening the passband of the filter and may result in multiple passbands if large (Chapter 5). Long chirped Moiré gratings of up to one metre in length have been fabricated using a scanning fibre/phase mask technique [36]. The results demonstrated the fabrication of two Bragg gratings in

one metre length of fibre one centred at 1531.9 nm and the other separated by 2.7 nm and two passband channels were produced each of width 2.7 nm.

A technique involving pulsed UV illumination of the hypotenuse face of an isosceles right-angled fused silica prism acting as an interferometer was used for direct inscription of Moiré gratings [37] e.g. a narrow resonance dip of 0.2 nm was obtained near the centre of the Bragg reflection at 1195 nm. Some of the light refracted off the hypotenuse face reaches the back face that reflects it to the bottom face where it interferes (on to the fibre) with the light that has been directly refracted from the hypotenuse face. The interfering beams have different phase because of the optical path difference created by the prism, which causes the formation of a Moiré grating. Zhang *et al* [38] fabricated very narrow passband but very wide stopband Moiré gratings by a holographic side-writing technique using dissimilar wavefronts. Their results produced a passband width of 0.036 nm (in a stop bandwidth of ~0.3 nm) in a 4 mm length of grating at a Bragg wavelength of 1557 nm. A simple demonstration of the Moiré effect is to write a Bragg grating using an UV interferometer. Another then follows this grating at the same location with same configuration and intensity profile but with an optical wedge placed in the path of one beam to alter the wavelength. The choice of the wedge angle determines the phase change required.

Figure 4.13 is the transfer function of a Moiré grating produced by superposing two 2 mm Bragg gratings having Bragg wavelengths of 514.5 nm and 514.455 nm. Again a transfer matrix approach was used to generate the transfer function (Chapter 5). The figure shows a passband appearing in the bandstop of the Bragg grating. These filters are similar to the DFG filter described in section 4.4 and their transfer functions are similar. A large refractive index modulation was used (5×10^{-5}) causing a large passband of about 0.05 nm (full width) and 0.025 nm (FWHM) to form. Again passbands of the order of 100 MHz are possible by adjusting the magnitude of the wavelength difference between the two gratings and controlling the strength of the grating as well as the grating length. The transfer function is thus suitable for frequency to intensity transduction in velocimetry with its features similar to those of the DFG filter (Section 4.4).

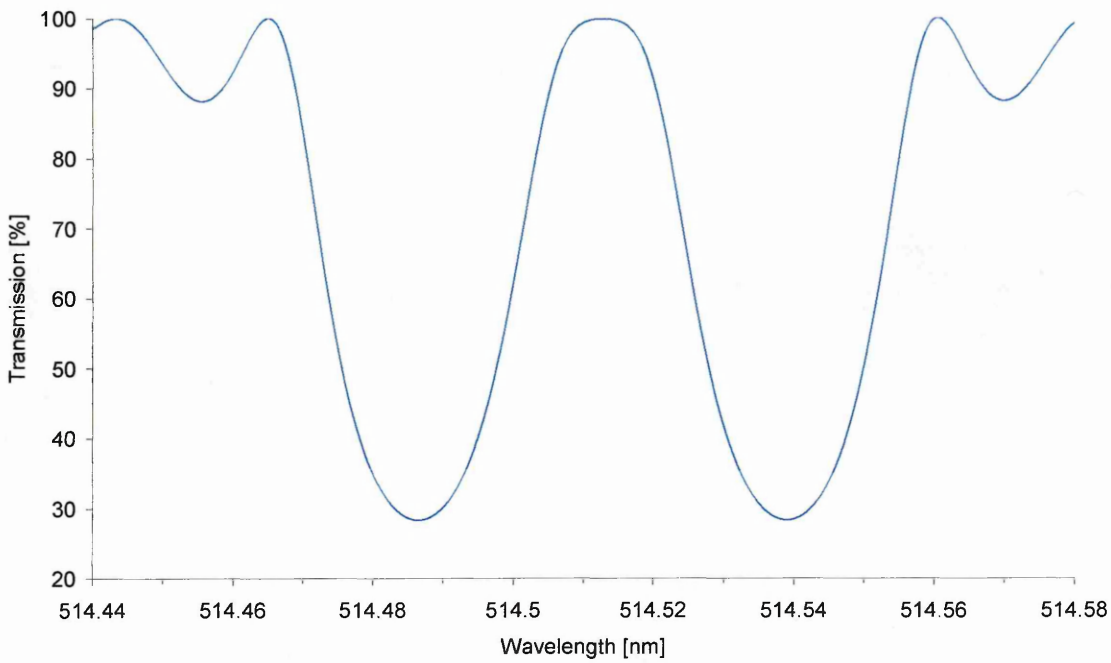

Figure 4. 13: Moiré grating transfer function (typical).

4.6 Interferometric Bandpass Filters

4.6.1 Michelson Interferometer

Narrow bandpass transmission filters that exhibit high return loss in excess of 30 dB (~ 99.9 % reflectivity) can be achieved by fabricating two identical Bragg gratings in adjacent arms of a fused coupler thereby forming a Michelson interferometer (Figure 4.14) [39]. Two approximately identical Bragg gratings (5 mm in length) with 0.25 nm bandwidths and 80 % reflectivity were fabricated. The two gratings are written in close proximity to the coupler and UV-light trimming is used to balance the interferometer in terms of optical path length as well as Bragg grating strength. The illumination of an optical fibre by an UV light beam is known as the UV trim. The effect is to raise the local refractive index of the fibre. If properly done it can result in an optical path difference of the two arms of the interferometer that causes the reflected light from both gratings to be antiphase at the input port while they contribute to approximately 100% of the reflected light at the output port. It is however difficult to suppress the reflected signal from appearing at the input port owing to the difficulty in matching the two

gratings in terms of their reflectivity, bandwidth and centre wavelength. The transfer function of the filter is a strong function of the optical path difference and there exists a rapid drop in transmission for a detuning of less than half a wavelength.

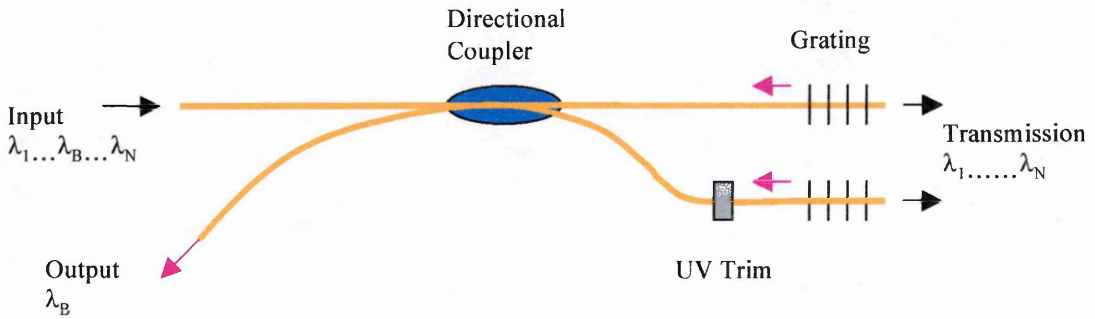

Figure 4. 14: Michelson bandpass transmission filter [40].

The transfer function of a Michelson interferometer is well known as sinusoidal [40]. The change in reflectivity of the Bragg gratings would therefore change the shape of the transfer function (i.e. the slope and transmission depth) but the passband frequency remains unchanged. This means the filter will only adjust the sensitivity of the velocity but not the range and resolution of velocity since these are dependent on the passband frequency. The linearity of the slope of the filter is also limited because of the sinusoidal shape.

4.6.2 Mach-Zehnder Interferometer

Two directional couplers may be joined together in close proximity with two identical Bragg gratings in the two arms (Figure 4.15) thereby forming a Mach-Zehnder interferometer. Such a set up is advantageous when the interferometer is used in transmission where the 50% signal of the Michelson interferometer can be improved to approximately 100%. This can be achieved by an UV trim in one arm of the device and close to the second coupler. The device can be athermalised by using a special glass substrate with a large negative thermal expansion coefficient (that is bonded to the gratings) and this was found to decrease the Bragg grating sensitivity to temperature by as much as 10 times over a temperature range of -40^0C to $+85^0$C [40]. The negative

temperature coefficient means that the substrate does not expand with temperature and will inhibit the thermal expansion of the grating (compensating for the effect of temperature change). The output port provides a narrow passband centred at the Bragg wavelength λ_B.

Kashyap et al [41] fabricated two gratings of over 90 % reflectivity at 1555.8 nm and the reflection signal in the input port was determined as 9.76 % while that in the output port was 58.8 % of the total input power.

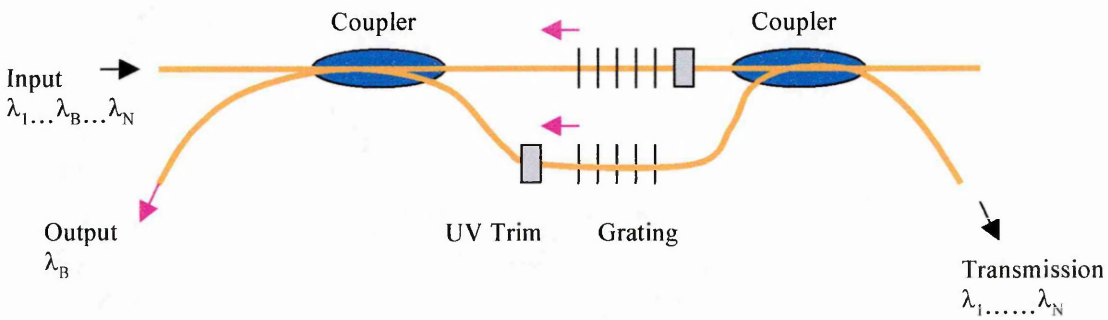

Figure 4. 15: Mach-Zehnder Interferometer bandpass transmission filter [38].

The transfer function of this filter is similar to that of the Michelson interferometer described in section 4.6.1 thus similarly has limited features for velocimetry application.

4.7 Applications

Several applications for FBG based filters are possible hinging on grating period and length, and strength of refractive index modulation for this determines whether it has a high or low reflectivity over a wide range of wavelengths. The gratings can be used as resonant reflectors in fibre laser cavities or externally as laser mode control. Hill et al [5] demonstrated a possible application of a filter as a distributed feed back device (DFB). The first DFB oscillation of a gas laser operating in the visible region of the spectrum was established by replacing the out put reflector of an argon-ion laser with a fibre Bragg grating thereby yielding stable CW oscillation at 488 nm. A FBG has been used to provide an external cavity to a semiconductor diode laser [40]. A narrow line

operation is achieved and an additional advantage to switch the laser from one mode to another is also possible by temperature or strain tuning of the grating.

Chirped FBGs are used to compensate for chromatic dispersion of short pulses in optical fibres for telecommunications [43]. A wavelength dependent propagation delay occurs in which light of different wavelength is reflected at a different point along the axis of the fibre (Figure 4.7). Use of Bragg gratings as wavelength selective filters allows removal of unwanted laser frequencies in fibre amplifiers [14]. Blazed gratings whose grating planes are tilted with respect to the fibre axis can be used to flatten the gain profile of fibre amplifiers as well as wavelength selective taps to the radiation modes (important for monitoring fibre networks) [44]. The ability to write multifilters or combfilters in the same fibre opens an attractive application for high capacity wavelength division multiplexing (WDM) or demultiplexing optical communication systems.

The sensitivity of FBGs to temperature and strain render them important devices as sensors for these and other physical quantities [45, 46] that include force, acoustic waves, pressure, strong magnetic field and vibration. Fibre Bragg grating sensors are based on the detection of the measurand-induced wavelength shift but measurement resolution is limited [47]. High resolution measurements usually rely on the detection of optical phase change using fibre optic interferometric sensors such as Bragg grating based Fabry-Perot cavities [48]. A fibre Fabry-Perot cavity consisting of two oppositely chirped Bragg gratings was demonstrated to have large dynamic range and high resolution capabilities that is useful for sensor applications [27]. This device was applied to measure a strain range of 3 to 1300 μstrain (at 1 μstrain resolution) with FSR ranging from 0.04 to 1.3 nm. Simultaneous measurement of strain and temperature has also been demonstrated [49]. The capabilities of a Bragg grating as a distributed vibration sensor were demonstrated by La Rochelle et al [50]. A photosensitive grating was detuned by acoustically inducing vibrations in the optical table and vibration amplitudes less then 50 nm could easily detune the grating. Current applications in these areas involve sensor multiplexing in which they are embedded in advanced composite

materials to provide an integrated sensory network (SMART materials and structures) [51].

It can be derived from the sensor applications described above that interferometric techniques with their inherent tuneability particularly the fibre Fabry-Perot interferometer can provide very high-resolution measurements. Such attributes are the reason for their choice for the application to this work. The synthesis of these filters with their tailored response characteristics for sensing the velocity-encoded Doppler frequency-shifted optical signal for laser velocimetry is described in the next chapter. The optical filter is required to directly convert Doppler frequency shifts emanating from the flow particles into intensity variations, which can be directly related to velocity.

4.8 Summary

This chapter has reviewed various Bragg grating based filters. Considered were the fabrication methods, filter transfer characteristics and their applications. The review showed that FP, DFG, Moiré and end-pumped gratings have suitable transfer functions for velocimetry applications and can have bandwidth as narrow as 100 MHz. However end-pumped grating fabrication is critical and coupled with lack of photosensitive optical fibres at the blue/green wavelength makes it difficult to fabricate high reflectivity gratings. Their long lengths make them prone to environmental perturbations and difficult to stabilize. On the other hand the fabrication of FP, DFB and Moiré could be made easier by using phase-masks and the filters can be fabricated at any desired wavelength unlike the end-pumped grating that forms only at the wavelength of fabrication. The FP is particularly attractive as it exhibits a well known transfer function but is rather long in size (typically 50 mm for this application) when compared to the DFB and Moiré which can be made very small e.g. 1 mm.

The Michelson and Mach-Zehnder filters consist of Bragg gratings in separate fibres of the coupler thus making them prone to phase instabilities and the optical path length difference was found to critically attenuate the device output. These factors together

with their transfer functions that are sinusoidal make them less attractive to velocimetry use.

Filter type	*Frequency bandwidth*	*Wavelength [nm]*	*Size or length*
End-pumped	~100 MHz – 1 GHz	488 & 514.5 nm	Up to 100 cm (LC)
FP	Any bandwidth possible	Any wavelength	A few cm – several cm
DFG	~100 MHz – few GHz	Any wavelength	~ 4 mm
Moiré	~100 MHz – few GHz	Any wavelength	~ 4 mm

Table 4. 1: Comparison of filter types. LC – limited by laser coherence length.

Table 4.1 compares the filters that were discovered to be particularly suitable for velocimetry applications. More comparisons are given in Table 5.3 in Chapter 5.

References

[1] A. Othonos, "*Fiber Bragg gratings*", Rev. Sci. Instrum. 68 (12), 1997.

[2] R. M. Atkins and V. Mizrahi, "*Observation of changes in UV absorption bands of single mode germanosilicate core optical fibres on writing and thermally erasing refractive index gratings*", Electronics Letters, vol. 28, no. 18, pp. 1743, 1992.

[3] B. Guo and D. Z. Anderson, "*Undepleted pump regime of Hill grating formation in optical fibres*", Applied Physics Letters 60 (6), 1992.

[4] D. P. Hand and R. St. J. Russell, "*Photoinduced refractive index changes in germanosilicate fibres*", Optics Letters, vol. 15, pp. 102, 1990.

[5] K. O. Hill, Y. Fuji, D. C. Johnson, and B. S. Kawasaki, "*Photosensitivity in optical fiber waveguide: Application to reflection filter fabrication*", Applied Optics Letters 32 (10), 1978.

[6] L. J. Poyntz-Wright, M. E. Fermann, and P. St. J. Russell, "*Nonlinear transmission and color-center dynamics in germanosilicate fibers at 420 – 540 nm*", Optics Letters, vol. 13, no. 11, 1988.

[7] L. J. Poyntz, and P. St. J. Russell, "*Spontaneous relaxation processes in irradiated germanosilicate fibres*", Electron Letters, vol. 25, no. 7, 1989.

[8] L. J. Poyntz, and P. St. J. Russell, "*Photochromic dynamics and nonlinear transmission at modulated CW blue/green wavelengths in germanosilicate optical fibres*", Electron Letters, vol. 24, no. 16, 1988.

[9] J. Stone, "*Photorefractivity in GeO_2-doped silica fibers*", Journal of Applied Physics, vol. 64, no. 11, pp. 4371-4374, 1987.

[10] D. K. W. Lam and B. K. Garside, "*Characterisation of single-mode optical fiber filters*", Applied Optics, vol. 20, no. 3, pp. 440-445, 1981.

[11] J. Lapierre, J. Bures, and G. Chevalier, "*Fiber-optic integrated interference filters*", Optics Letters, vol. 7, no. 1, pp. 37-39, 1982.

[12] G. Meltz, W. W. Morey, and W. H. Glenn, "*Formation of Bragg gratings in optical fibres by transverse holographic methods*", Optics Letters, vol. 14, no. 15, pp. 823, 1989.

[13] R. J. Campbell and R. Kashyap, "The *properties and applications of photosensitive germanosilicate fibre*", International Journal of Optoelectronics, Vol. 9, No. 1, pages 33 – 57, 1994.

[14] P. St. J. Russell, J-L. Archambault, and L. Reekie, "*Fibre gratings*", Physics World, 1993.

[15] D. L. William and R. P. Smith, "*Accelerated lifetime tests on UV written intracore gratings in boron germanium co-doped silica fibre*", Electronics Letters, vol. 31, no. 24, pp. 2120-2121, 1995.

[16] M. L. Dockney, "*Fabrication of Wavelength Division Multiplexed in-Fibre Bragg Grating Arrays for Structural Monitoring Applications*", Ph.D. Thesis, Cranfield University, UK, 1997.

[17] R. Kashyap, "*Photosensitive optical fibers: Devices and Applications*", Optical Fiber Technology 1, pages 17 – 34, 1994.

[18] K. O. Hill, B. Malo, F. Bilodeau, D. C. Johnson, and J. Albert, "*Bragg grating fabricated in monomode photosensitive optical fiber by UV exposure through a phase mask*", Applied Physics Letters, vol. 62, no. 10, pp. 1035, 1993.

[19] J. D. Proshaska, E. Snitzer, S. Rishton, and V. Boegli, "*Magnification of mask fabricated fibre Bragg gratings*", Electron Letters, 29, pp. 1614-1615, 1993.

[20] R. Kashyap, P. F. McKee, R. J. Campbell and D. L. Williams, "*Novel method of producing all fibre photoinduced chirped gratings*", Electronics Letters, vol. 30, no. 12, pp. 996-997, 1994.

[21] K. Sugden, I. Bennion, A. Molony, and N. J. Copner, "*Chirped gratings produced in photosensitive optical fibres by deformation during exposure*", Electronics Letters, vol. 30, no. 5, pp. 440, 1994.

[22] I. Bennion, J. A. R. Williams, L. Zhang, K. Sugden, and N. J. Doran, "*UV – written in-fibre Bragg gratings*", Optical and Quantum Electronics 28, pp. 93 – 135, 1996.

[23] K. C. Byron and H. N. Rourke, "*Fabrication of chirped fibre gratings by novel stretch and write technique*", Electronics Letters, vol. 31, no. 1, pp. 60-61, 1995.

[24] K. C. Byron, K. Sugden, T. Bircheno, and I Bennion, "*Fabrication of chirped Bragg gratings in photosensitive fibre*", Electronics Letters, vol. 29, no. 18, pp. 1659, 1993.

[25] S. Legoubin, M. Douay, P. Bernage, P. Niay, S. Boj and E. Delevaque, "*Free spectral range variations of the grating-based Fabry-Perot filters photowritten in optical fibres*", Journal of Optical Society of America A, vol. 12, no. 8, pp. 1687 – 1694, 1995.

[26] G. E. Town, K. Sugden, J. A. R. Williams, I. Bennion and S. B. Poole, "*Wide-Band Fabry-Perot –Like Filters in Optical Fibre*", IEEE Photonics Technology Letters, vol. 7, no. 1, pp. 78 – 80, 1995.

[27] K. P. Koo, M. LeBlanc, T. E. Tsai, and S. T. Vohra, "*Fiber-Chirped Grating Fabry-Perot Sensor with Multiple-Wavelength-Addressable Free-Spectral Ranges*", IEEE Photonics Technology Letters, vol. 10, no. 7, 1998.

[28] R. Kashyap, P. F. Mckee and D. Armes, "*UV written reflection grating structures in photosensitive optical fibres using phase-shifted phase masks*", Electronics letters, vol. 30, no. 23, pp. 1977 – 1978, 1994.

[29] J. Canning and M. G. Sceats, "*π-phase-shifted periodic distributed structures in optical fibres by UV post-processing*", Electronics Letters, vol. 30, no. 16, pp. 1344 – 1345, 1994.

[30] L. Zhang, K. Sugden, J. A. R. Williams, I. Bennion, D. C. J. Reid and C. M. Ragdale, "*Postfabrication exposure of gap-type bandpass filters in broadly chirped fibre gratings*", Optics letters, vol. 20, no. 18, pp. 1927 – 1929, 1995.

[31] M. C. Farries, K. Sugden, D. C. J. Reid, I. Bennion, A. Malony and M. J. Goodwin, "*Very broad reflection bandwidth (44 nm) chirped fibre gratings and narrow bandpass filters produced by the use of an amplitude mask*", Electronics Letters, vol. 30, no. 11, pp. 891 – 892, 1994.

[32] F. Bakhti and P. Sansonetti, "*Wide bandwidth, low loss and highly rejective doubly phase-shifted UV-written fibre bandpass filter*", Electronics Letters, vol.32, no. 6, pp. 581 – 582, 1996.

[33] L. Wei and J. Y. Lit, "*Phase-Shifted Bragg Grating Filters with Symmetrical Structures*", Journal of Lightwave Technology, vol. 15, no. 8, pp. 1405 – 1410, 1997.

[34] F. Bakhti and P. Sansonetti, "*Design and Realisation of Multiple Quarter-Wave Phase-Shifts UV-Written Bandpass Filters in Optical Fibres*", Journal of Lightwave Technology, vol. 15, no. 8, pp. 1433 – 1437, 1997.

[35] K. Sugden, L. Zhang, J. A. R. Williams, R. W. Fallon, L. A. Everall, K. E. Chisholm and I. Bennion, "*Fabrication and Characterisation of Bandpass Filters Based on Concatenating Chirped Fibre Gratings*", Journal of Lightwave Technology, vol. 15, no. 8, pp. 1424 – 1432, 1997.

[36] M. Isben, M. K. Durkin and R. I. Laming, "*Chirped Moiré fibre gratings Operating on Two-Wavelength Channels for use as Dual-Channel Dispersion Compensators*", IEEE Photonics Technology Letters, vol. 10, no. 1, pp. 84 – 86, 1998.

[37] S. Legoubin, E. Fertein, M. Douay, P. Bernage and P. Niay, "*Formation of Moiré grating in core of germanosilicate fibre by transverse holographic double exposure method*", Electronics Letters, vol. 27, no. 21, pp. 1945 – 1946, 1991.

[38] L. Zhang, K. Sugden, I. Bennion and A. Molony, "*Wide-stopband chirped fibre moiré grating transmission filters*", Electronics Letters, vol. 31, no. 6, pp. 477 – 479, 1995.

[39] F. Bilodeau, K. O. Hill, B. Malo, D. C. Johnson and J. Albert, "*High-Return-Loss Narrowband All-Fibre Bandpass Bragg Transmission Filter*", IEEE Photonics Technology Letters, vol. 6, no. 1, pp. 80 – 82, 1994.

[40] R. Kashyap, "*Fibre Bragg Gratings*", Academic Press, 1999.

[41] R. Kashyap, G. D. Maxwell, and B. J. Ainslie, "*Laser-Trimmed Four-Port Bandpass Filter Fabricated in Single-Mode Photosensitive Ge-Doped Planar Waveguide*", IEEE Photonics Technology Letters, vol. 5, no. 2, 1993.

[42] D. M. Bird, J. R. Armitage, R. Kashyap, R. M. A. Fatah, and K. H. Cameron, "*Narrow line semiconductor laser fibre grating*", Electronics Letters, vol. 27, pp. 1115, 1991.

[43] F. Oullette, "*Dispersion cancellation using linearly chirped Bragg grating filters in optical waveguides*", Optics Letters, vol. 12, no. 10, pp. 847, 1987.

[44] R. Kashyap, R. Wyatt, and P. F. McKee, "*Wavelength flattened saturated erbium amplifier using multiple side-tap Bragg gratings*", Electronics Letters, vol. 29, no. 11, pp. 1025, 1993.

[45] G. B. Hocker, "*Fiber-optic sensing of pressure and temperature*", Applied Optics, vol. 18, no. 9, pp. 1445-1448, 1979.

[46] C. M. Lawrence, D. V. Nelson and A. Makino, "*Modelling of the Multi-parameter Bragg Grating Sensor*", SPIE vol. 3180, pp. 42-49, 1997.

[47] Y. J. Rao, "*In-fibre Bragg grating sensors*", Measurement Science and Technology, vol. 8, pp. 355-375, 1997.

[48] Y. J. Rao, M. R. Cooper, D. A. Jackson, C. N. Pannell, and L. Reekie, "*Absolute strain measurement using an in-fibre-Bragg-grating-based Fabry-Perot sensor*", Electronics Letters, vol. 36, no. 8, 2000.

[49] W. C. Du, X. M. Tao, and H. Y. Tam, "*Fiber Bragg Grating Cavity Sensor for Simultaneous Measurement of Strain and Temperature*", IEEE Photonics Technology Letters, vol. 11, no. 1, 1999.

[50] S. LaRochelle, V. Mizrahi, K. D. Simmons, G. I. Stegeman, and J. E. Sipe, "*Photosensitive optical fibers used as vibration sensors*", Optics Letters, Vol. 15, No. 7, 1990.

[51] E. Udd, K. Black, W. Schulz, S. Kreger, M. Kunzler and D. Heider, "*In-situ evaluation of composite structural performance in presence of high stress/strain gradients using multi-axis fiber grating strain sensors*", 15th Optical Fiber Sensors Conference (2002) technical digest, pp. 79-82, 2002.

CHAPTER 5

Theoretical Modelling of Fibre Optic Filters

5.1 Introduction

A theoretical study of the various fibre-optic filters is necessary to determine their suitability for Doppler frequency discrimination. The motivation is to design filters whose parameters can be manipulated to suit turbomachinery (high speed) and wind tunnel (low speed) flows. Such filter parameters include the frequency linewidth and the slope of the transfer function, which respectively determine the magnitude of the velocity and its resolution, and sensitivity.

The chapter will begin by introducing the properties of optical fibres and their guided modes. Usually the modes will not interact with each other except in the presence of a perturbation such as a bend, twist, grating etc [1]. The mode interactions are largely described by a fundamental theory known as the coupled mode theory but are usually modelled by a technique known as the transfer matrix model. Both techniques are implemented and results (that include the effects of temperature and strain perturbations) are given. The results from the models are used in chapter 7 to set fabrication parameters for the filters.

5.2 Properties of Optical Fibre

Glass optical fibres are usually cylindrical (Figure 5.1) and they normally have cylindrically symmetric refractive index profiles. The core transmits the light while the cladding/core interface causes total internal reflection to light that is incident on the interface thus confining the light within the core [2, 3]. This is made possible because of the refractive index of the cladding that is lower than that of the core. The refractive index profile across the fibre cross-section from cladding to core is either a step function

(step index profile) or a graded function (graded index profile). Fibres are further classified as either single mode or multimode with the former exhibiting step refractive index profile while the later can have either step or graded index profile. A single mode fibre has a small core radius relative to that of a multimode fibre. Singlemode fibres support one mode of propagation of light as compared to multimode fibres that support many modes.

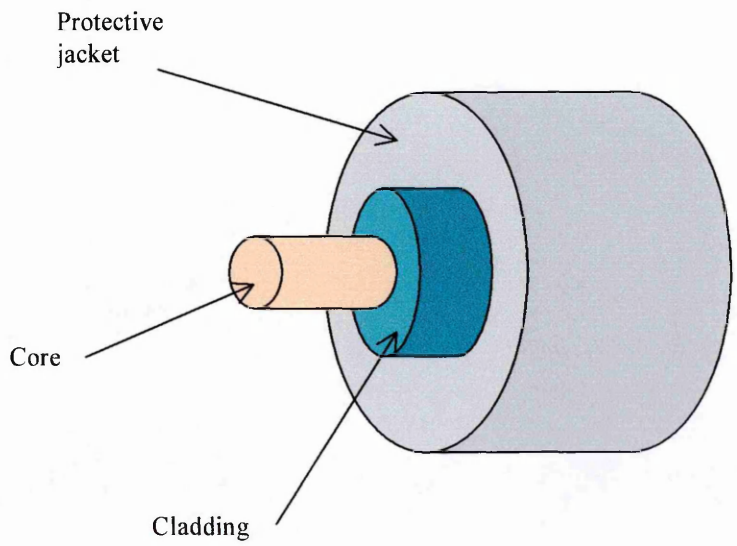

Figure 5. 1: Geometry of an optical fibre.

The refractive index between the core and cladding of a single mode fibre is small (< 1%) and the fibres are referred to as weakly guiding [4]. The waveguiding properties of an optical fibre can be obtained by solving the propagation wave equations that are derived from Maxwell equations. The tangential electric and magnetic field solutions for the cladding and core are required to be continuous at the core/cladding interface and this allows for exact solutions to be obtained.

Globe [4] derived the modal properties of the weakly guiding fibres. If the refractive indices of the core and cladding are n_1 and n_2 respectively then the propagation constant β of any guided mode in the fibre satisfies, $n_2k \leq \beta \leq n_1k$, where $k=2\pi/\lambda_0$ is the propagation constant in vacuum and λ_0 is the vacuum wavelength of light. Parameters U

and W that relate to light propagation in the core and cladding respectively, are defined as

$$U = a\left(k^2 n_1^{\,2} - \beta^2\right)^{\frac{1}{2}} \tag{5.1}$$

$$W = a\left(\beta^2 - k^2 n_2^{\,2}\right)^{\frac{1}{2}} \tag{5.2}$$

where a is the radius of the core. The radial dependence of the magnitude of the electric field vector for the guided mode can be expressed by the Bessel function, $J(Ur/a)$ inside the core and the modified Hankel function, $K(Wr/a)$ in the cladding. The fields at the core/cladding interface are therefore given by $J(U)$ and $K(W)$ where $r=a$. A parameter, V, called the normalised frequency of a fibre is defined by

$$V = \left(U^2 + W^2\right)^{\frac{1}{2}} = ak\left(n_1^{\,2} - n_2^{\,2}\right)^{\frac{1}{2}} \tag{5.3}$$

The normalised frequency marks the cut-off values of the modes such that as a mode approaches cut-off the fields extend well into the cladding thus causing poor mode confinement. For frequencies far above (or wavelengths below) cut-off, the mode is tightly confined to the core and the index of the mode tends that of the core.

The solutions to the wave equations obtained by assuming that $n_1 \approx n_2$ solutions are known as the linearly polarised (LP) modes. The LP modes are almost transverse polarised, being dominated by one transverse electric field component and one transverse magnetic field component (i.e. E_x and H_y for x-polarised or E_y and H_x for y-polarised). LP_{01} is the lowest order mode and is radially symmetric. The E (electric field) vector lies along the radial direction with H (magnetic field) vector on an orthogonal radial direction. To this mode there exists an independent but orthogonal mode and the two modes are degenerate. The single mode condition for an optical fibre is $V<2.405$. A mathematical treatment of the mode theory is outside the scope of this work but may be found elsewhere [5]. Particular modes will couple to each other in the presence of a Bragg grating or other perturbations and this concept is discussed in section (5.3).

5.3 Fibre Bragg Grating Models

The formation of Bragg and superstructure gratings has already been described in chapter 4. Here the theories behind the wave interactions producing the refractive index gratings have been developed in Fortran 90 and some results are presented. These models are useful for determining filters of appropriate features for velocimetry applications. Also required is the determination of grating parameters that are required for the fabrication of the filters.

5.3.1 Coupled Mode Theory

The refractive index modulation, $\delta n(z)$ of the grating may be defined by the real part of equation (5.4) where $\Delta\overline{n}$ is the dc refractive index change over a single period, Λ of the grating and $V, \Phi(z)$ are respectively the visibility of the fringes and the grating phase [6]. In equation (5.4) only the contribution due to first order diffraction is considered to be sufficient.

$$\delta n(z) = \Delta\overline{n} \cdot \left\{ 1 + \tfrac{V}{2} \cdot \left(e^{i\left[\frac{2\pi}{\Lambda} Z + \Phi(Z)\right]} \right) \right\} \qquad (5.4)$$

Important parameters for the Bragg grating are $\Delta\beta$ the phase mismatch (detuning parameter), k_{dc} the dc coupling coefficient, and k_{ac} the ac coupling coefficient. The coupling coefficients describe the interaction between the two counter propagating fields with k_{ac} describing the modulated interaction due to Δn the refractive index modulation and k_{dc} gives a constant interaction caused by $\Delta\overline{n}$ the average refractive change. Equation (5.5) and (5.6) can approximate these coupling coefficients if the Bragg grating supports only the fundamental mode.

$$k_{dc} = \frac{2\pi}{\lambda_B} \cdot \Delta\overline{n} \qquad (5.5)$$

$$k_{ac} = \frac{V \cdot k_{dc}}{2} \qquad (5.6)$$

$$\Delta\beta = \beta - \frac{\pi}{\Lambda} \qquad (5.7)$$

The general coupled mode equations for identical contradirectional propagating modes in an optical fibre containing a grating is given by [6]

$$\frac{dI}{dz} + i\left[k_{dc} + \Delta\beta - \tfrac{1}{2}\cdot\frac{d\Phi(z)}{dz}\right]\cdot I = -ik_{ac}^{*}\cdot U \qquad (5.8)$$

$$\frac{dU}{dz} - i\left[k_{dc} + \Delta\beta - \tfrac{1}{2}\cdot\frac{d\Phi(z)}{dz}\right]\cdot U = ik_{ac}\cdot I \qquad (5.9)$$

The imaginary part of the dc coupling coefficient can be taken to include absorption, gain or scattering losses. The phase term in the coupled mode equations, if non-constant signifies chirp in the grating period (for non-uniform grating) and has the tendency of detuning the grating. Equation (5.8) and (5.9) are solved by separation of the variables through the formation of second order differential equations from which general solutions are obtained. Application of the appropriate boundary conditions usually *I(0)=1* (normalised input) and *U(L)=0* (no input backward wave) where L is the grating length results in a particular solution. The coupled mode equations have been solved in [section 5.2] and the resulting power reflectivity R is reproduced as equation (5.10) and (5.11) below.

$$R = \frac{|k_{ac}|^2 \cdot \sinh^2(SL)}{|k_{ac}|^2 \cdot \cosh^2(SL) - \delta^2} \qquad |k_{ac}| > \delta \qquad (5.10)$$

$$R = \frac{|k_{ac}|^2 \cdot \sin^2(SL)}{\delta^2 - |k_{ac}|^2 \cdot \cos^2(SL)} \qquad |k_{ac}| < \delta \qquad (5.11)$$

Parameters δ (dc self-coupling coefficient) and S are defined as

$$\delta = k_{dc} + \Delta\beta - \frac{1}{2}\cdot\frac{d\Phi(z)}{dz} \qquad (5.12)$$

$$S = \sqrt{|k_{ac}|^2 - \delta^2} \qquad (5.13)$$

Maximum reflectivity R_{max} is obtained when $\delta=0$, when the phase matching condition $\lambda_B=2n_{eff}\Lambda$ is satisfied.

$$R_{\max} = \tanh^2(k_{ac}\cdot L) \qquad (5.14)$$

Parameters λ_B and n_{eff} are respectively the Bragg wavelength and effective refractive index. The first two zeros of equation (5.10) may be used to approximate the full Bragg grating bandwidth $2\Delta\lambda$ as in equation (5.15).

$$\Delta\lambda = \frac{\lambda^2}{2\pi n_{eff}\cdot L}\cdot\sqrt{(k_{ac}\cdot L)^2 + \pi^2} \qquad (5.15)$$

An assumption of a weak grating requires that $k_{ac}\cdot L<<\pi$ and the bandwidth of the grating at full width and half maximum (FWHM) is thus given by

$$\Delta\lambda = \frac{\lambda^2}{2n_{eff}\cdot L} \qquad (5.16)$$

This equation is characteristic of a length-limited grating that normally applies to internally written gratings. In the strong grating limit $k_{ac}\cdot L>>\pi$ the bandwidth is independent of the length of the grating but directly proportional to induced index change through the coupling coefficient as in equation (5.17).

$$\Delta\lambda = \frac{k_{ac}\cdot\lambda^2}{2\pi n_{eff}} \qquad (5.17)$$

5.3.2 Transfer Matrix Model

The analytical solutions of the coupled mode equations are limited to analysing Bragg gratings with approximately uniform period and refractive index modulation. It is therefore insufficient for characterising real gratings that are bound to have varying parameters due to the laser beam profile, experimental configuration, fibre properties and the prevailing environmental conditions. The coupled mode theory is also derived on the basis of a Bragg grating that has weak coupling (slow amplitude variation) and is only approximate for strong gratings.

Uniform Bragg gratings are characterised by side-lobe structure due to the sudden start and end of the grating. The ability to chirp the grating period or apodise the refractive index modulation may result in a grating that has a gradual start and end an effect that suppresses the side-lobe structure. It is desirable to design in-fibre Bragg grating devices with controlled transfer characteristics that require the manipulation of such parameters as chirp, apodisation and index modulation for various specific applications. Most notable applications are in optical fibre communications, distributed feedback lasers and filters. Analytical solutions for such devices are complicated to produce if not impossible. Numerical solutions such as the adaptive-stepwise Runge-Kutta method may be used but are very time consuming and so is the Rouard analysis technique [7, 8]. The transfer matrix method (TMM) is most preferred because it provides a more accurate and fast technique for grating simulation [9].

The technique involves dividing the grating length, L, into a large number, N, of layers each of length δL. The length, δL, is defined such that N is an integer otherwise a phase discontinuity will exist in the structure that may cause extra features such as ripples in the spectrum. Parameters such as index change, grating period and coupling coefficient are taken to be constant within a subsection. This enables the solutions of the coupled mode equation (5.8) and (5.9) to be applied to each grating layer. The input and output field amplitudes including their phase are thus calculated via a linking matrix M_i for the i^{th} layer of length δL_i. The outputs of this layer are used as inputs to the next $(i+1)^{th}$ layer where coupled mode solutions are again invoked in-order to obtain the output field

amplitudes via a second transfer matrix M_{i+1}. The process is repeated until N matrices are generated for the entire length of the grating. The inputs at one end of the grating and the outputs at the other end are linked together by a total transfer matrix, M that is a product of all the individual matrices. The matrix simulation is started at the far end of the grating and propagated backwards. This requires that the boundary condition $I_o=I(L)=1$ (normalised output) and $U_o=U(L)=0$ (no incident field from the output end). The input fields at the beginning of the grating are calculated as $I(0)=I_N$ and $U(0)=U_N$. The index modulation for a single grating section with two inputs and two outputs is shown in the Figure 5.2.

The laser beam profile used to write the grating will influence the induced index variation. A Gaussian beam is assumed to affect the dc index change $\delta\bar{n}_{eff}(z)$ by [10]

$$\delta\bar{n}_{eff}(z) = \Delta\bar{n} \cdot \exp\left[-\frac{4\ln 2}{FWHM^2} \cdot z^2\right] \qquad (5.18)$$

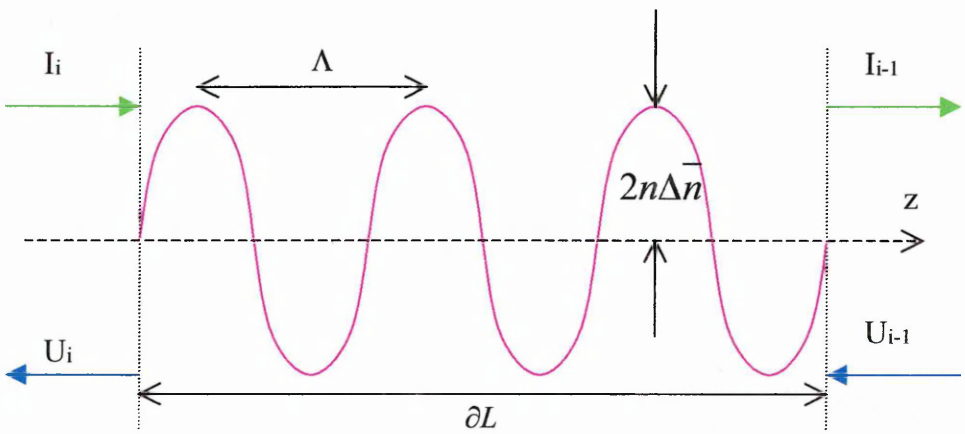

Figure 5. 2: A single grating-section showing 2 inputs and outputs.

In equation (5.18) *FWHM* is the bandwidth of the grating profile defined as full width at half maximum height. To start the simulation constant values of $\Delta\bar{n}, k_{dc}, k_{ac}$ and $\frac{1}{2}\cdot\frac{d\Phi}{dz}$ is assigned to the first grating section and because they are generally dependent on z they are evaluated at the centre of the section.

$$\begin{bmatrix} I_i \\ U_i \end{bmatrix} = M_i \cdot \begin{bmatrix} I_{i-1} \\ U_{i-1} \end{bmatrix} \tag{5.19}$$

The matrix M_i takes two forms that are governed by the value of parameter S redefined from equation (5.13) by

$$S_i = \sqrt{|k_{ac}|_i^{\,2} - \delta_i^{\,2}} \tag{5.20}$$

The subscript, i refers to the parameter values in the i^{th} grating section. The grating phase, $\Phi(z)$ is given by

$$\Phi(z) = \frac{2\pi n_{eff}}{\lambda_B} \cdot z \tag{5.21}$$

Linear chirp due to the variation in the phase is obtained by differentiating equation (5.21) leading to equation (5.22) below.

$$\frac{1}{2}\frac{d\Phi(z)}{dz} = -\frac{4\pi n_{eff}}{\lambda_B^{\,2}} \cdot z \cdot \frac{d\lambda_B}{dz} \tag{5.22}$$

In equation (5.22) $d\lambda_B/dz$ is the chirp gradient of the Bragg wavelength. This chirp term is incorporated in equation (5.12).

When $|k_{ac}|_i \rangle |\delta_i|$ then M_i is given by

$$M_i = \begin{bmatrix} \cosh(S_i\delta L) - j\frac{\delta_i}{S_i}\sinh(S_i\delta L) & -j\frac{|k_{ac}|_i}{S_i}\sinh(S_i\delta L) \\ j\frac{|k_{ac}|_i}{S_i}\sinh(S_i\delta L) & \cosh(S_i\delta L) + j\frac{\delta_i}{S_i}\sinh(S_i\delta L) \end{bmatrix} \tag{5.23}$$

The parameter δL is defined as $\delta L = L/N$, the length of a grating section.

When $|k_{ac}|_i < |\delta_i|$ then S_i is imaginary and M_i is given by

$$M_i = \begin{bmatrix} \cos(S_i\delta L) - j\frac{\delta_i}{S_i}\sin(S_i\delta L) & -j\frac{|k_{ac}|_i}{S_i}\sin(S_i\delta L) \\ j\frac{|k_{ac}|_i}{S_i}\sin(S_i\delta L) & \cos(S_i\delta L) + j\frac{\delta_i}{S_i}\sin(S_i\delta L) \end{bmatrix} \tag{5.24}$$

The components of matrix M_i are solutions to coupled mode equation (5.8) and (5.9). The total transfer matrix, M is given by

$$M = M_N \cdot M_{N-1} \ldots\ldots\ldots M_i \ldots\ldots\ldots M_2 \cdot M_1 \tag{5.25}$$

The output amplitude and phase response is thus obtained from

$$\begin{bmatrix} I_N \\ U_N \end{bmatrix} = M \cdot \begin{bmatrix} I_0 \\ U_0 \end{bmatrix} \tag{5.26}$$

The boundary conditions given above are now applied and equation (5.23) is modified to equation (5.24).

$$\begin{bmatrix} I_N \\ U_N \end{bmatrix} = \begin{bmatrix} M_{11} & M_{12} \\ M_{21} & M_{22} \end{bmatrix} \cdot \begin{bmatrix} 1 \\ 0 \end{bmatrix} \tag{5.27}$$

The power reflectivity, R of the grating is given by

$$R = \left| \frac{M_{21}}{M_{11}} \right|^2 \tag{5.28}$$

The power transmissivity T is deduced from the relation $T=1-R$.

The accuracy of grating simulation by this technique is strongly dependent on the choice of N, the number of grating sections. It is important to make it sufficiently large but not too large otherwise the coupled mode theory collapses, it should however suffice to choose $\delta L >> \Lambda$.

5.3.3 Strain Effects

Bragg grating structures are sensitive to applied strain and environmental effects such as vibrations. This effect has the tendency of changing the period of a grating and thus causes a wavelength shift. Strain can be used to tune the grating after fabrication in order to change the grating performance e.g. centre wavelength may be shifted from the design wavelength, and it is also possible to change the reflectivity and profile of the grating. Strain modelling is therefore a necessary tool.

The strain-induced change in detuning $\Delta\beta_s$ can be obtained by differentiating the equation for the phase matching condition $\lambda_B = 2n_o\Lambda$ [11].

$$\Delta\beta_s = \left[\beta_0 \frac{1}{n_0}\frac{\partial n_0}{\partial s} + \frac{\pi}{\Lambda}\right] \cdot \frac{\Delta L}{L} \qquad (5.29)$$

where ΔL, n_o, s and $\beta_o = 2\pi n_o/\lambda_B$ are respectively the length change, refractive index of the fibre without the grating, strain and wave vector. The first term in the bracket is the elasto-optic coefficient and is given by [11]

$$\frac{1}{n_0}\frac{\partial n_0}{\partial s} = -0.29 \qquad (5.30)$$

5.3.4 Temperature Effects

A temperature change applied to a grating has the tendency to change the profile of the grating. This detuning occurs via the modification of the grating period due to fibre

expansion and the change in the refractive index. The grating sensitivity to temperature variations is very important for a full knowledge of the filter performance.

Differentiating the equation $\lambda_B=2n_o\Lambda$ with respect to temperature gives

$$\frac{\Delta\lambda}{\lambda}\approx\frac{1}{n_0}\cdot\left(\frac{\partial n_0}{\partial T}\right)\cdot\Delta T+\frac{1}{\Lambda}\cdot\left(\frac{\partial\Lambda}{\partial T}\right)\cdot\Delta T \qquad (5.31)$$

Parameters $\Delta\lambda$ and ΔT are respectively the wavelength change due to the applied temperature and the temperature change. The following substitution for the coefficients is made.

$$\frac{1}{n_0}\cdot\frac{\partial n_0}{\partial T}=8.6\times10^{-6}/^0C \quad \text{thermo-optic coefficient [12].} \qquad (5.32)$$

$$\frac{1}{\Lambda}\cdot\frac{\partial\Lambda}{\partial T}=0.55\times10^{-6}/^0C \quad \text{thermal expansion coefficient [12].} \qquad (5.33)$$

Differentiating the wave vector $\beta_o=2\pi n_o/\lambda_B$ leads to

$$\frac{\Delta\lambda}{\lambda_B}=\left|\frac{\Delta\beta}{\beta_0}\right| \qquad (5.34)$$

Equation (5.33) can now be written in terms of the temperature detuning parameter as follows

$$\Delta\beta_T=9.15\times10^{-6}\cdot\frac{2\pi n_0}{\lambda_\beta}\cdot\Delta T \qquad (5.35)$$

Equation (5.29) and (5.35) are a measure of how much the centre wavelength λ_B of the grating shifts in response to the applied strain and temperature respectively and can be termed phase mismatch or detuning parameters. The values calculated from these

equations are added to the detuning parameter of equation (5.7) and thus affect the grating through the dc self-coupling coefficient in equation (5.12), which is also phase dependent. The presence of temperature and strain variations on the grating means that the grating will not be at the design wavelength.

5.4 Optical Fibre Fabry-Perot Filter

5.4.1 Coupled Mode Theory

In this section coupled mode theory is applied as an approximate way of analysing the characteristics of a Fabry-Perot interferometer made up of two Bragg gratings of identical features, a case that will not always represent real gratings. The formulation is nevertheless more insightful as it provides the fundamental understanding of the electric field interactions that brings about the dispersive properties as well as the phase response characteristics of the Fabry-Perot grating [6]. This analysis therefore forms a building block in the development of other more flexible mathematical tools for spectral analysis of in-fibre gratings (section 5.4.2). The propagation of oppositely directed fundamental modes through the optical fibre is assumed. The symbols E_f for the forward and E_b for the backward electric fields are used and are given by the following expressions [5]

$$E_f = B(z)\cdot\exp[i(\omega t - \beta z)] \qquad (5.36)$$

$$E_b = A(z)\cdot\exp[i(\omega t + \beta z)] \qquad (5.37)$$

The symbol $B(z)$ and $A(z)$ represent the complex amplitudes of the fields while β is the wave vector. It can be shown that continual energy exchange between two-contrapropagating modes is given by the following coupled mode equations where $\Delta\beta$ is the phase matching parameter and K is the coupling coefficient [5].

$$\frac{dA}{dz} = iK^* \cdot Be^{-i2(\Delta\beta)z} \qquad (5.38)$$

$$\frac{dB}{dz} = -iK \cdot A \cdot e^{i2(\Delta\beta)z} \qquad (5.39)$$

These coupled-mode equations lead to the following second-order differential equations.

$$\frac{d^2A}{dz^2} + i2(\Delta\beta)\cdot\frac{dA}{dz} - K^2A = 0 \qquad (5.40)$$

$$\frac{d^2B}{dz^2} - i2(\Delta\beta)\cdot\frac{dB}{dz} - K^2B = 0 \qquad (5.41)$$

The following general solutions are obtained:

$$B(z) = G\cdot\exp\left\{\left[i(\Delta\beta)+\sqrt{K^2-(\Delta\beta)^2}\right]z\right\} + F\cdot\exp\left\{\left[i(\Delta\beta)-\sqrt{K^2-(\Delta\beta)^2}\right]z\right\} \qquad (5.42)$$

$$A(z) = C\cdot\exp\left\{\left[-i(\Delta\beta)+\sqrt{K^2-(\Delta\beta)^2}\right]z\right\} + D\cdot\exp\left\{\left[-i(\Delta\beta)-\sqrt{K^2-(\Delta\beta)^2}\right]z\right\} \qquad 5.43)$$

The letters C, D, G and F are constants to be determined given some boundary conditions. The next section establishes the transmission spectrum of the fibre Fabry-Perot structure by applying equation (5.42) and (5.43) to appropriate boundary conditions. The time dependence of the electric fields is ignored, as it is common to all terms of the boundary conditions. The boundary conditions shown in the diagram and indicated by the arrows are applied to equation (5.42) and (5.40) with the resulting constants being substituted in equation (5.42) to produce the following input field.

$$B(z) = e^{i(\Delta\beta)z}\left\{\frac{i(\Delta\beta)\cdot\sinh[S(L-z)]+S\cdot\cosh[S(L-z)]}{Q}B(0) - \frac{iK\cdot e^{i(\Delta\beta)L}\cdot\sinh(Sz)}{Q}A(L)\right\} \qquad (5.44)$$

Parameters S and Q are defined by

$$S = \sqrt{K^2-(\Delta\beta)^2} \qquad (5.45)$$

$$Q = i(\Delta\beta)\cdot\sinh(SL)+S\cdot\cosh(SL) \qquad (5.46)$$

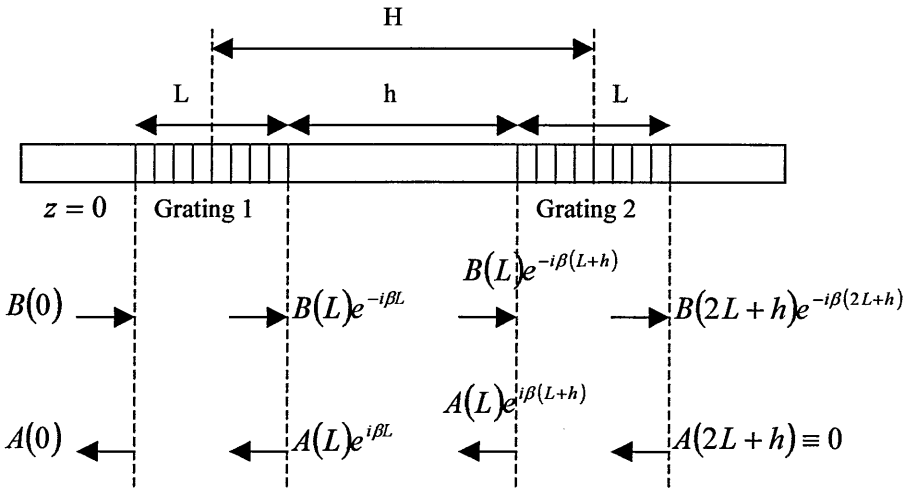

Figure 5. 3: Fabry-Perot structure with 2 uniform and identical Bragg gratings.

H – Fabry-Perot cavity length, h – un-irradiated cavity length, L – grating length, A and B - amplitudes

Equation (5.47) is the backward field out of the fibre produced by applying boundary conditions (indicated by arrows) from Figure 5.3 to equation (5.43) and (5.38).

$$A(z) = e^{-i(\Delta\beta)z}\left\{\frac{-iK^* \cdot \sinh[S(L-z)]}{Q} B(0) + e^{i(\Delta\beta)L}\left[\frac{i(\Delta\beta)\cdot\sinh(Sz) + S\cdot\cosh(Sz)}{Q} A(L)\right]\right\} \tag{5.47}$$

Equation (5.44) and (5.47) govern the contrapropagating fields of the fundamental mode through the first grating of the Fabry-Perot. The relationship among the complex field amplitudes is established by setting z equal to L in either equation (5.44) or (5.47), which leads to the expression of equation (5.48) below.

$$B(L) = e^{i(\Delta\beta)L} \cdot \left[\frac{S}{Q}\cdot B(0) - \frac{iK\cdot e^{i(\Delta\beta)L}\cdot\sinh(SL)}{Q}\cdot A(L)\right] \tag{5.48}$$

A similar analysis that applies the boundary conditions of the second grating that are shown in the diagram to equation (5.40) and (5.42) leads to the following forward and backward fields.

$$B(z)=\frac{i\Delta\beta\cdot\sinh[S(2L+h-z)]+S\cdot\cosh[S(2L+h-z)]}{Q}\cdot e^{-i\beta(L+h)}\cdot e^{-i\Delta\beta(L+h-z)}\cdot B(L) \tag{5.49}$$

$$A(z)=\frac{-iK^{*}\cdot e^{-i\Delta\beta(L+h+z)}\cdot\sinh[S(2L+h-z)]}{Q}\cdot e^{-i\beta(L+h)}\cdot B(L) \tag{5.50}$$

Equation (5.49) and (5.50) govern the contrapropagating fields of the fundamental mode through the second grating. The relationship among the complex field amplitudes is established by setting z to $2L+h$ in equation (5.49) and $L+h$ in (5.50), which leads to equation (5.51) and (5.52) respectively.

$$B(2L+h)=e^{i\Delta\beta}\cdot e^{-i\beta(L+h)}\cdot\left[\frac{S}{Q}\cdot B(L)\right] \tag{5.51}$$

$$A(L)\cdot e^{i\beta(L+h)}=\frac{-iK^{*}\cdot\sinh(SL)\cdot e^{-i2\Delta\beta(L+h)}}{Q}\cdot e^{-i\beta(L+h)}\cdot B(L) \tag{5.52}$$

The Fabry-Perot amplitude and phase transmission coefficient may be expressed as

$$t=\frac{B(z)_{FBG2}}{B(0)} \tag{5.53}$$

The numerator represents the forward output field from the second Bragg grating. Equation (5.54) is produced by substitution of the result of a system of equations (5.48), (5.51) and (5.52) into equation (5.53).

$$t = \frac{S^2 \cdot e^{i2\Delta\beta L} \cdot e^{-i\beta(2L+h)} \cdot e^{-i\beta(L+h)}}{Q^2 + K^2 \cdot \sinh^2(SL) \cdot e^{i2\Delta\beta h} \cdot e^{-i2\beta(L+h)}} \tag{5.54}$$

The transmittance, T of the fibre-optic Fabry-Perot is obtained from

$$T = t \cdot t^* \tag{5.55}$$

$$T = \frac{1}{1 + 4\left\{\frac{K^2 \cdot \sinh^2(SL) \cdot \left[K^2 \cdot \cosh^2(SL) - \Delta\beta^2\right]}{\left(K^2 - \Delta\beta^2\right)^2}\right\} \cos^2\left[\Delta\beta h - \beta(L+h) - \frac{\phi}{2}\right]} \tag{5.56}$$

where ϕ is given by

$$\tan(\phi) = \frac{2 \cdot S \cdot \Delta\beta \cdot \sinh(SL) \cdot \cosh(SL)}{S^2 \cdot \cosh^2(SL) - \Delta\beta^2 \cdot \sinh^2(SL)} \tag{5.57}$$

The maximum reflectivity, R_{max}, of the Fabry-Perot is obtained when its transmittance is a minimum. This, by inspection of equation (5.56) requires that the cosine term be identically equal to unity while considering the phase matched condition of $\Delta\beta=0$ so that

$$R_{\max} = \frac{4 \cdot R_G}{\left[1 + R_G\right]^2} \tag{5.58}$$

where R_G is the reflectivity of the grating at the Bragg wavelength. This equation is identical to that of a bulk Fabry-Perot interferometer with two identical mirrors of reflectivity R_G. A similar analysis also produced the same result [13]. Some results of the coupled mode theory are summarised in Table 5.1. The results show that the filter measurement sensitivity (gradient of transfer function) is strongly influenced by the cavity length and the reflectivity.

Cavity H (cm)	*Transmission (%)*	*Finesse*	*FWHM (MHz)*	*Gradient x 10^{-3} (MHz^{-1})*
1	88	5	907	1.06
2	88	5	465	2.47
4	82	4	312	2.82
6	63	3	283	2.82
8	39	2	261	1.94
10	28	2	227	1.62

Table 5. 1: Fabry-Perot sample results calculated from the coupled mode theory.

Figure 5.4 shows a typical transfer function of a FP filter which explains how the table values were calculated. The FWHM is the frequency bandwidth of a passband at 50 % transmission while FSR is the passband periodic frequency. The Finesse is calculated from the ratio of FSR to FWHM. The gradient of the transfer function is calculated from a line of maximum slope (blue line) that passes through point P.

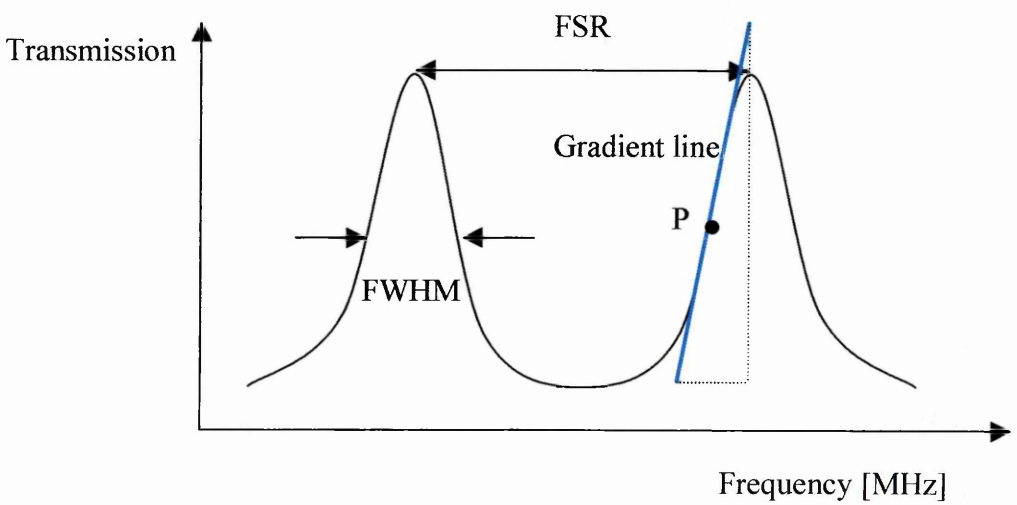

Figure 5.4: Typical transfer function of a FP filter.

P – Point of maximum gradient, FWHM – full width at half maximum bandwidth, FSR – free spectral range.

5.4.2 Transfer Matrix Model

The coupled mode theory that was applied to the Fabry-Perot is only applicable to two perfectly identical Bragg gratings inscribed in a single fibre. The two are uniform Bragg gratings having uniform index modulation and period, which may not closely characterise a more realistic in-fibre Fabry-Perot filter that is bound to have gratings of differing features. Such variations in grating features could be imposed by laser beam profile variations with time, changes to prevailing environmental conditions, changes in the properties of the fibre, and variations in strain when the fibre is translated to a new fabrication position. It is also important to deliberately manufacture such gratings as it allows for flexibility of the design of any desired filter. This enables the manipulation of the available filter characteristics through variation of such parameters as grating length, chirp, refractive index modulation, and apodisation. The transfer matrix approach is adopted.

The individual gratings forming the Fabry-Perot may separately have differential temperature and strain gradients applied to them (section 5.3). The in-fibre Fabry-Perot is a sensitive device given that it consists of distributed mirrors that result in a non-fixed cavity length and hence non-constant free spectral range.

A phase-shift matrix FP_i that describes wave propagation through the Fabry-Perot unperturbed cavity-length h is inserted between the matrices M_N^1 (last matrix of the first grating) and M_1^2 (first matrix of the second grating). Matrix multiplication continues until the last matrix of the second grating M_N^2 has been considered. The phase-shift matrix is required because only the phase of the electric field changes with distance of propagation while the amplitude remains constant in the region of no grating (assuming no loss).

Figure 5.5 shows that the un-irradiated cavity length, h of the bottom Fabry-Perot that is perturbed by an applied strain, ζ is given by

$$h = 2y \cdot (1 + \zeta). \qquad (5.59)$$

The first Fabry-Perot is a normal un-perturbed cavity. The parameters, h_1 and h_2, are the cavity lengths for the un-perturbed and perturbed FP filters respectively and are defined to the reflection points of the gratings marked by the green dotted lines.

$$h_1 = 2y + L$$
$$h_2 = (2y + L)\cdot(1 + \zeta) \qquad (5.60)$$

The numerator in brackets represents length perturbation of each grating. The calculated value of h is used in equation (5.61) below. The wave propagation matrix is given by [10]

$$FP_i = \begin{bmatrix} \exp\left(-j\frac{2\pi n_{eff} h}{\lambda}\right) & 0 \\ 0 & \exp\left(j\frac{2\pi n_{eff} h}{\lambda}\right) \end{bmatrix} \qquad (5.61)$$

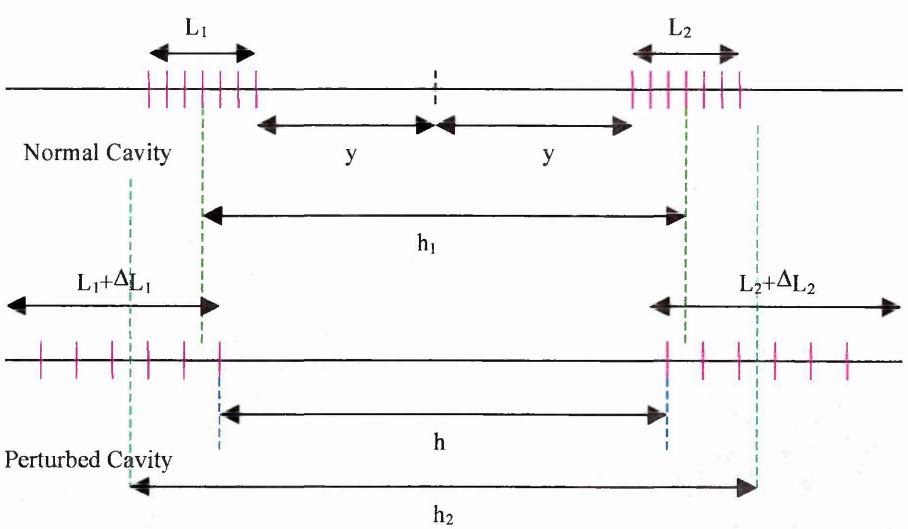

Figure 5. 5: FP-cavity length variation under perturbations (such as strain) that are separately applied to the grating.

L – grating length, 2y – un-irradiated cavity length, ΔL – change in grating length.

5.4.3 Fabry-Perot Parameter Estimates for Fabrication

A bulk-optic Fabry-Perot is considered for the development of theoretical estimates for the physical parameters required for the fabrication of the fibre-based FP. The following equation was derived and Figure 5.6 is its graphical representation.

$$L = \frac{c(1-R)}{2n\pi(\Delta\nu_{FP})\sqrt{R}} \qquad (5.61)$$

The FP cavity length is denoted by L, speed of light by C, Bragg grating reflectivity by R and the transmission bandwidth (FWHM) of the Fabry-Perot is given by $\Delta\nu_{FP}$.

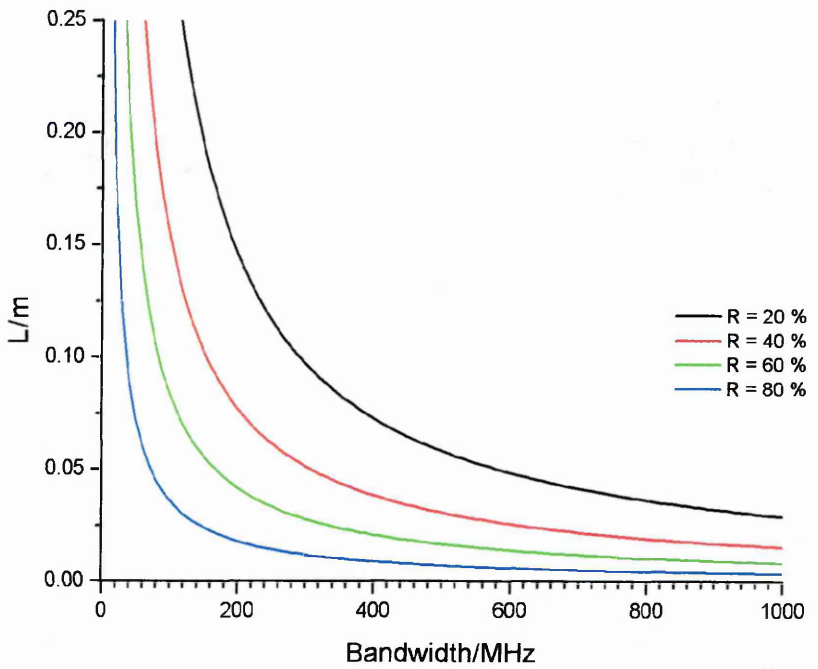

Figure 5. 6: Dependence of FP spectral bandwidth (FWHM) on cavity length, L and grating reflectivity, R as computed from equation (5.64).

These graphs show that the higher the grating reflectivity the shorter the cavity length required for a given FP transmission bandwidth.

5.5 Distributed Feedback Grating

5.5.1 Coupled mode Theory

A theoretical characterisation of the DFG grating can be obtained from the coupled-mode analysis that was applied to a fibre-optic Fabry-Perot (section 5.4.1). A value for h, the cavity length is chosen such that it matches the phase step required. The cavity length is $\lambda/2n$ for a phase step of π where λ is the wavelength and n is the effective refractive index of the fibre.

5.5.2 Transfer Matrix Model

A phase-shift matrix F_i is inserted between the grating section matrices M_i and M_{i+1} for a phase shift at the interface of the sections (section 5.3.2). The matrix F_i where Φ_i represent the phase is given by [10]

$$F_i = \begin{bmatrix} \exp\left(-j\frac{\Phi_i}{2}\right) & 0 \\ 0 & \exp\left(j\frac{\Phi_i}{2}\right) \end{bmatrix} \qquad (5.63)$$

The effects of chirp, apodisation, temperature, strain and variation in index modulation are included in the simulation as already described [section 5.3].

5.6 Moiré Grating

5.6.1 Theory

It is assumed that the fringe pattern used to produce Bragg gratings is perfectly sinusoidal and thus results in sinusoidal index modulation. Two such sinusoidal index modulations of slightly different periods but equal amplitudes are superimposed to yield a beat refractive index modulation characterising a Moiré grating.

The total index modulation, $\Delta n(z)$ of the Moiré grating is the sum of the index modulations Δn_1 and Δn_2 from first and second gratings respectively [14].

$$\Delta n_1(z) = \Delta n \cdot \left[1 + \cos\left(\frac{2\pi}{\Lambda_1} \cdot z\right)\right] \tag{5.64}$$

$$\Delta n_2(z) = \Delta n \cdot \left[1 + \cos\left(\frac{2\pi}{\Lambda_2} \cdot z\right)\right] \tag{5.65}$$

$$\Delta n(z) = \Delta n_1 + \Delta n_2 \tag{5.66}$$

$$\Delta n(z) = 2 \cdot \Delta n \cdot \left[1 + \cos\left(\frac{2\pi}{\Lambda_s} \cdot z\right) \cdot \cos\left(\frac{2\pi}{\Lambda_c} \cdot z\right)\right] \tag{5.67}$$

Quantities Λ_s and Λ_c are defined by

$$\Lambda_s = \frac{2 \cdot \Lambda_1 \cdot \Lambda_2}{\Lambda_1 + \Lambda_2} \tag{5.68}$$

$$\Lambda_c = \frac{2 \cdot \Lambda_1 \cdot \Lambda_2}{\Lambda_1 - \Lambda_2} \tag{5.69}$$

The quantities Λ_s and Λ_c respectively represent the rapidly and slowly varying components of the grating index. The cosine variation of the envelope causes the phase of the grating to change intrinsically by π at the crossover point. One period of the Moiré grating is therefore equivalent to $\lambda/4$ optical phase-shifted grating. However phase shifts other than $\lambda/4$ can be obtained if different index modulations are used for each grating fabricated [14].

5.6.2 Transfer Matrix Model

Moiré gratings are formed from the superposition of two Bragg gratings that differ in Bragg wavelength. The transfer matrix method is invoked as a design tool since the

coupled mode theory will only work in the case of two identical gratings. The simulation is similar to that of the normal Bragg grating (section 5.3.2) and the only modification is that the dc refractive index change, Δn_{dc} and fringe visibility, V is given by

$$\Delta n_{dc} = 2\Delta n \tag{5.70}$$

$$V = 2\cos\left(\frac{2\pi z}{\Lambda_c}\right). \tag{5.71}$$

5.7 Simulation Results

5.7.1 Fibre Bragg Gratings

The effects of temperature and strain (Figure 5.7) on a uniform Bragg grating of 1 mm in length are modelled in Fortran90 using the transfer matrix technique (section (5.3.2)). A grating of 0.2-nm full bandwidth with a centre wavelength of 514.5 nm is shown completely detuned by a temperature change of +20 ^{0}C i.e. a 0.1 nm shift in the centre wavelength (Figure 5.7 (a)). The same grating is shown completely shifted by the same amount by strain less than 300 μstrain (Figure 5.7 (b)).

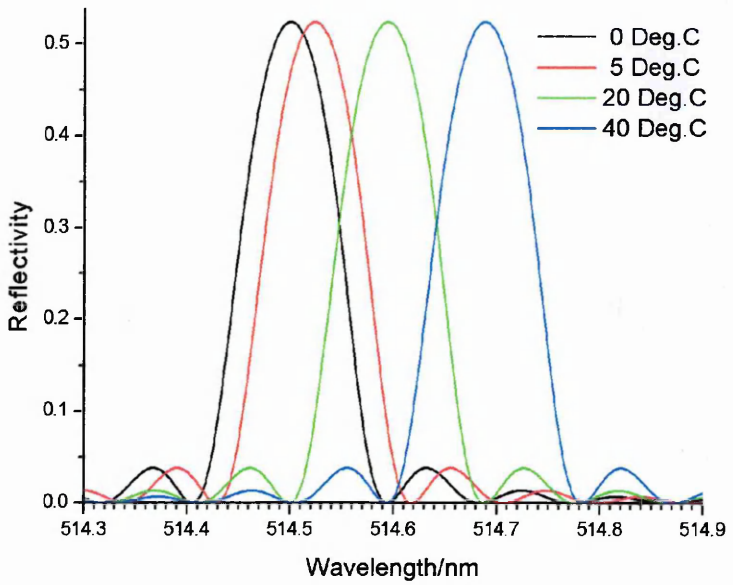

Figure 5. 7 (a): Effects of temperature on a uniform 1-mm long Bragg grating.

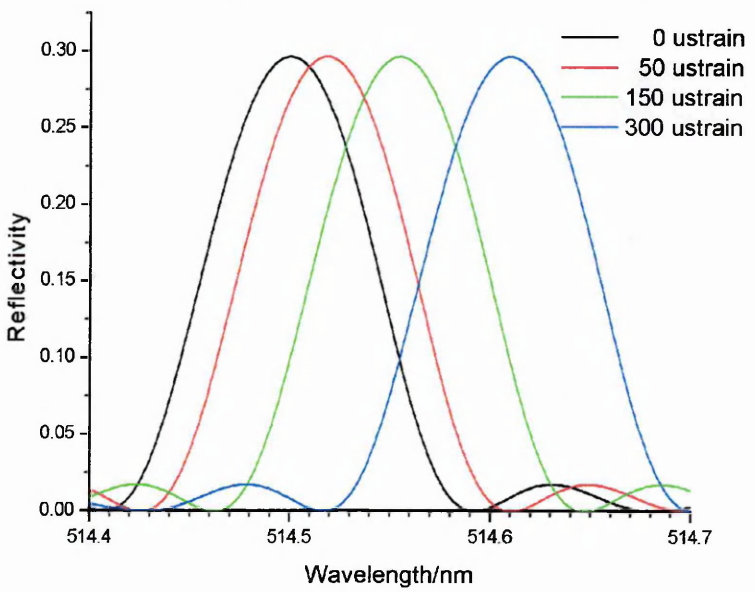

(b)

Figure 5. 7(b): Effects of strain on a uniform 1-mm long Bragg grating.

5.7.2 Fibre Fabry-Perot Filter

The graphs of figure 5.8 are the results of a transfer matrix simulation detailed in section 5.3.2 and section 5.4.2 that was modelled in Forttran90 for a Fabry-Perot with gratings written at 514.5 nm. The FP is made from two 1-mm long identical Bragg gratings of 30% reflectivity and a centre-to-centre cavity length of 6 cm. The application of

temperature on one FBG will cause detuning of that grating with respect to the other and the visibility function of the FP decreases and transmission peaks are shifted to the longer wavelength side (Figure 5.8 (a)). A continued increase of temperature on this grating will cause the FP to completely disappear when the 2 gratings cease to overlap in wavelength. The shift in the FP transmission peaks and the decrease in visibility is more pronounced when temperature is applied to both gratings (Figure 5.8 (b)) if laser illumination is assumed. Both gratings are detuned from the laser wavelength thus a reduced reflectance is encountered.

These graphs show that the transfer characteristics of a FP filter can be tailored through the manipulation of their temperature sensitivity. The shape of the transfer function is seen to alter in terms of the visibility, slope and bandwidth, which relate to range, sensitivity and resolution when used for velocity measurement. Similar effects are also obtained if strain is applied to the FP cavity or to its individual gratings.

The graph of Figure 5.9 shows the variation of the filter sensitivity (obtained from the transfer matrix model) as given by the gradient of the linear portion of a flank of the transfer function as a function of the FSR of the FP filter at constant finesse. The part of the flank with the largest gradient was considered for this calculation (Figure 5.4). The graph shows that higher sensitivities can be produced at higher finesse.

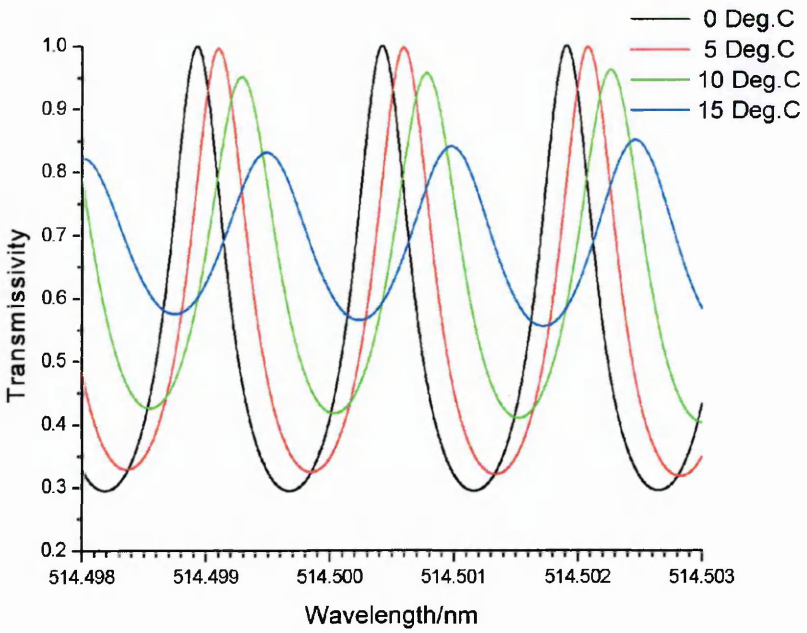

(a)

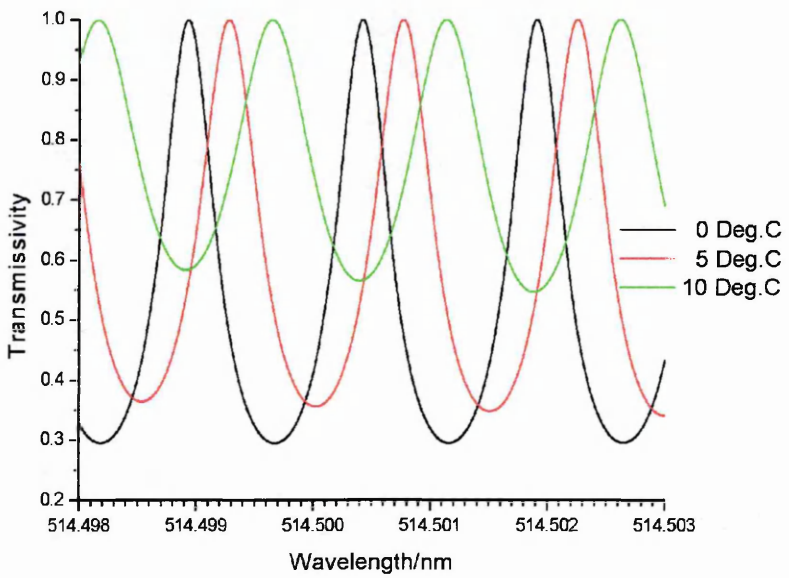

(b)

Figure 5. 8: FP-Transmission with temperature detuning on (a) one grating and (b) both gratings assuming laser illumination.

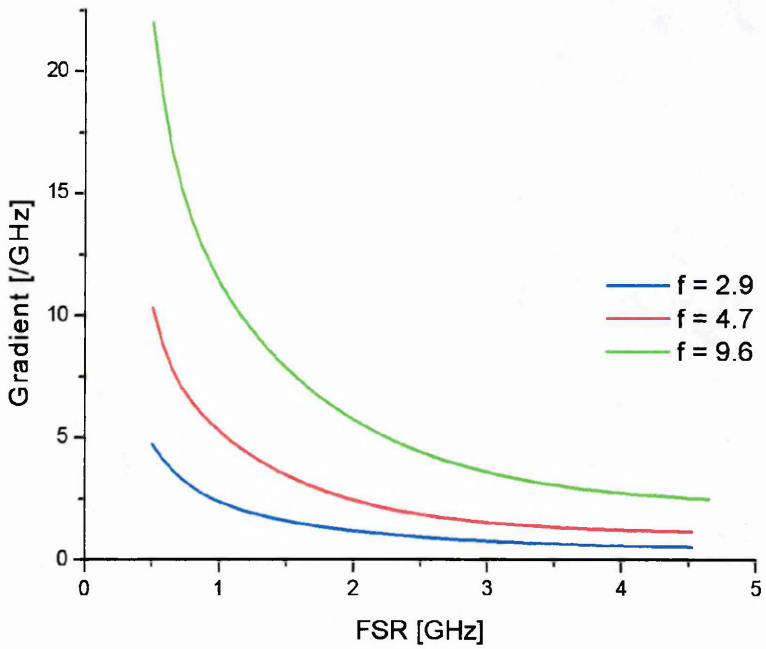

Figure 5.9: FP-filter sensitivity (defined as the slope) as a function of FSR at constant finesse

5.7.3 Distributed Feedback Grating

A model was set up in Fortran90 based on the transfer matrix approach (sections 5.3.2 and 5.5.2) to study the available properties of phase-shifted gratings that could be applied to flow velocity measurement. A 1 mm long Bragg grating of 54% reflectivity and bandwidth of 0.1 nm (FWHM) is phase shifted by π radians to produce a passband of 35% transmissivity and 0.06 nm bandwidth (FWHM) in an increased stopband width of about 0.22 nm (FWHM) (Figure 5.10 (a)). In Figure 5.10 (b) 4 effects can be noticed for a phase-shifted grating that has been chirped. The increase in chirp rate causes the widening of the passband, reduced passband transmissivity, reduced linearity, and reduced slope of passband. These characteristics would provide tuning to device sensitivity, range, resolution and linearity when applied to the measurement of flow velocity.

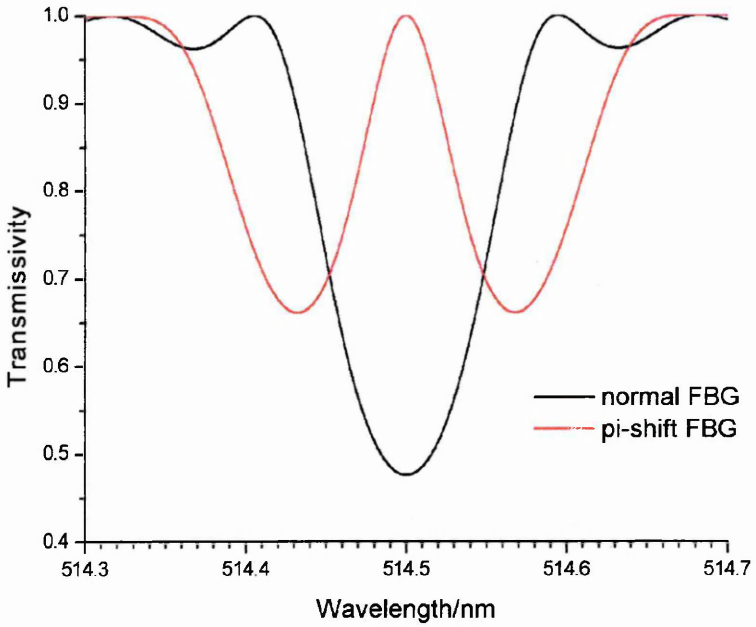

Figure 5. 10 (a): The transmission of π-phase shifted Bragg grating.

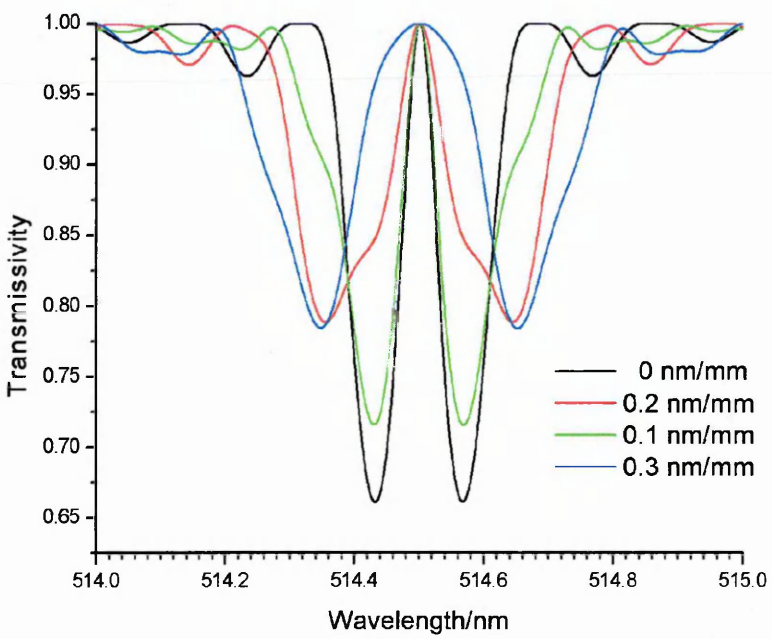

(b)

Figure 5.10 (b): The transmission of a chirped Bragg grating with a π-phase shift in the middle for a laser operating at 154.5 nm.

Figure 5.11 (a) is for a 1 mm long π phase shifted grating that is shown completely detuned by a temperature of less than 40 ^{0}C for a laser operating at 514.5 nm. Figure

5.11 (b) shows high sensitivity exhibited by the FP filter as shown by the passband wavelength shift when low level strain is applied to it.

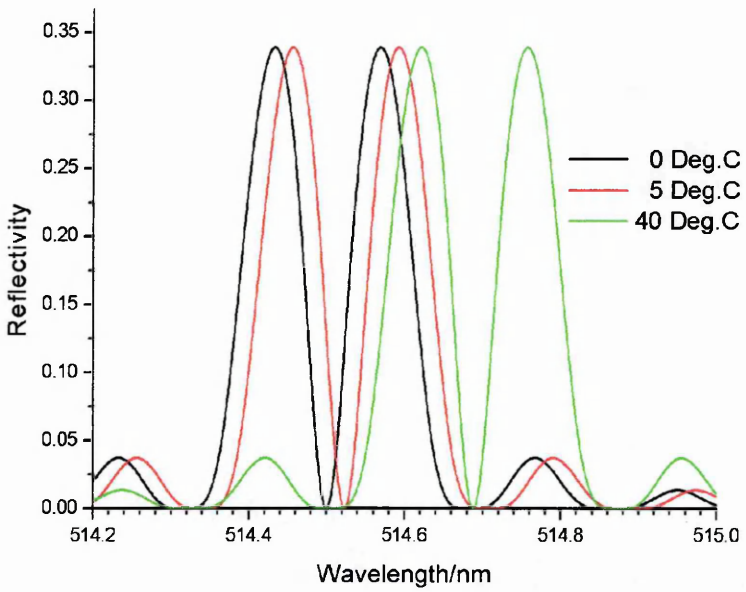

Figure 5.11 (a): The transmission of a π-phase shifted Bragg grating that is temperature detuned.

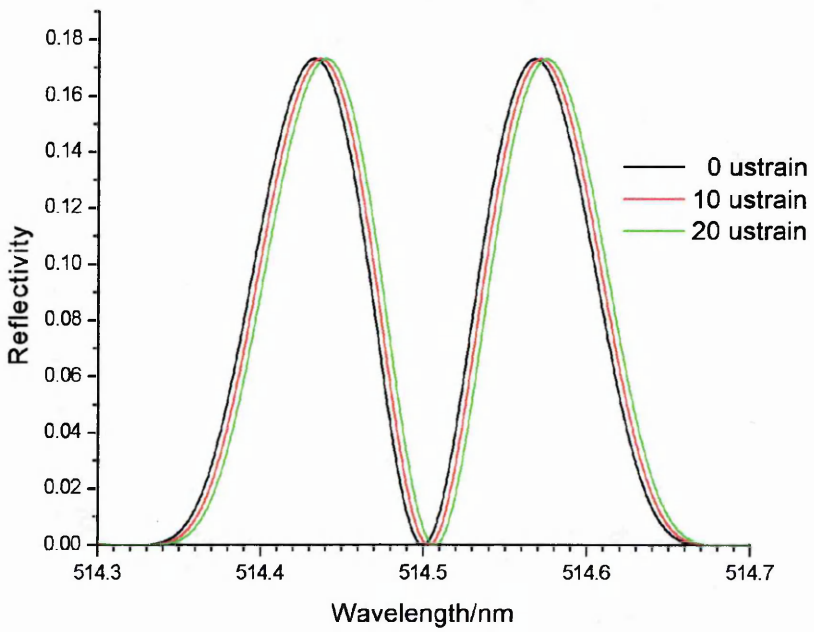

(b)

Figure 5. 11 (b): The transmission of π-phase shifted Bragg grating with strain detuning.

5.7.4 Moiré Grating

The graphs of Figure 5.12 (a) show the effect of the difference in the centre wavelength of the 2 gratings used to form a Moiré grating. An increase in the wavelength difference results in a broader passband and flatter top. Any further increase in the wavelength difference will cause the passband to split into more passbands and the black graph marks the beginning of this splitting. Decreasing the wavelength separation of the 2 gratings, an effect that also reduces the transmissivity, may produce a sharper and narrower passband. Figure 5.12 (b) is for various chirps that are applied to the grating represented by the red graph of Figure 5.12 (a). The introduction of chirp attenuates the transmissivity of the Moiré grating but hardly changes the passband width and the slope. No benefit can therefore be derived from chirped Moiré gratings when used for velocity measurement.

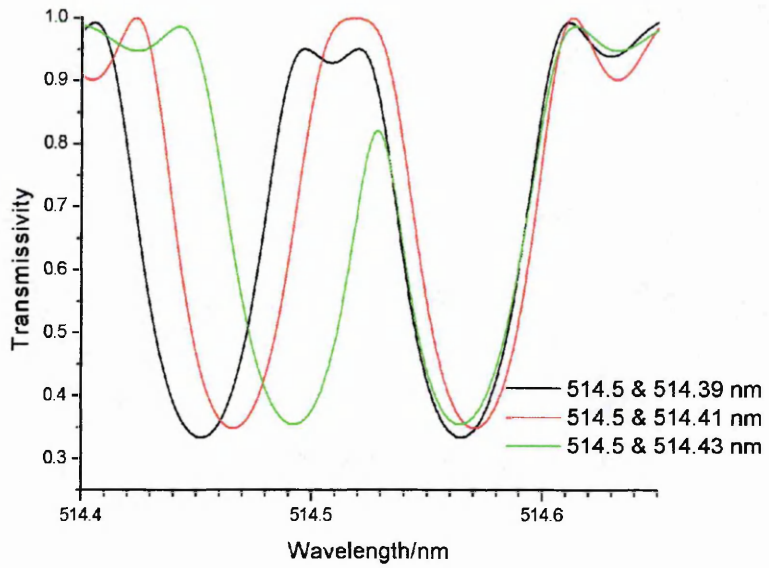

(a)

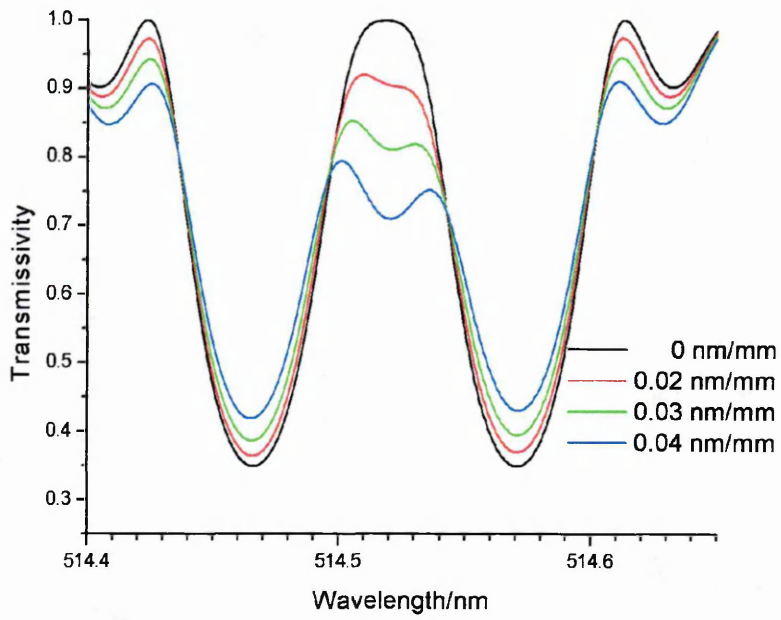

(b)

Figure 5. 12: The transmission of Moiré gratings (a) with variation in the difference of the two Bragg wavelengths and (b) with variation in chirp rate of the two gratings.

5.8 Transversely Coupled Fibre Fabry-Perot Resonator

The transversely coupled fibre Fabry-Perot interferometer (TCFFP) is based around a fibre coupler to provide a much more efficient interferometer when compared to ring

resonators (that introduce high bending losses) and fibre FP interferometers consisting of mirrors (that pose practical difficulties including that of coupling through the mirrors) [15]. This type of interferometer will have two dielectric mirrors butted on two arms of a directional coupler and two such configurations have been used (Figure 5.13).

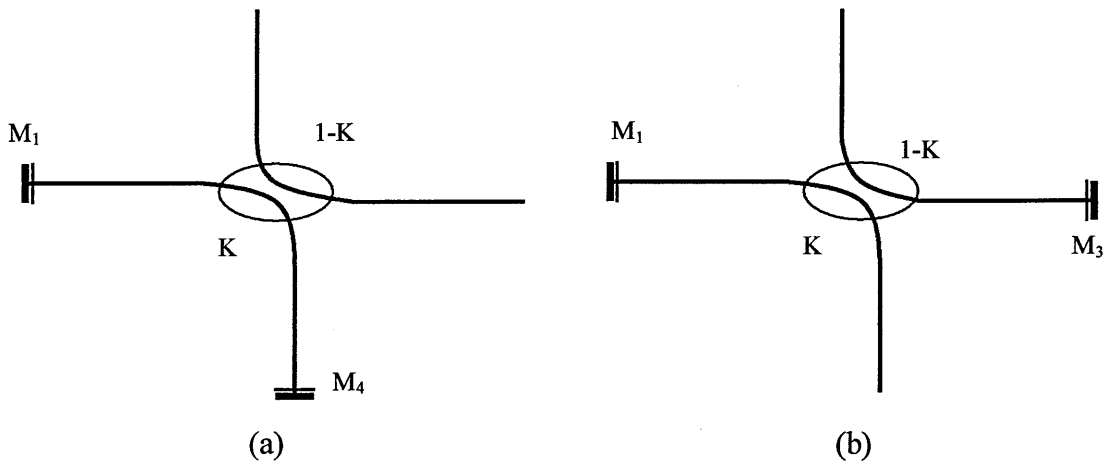

Figure 5. 13: Transversely coupled fibre Fabry-Perot resonator (a) type I and (b) type II. K – coupling coefficient, M – mirror.

Light that is weakly coupled into the cavity contained by mirrors M_1 and M_4 is stored and thus a particular wavelength will be brought into resonance through multiple reflections if the length of cavity is equal to an integer multiple of that wavelength (Figure 5.13 (a)). A low coupling coefficient is desirable because high finesse is obtainable by a large number of low amplitude electric field beams for low cavity losses. The transfer function of the TCFFP is obtained by equating the fields leaving the coupler to those entering the coupler and the output field is obtained from the field in the cavity, a method known as "equating the fields" as opposed to the usual technique of summing the fields [16]. The transfer function utilising an unmirrored input and output of type I resonator is given by the equation

$$\frac{I^{out}}{I^{in}} = (1-K)\frac{\left[1-(R_1R_4+R_1'R_4')\right]^2+4(R_1R_4+R_1'R_4')\sin^2\left[\beta(l_1+l_4)\right]}{(1-R_1R_4)^2+4R_1R_4\sin^2\left[\beta(l_1+l_4)\right]} \qquad (5.72)$$

while equation (5.73) is for the input and output making use of the same unmirrored arm.

$$\frac{I^{out}}{I^{in}} = \frac{K(1-\gamma)(R_4')^2}{(1-R_1R_4)^2 + 4R_1R_4\sin^2[\beta(l_1+l_4)]} \tag{5.73}$$

Type II TCFFP would, for the same input-output combination give

$$\frac{I^{out}}{I^{in}} = K\frac{(1+R_1R_3+R_1'R_3')^2 - 4(R_1R_3+R_1'R_3')\sin^2[\beta(l_1+l_3)]}{(1+R_1'R_3') - 4R_1'R_3'\sin^2[\beta(l_1+l_3)]} \tag{5.74}$$

for the unmirrored input and output and

$$\frac{I^{out}}{I^{in}} = \frac{(1-K)(1-\gamma)R_3^{\,2}}{(1+R_1'R_3') - 4R_1'R_3'\sin^2[\beta(l_1+l_3)]} \tag{5.75}$$

for the unmirrored input and output on the same arm. In these equations

$$R_i = r_i(1-K)^{1/2}(1-\gamma)^{1/2}\exp(-2\alpha l_i); \qquad i = 1,3,4 \tag{5.76}$$

$$R_i' = r_i K^{1/2}(1-\gamma)^{1/2}\exp(-2\alpha l_i); \qquad i = 1,3,4 \tag{5.77}$$

where K, γ, r_i, α and l_i are respectively the coupling coefficient, intensity loss, mirror amplitude reflectivity, fibre field loss and coupler arm length. The finesse of the type I interferometer is given by

$$F_I = \frac{\pi\sqrt{R_1R_4}}{(1-R_1R_4)} \tag{5.78}$$

while that of type II is defined by

$$F_{II} = \frac{\pi\sqrt{R_1'R_3'}}{(1-R_1'R_3')}. \tag{5.79}$$

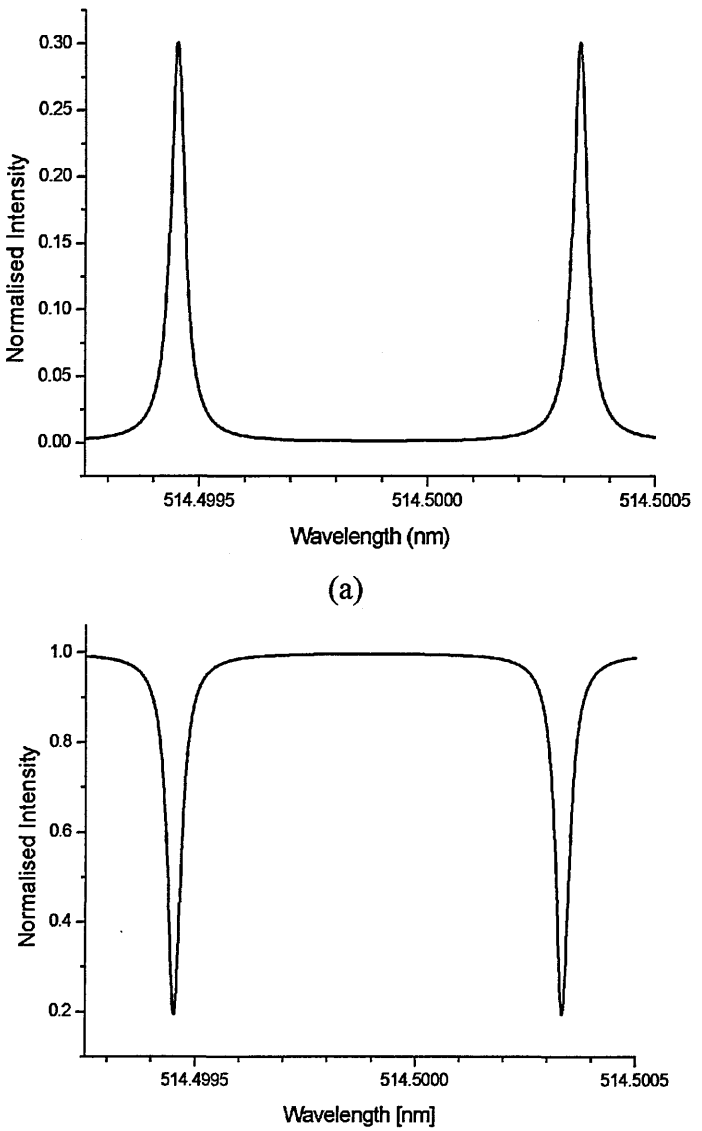

Figure 5. 14: Type I TCFFP for a low coupling coefficient with (a) input and output at the same unmirrored port of the coupler and (b) input and output at the unmirrored ports.

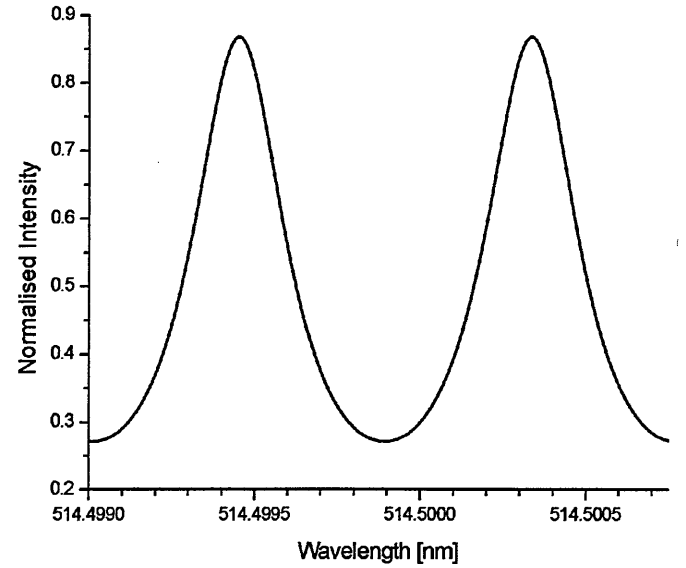

(a)

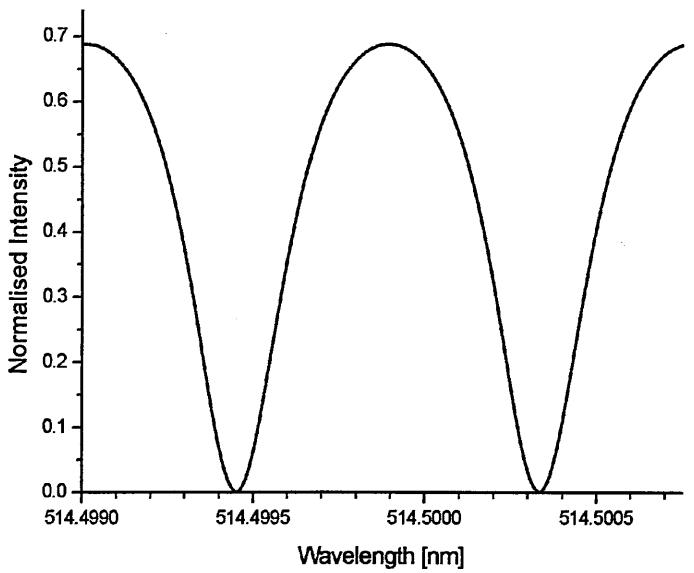

(b)

Figure 5. 15: Type I TCFFP for a high coupling coefficient with (a) input and output at the same unmirrored port of the coupler and (b) input and output at the unmirrored ports.

Figure 5.14 and 5.15 demonstrates the interferometer's ability to provide both bandpass and bandstop outputs. An important attribute of the TCFFP interferometer is the ability to vary the finesse, visibility, slope and free spectral range of the transfer function by varying the coupling coefficient of the fibre coupler. These graphs show that higher finesse is obtained by lowering the coupling coefficient i.e. for a type I resonator.

5.9 Summary

A detailed study of fibre optic filters was implemented in-order to investigate their suitability for Doppler frequency discrimination for laser velocimetry. The coupled mode theory, which is the underlying principle in the formation of fibre Bragg grating based filters was discussed in detail and extended to a transfer matrix model that allows flexible filter design to be implemented. The filter sensitivity in relation to applied temperature and strain was modelled and results show that suitably designed filters can be made sufficiently sensitive to frequency measurement while they exhibit minimum sensitivity to environmental perturbations. The model results are also required to set parameters for fabricating these filters. Also discussed was the transversely coupled fibre Fabry-Perot resonator based on a variable splitting ratio coupler providing tuneable transfer function characteristics for the filter. The mirrors on this device could be replaced by fibre Bragg gratings thus offering increased tuneability.

Table 5.2 compares the two approaches i.e. the coupled mode theory and the transfer matrix method that were adopted to model the Bragg grating based filters. Various features of these filters are summarised in Table 5.3 while more comparison was given in Table 4.1 (Chapter 4).

Modelling Technique	*Assumptions and/or Procedure*	*Advantages*	*Disadvantages*
Coupled mode theory (CMT)	-Mode fields unchanged for unperturbed fibre in presence of weak perturbation. -weak grating -constant refractive index modulation. -constant grating period	- provides analytical solution -quick solution to a single normal Bragg grating	-only an approximation to real gratings. -superstructures need to have identical uniform gratings but analytical solutions are cumbersome
Transfer matrix method (TMM)	-division of grating into a large number of sections. -constant refractive index (unique) within a section. -constant (unique) period in a section. -CMT holds within a section.	-models practical gratings -fast simulation -index chirping -period chirping -apodisation -inscription of phase or phase variation -synthesis of complex grating structures -strong and weak grating	-solution is not analytical but a simulation

Table 5. 2: Summary of the modelling techniques.

Filter Type	*Advantages and Disadvantages*
End-pumped	-forms at the laser wavelength but not compact thus difficult to stabilise -narrow bandwidth controlled by grating length ideal for velocimetry -fabrication is critical and there is lack of photosensitive fibre
Fabry-Perot	-easy to fabricate and forms at any wavelength -well known transfer function features controlled by the finesse thus ideal for velocimetry applications -there exists a cavity length for minimal temperature sensitivity -passive strain and temperature compensation are possible -compact and easy to stabilise
DFB	-forms at any wavelength but requires phase-mask for accuracy -narrow passband e.g. 100 MHz -transfer function features controlled by chirp rate thus ideal for velocimetry use -compact and easy to stabilise -less sensitivity to temperature than FBG (sensitivity is halved)
Moiré	-forms at any wavelength but requires phase-mask for accuracy -compact and easy to stabilise -narrow passband e.g. 100 MHz -transfer function features controlled by size of wavelength difference between the gratings -similar to DFB thus ideal for velocimetry applications
TCFPF	-transfer function features are controlled by the coupling ratio of directional coupler and are ideal for velocimetry applications -dielectric mirrors (expensive) may be replaced by identical gratings fabricated in two output arms of coupler

Table 5. 3: Summary of the fibre-optic filters.

References

[1] J. Wilson and J. Hawkes, "*Optoelectronics: An introduction*", Prentice Hall, 1983

[2] J. Midwinter, "*Optical fibres for transmission*", Wiley, 1979.

[3] H. G. Unger, "*Planar optical waveguides and fibres*", Clarendon Press, 1977.

[4] D. Globe, "*Weakly guiding fibres*", Applied Optics, 10, pp. 2252, 1971.

[5] A. Yariv, "*Optical Electronics in Modern Communications*", Fifth Edition, pp. 77-120 & 491-515, Oxford University Press, 1997.

[6] R. Kashyap, "*Fibre Bragg Gratings*", Academic Press, 1999.

[7] L. M. Zhang and J. E. Caroll, "*Large-Signal Dynamic Model of the DFB Laser*", IEEE Journal of Quantum Electronics, vol. 28, no. 3, 1992.

[8] L. A. Weller-Brophy, and D. G. Hall, "*Analysis of waveguide gratings: a comparison of the results of Rourd's method and coupled mode theory*", J. Opt. Soc. Am., vol. 4 , no. 1, pp.60-65, 1987.

[9] M. Yamda and K. Sakuda, "*Analysis of almost-periodic distributed feedback slab waveguides via a fundamental matrix approach*", Applied Optics, vol. 26, no. 16, pp. 3474-3478, 1987.

[10] T. Erdogan, "*Fibre Grating Spectra*", Journal of Lightwave Technology, vol. 15, no. 8, pp. 1277-1294, 1997.

[11] S. LaRochelle, V. Mizrahi, K. D. Simmons, G. I. Stegeman, and J. E. Sipe, "*Photosensitive optical fibres used as vibration sensors*", Optics Letters, vol. 15, no. 7, pp. 399-401, 1990.

[12] A. Othonos, "*Fibre Bragg Gratings*", Rev. Science Instrument 68, no. 12, pp. 4309-4339, 1997.

[13] S. Legoubin, M. Douay, P. Bernage, P. Niay, S. Boj, and E. Delevaque, "*Free spectral range variations of the grating-based Fabry-Perot filters photowritten in optical fibres*", Journal of Optical Society of America A, vol. 12, no. 8, pp. 1687-1694, 1995.

[14] L. A. Everall, K. Sugden, J. A. R. Williams, I. Bennion, X. Liu, J. S. Aitchison, S. Thom, and R. M. De La Rue, "*Fabrication of multi-pass band moiré resonators in fibres by the dual-phase-mask exposure method*", Optics Letters, vol. 22, no. 19, pp. 1473-1475, 1997.

[15] M. Brierley and P. Urquhart, "*Transversely coupled fiber Fabry-Perot resonators: performance characteristics*", Applied Optics, vol. 26, no. 22, 1987.

[16] P. Urquhart, "*Transversely coupled fiber Fabry-Perot resonator: theory*", Applied Optics, vol. 26, no. 3, 1987.

CHAPTER 6

Optical Components for Laser Doppler Velocimetry

6.1 Introduction

Laser velocimetry systems are comprised of various electronic and optical components whose performance characteristics need to be carefully chosen. This chapter discusses the principles and some performance implications of some components that are integrated into the new velocimetry system.

6.2 Laser Source

Laser Doppler velocimetry requires a light beam as a means of probing the flow and gathering the Doppler frequency shift information that defines the flow velocity. Quite often the polarisation of light delivered to the flow is required to be linear and controllable since Mie scattering is polarisation sensitive (Appendix C). This and the need to avoid broadening in the measured Doppler frequency, demand that the light source be a laser with a narrow frequency bandwidth. Other factors to be considered when lasers are assessed for flow diagnostics are power output, mode structure, and power and wavelength stability. The environment in which the laser is to be used may have adverse stability implications on both output power and wavelength.

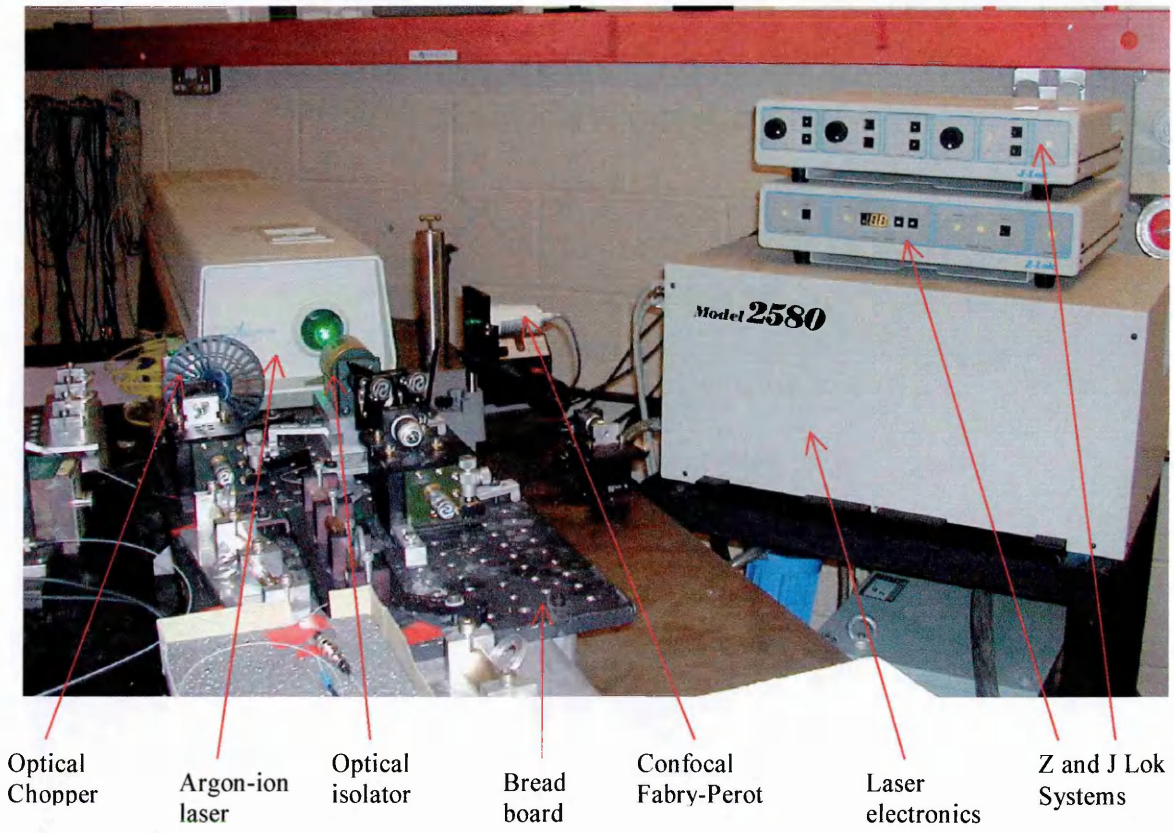

Figure 6. 1: Argon-ion laser system.

An argon-ion laser by Spectra Physics (model 2060-10) (Figure 6.1) was used as the light source and a Faraday isolator was placed immediately after the laser to stop optical feedback into the laser cavity that would otherwise cause instability. The laser is installed with a temperature-controlled etalon to ensure single mode operation. A new laser would provide a maximum of about 2.4 W of optical power at 514.5 nm when the etalon temperature is tuned so that its minimum loss curve coincides with the centre of the laser gain curve but our laser produced 1.2 W due to the aging of the plasma tube. The laser control system is fitted with two independent frequency stabilisation mechanisms, the first of which operates via control of the etalon temperature to counter slow frequency drifts such as those experienced under variations of ambient temperature. The second feedback loop controls the laser cavity length via movements of the output mirror, which is piezoelectrically driven. This compensates for jitter i.e. vibration of the centre wavelength in the range from 10 to 500 Hz, the main cause of which is water hammer from the laser cooling pipes. The stabilised laser has a linewidth

of about 3 MHz and an overall residual jitter of about 2 MHz [1]. The laser drifts at a frequency of about 50 MHz/^{0}C and drifts of several hundred MHz can occur in the centre frequency over longer periods if the ambient temperature changes. Mode hoping is almost completely eliminated unless drastic and sudden changes of ambient temperature are experienced.

The choice of the laser was influenced by output power and wavelength considerations. Argon-ion laser power is considerably larger than that of semiconductor laser diodes that are usually used at higher wavelengths in the infrared. The Mie scattering theory shows that particle scattering efficiency is higher for shorter wavelengths e.g. the scattered light signal from 514.5 nm is about 8 times more than that from 870 nm.

Temperature for mode-hop free operation in lock mode	$\leq 10\ ^0$C
Frequency drift	< 50 MHz/^{0}C
External locking to iodine cell	< 10 MHz/^{0}C
Cavity length without prism	1.10 m
Cavity length with prism	1.17 m
Mode spacing with prism	133 MHz
Frequency jitter with J-lok	$\leq$ 2MHz
Frequency jitter without J-lok	≤ 10 MHz

Table 6. 1: Argon-ion laser specifications.

The frequency to voltage coefficient of the laser was experimentally determined in order to recalibrate the frequency offset numerals of the laser and this was also required to make accurate frequency scans of the iodine cell. A frequency stabilised Helium neon (HeNe) laser beam was colinearly coupled with the argon-ion laser beam into a scanning FP etalon. The two signals were simultaneously monitored on a Lecroy digital oscilloscope while the argon-ion laser was scanned through 0.5 V. A frequency change of 2.10 ± 0.01 GHz was measured for the argon laser signal over this scan voltage with the HeNe signal used as the reference. This laser reference was needed such that any drift due to temperature in the FP etalon did not affect the measurements. The HeNe

laser was stable to within 10 MHz. The argon-ion laser offset numerals changed from -0.8 to 1.4. This value gives the laser frequency to voltage coefficient of 4.2 GHz/V. The change in each step of the frequency offset numeral was determined as 0.1 per 95.45 MHz.

6.3 Optical Fibres for Flow Diagnostics

Modern trends in laser velocimetry make use of optical fibres as a means to deliver light to and to collect light from the measurement location to deliver it to a detector that may be remotely placed. Developments in fibre-optic technology have seen the birth of singlemode fibres and polarisation preserving fibres. This particularly developed the laser Doppler velocimetry (LDV) technique, which often requires the maintenance of coherence, polarisation and minimum signal attenuation.

6.3.1 Guiding and Polarisation Maintaining Properties

An ordinary optical fibre would normally have circular symmetry. It consists of a central core surrounded by a lower refractive index cladding, both of which are of dielectric material. This index difference gives the optical fibre its guiding properties through total internal reflection at the core-cladding interface. Three types of fibre namely multimode step index, multimode graded index, and monomode step index fibre exist. Of interest to this work is the monomode step index fibre due to its ability to maintain coherence over large distances. Polarisation maintaining fibre is also important for this work for delivering light of known polarisation to the flow (Chapter 9) as well as for polarisation beam multiplexing in the filter required for active stabilisation (Chapter 8).

Polarisation maintaining fibre was developed by introducing intrinsic birefringence that is much greater than any possible external birefringence. The result was a highly birefringent fibre (Hi-Bi) that has two principal axes with very different propagation constants. Thus polarised light launched down one of these principal axes will retain its state of polarisation along the entire fibre length.

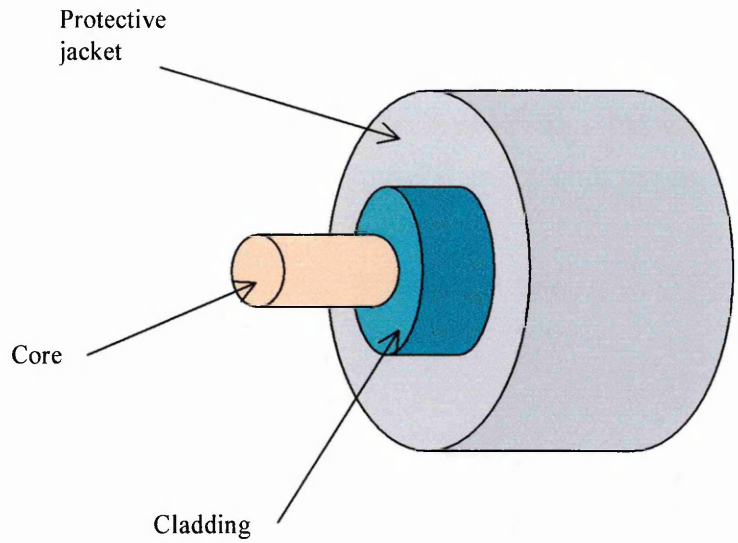

Figure 6. 2: Schematic of an optical fibre.

There are several types of Hi-Bi fibre in the commercial market all of which are produced by varying technologies either based on the non-circular geometry of the core or cladding, or based on some means of internal stress application [2]. The scope of this thesis is only interested in the practical exploitation of the properties of the Hi-Bi and singlemode fibres and therefore details of their geometry or their manufacturing process will not be discussed.

In this thesis Hi-Bi fibres have been used as part of a LDV probe head system that delivered and collected light of known polarisation to and from the measurement location. The laser Doppler velocimetry presented in this work would have benefited immensely from an all-polarisation maintaining system that includes all optical fibres and directional couplers. However the unavailability of components at 514 nm in the commercial market has led us to use singlemode components. Bragg gratings were fabricated in singlemode fibres and single mode couplers were used. Because the polarisation of light through these components had to be maintained, polarisation state controllers had to be used [3].

The polarisation state controllers apply bending stress to the optical fibre thereby introducing external birefringence that is much larger that the intrinsic birefringence of

the fibre. The result is that the degeneracy of the x-polarised and y-polarised sets of linearly polarised (LP) modes is broken and thus the two modes will have different propagation vectors which lead to a retardation mechanism between the two modes. Such devices were successfully used in this work and a cross-talk suppression or extinction ratio of 21 dB was achieved.

The device is a system of three circular rings of identical diameter upon which the fibre is wound in such a way that each ring can be rotated through angles greater than 180^{0}. Such a device is completely equivalent to fractional wave plates of classical optics. The two outer rings are used as quarter wave plates by making them have identical number of turns of fibre which is at the same time half that of the middle ring acting as a half wave plate. The quarter wave rings control the ellipticity while the half wave coil controls the orientation of any desired output polarisation. The device may be located at any place along the length of the fibre. We have constructed these devices in our laboratory with the theory of design based on a paper by Lefevre [3].

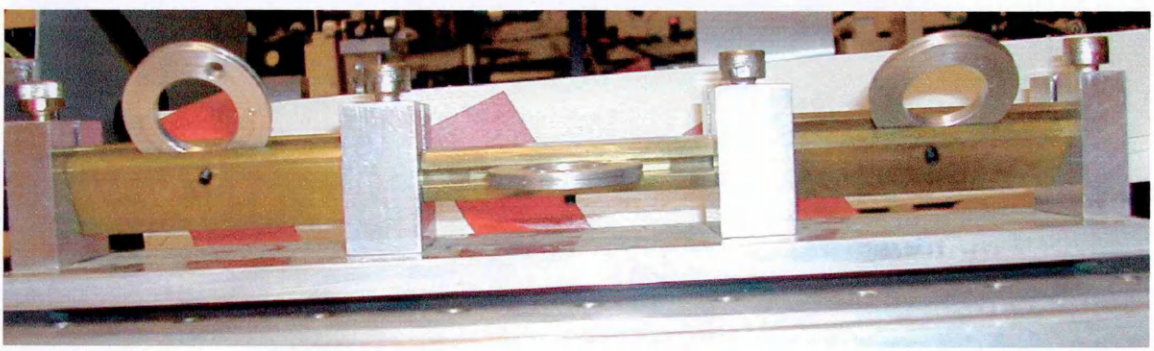

Figure 6. 3: Photograph of polarisation state controller showing the three rings.

6.3.2 Power Restrictions in Optical Fibres

Transmission of high laser power through monomode optical fibre tends to be limited by the onset of non-linear effects which among other consequences depletes the power throughput. This could be particularly detrimental in flow measurement where as much power as possible is required into the flow region since the scattered light intensity (from particles in the flow) collected by the optics is often very small.

One such non-linear effect is known as stimulated Brillouin scattering (SBS) which manifests itself through the generation of a backward-propagating Stokes wave that carries most of the input energy, once the Brillouin threshold is reached. SBS can account for more than 50 % of the transmitted light being sent back to the laser. This effect has been experimentally demonstrated in a 50-m length of optical fibre with an argon-ion laser operating at 514-nm [4]. It should be noted that this effect while being a hindrance to the work presented here could be useful through fibre-Brillouin lasers and amplifiers [5] and frequency shifters [6]. The Brillouin threshold or critical pump power $P_{critical}$ may be approximated by

$$P_{critical} \approx \frac{21}{g_B \cdot L_{eff}} \cdot A_{eff} \qquad (6.1)$$

The parameter A_{eff} is the effective area of the fibre core, L_{eff} is the effective interaction length, and g_B is the Brillouin gain coefficient that is independent of pump wavelength [5]. Equation (6.1) will show that a fibre core of diameter 4 μm and length of about 5.3 m sets a critical pump power of 1 W. Such a power level and length of fibre are typical values for a LDV set up and hence there is a need to address the SBS problem.

Also of concern are non-linear properties of germania-doped silica fibre (well known as photosensitivity) discovered by Hill et al [7]. The effect is the formation of permanent narrow-bandwidth Bragg gratings along the whole length of fibre when high laser intensity in the blue/green spectrum is coupled through the fibre. The Bragg grating depending on laser intensity may grow with time until nearly all the light intended for transmission is reflected back (Chapter 4).

Grating formation is triggered by fibre end reflections that form a standing wave whose growth with time will reach the threshold and thus depletes the power throughput. In this work Bragg grating formation was prevented by angle-polishing one end of each fibre at 8^0. A Panda Hi-Bi fibre from Fujikura that was specially made for high power transmission (cut-off wavelength of 480 nm) was used [480P]. The fibre had a lower germanium dopant (to stop grating formation) and larger core diameter. The formation

of SBS was avoided by limiting power transmission to about 300 mW (less than the critical pump power) through a fibre length of about 3 m.

6.4 Probe head

Optical flow measurement being laser based requires an efficient means of coupling light to and from the measurement volume. It is desirable for any point measurement technique to have a well-defined measurement volume that provides highly localised velocity data and therefore high spatial resolution. Optical probe heads [8] comprising a system of lenses normally meets this requirement. We present here the design and working principle of a two-headed optical-fibre linked probe head that was constructed in-house for turbomachinery applications [9, 10].

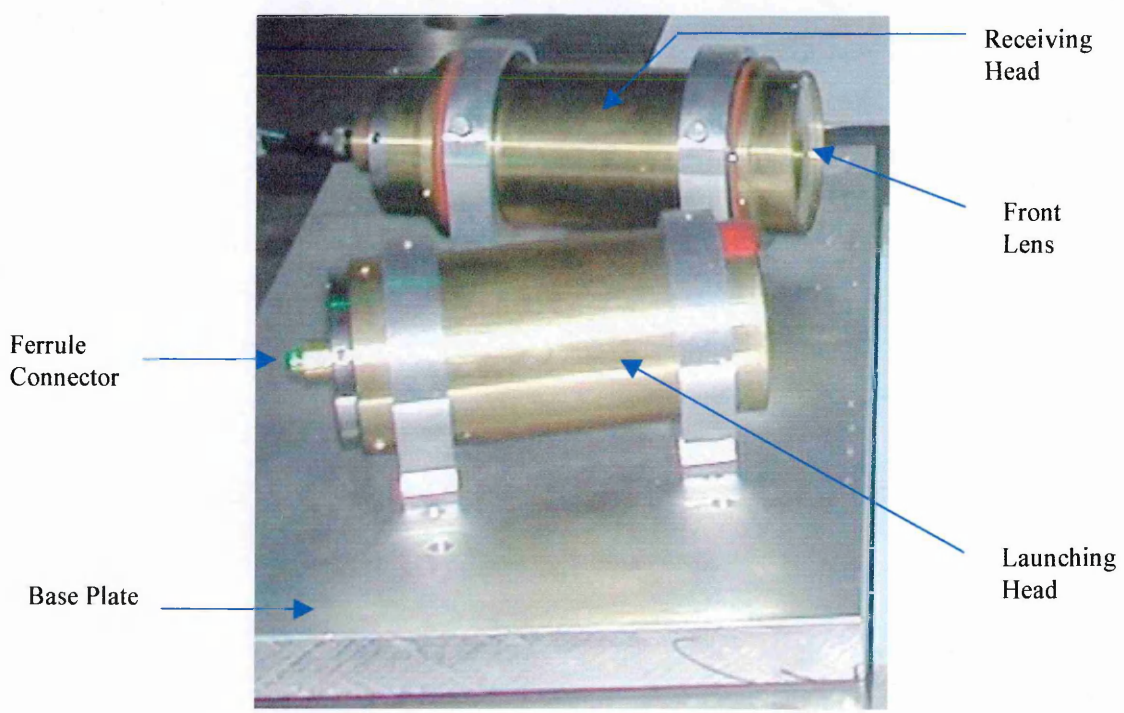

Figure 6. 4: Photograph of LDV probe head.

6.4.1 Probe Head Assembly

The design and construction of the two heads is similar. The lens configuration of the probe head is given in Figure 6.5. Light delivered to the probe head is first collimated by an achromatic lens and next expanded by a plano concave lens. Both lenses are 10 mm in diameter and 20 mm in focal length. The symmetrical singlet, 50 mm in diameter and 38 mm focal length, collimates the resultant beam to the negative meniscus lens also of 50 mm diameter, which focuses the beam to a point 400 mm away from its surface. This becomes the position of best focus thus defines the working distance from the probe head to the measurement volume. The lenses are not anti-reflection coated and thus the system suffers from loss of up to 30%. Both the delivery and collection head are designed to operate at an f-number of approximately 8 that defines a measurement volume of about 70 μm in width and 345 μm in length for an angle of about 20^0 between the heads. The measurement volume is defined by the common focus of the two heads such that if the two were simultaneously illuminated by light their overlapping light defines this volume. The lens types and system assembly was based on a model using Zeemax optical software. The base unit on which both heads were mounted was designed such that the angle between the two heads could be varied (Figure 6.6).

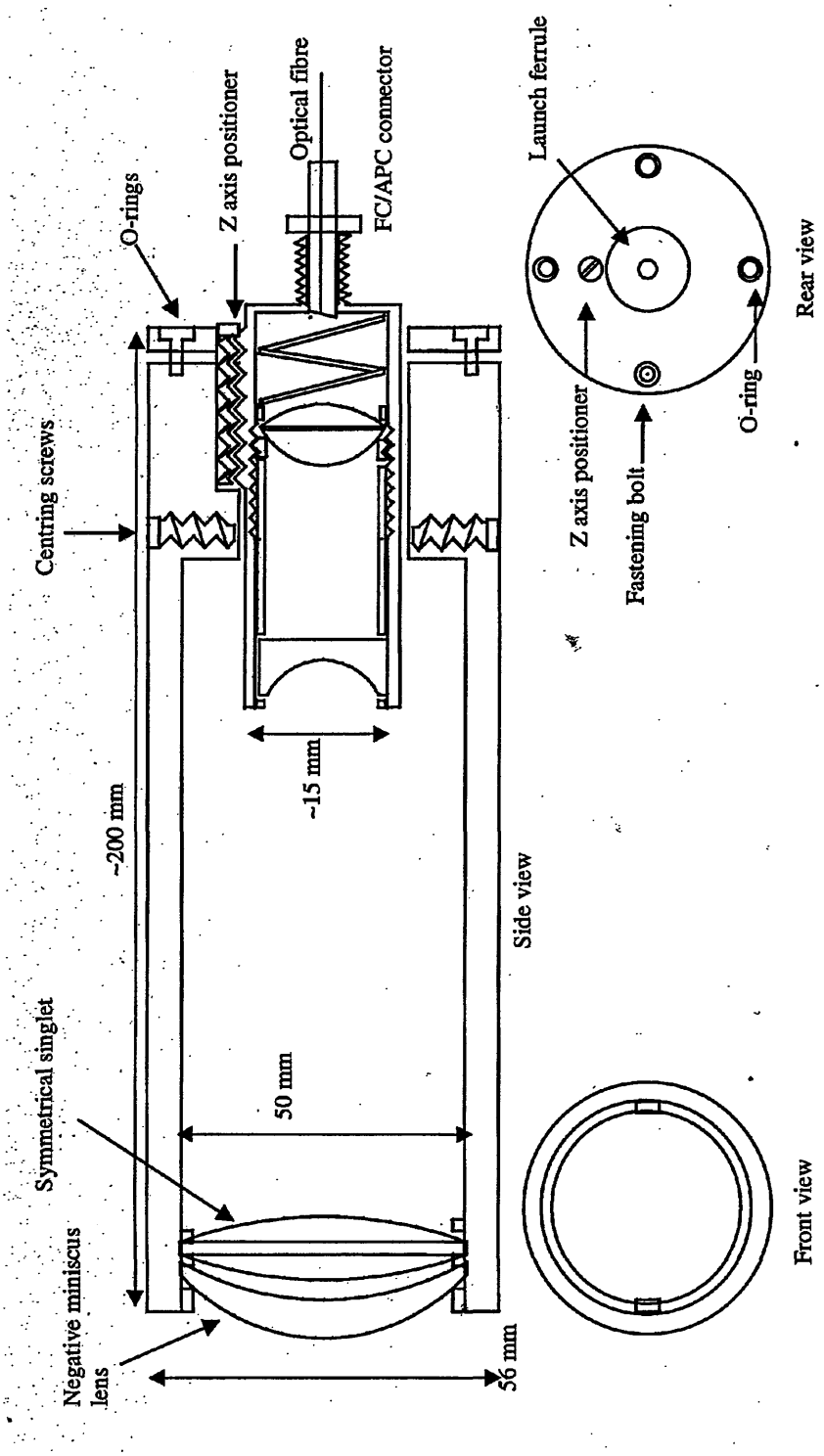

Figure 6. 5: Lens configuration of the probe head [10].

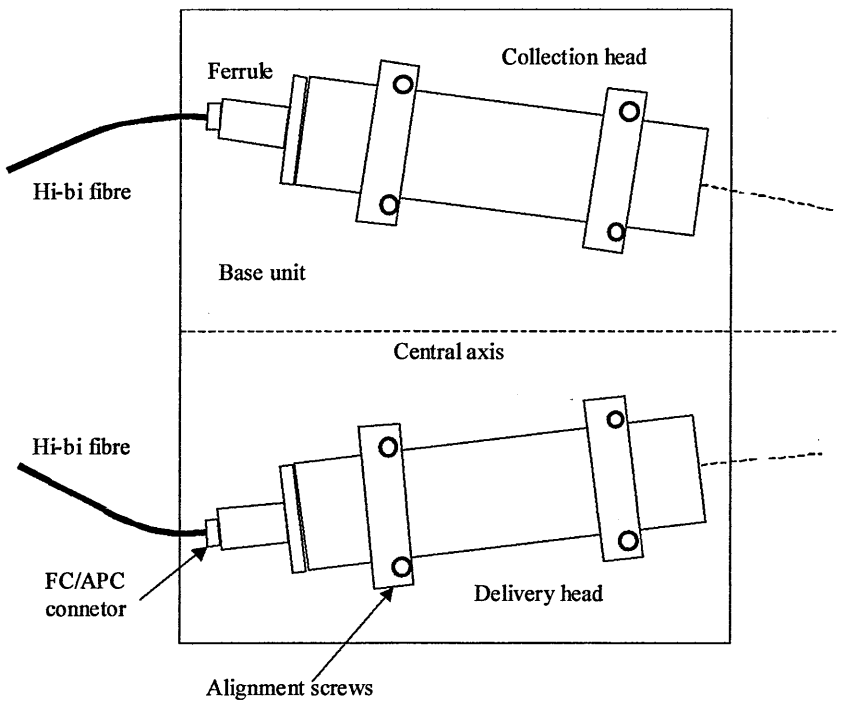

Figure 6. 6: Plan view of the probe head alignment assembly.

6.4.2 Probe Head alignment

The initial alignment of the probe head was done by placing an aluminium target at 400 mm from the front face of the delivery head and the position of best focus was determined by looking for maximum speckle size in the scattered light during focus adjustments. Axial adjustment of the ferrule position consisting of the first two lenses responsible for focusing altered the beam focus. The entire head was rotated about its axis and adjusters that alter the angle of the ferrule axis eliminated any eccentricity. The target was moved to a position 400 mm from the front face of the whole probe head but along the central axis and adjusters on the delivery head were used to bring the focused beam to this target. The initial alignment of the other head required back illumination through a single-mode fibre. A 100 mW Nd: YAG laser was used for this purpose and the position of best focus determined from maximum speckle size was obtained by adjusting the axial position of the central ferrule. Additional adjusters on the collection head were used to overlap the two beams so that they had a common focal point.

The final and optimum adjustment of the probe head is achieved by simultaneously coupling the argon-ion laser beam at 514.5 nm and a Nd: YAG laser at 532 nm through the delivery and collection heads respectively. A Spiricon laser beam analyser (model LBA-100A) using a CCD detector array captured and displayed the beam images at the focus (Figure 6.7) while focus adjustments on the heads were performed as before. The two beam foci were overlapped on a CCD camera of 13-μm spatial resolution. Optimised collection of the scattered light from an aluminium plate was of the order of 10 μW and up to a microwatt from stationery white-painted perspex disc with 120 mW of optical power in the measurement volume. The laser was operated at about 340 mW output power and fibre coupling efficiency was about 51 % while a further 30 % loss of power was incurred in the probe head.

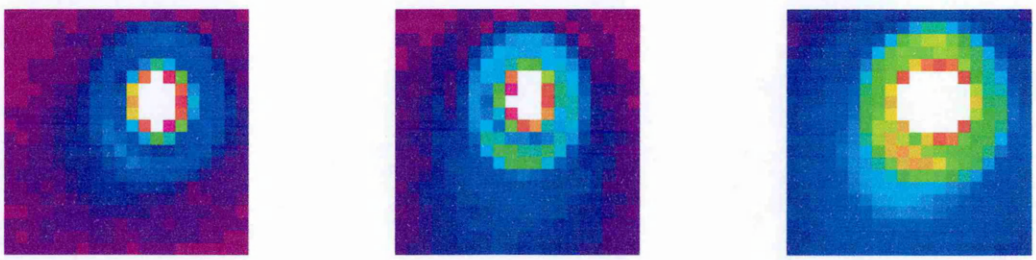

Figure 6. 7: Delivery head image at the focus (a) sending, (b) receiving, and (c) combined beam.

The angle between the two heads was adjustable and this in turn varied the size of the measurement volume as well as the sensitivity to the on-axis velocity component. Figure 6.8 shows that the larger this angle is the smaller the length of the measurement volume. The probe head was operated at an angle of 20^{0} thus giving a length of 345 μm and width 70 μm.

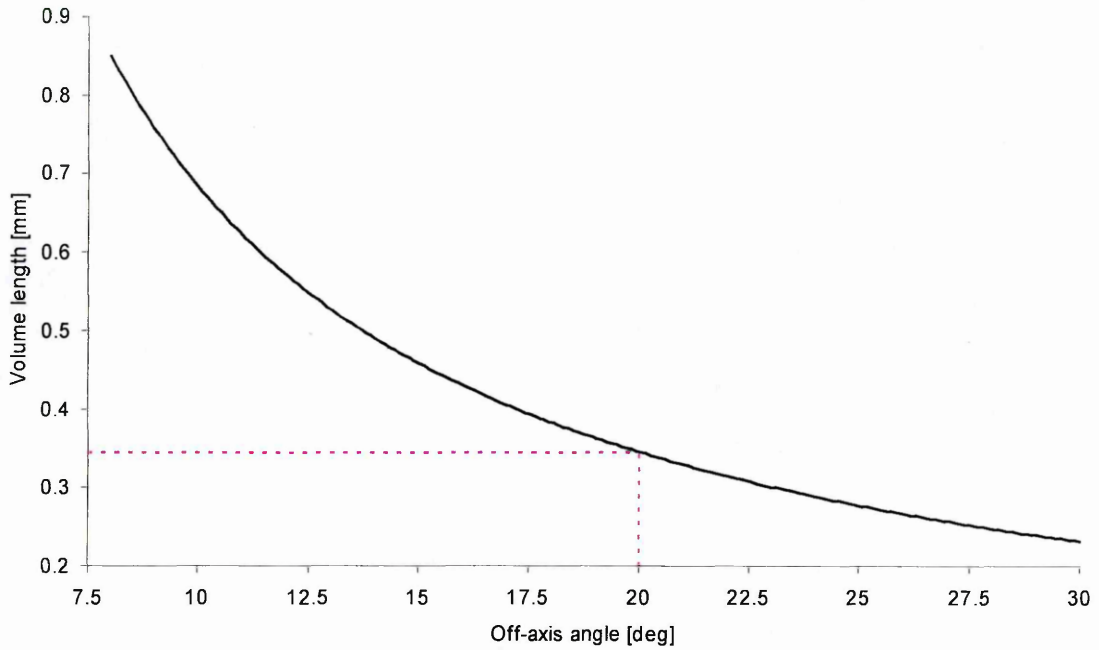

Figure 6. 8: Length of the measurement volume as function of the angle between the heads.

6.5 Iodine Cell Assembly

The author would like to acknowledge Dr David Nobes (Cranfield University) for providing the iodine cell that was used in this work. Doppler frequency shifts caused by particles entrained in the flow are normally measured by an absorption line of a molecular iodine vapour. The vapour that is enclosed in a high quality glass cell transduces frequency shifts (of the order of MHz) to changes in intensity level. The iodine vapour has many absorption lines corresponding to wavelength emission of many laser sources that include the 514.5 nm of the argon-ion laser.

The cell that was adopted for this work was originally developed in the laboratory for a related planar Doppler velocimetry system [11]. The 514.5 nm line of the iodine vapour cell was used to monitor the stability of the argon-ion laser wavelength. This was used to stabilise the laser wavelength in a closed loop feed back format (Chapter 8). The cell consisted of a main body and a side stem (cold finger) and was contained in a specially made oven (Figure 6.9). The temperature and thus vapour pressure was controlled by a proportional-integral-derivative (PID) temperature controller. The vacuum sealed cell

was contained in a sealed insulated box with a resistive heating element situated near the base. A re-circulated air, fan driven over the heating element heated the glass cell such that temperature gradients were minimised. A thermocouple feedback loop sensor was used with the PID controller system. The cold finger was heat controlled by a peltier element that was driven by a peltier element controller. A heat sink was placed below the fan.

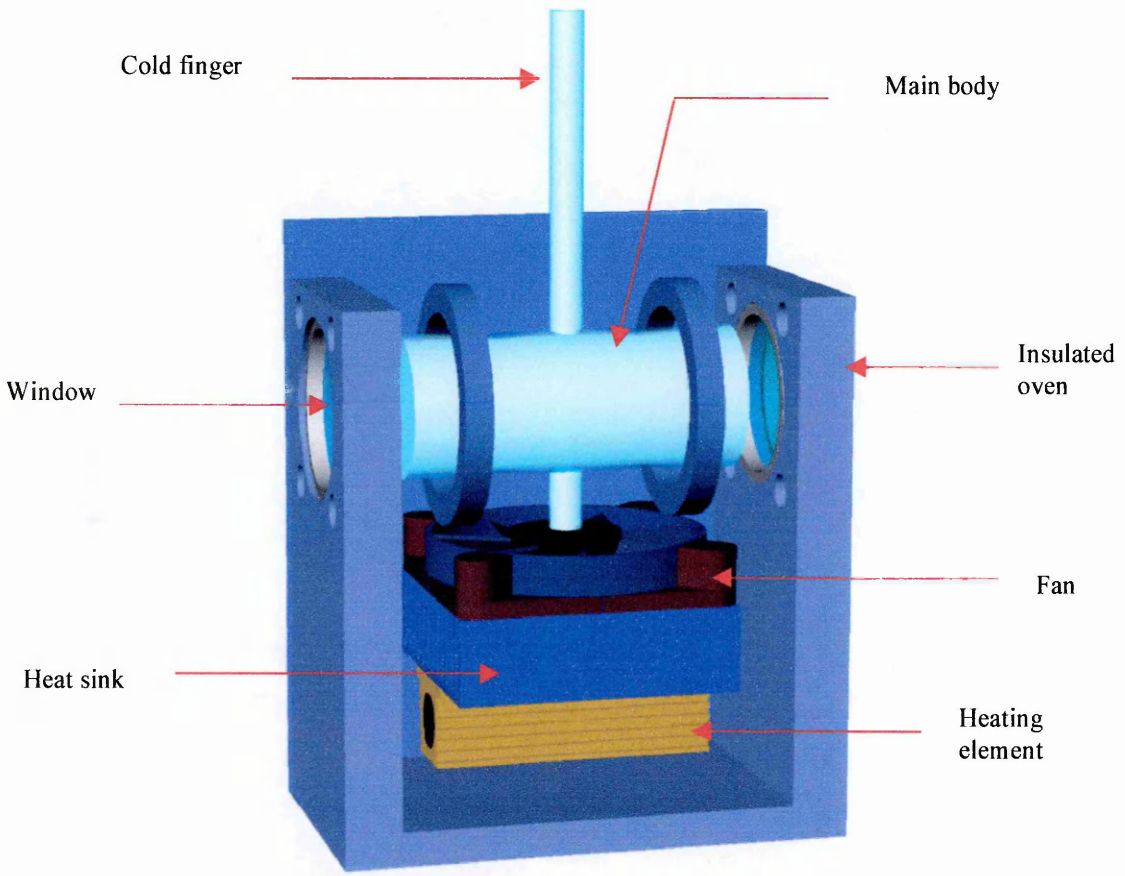

Figure 6. 9: Side view of iodine cell design.

6.6 Signal Processing

The scattered light levels from the measurement volume can be as low as sub-nanowatts to the order of a few microwatts depending on the laser wavelength and power, the speed and nature of the scatterers. Such signal levels require high sensitivity and extremely low-noise detection electronics in order to retrieve the Doppler signals that

contain the velocity information. Bandwidth requirements in the optical filter based velocity measurement systems are different from conventional interferometric systems. The optical filter transfer function measures frequency by directly converting the Doppler frequency shifts into intensity variations. A higher frequency and hence velocity resolution therefore requires a low bandwidth filter that has a steep slope in the transfer function. This is particularly useful for the measurement of low velocities. The conventional interferometric systems on the other hand (LDV) require electronic bandwidths of the order of 100 MHz or more in order to measure velocities above 30 ms^{-1}. Several factors have to be considered when choosing the appropriate detection for a given application.

1) Sparse seeding: this is characterised by low light levels in the scattered signal that requires the use of a detector with high gain and high quantum efficiency. An external low-noise amplifier may be necessary although its inclusion could compromise the electronic bandwidth of the detector and proper precautions should also be taken to avoid deterioration of the signal to noise ratio (SNR).

2) Single particle transit: Sparse seeding means there is high probability of a single particle existing at any one time in the measurement volume. It may be necessary to detect individual particle transits and go on to perform temporal averaging under conditions of a stationary flow. Such a detection system requires a high electronic bandwidth detector that can resolve the transit time of individual particles. The signal that is detected under these conditions is pulsating. An attempt to record the average signal may prove to be impossible as the average may be very much lower than the pulse amplitude and thus the signal to noise ratio may be poor if not below detection level.

3) Unsteady flow: Turbulent flows are also characterised by highly fluctuating signals and a good detection system should be able to differentiate between this type of signal variation and that caused by the particle concentration or size. If a stationary flow were assumed then for conditions of uniform sparse seeding the light pulses would be approximately periodic. A complication would exist if the flow were

turbulent with non-uniformly distributed particles of a wide range of size. Such an application requires a detection system that can resolve times that are much smaller than the individual particle transits. Detection in photon counting mode may therefore be necessary.

The readily available detectors that suit the above conditions include photodiodes, photomultiplier tubes (PMT) and avalanche photodiodes (APD). The quantum efficiency of the APDs has a maximum in the infrared while PMTs and photodiodes peak in the visible spectrum. PMTs were chosen as the detectors because of their high sensitivity in the visible.

Figure 6.10 shows the signal to noise ratio (SNR) of the PMT detector modules (Hamamatsu H5783-01) for laser power of up to 1 μW (maximum signal that was available from the scattering). The result is a computation from equation (6.2) using the detector characteristics. The graph is non-linear especially for low power because the first term in denominator of equation (6.2) becomes small and the other (noise terms) terms therefore dominate.

$$SNR = \frac{\frac{\eta \cdot q \cdot P \cdot \lambda}{h \cdot c}}{\left[2 \cdot q \cdot B \cdot \left(\frac{\beta}{\beta - 1}\right) \cdot \left(\frac{\eta \cdot q \cdot P \cdot \lambda}{h \cdot c} + 2 \cdot I_d\right) + N_A{}^2\right]^{\frac{1}{2}}} \qquad (6.2)$$

The symbols η, λ, β, q, h, c, P, B, I_d and N_A represent the quantum efficiency, wavelength, secondary emission ratio, electronic charge, plank's constant, speed of light, laser power, Bandwidth (Hz), dark current (A) and noise of amplifier circuit respectively. The values of these constants are given in Table 6.2.

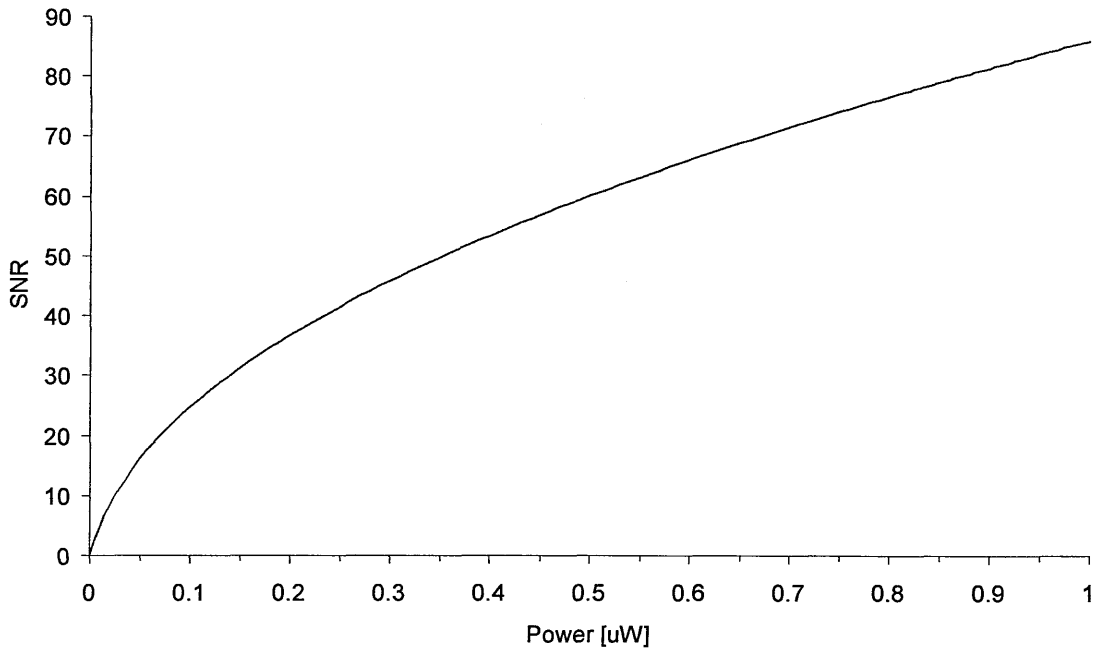

Figure 6. 10: PMT signal to noise ratio (SNR).

h	6.62×10^{-34} Js
c	3×10^{8} ms^{-1}
q	1.6×10^{-19} C
λ	514.5 nm
η	0.7 AW^{-1}m^{-1}
β	6
P	0 – 1 μW
B	100 MHz
I_d	0.1 nA
N_A	0.5 nA

Table 6. 2: Constants used to calculate the signal to noise ratio of the photomultiplier tube.

Figure 6.11 shows a simple detection configuration for high-speed and pulsed light signals that was used in all our experiments. Current to voltage (I-V) converters making use of FET operational amplifiers are required. Ringing suppression measures require that matching resistors at both ends of the coaxial cable be used. However matching resistors tend to reduce the pulse amplitude of the signal by half. If amplification is

required then a low-noise amplifier with short wiring cables would have to be connected to the PMT output followed by the oscilloscope.

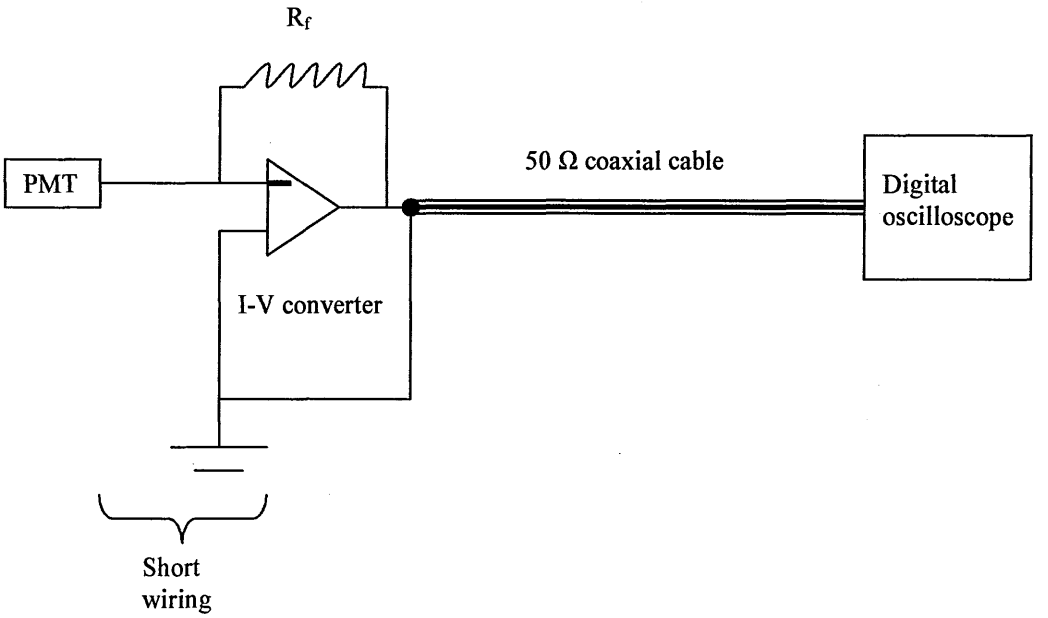

Figure 6. 11: Detection system that was used in our experiments.
PMT – photomultiplier, R_f – feedback resistor, I-V – current to voltage.

When the PMT output is very low, varying direct current, the zero-drift of the amplifier can be a significant source of error. This problem may be overcome by chopping the PMT signal at a frequency much higher than its own range of variation. The resulting modulated squarewave is amplified in a stable a.c amplifier, demodulated and then lowpass filtered to retain the original but amplified dc signal. Photon counting is alternatively the most effective and stable way to use a PMT for measuring very low light levels [12] while at the same time eliminating the dc component of the dark current and eliminating spurious pulses that are not of photoelectric origin (Figure 6.12).

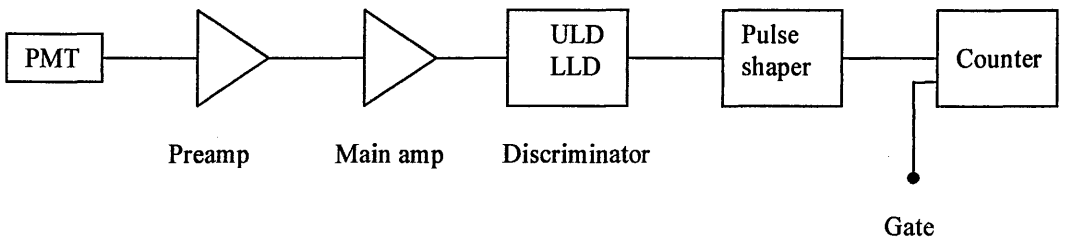

Figure 6. 12: Photon counting detection scheme.

PMT – photomultiplier, ULD – upper level discrimination, LLD – lower level discrimination, amp – amplifier.

The low light levels incident on the PMT causes the cathode to emit single electrons. The individual anode charges due to these electrons are converted to voltage using a wide-band preamplifier and amplified by the main amplifier to produce proportional voltage pulses which are passed by a pulse-height discriminator to a pulse counter whose output over a set time (gate) is a measure of the incident flux. The discriminator allows optimisation of the SNR by adjusting the lower level discrimination (LLD) and the upper level discrimination (ULD) pulse height to give the best pulse-amplitude window. Pulses of amplitude less than LLD (noise) and those greater than ULD (cosmic rays) are rejected but some dark pulses still exist within the discrimination window.

6.7 Digital Lock-in Amplifiers

A lock-in amplifier is used to detect and measure very small a.c signals as low as the order of nanovolts, which may be completely obscured by noise. It is a phase-sensitive detector that singles out the component of the signal at a specific reference frequency and phase while rejecting noise signals at frequencies other than the reference frequency. The reference signal for the lock-in amplifier is derived from the fixed frequency (from a function generator) used to excite the experiment and the lock-in amplifier then detects the response from the experiment at this reference frequency. The lock-in amplifier then generates its own reference, which it uses to multiply with the amplified signal using a phase-sensitive detector. Figure 6.13 is an example of the three signals.

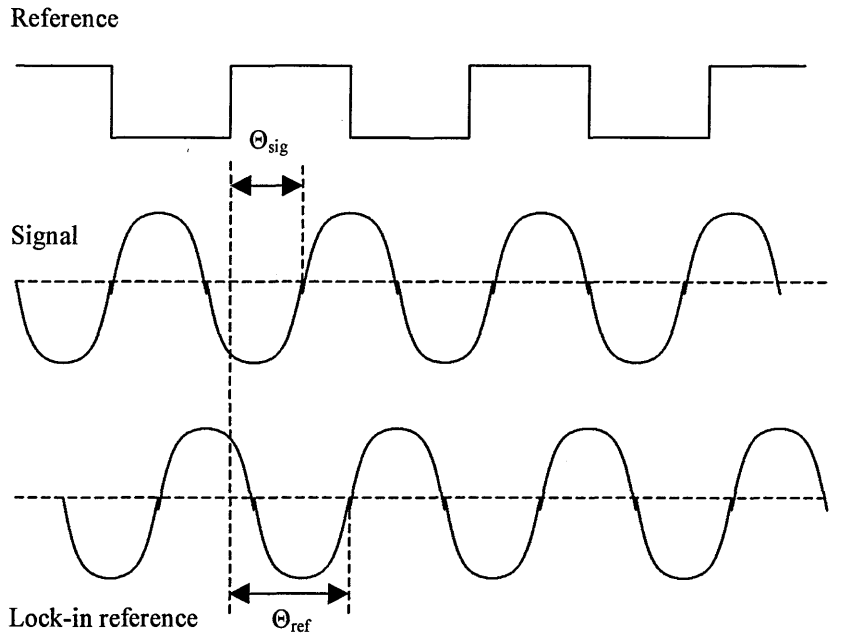

Figure 6. 13: Lock-in amplifier principle of measurement.

Suppose the measured signal V_{expt} from the experiment is given by

$$V_{expt} = V_{sig} \cdot \sin(\omega_r \cdot t + \theta_{sig}) \qquad (6.3)$$

where ω_r is the reference frequency (excitation), V_{sig} and θ_{sig} are respectively the signal amplitude and phase. The lock-in amplifier generates its own reference signal V_{ref} of amplitude V_L, frequency ω_L and phase θ_{ref} given by

$$V_{ref} = V_L \cdot \sin(\omega_L \cdot t + \theta_{ref}) \qquad (6.4)$$

The output of the phase-sensitive detector V_{psd} is the product of equation (6.3) and (6.4) given by

$$V_{psd} = \tfrac{1}{2} V_{sig} V_L \cos[(\omega_r - \omega_L)t + \theta_{sig} - \theta_{ref}] - \tfrac{1}{2} V_{sig} V_L \cos[(\omega_r + \omega_L)t + \theta_{sig} + \theta_{ref}] \qquad (6.5)$$

Thus the phase-sensitive detector output is two a.c signals one at the difference frequency and the other at sum frequency. The signal is passed through a low pass filter and if ω_r and ω_L are equal then

$$V_{psd} = \tfrac{1}{2} \cdot V_{sig} \cdot V_L \cdot \cos(\theta_{sig} - \theta_{ref}) \qquad (6.6)$$

Therefore the phase-sensitive detector output is a d.c signal proportional to the signal amplitude. Several outputs may be obtained from the lock-in amplifier e.g. signal amplitude, phase or quadrature signals.

Stanford Research Systems lock-in amplifiers (SR850) with digital phase sensitive detectors were used in this work. It has a high dynamic reserve of more than 100 dB and digital low pass filters of up to 24-dB/octave of roll off. The lock-in amplifier consists of synchronous filters that notch out noise components at multiples of the reference frequency.

6.8 Summary

Some of the key components used in the velocimeter have been discussed. The argon-ion laser system was described in some detail including the experiments carried out to determine the laser frequency to voltage coefficient (4.2 GHz/V) which is an important parameter for the operation of the velocimeter. Since the velocimeter presented in this thesis (Chapter 9) uses polarisation multiplexing and de-multiplexing the properties of the optical fibres were also discussed and these included the guiding and birefringent properties. Transmission of high power visible radiation through single mode fibre produces non-linear effects and these including their implication to the implementation of the velocimeter have been discussed. The structure, alignment and operation of the optical fibre linked probe head was discussed in some detail. The Chapter concluded with the description of the signal processing based around the photomultiplier tube detector and the principle of phase-locking by digital lock-in amplifiers.

References

[1] Spectra Physics Beamlok Laser Manual.

[2] D. N. Payne, A. J. Barlow and J. J. Ramskov Hansen, "*Development of low and high birefringence optical fibres*", IEEE Journal of Quantum Electronics, QE18, pp. 477, 1982.

[3] H. C. Lefevre, "*Single-mode fibre fractional wave devices and polarisation controllers*", Electronics letters, vol. 16, no. 20, 1980.

[4] P. Labudde, "*Transmission of narrow band high power laser radiation through optical fibres*", Opt Comm, vol. 32, pp. 385, 1980.

[5] G. P. Agrawal, "*Nonlinear Fiber Optics*", Academic Press, San Diego, California, 1989.

[6] C. J. Duffy and R. P. Tatam, "*Optical frequency shifter technique based on stimulated Brillouin scattering in birefringent optical fiber*", Applied Optics, vol. 32, no. 30, 1993.

[7] K. O. Hill and G. Meltz, "*Fiber Bragg Grating Technology Fundamentals and Overview*", Journal of Lightwave Technology, vol. 15, no. 8, 1997.

[8] S. W. James, R. P. Tatam, and R. L. Elder, "*Design Considerations for 3D Fibre Optic Laser Doppler Velocimeter for Turbomachinery Applications*", Review Science Instruments 68, pp. 3241-6, 1997.

[9] D. A. Egan, S. W. James, and R. P. Tatam, "*On-axis laser Doppler velocimetry for turbomachinery applications using optical fibre techniques*", Proceedings of SPIE: Optical Technology in Fluid, Thermal, and Combustion Flow 111, vol. 3172, pp. 17-26, 1997.

[10] D. Egan "*In-Line Fibre Optic Laser Doppler Velocimetry for Turbomachinery Applications*", PhD Thesis, 2000.

[11] D. S. Nobes, H. D. Ford, and R. P. Tatam, "*Instantaneous, two camera, three dimensional planar Doppler velocimetry using imaging fibre bundles*", Optical Diagnostics for Fluids, Solids, and Combustion, Proceedings of SPIE, vol. 4448, pp. 283-294, San Diego, USA, 2001.

[12] Hamamatsu photomultiplier tube detector manual.

CHAPTER 7

Fabrication of Bragg Grating Based Filters

7.1 Introduction

All the Bragg grating based filters were discussed in chapter 4 and modelled in chapter 5. This chapter will first describe the experimental configurations that were used to fabricate the internally written gratings at 514.5 nm using the argon ion laser as well as the methods used to read their frequency spectra, which consists of typically very narrow bandwidths e.g. 100 MHz. Also discussed are the Bragg grating and Bragg grating based Fabry-Perot interferometer fabrication experiments by the holographic side exposure of hydrogen-loaded single mode fibres to UV radiation at ~ 245 nm. The experiments used to characterise the frequency spectra of the filters are presented and the results are given. The ability to tune the transfer function of the filters is also demonstrated.

7.2 Internally written Bragg Gratings

The internally written or end-pumped Bragg grating forms throughout the whole length of a single mode fibre when a high-intensity argon-ion laser beam at either 488 nm or 514.5 nm is passed through it. The grating is sometimes known as length limited due to its bandwidth, which is strongly controlled by the length of the grating. The filter fabricated by this method is potential attractive in this application primarily because of its narrow bandwidth and its wavelength of formation that is identical to that of the illuminating laser (Chapter 4). The theory of the grating filters was given in Chapter 5.

An intense single longitudinal mode argon-ion laser-beam at 514.5 nm illuminates the fibre. The two ends of the optical fibre are carefully cleaved and/or polished so that the two facets are flat and parallel thereby simulating a low-contrast Fabry-Perot

interferometer (Figure 7.1 (a)). The interference of the forward going wave and the Fresnel back reflection from the fibre facet will occur when the length of fibre is an integer multiple of the laser wavelength to produce a standing wave. Figure 7.1 (b) shows the principle of bootstrap growth in the interference fringes for a system well isolated from thermal and vibration effects.

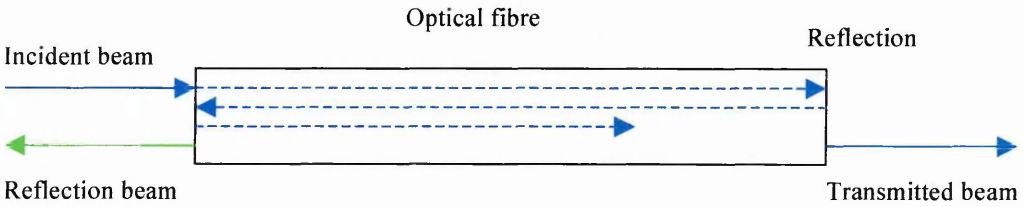

(a)

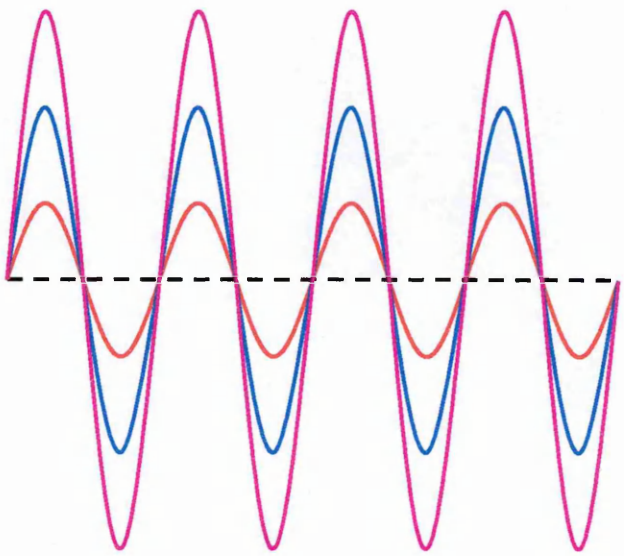

(b)

Figure 7. 1: Principle of formation of end-pumped grating (a) interaction of forward and backward going fields and (b) the growth with time of interference fringes.

7.2.1 Filter Fabrication

The optical fibre is held horizontally and straight under slight tension with each end fixed in a magnetic v-grove or a glass ferrule (Figure 7.2). The alignment and launch optimisation is performed with the variable attenuator set such that about 1 mW of the

argon-ion laser power is available for launch. This ensures that no grating formation takes place during this period. Once the alignment is over the attenuator is adjusted to the required writing intensity.

Other researchers have aligned the polarisation of the optical beam with an eigen-axis of the optical fibre using a half wave plate even for fibre with slight birefringence, a precaution that was meant to reduce noise in the transmission profile [1]. Bragg grating formation is very sensitive to environmental conditions such as temperature fluctuations, temperature gradients, vibrations and mechanical stress, which in the worst case can result in washing out the grating. In this work temperature and vibrations were minimised by enclosing the optical fibre in a plastic insulating tube, foam rubber shielding and then covered in polystyrene. This however does not account for temperature changes due to the internal heating of the optical fibre that result from the absorbed energy of the illuminating optical beam.

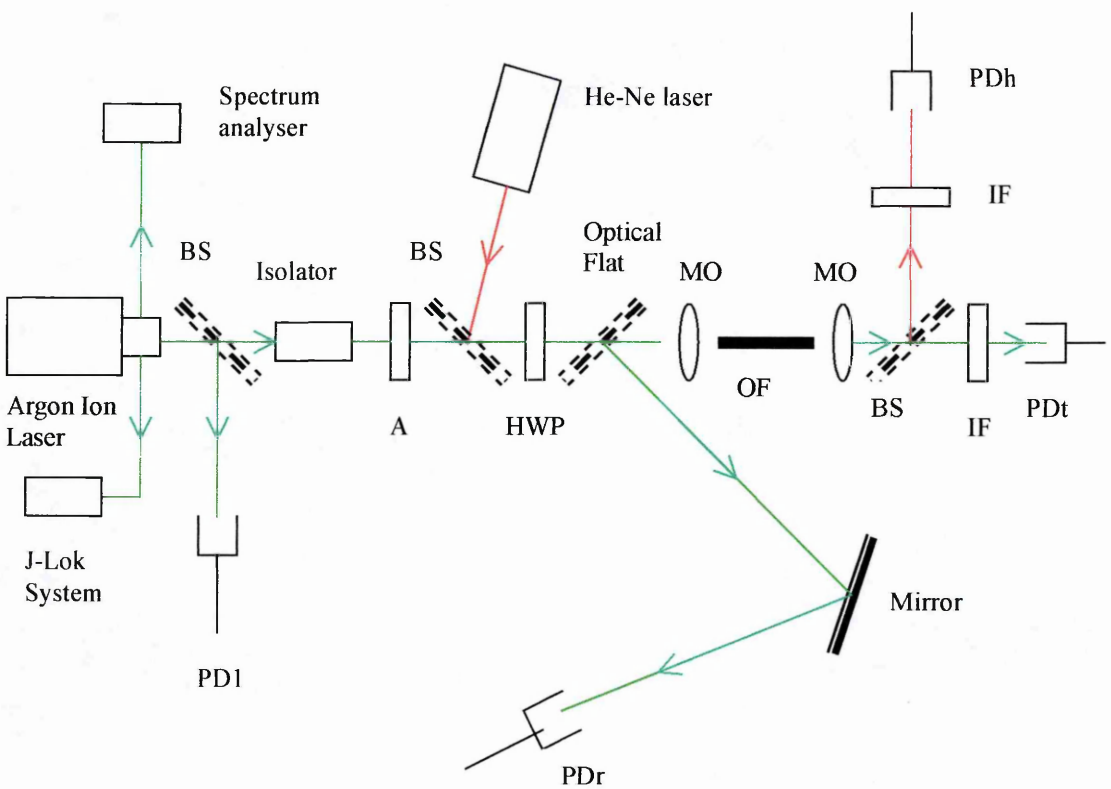

Figure 7. 2: Experimental configuration for grating fabrication.

A – variable attenuator, BS – beam splitter, HWP – half wave plate,
MO – microscope objective, OF – optical fibre,
IF – interference filter, and PD – photodetector.

Optical fibres that are single mode at the writing wavelength (Fibrecore SM450 fibre cut-off wavelengths of 402 and 449 nm) were used to avoid multiple peaks that occur in the reflection profile of the filter if the fibre were multimode [2]. Single-frequency highly stabilised laser illumination with stable output power is required. Additional servos may be necessary to actively control the laser wavelength and or actively stabilise the phase of the filter by locking it to the laser wavelength (Chapter 8 and Appendix D & E). A single frequency stabilised He-Ne laser was also launched colinearly with the argon-ion laser to monitor the launch efficiency of light coupled into the fibre during the grating fabrication (Figure 7.2). Thermocouple sensors placed in contact with the fibre were used to monitor the temperature of the fibre along its length during the fabrication process.

The Faraday isolator prevents any feedback into the laser cavity that may cause instabilities and the half wave plate is used to rotate and match the plane of polarisation of the illuminating argon-ion beam with one of the eigen-axis of the optical fibre. The polarisation of the He-Ne laser beam was adjusted such that most of this beam was directed towards the photodiode detector, PDh, while the argon-ion beam was directed to detector, PDt. Interference filters were used to cut out the unwanted stray light. An optical flat was used to direct the signal reflected back from the grating to a photodiode detector, PDr. The argon-ion laser was operated with both the Z-lok and J-lok systems engaged for wavelength stabilisation (Chapter 8) while the optical spectrum analyser was used to monitor any drift in the wavelength.

The data acquisition of 5 channels and a signal processing program were set up in LabView^{TM}. Four photodiode detectors that accommodate interference filters were constructed in the laboratory and the fifth was a thermocouple sensor that monitored the fibre temperature. The electronics for matching the detectors and gain adjustments were constructed in the laboratory to include optional 4 four-stage low-pass RC Bessel-filters each with an 80-dB roll-off and cut-off frequency of 12 Hz. The filter was required to eliminate signal interference from a 50 Hz ambient light as well as from the detector power supply.

The fibre coupling efficiency was about 25 % and ~60 mW of optical power was coupled into the optical fibre at the start of the fabrication process. The transmitted power dropped from this value to about 54 mW while the reflected power rose by approximately 6 mW. These results corresponding to a grating formation of about 10 % reflectivity could be improved by using photosensitive fibres which however were not available at 514.5 nm. The HB450 (Hi-Bi) fibre with a cut-off wavelength of 449 nm was placed in a tube pressurised with hydrogen for a period of at least a week, a process known as hydrogen loading for increasing the photosensitivity of the optical fibre. When laser light was launched into the hydrogenated fibre launch efficiencies of less than 10 % were achieved which were not sufficient for grating fabrication. The fibre tended to glow and it lost its birefringence from an original extinction ratio of 1:400 to about 1:2. After a period of two weeks the fibre regained its birefringence and original launch efficiencies of the order of 25 % were obtained. This effect has not been reported before and the cause is currently not known.

The results in Figure 7.3 were obtained from the experimental configuration of Figure 7.2. The growth in the reflection and the decay in the transmission signals are complimentary and thus indicate the formation of the grating. The experiment was stopped before these signals were in saturation and this resulted in a weak grating. Longer exposure times tended to result in grating erasure. The temperature monitor showed temperature excursions of the order of $\pm$ 0.6^0 C and this could explain why longer exposures tended to wash out the gratings.

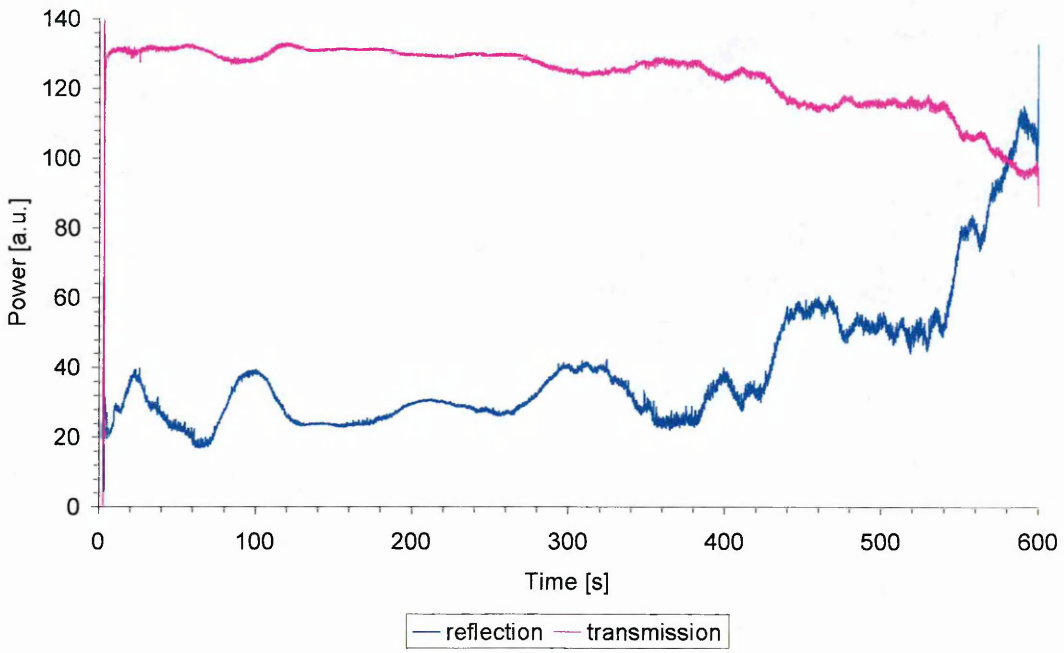

Figure 7. 3: Real time transmission and reflection signals through the fibre during grating formation.

Graph (a) of Figure 7.4 shows that the laser power during the time the results of Figure 7.3 were captured was fluctuating about a constant average value of about 5.5 (a.u.). The vibrations of the laser head due to the cooling water may have caused these power fluctuations. Figure 7.4 (b) displays the real time signal of the stability of the launch efficiency, which shows a drift or oscillation of about 5% of the total launched power. The argon-ion laser power at the front face of the fibre was about 240 mW, which was high enough to generate heat to damage the fibre face thereby resulting in launch efficiency variation as revealed by the HeNe laser signal. Figure 7.4 (c) shows temperature excursions of $\pm$ 0.7 ^{0}C throughout the data acquisition period. There is no noticeable correlation between features in the temperature plot and the growth of the Bragg grating. The temperature fluctuations of the fibre could be due to the heating up of the fibre by the laser beam apart from environmental temperature fluctuations. Strong gratings can only be obtained under very stable temperature conditions of at least < 0.1 ^{0}C with 0.001 ^{0}C being ideal [3]. Such conditions may require the setting up of an active temperature stabilisation system for the fibre (Appendix F).

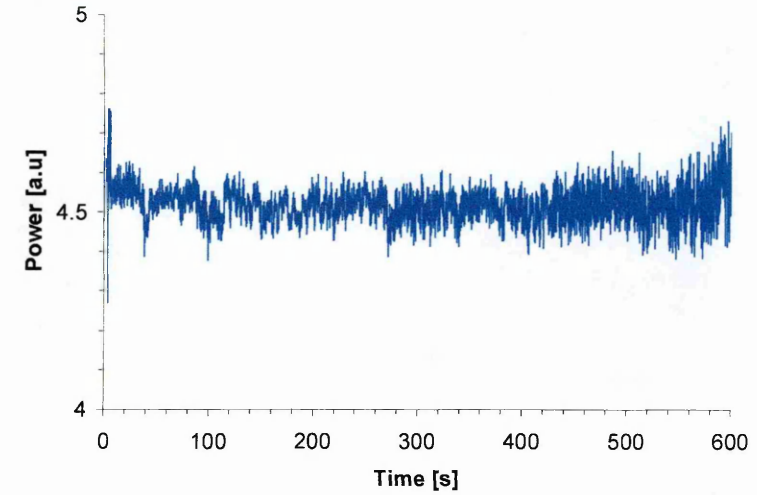

(a)

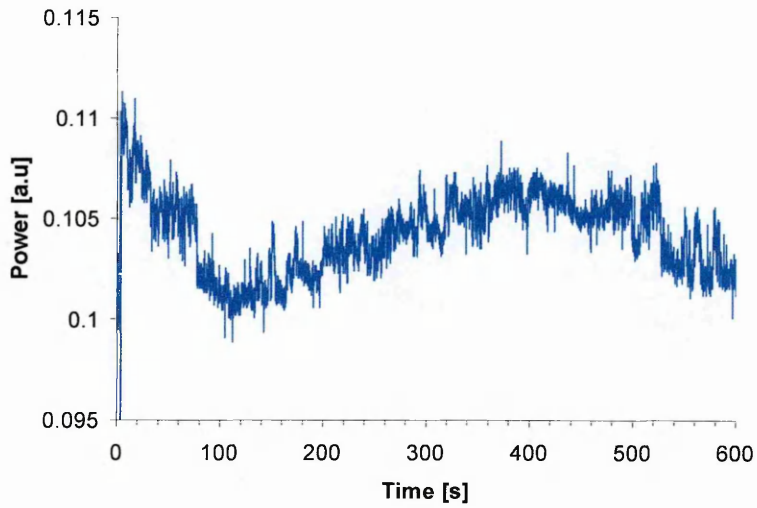

(b)

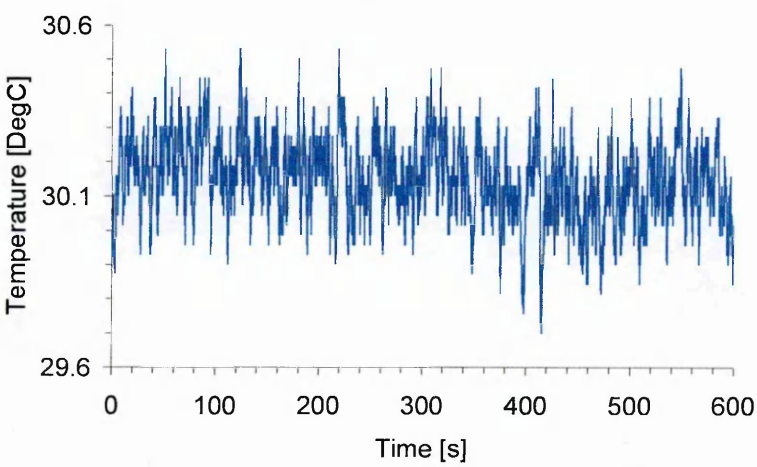

(c)

Figure 7. 4: Real time signals of (a) Argon-ion laser power and (b) He-Ne laser power monitors, and (c) Temperature of the fibre.

7.2.2 Characterisation of Filter Transfer Function

Described here are non-standard techniques that had to be adopted because there are no available commercial spectrometers with the required resolution to characterise the narrow-band filters that form the basis of this work. The grating transfer function could only be read after fabrication and this was done in two ways. Firstly the fibre was uniformly strained by application of a linear voltage ramp from a function generator (Stanford Research Systems DS345) onto a piezoelectric driven translation stage (Photon Control, type 17 PAS 013) over an extension span of about 1 μm for a 1 m length of fibre (i.e. 1 μstrain range) and this is done with the laser wavelength fixed at 514.5 nm. The function generator supplied a linear voltage ramp of amplitude 0.1 V to the piezo-controller (Photon Control, type MD3-75C) at a frequency of 0.001 Hz. Data capture at 10 Hz and processing was done by a program set up in LabView™. The relation between the frequency bandwidth, $\Delta\nu$, and fibre extension, ΔL, for a grating length, L, is given by [4]

$$\Delta\nu = -\left(1+\frac{1}{n}\frac{\partial n}{\partial s}\right)\cdot\frac{c}{\lambda}\frac{\Delta L}{L} \qquad (7.1)$$

where n is the refractive index of the fibre, c is the speed of light in vacuum, λ is the vacuum wavelength of the laser, s is strain and $(1/n)(\partial n/\partial s)$ is the elasto-optic coefficient given as -0.29 [4].

The second method took advantage of the fast jitter-stabilisation electronics of the laser that normally applies fast correction movements onto the piezo-controlled laser output coupler (see Chapter 6). This is adapted by applying a linear voltage ramp of 1.5 V amplitude from a function generator to allow scanning the laser wavelength through 180 MHz at a frequency of either 0.1 or 0.2 Hz. The method is capable of scanning through a maximum of 300 MHz and this can be done in a time as fast as 1 ms.

The results of Figure 7.5 (a) and (b) (calculated using Equation 7.1) show that the grating bandwidth is about 90 MHz (full width), which compares fairly well with a

theoretically calculated value of 100 MHz for a 1m-length grating. The approximate reflectivity from these graphs is 10%. The results of Figure 7.6 (a) and (b) give an approximate bandwidth value of 85 MHz. This method is not expected to give accurate values, as the initial strain of the grating (before application of the voltage ramp) can not be known accurately. Furthermore these graphs are noisy and this is probably due to non-uniform extension and relaxion of the optical fibre. This could be caused by e.g. fibre material property behaviour, possible backlash in the motion of the strain rig and possible hysteresis in the piezo-electric element.

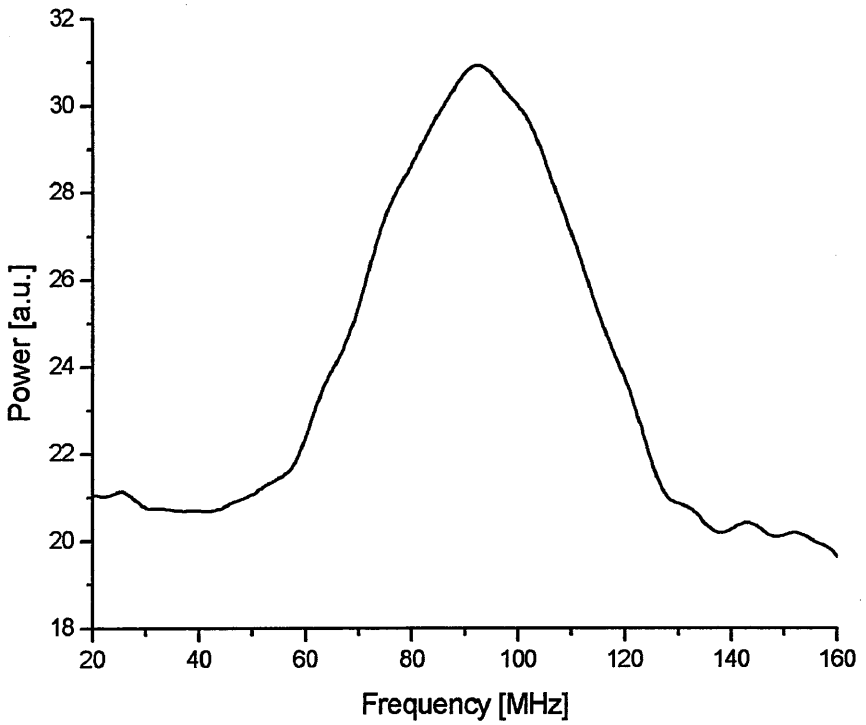

(a)

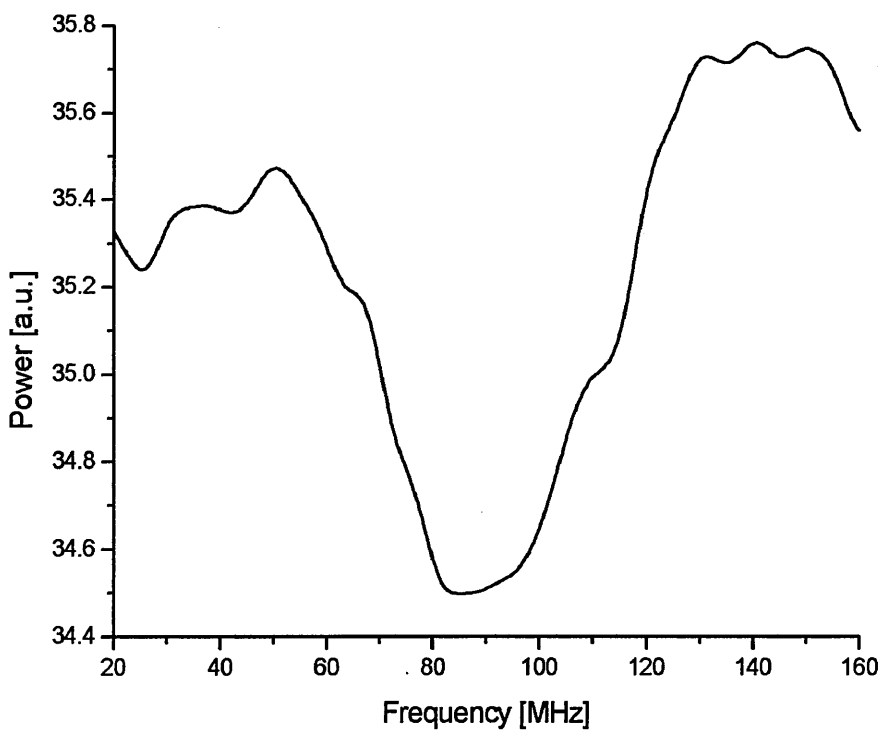

(b)

Figure 7. 5: A strain scan of the spectral bandwidth of the grating in (a) reflection mode and (b) transmission mode.

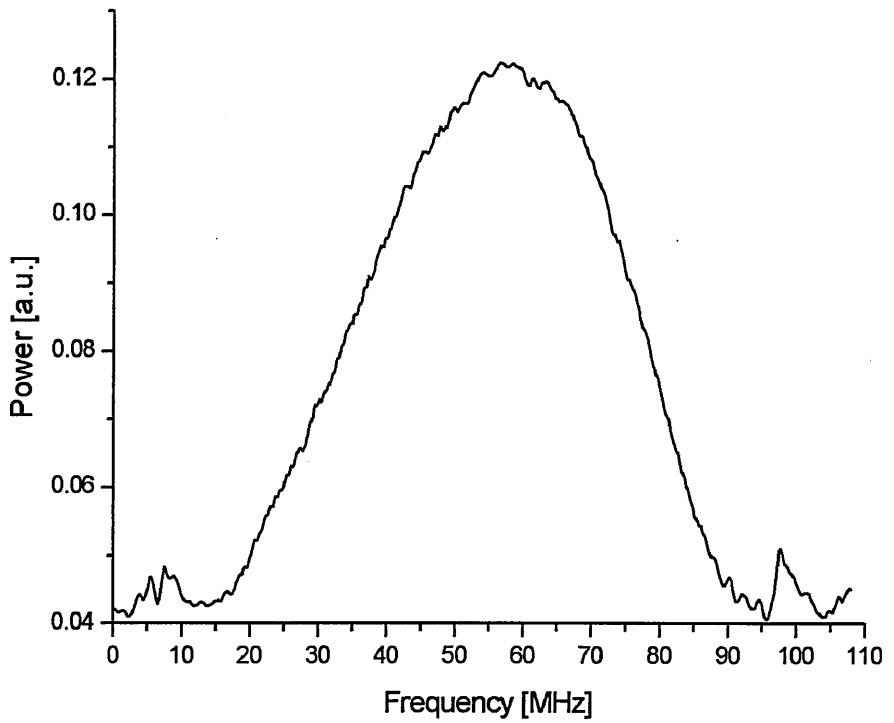

(a)

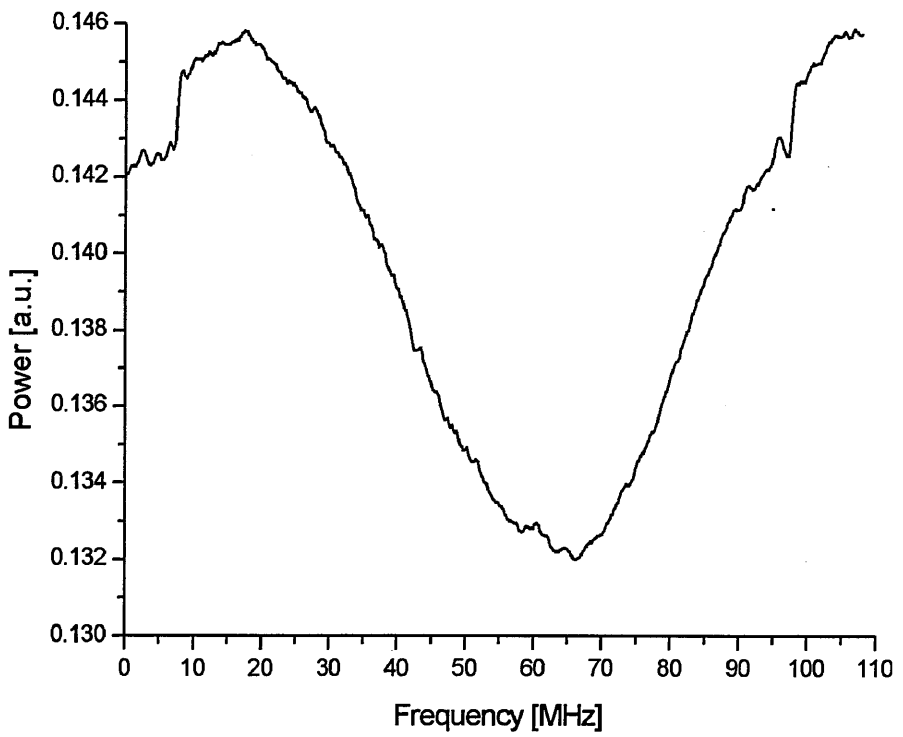

(b)

Figure 7. 6: Laser scan of the spectral bandwidth of the grating in (a) reflection mode and (b) transmission mode.

Experiments were also carried out on a fibre sample from Andrew Corporation (fibre number 881206B) believed to be photosensitive at argon-ion wavelength. The fibre has a cut-off wavelength of 436 nm and has elliptical core of diameters 1 and 2 μm but no dopants were specified. The small sized core meant that the launched laser power was always going to be small unless the coupling optics was redesigned. A launched power of 30 mW was not enough to reveal any photosensitivity of the fibre.

Manufacturer	*Fibre Type*	*Core Diameter* μm	*Cladding Diameter* μm	*Cut-Off Wavelength* nm
Fibrecore	SM450	4	125	402
Fibrecore	SM450	4	125	449
Fibrecore	HB450	8	125	450
Andrew Corp.	No. 881206B	1 x 2 (elliptical)	60	436

Table 7. 1: Types of optical fibre used and their parameters

7.3 UV Written Bragg Gratings and Interferometers

The method of grating fabrication had to be changed since high reflectivity could not be obtained with the method of end-pumping. There are no photosensitive optical fibres around the argon-ion laser wavelengths that are used in this technique and furthermore the demands on the temperature and laser stability are very high. It was therefore decided to move to the side-writing technique using UV radiation. This process is via a single photon absorption (unlike the 2 photon for the end-pumped grating) (Chapter 4) and so high reflectivities are easily obtained and could even approach 100 % if the fibre was hydrogenated.

7.3.1 Filter Fabrication

A fibre Bragg grating (FBG) was fabricated interferometrically using an ultra-violet (UV) beam at 245 nm in a holographic side writing technique (Figure 7.7) [5]. The IR

beam from an injection seeded Nd: YAG laser was frequency doubled and used to pump a dye laser: Injection seeding improves the coherence length and the beam profile. The dye laser output was frequency doubled to 320 nm. This output was then sum frequency mixed with residual 1064 nm YAG light that produces tuneable UV light from 240 to 260 nm. A phase mask (manufactured by Lasiris was 1 inch in diameter and had a pitch of 896 nm) was used to provide two diffracted beams that were focussed by separate cylindrical lenses to interfere in the core of a single mode fibre over an overlap length of 3 mm. The fibres that were used are manufactured by Fibrecore and have cut-off wavelengths of 402 and 449 nm (Table 7.1). The optical fibre was soaked in hydrogen gas pressurised at 150 bars and maintained at room temperature for a period of up to two weeks to enhance its photosensitivity prior to fabrication.

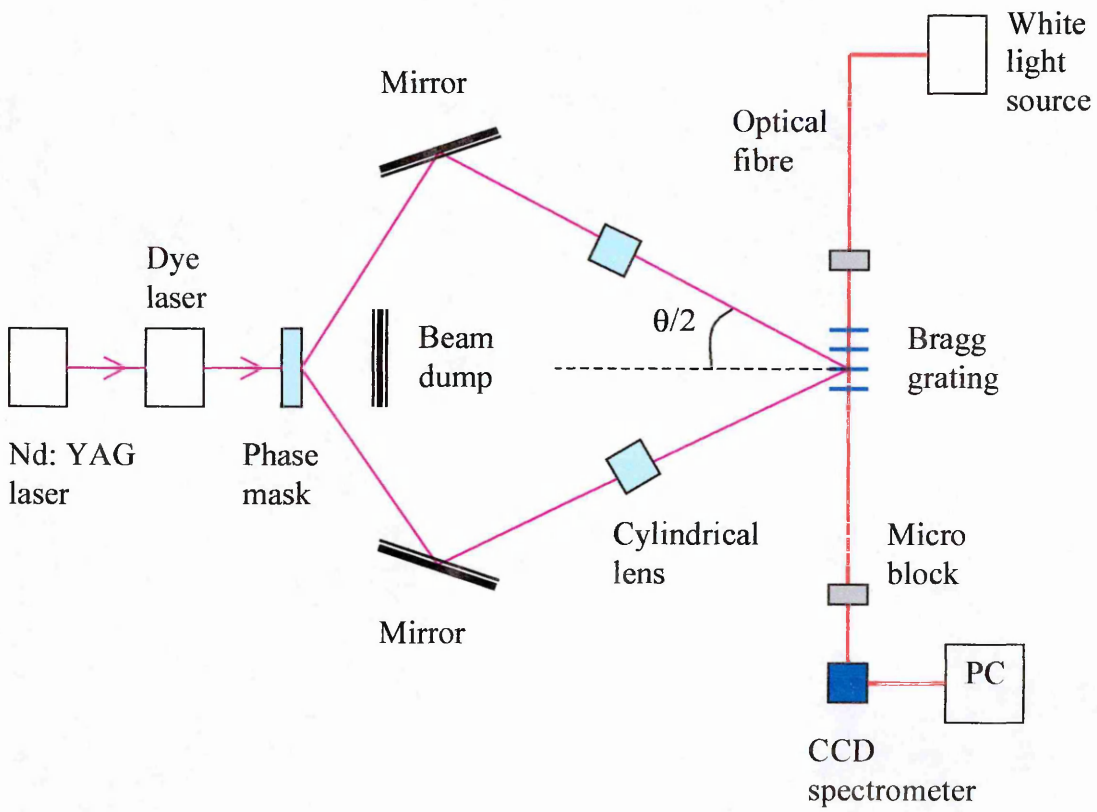

Figure 7. 5: Schematic of an interferometric Bragg grating fabrication facility.

PC – personal computer.

The normal procedure to read the grating during formation is to use a directional coupler and monitor in real time the profile of the signal received in reflection. This

however could not be used as power losses in the FC/PC connectors and mismatch of the fibre cores of the directional coupler and that of the grating resulted in insufficient signal detection. The transmission of the grating was then monitored using a white light source and a charge coupled device (CCD) spectrometer (Ocean Optics, type S200) with a wavelength range of 350 - 850 nm (Figure 7.7). The spectrum of the first grating was stored in the program (that runs the CCD spectrometer) and was used as the reference signal for the second grating.

The inclination of each beam to the horizontal axis (θ/2) was calculated using equation (7.2) [6] determined from the fringe spacing of the interference pattern.

$$\lambda_B = \frac{n\lambda_{UV}}{\sin(\theta/2)} \qquad (7.2)$$

This half angle was calculated to be 48.9^0 for a Bragg wavelength, λ_B of 514.5 nm with n taken as 1.47. Such a large angle resulted in the fibre position being very close to the cylindrical lenses and this caused problems in alignment. The fringe spacing is reduced (and hence the Bragg wavelength is shortened) by increasing the value of θ. A grating was written in one position before translating the fibre through a desired distance to write the next grating with approximately the same conditions thereby constituting a Fabry-Perot interferometer.

The cut-off wavelengths for the optical fibres used in the graphs of Figure 7.8 and Figure 7.9 are respectively 402 nm and 449 nm. The grating parameters chosen in both cases were expected to give a bandwidth of about 250 MHz for an optimised FP cavity. The grating reflectivity was at least 40 % but the grating bandwidth as measured in Figure 7.9 is not reliable, as the resolution of the CCD spectrometer used in the fabrication of the grating was only 0.3 nm. A 3-mm long grating with a reflectivity around 50% is expected to have a bandwidth of around 0.2 nm.

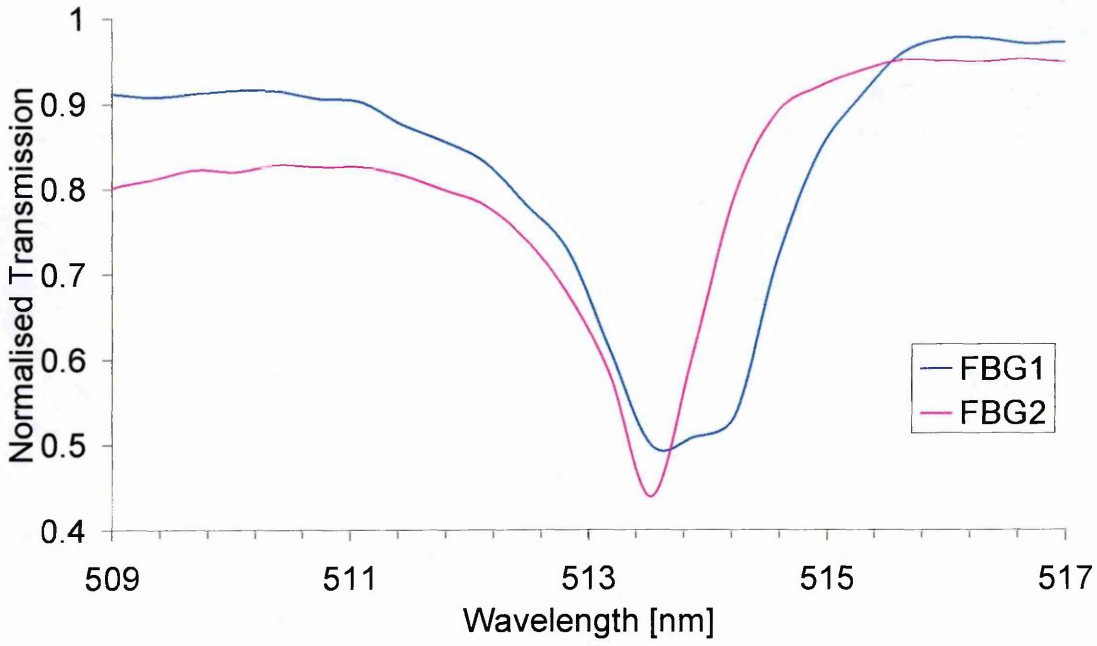

Figure 7. 6: The two FBGs are each of 3-mm in length separated by 7 cm to form a FP cavity.

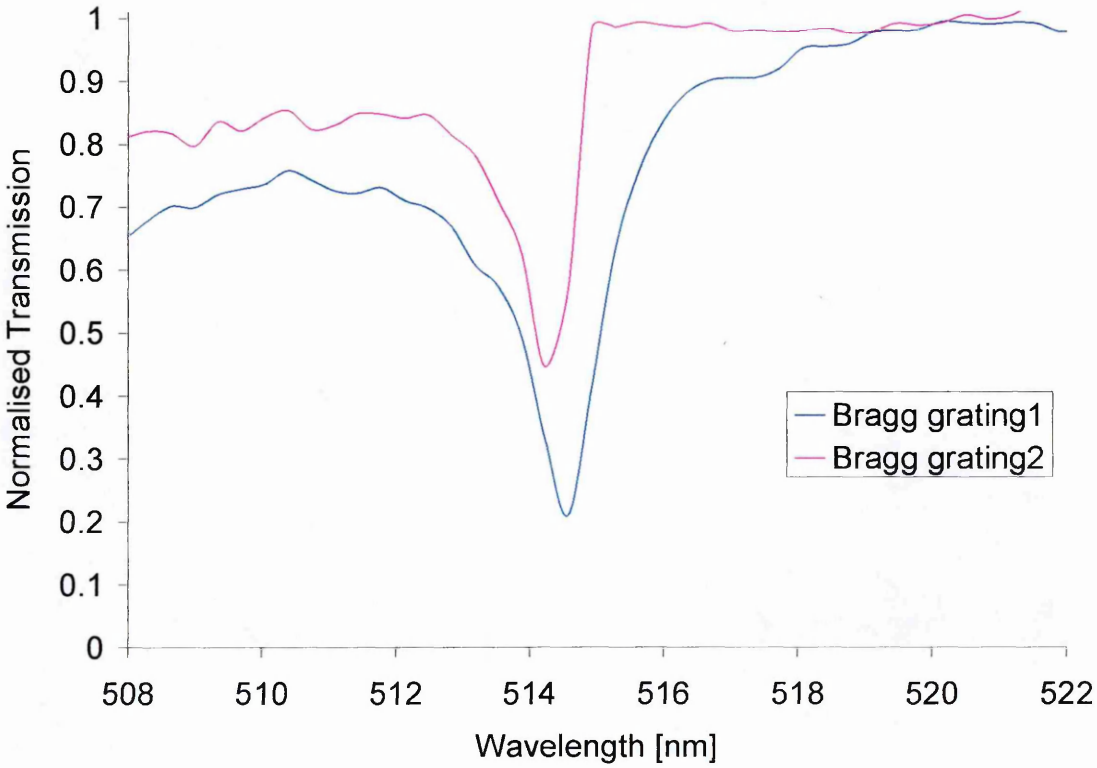

Figure 7. 7: The two FBGs are each of 3-mm in length separated by 6.3 cm to form a FP cavity.

The side exposure technique does not guarantee identical gratings despite the use of same configuration and beam dose. The reason for which could be the change in the tension of the fibre when translated to write a new grating in a different location. Also temperature fluctuations and vibrations may result in a change of the beam profile and wavelength. The two gratings of the Fabry-Perot filter will always differ in centre-wavelength, index modulation and bandwidth. The gratings fabricated would normally have a bandwidth of approximately 0.2 or 0.3 nm if no chirp were incorporated. This narrow bandwidth would normally result in the two gratings partially overlapping in wavelength and thus the FP interferometer will not be optimised but will have low finesse. Such was the case with all the gratings that were fabricated for the argon ion laser wavelength of 514.5 nm. This problem could be avoided by fabricating wider bandwidth Bragg gratings of at least 1 nm bandwidth with of course consequences of lower index modulation. This however could not be done for gratings at 514.5 nm as the interferometer beam angles were so large that the cylindrical lenses were very close to the fibre leaving no space for the introduction of optics for chirping. It is necessary to accurately determine the transfer function of each grating and obtain accurate values of the centre wavelengths and bandwidths in-order to determine their wavelength separation. Such a procedure makes it possible to determine the amount of strain that can be applied to one or both grating(s) in-order to overlap their centre wavelengths and bandwidths and thus form a Fabry-Perot interferometer with optimised finesse.

7.3.2 Fabry-Perot Filter Transfer Function

The transfer function of the FP interferometer could be obtained by either scanning the laser wavelength while keeping the FP cavity fixed or by strain modulation of the FP cavity while keeping the laser wavelength fixed. The features and operation of the laser system are discussed in Chapter 6.

7.3.2.1 Laser scan

Two methods were possible for scanning the laser wavelength while keeping the fibre Fabry-Perot undisturbed. One method involved heating the intra-cavity Fabry-Perot

etalon to change the laser wavelength by up to 2 GHz or even more by offsetting the starting position. A linear voltage ramp of 0.5 V amplitude supplied from a Stanford function generator was applied to the etalon through the Z-lok electronics that are normally used for wavelength stabilisation. This technique was however unreliable for such a sensitive device as the fibre Fabry-Perot interferometer as the method required at least 2.5 hours to scan over 2 GHz. Any attempts to scan faster would cause the laser to mode hop. Any problems with mode hops, laser power glitches, or changes in fibre temperature and its environment over such long scanning periods rendered the technique unworkable. A faster scanning technique was therefore required.

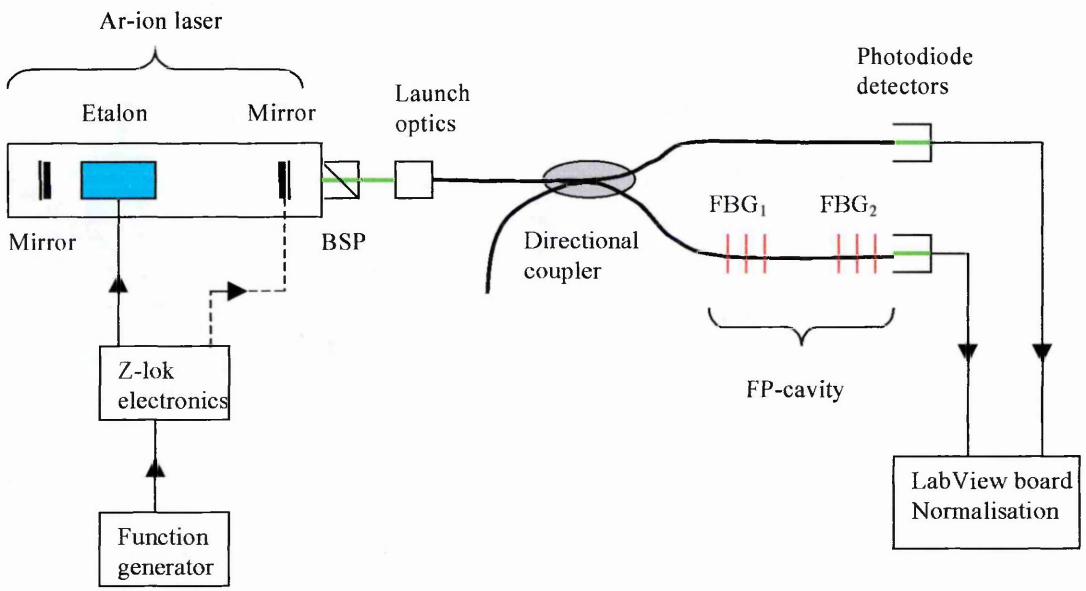

Figure 7. 8: Schematic of the laser-scan experiment.

BSP – beam splitter (99:1), FBG – fibre Bragg grating, and FP – Fabry-Perot

The second technique improved on the scanning period as up to 300 MHz could be scanned in a time duration of the order of a millisecond. A linear voltage ramp of amplitude 10 V from a Stanford function generator was applied to the laser output coupler (piezo-electric driven) through the J-lok electronics that are normally used to correct for wavelength jitter. The technique was time consuming since an offset in the starting point of a scan was required in-order to increase the scanning range. The fibre FP could not be read after covering over 14 GHz in frequency. The small power fluctuations in the laser due to the movement of the output mirror also hindered the

observation of the FP signal. The method was tedious and the system was noisy so that it had to be abandoned.

7.3.2.2 Grating Scan

The technique requires that the laser wavelength be fixed while the filter is strain modulated over a known wavelength bandwidth. The initial set up involved fixing the fibre consisting of a 6.3 cm cavity Fabry-Perot filter to two-translation stages 10 cm apart using superglue such that the two gratings could be strained simultaneously (Fig.7.11).

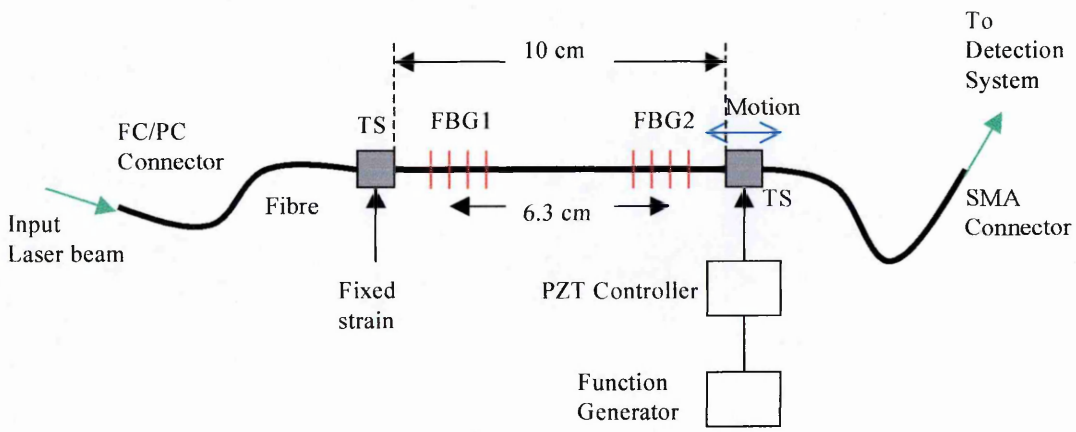

Figure 7. 9: Experimental arrangement for fibre FP characterisation by strain modulation of the whole cavity.

The symbols TS, FBG and PZT respectively represent the translation stage, fibre Bragg grating and the piezoelectric transducer.

The second grating, FBG2, had a centre wavelength shorter than that of FBG1 (Figure 7.9) and a pre-strain was necessary to increase the Bragg wavelength by 0.15 nm (a voltage of 2 V) to match it to the wavelength of the laser and to the Bragg wavelength of FBG1. The application of an amplitude modulation to the strain of the cavity made it possible to characterise the fibre Fabry-Perot cavity. A triangular or saw-tooth voltage modulation, 0.313 V in amplitude was applied from a Stanford function generator to one of the piezo-controlled translation stages at a modulation frequency of 0.1 Hz. This scanned the filter through a wavelength bandwidth of 0.02 nm. An applied voltage of 5 V corresponds to 100-μm movement of the translation stage, which for a 10-cm fibre is

equivalent to 1000 μstrain. The pre-strain however affected both gratings such that FBG1 was actually being detuned from the required optimum condition. This and the small free spectral range variations caused by modulating the whole cavity produce low visibility fringes, which were rather noisy. The experimental arrangement of Figure 7.12 was then adopted to improve on the quality of the filter transfer function.

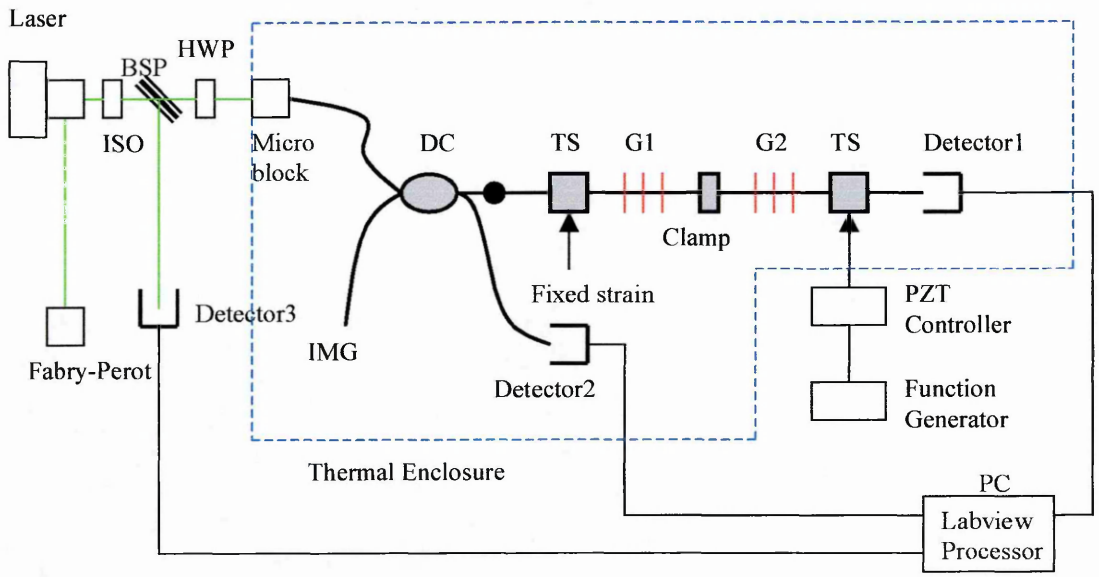

Figure 7. 10: Fibre Fabry-Perot filter characterisation system employing strain modulation.

ISO – optical isolator, BSP – beam splitter (90:10 ratio), HWP – half wave plate, 514 nm directional coupler, IMG – index matching gel, TS – translation stage, G1 and G2 – gratings.

In the experimental arrangement of Figure 7.12 the translation stages were kept at 10 cm apart but a clamp 1 cm wide was glued to the middle of the cavity. The glued section of the fibre had its plastic jacket removed. Any thermal expansion in the block would cause undesirable variations in the free spectral range of the filter. The length of fibre each translation stage could move was reduced to only 4.5 cm and consisted of one grating only. It was then possible to fix the Bragg wavelength of one grating at the laser wavelength throughout the experiment. The second grating was initially pre-strained to the wavelength of the laser before applying a small strain modulation in-order to observe the FP transmission profile. The scan rate was increased from 0.1 Hz to 2 Hz so that dephasing effects contributed to by laser wavelength variation, temperature effects

and additional interferometric cavities formed between fibre connectors could be resolved. All the fibres in the system were polished and connectorised by FC/PC connectors and refractive index matching gel was used to minimise the formation of additional reflecting cavities in the system.

Originally the system was implemented without the half wave plate and thermal isolation on the directional coupler. The fibre FP signal amplitude was found to drift rather slowly with time at a rate approximately between 0.1 and 1 Hz. The directional coupler (specified as non-polarising) was tested and found to be considerably polarisation sensitive with an extinction ratio of 1:400. The half wave plate was then introduced to maintain the polarisation of light transmitted to the fibre Fabry-Perot filter. The directional coupler was also thermally isolated. The stability of the system improved to a few minutes, which allowed accurate measurements to be taken. The residual drift in the system could be caused by the laser frequency drift and phase changes of the filter. The introduction of the directional coupler in the system further reduced the overall noise by normalisation of signals from detector1 and detector2. Detector3 served to monitor the stability of the laser output power.

Fibre Directional Coupler (Supplied by Laser2000)	
Description	FSMC-514-50
Bandpass	± 10 nm
Wavelength	514.5 nm
Polarisation extinction ratio	1:400
Split ratio (measured)	46:54
Numerical aperture	0.11
Mode field diameter	3.4 μm

Table 7. 2: Fibre directional coupler parameters.

The graph of Figure 7.13 is the result of a transfer matrix simulation of a fibre FP filter with the above experimental setting that was modelled in Fortran90. The free spectral range is calculated to be 1.55 GHz which compares closely to 1.59 GHz for a cavity that is assumed to be bulk optic, and to the experimental value of 1.57 ± 0.02 GHz. The

visibility is approximately 88 % that also compare very well to 89 % for a bulk optic cavity. This visibility is much higher than that observed in Figure 7.14, which means the FP cavity could still be tuned to optimum settings.

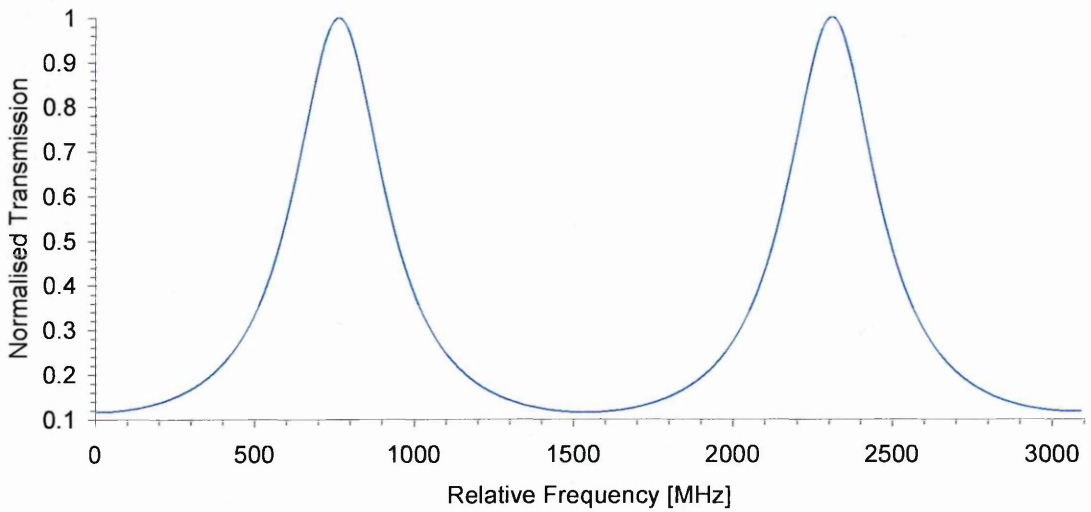

Figure 7. 13: Normalised transmission function of a 63 mm cavity FP filter with Bragg grating reflectivity of 40 % obtained by the theoretical transfer matrix model (Chapter 5).

7.3.2.3 Filter Tuning

The FP filter spectrum can be strain-tuned to effectively change the finesse, visibility, bandwidth and slope of the transfer function. These are important features for the velocimetry application discussed in Chapter 9. Figure 7.14 shows some of these properties. Different levels of pre-strain have been applied to the second grating, G2 (Figure 7.12) before the application of an amplitude modulation and this gave different filter transfer functions as indicated by Figure 7.14. The transfer function of the green graph gives a visibility of 15 %, frequency bandwidth (full width) of 1.27 GHz, 0.62 GHz (FWHM), finesse of ~2.6 and a slope of 0.5 $[GHz]^{-1}$. These have been obtained with the second grating, G2 in Figure 7.12 pre-strained by 0.2 nm and followed by a strain scan through a wavelength bandwidth of 0.02 nm. The graph in purple has a more linear transfer function. The visibility and gradient has increased to 22 % and 1.4 $[GHz]^{-1}$ respectively while the full bandwidth decreased to 0.67 GHz, (FWHM of 0.27 GHz) and finesse increased to ~6. The graph in blue has finesse of ~3, full bandwidth of

1.41 GHz, FWHM of 0.51 GHz, and approximately 22 % visibility while the slope is 1.29 $[GHz]^{-1}$.

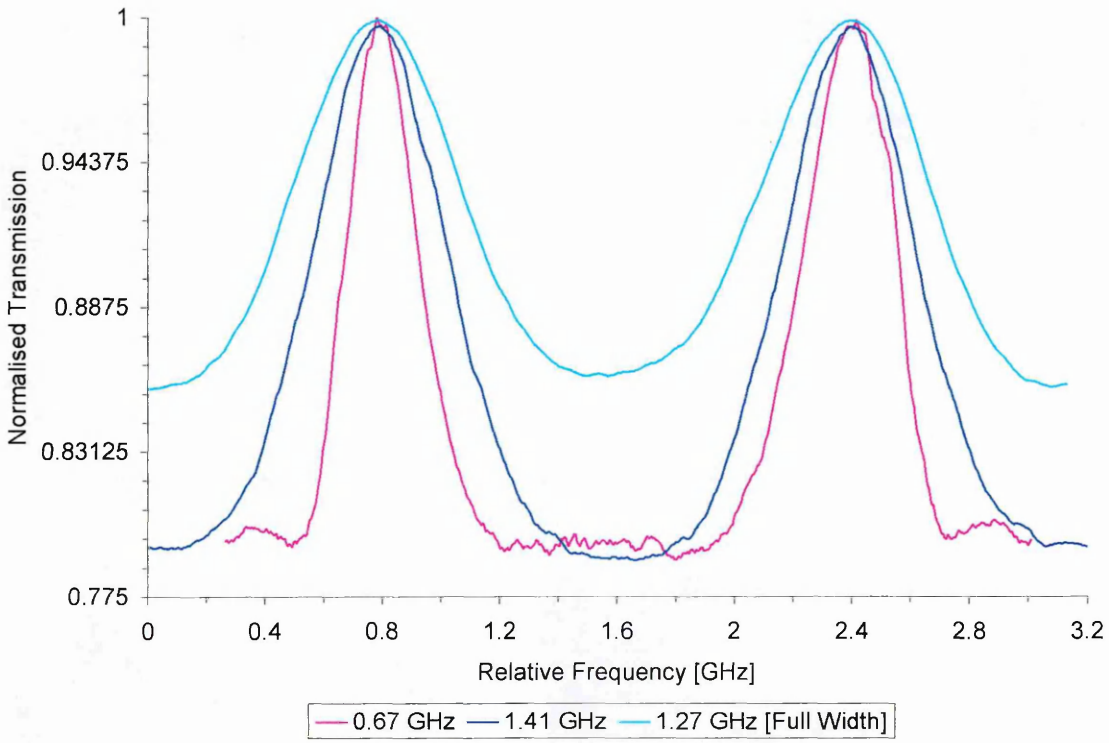

Figure 7. 14: Comparison of the normalised transmission functions of a FP filter obtained by the experimental configuration of Figure 7.12 showing the tuning property.

Graph	*Finesse*	*Visibility [%]*	*FWHM [GHz]*	*Full bandwidth [GHz]*	*Gradient* $[GHz]^{-1}$
Green	2.6	15	0.62	1.27	0.5
Purple	6	22	0.27	0.67	1.4
Blue	3	22	0.51	1.41	1.29

Table 7. 3: Summary of the results of Figure 7.14 for the tuning of the fibre-optic FP by application of strain.

It can be noticed that the lowering of the finesse of the filter leads to low contrast and thus poor signal to noise ratio for the measurements. The implication of this is to limit

the maximum measurable velocity range while not compromising the signal to noise ratio.

7.4 Summary

This chapter presented the fabrication experiments of two types of filters namely the length limited Bragg grating and the Bragg grating based Fabry-Perot interferometer. The most important feature of these filters is their small frequency bandwidth, which can be of the order of a few hundred MHz making them suitable for velocimetry applications that is discussed in Chapter 9.

The formation of a length-limited grating is negatively influenced by environmental perturbations and thus proper thermal isolation is mandatory. One advantage with the filter is that it forms at the exact argon ion laser wavelength of 514.5 or 488 nm and thus requires no further tuning when used in laser Doppler velocimetry. One set back with the filter is that it forms throughout the whole length of fibre and so any form of temperature stabilisation will have to be applied to the whole length of fibre. Fabry-Perot interferometers can however be made as small as a few centimetres, which is easily stabilised against temperature or any dephasing effects (Chapter 8). The filters do not form at the exact laser wavelength owing to the alignment problems but can be easily tuned to the laser wavelength by applying small amounts of strain. The visibility of both types of filters is not so high owing to the fibres being non-photosensitive at the lower wavelength of the argon-ion laser. The UV fabricated filters can however use hydrogen-loaded fibres to enhance the photosensitivity. More control over the parameters of these filters may be obtained by using well-designed phase masks. The current technique writes Bragg gratings with about 0.2-nm bandwidth and it would be desirable to use a chirped phase mask in order to increase this bandwidth and thus improve upon the tuneability of the FP interferometer after fabrication. The mask also gives a precisely defined centre wavelength.

The tuneability of the frequency spectrum of the filters has been discussed in terms of bandwidth, gradient and visibility. The implications of these parameters on the velocity

measurement are to provide adjustable measurement resolution, sensitivity and velocity range respectively (Chapter 9).

References

[1] F. Ouellette, D. Gagnon, and M. Poirier, "*Permanent photoinduced birefringence in Ge-doped fiber*", Applied Physics Letters, vol. 58, no. 17, 1991.

[2] J. Stone, "*Photorefractivity in GeO_2 – doped silica fibers*", Journal of applied Physics, vol. 62, no. 11, 1987.

[3] B. Guo and D. Z. Anderson, "*Undepleted pump regime of Hill grating formation in optical fibers*", Applied Physics Letters, vol. 60, no. 6, 1992.

[4] B. S. Kawasaki, K. O. Hill, D. C. Johnson, and Y. Fujii, "*Narrow-band Bragg reflectors in optical fibers*", Optics Letters, vol. 3, no. 2, 1978.

[5] M. L. Dockney, S. W. James and R. P. Tatam, "Fibre Bragg gratings fabricated using a phase mask based interferometer and tuneable UV source", Measurement Science and Technology Rapid Communications, vol. 7, pp. 445 - 458, 1996.

[6] R. Kashyap, "*Fiber Bragg Gratings*", Academic Press, 1999.

CHAPTER 8

Experimental Signal Drift

8.1 Introduction

The Fabry-Perot interferometer that is made up of two Bragg gratings in a single mode optical fibre is prone to phase drift. Bragg-grating devices form good temperature and strain sensors [1] thus temperature fluctuations and vibrations around the gratings will cause the phase to drift. The laser wavelength drift in the case of an unstable or insufficiently stabilised laser may also introduce indistinguishable effect. The intended use of the interferometer as a spectroscopic filter requires a very high degree of stability otherwise the spurious phase drift would impress upon false velocity information. Discussed in this chapter are two techniques that were designed to perform active control of the laser wavelength and the phase of the interferometer by two independent electronic-based feedback systems.

8.2 Principles of Automatic Process Control

In many plants or process systems, process variables are required to follow, or hold, some desired value. This control is achieved by manipulating plant actuators. Figure 8.1 shows the basis of an automatic process control system. A control algorithm looks at the desired value, the actual value and possible outside influences affecting the plant, and on the basis of these observations adjust the plant actuators to bring the process variable to the desired value. The control algorithm is designed to cope with circumstances where the process variable may be affected by disturbances and/or a desired value that may be changing continuously. Control strategies range from the simplest bang/bang servo to sophisticated proportional-integral and derivative (PID) controllers [2, 3].

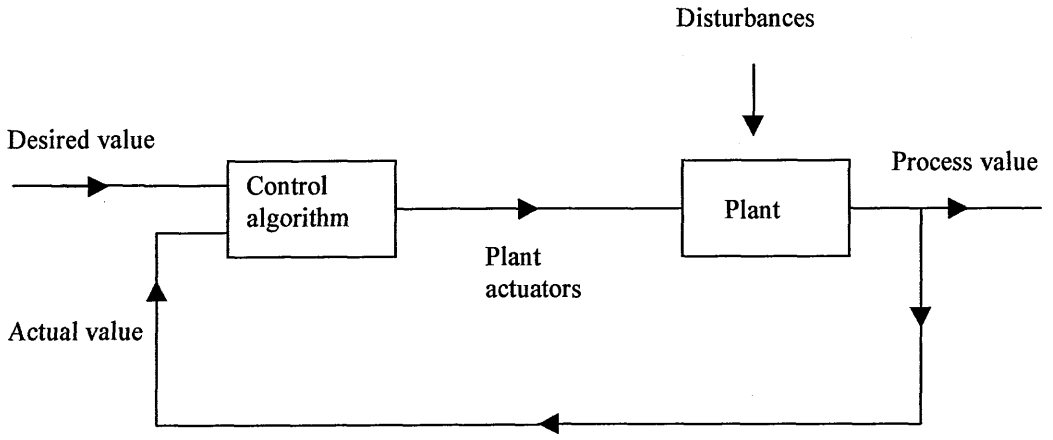

Figure 8. 1: Principle of automatic process control.

An on/off servo turns the control power on when the process variable falls below the desired value and off when it goes above. Such a control system thus maintains the process variable at the desired value by cycling power. However even in the steady state the process variable oscillates about the desired value and will therefore be insufficient for precision control.

Precision control in well designed closed loop feedback systems was desired for laser wavelength and fibre FP interferometer automatic control, otherwise the act of control could further destabilize the system. It was required that there be a large corrective action when the error is large and a small corrective action when the error is small. Such a control forms the basis of a proportional control (P) system (Figure 8.2) characterized by an adjustable gain factor K, which is an amplification factor of the error signal. The range over which the controller operates is known as the proportional band (PB) expressed as percentage. Proportional control compensates partially for disturbances and together with the presence of losses, an offset error will occur in the steady state.

A proportional controller will therefore require some form of automatic reset to remove the offset error. A scaled time integral of the error is therefore necessary to bring the error to zero, which constitutes what is known as an integral controller. A combined controller is thus known as proportional plus integral (PI) control. The integral controller is characterized by the integral time, T_i the inverse of which is the gain M.

The integral action is increased by decreasing the integral time, which will however tend to destabilize the system [4].

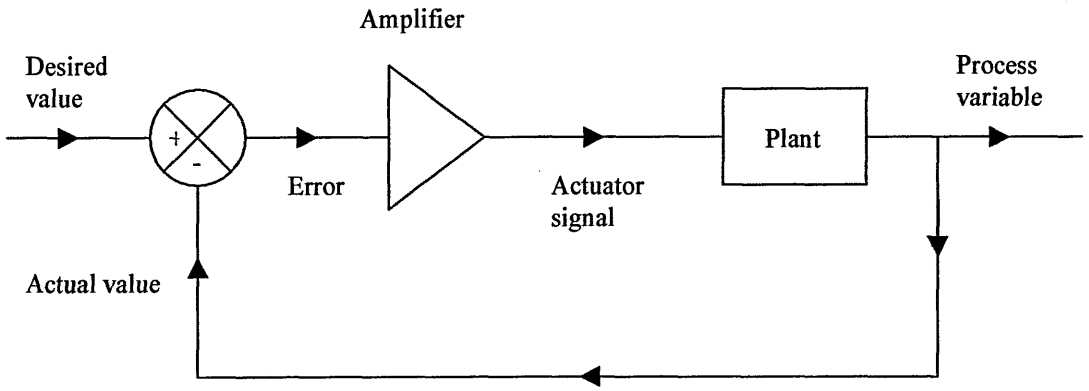

Figure 8. 2: Proportional control system.

A controller based on P and I actions is dependent on the magnitude of the error and thus any disturbance to the plant may take a long time to eliminate particularly if the inertia of the plant is high. An additional control action is therefore desired that is capable of anticipating, to some extent, the control action required and compensates for the inertia induced lag. It is desirable to base this action on the rate of change of error and apply appropriate corrective action. Such a system forms the basis of a derivative action in a controller. The derivative control action is characterized by a derivative time T_d and the longer this time is the more contribution the derivative action will have on the output actuator signal.

A 3-term controller i.e. PID would bring the process variable to its desired value without overshoot in the shortest possible time. Two such controllers were designed for the laser wavelength and fibre FP interferometer phase stabilization. The adopted process control is illustrated in the block diagram of Figure 8.3. The plant represents the argon-ion laser or the fibre-optic Fabry-Perot (FP) interferometer for the two independent control systems described in this chapter. The transducer for a wavelength stabilization system is the combination of the iodine cell and the photodiode detectors. The FP filter, photomultiplier tube detectors and the lock-in amplifiers form the transducer for the phase control system. The etalon and the piezoelectric translation stage are actuators for the laser wavelength and FP phase control systems respectively.

The actual value which is the transduced process variable is compared to the desired value i.e. subtracted to get the error signal. The integral and proportional actions operate on the error signal while the derivative action operates on the actual value and the results of the 3 actions are added together and acted upon by an amplifier of some gain *K*. The derivative control thus monitors and controls only changes in the process variable. The control algorithm is represented by the equation (8.1) [4].

$$V_{control} = K\left(E + \frac{1}{T_i}\int E \cdot dt + T_d \cdot \frac{dPV}{dt}\right) \qquad (8.1)$$

The actuator signal is given by $V_{control}$ where E is the error signal, PV is the process variable and t is the time variable.

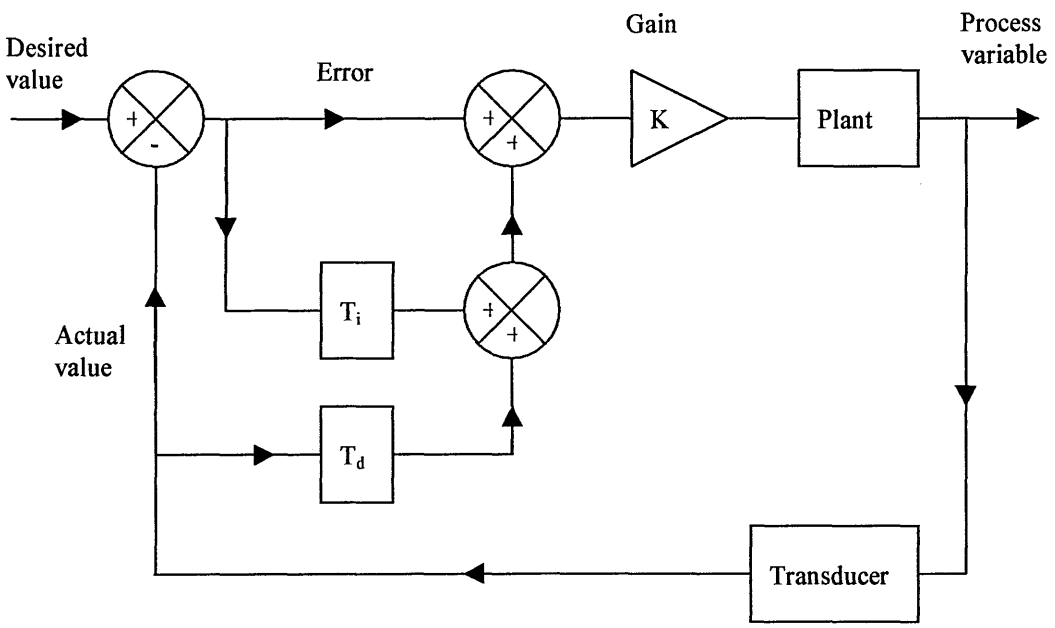

Figure 8. 3: PID control for closed loop feedback system.

8.3 Laser Wavelength Control System

The argon-ion laser (Spectra Physics Model 2060-10) consists of two independent frequency stabilisation mechanisms namely the Z-lok and the J-lok for slow and rapid frequency drifts respectively (Chapter 6). The stabilised laser would have a linewidth of

about 3 MHz and overall residual jitter of 2 MHz. The frequency-temperature coefficient of the laser is 50 MHz/ ^{0}C and typical drifts of the order of 600 MHz were observed over typical time duration of about 2 hours that depended on the temperature environment. This drift and jitter in the centre wavelength of the laser is required to be a minimum particularly as the laser Doppler velocimeter requires that a point on the flank of the filter transfer function be accurately tuned to the laser wavelength and remain stable over the measurement period (Chapter 2). In addition the fibre-optic Fabry-Perot (FP) filters used in this work (Chapter 7) had narrow frequency bandwidths whose typical tuning range was 400 to 800 MHz, small enough to cause high sensitivity to wavelength fluctuations. An additional active feedback stabilisation system was therefore desired to deal with the frequency drift mainly caused by temperature drifts.

8.3.1 The Wavelength Servo

The author would like to acknowledge Dr David Nobes (Cranfield University) for providing the iodine cell and the associated proportional-integral-derivative (PID) temperature controller that was used in the locking system described here. An active feedback control-loop was designed to lock the laser wavelength to a 50 % transmission point on a Doppler broadened absorption line of molecular iodine vapour enclosed in a glass cell [5]. Figure 8.4 illustrates the schematic of the experimental layout in which a single mode directional coupler with a split ratio of 50:50 was used to provide two signals. This coupler was polarization insensitive and was not used in the velocimeter because the fourth arm had broken off. The iodine cell (Chapter 6) consisted of a main body that was maintained at 55 ^{0}C and a cold finger at 40 ^{0}C, a condition that resulted in a maximum depth and slope of the absorption line (Figure 8.5). Two photodiodes (BPX65), one looking through the iodine cell placed in one output arm of the coupler and the other in the second output arm, were used as detectors.

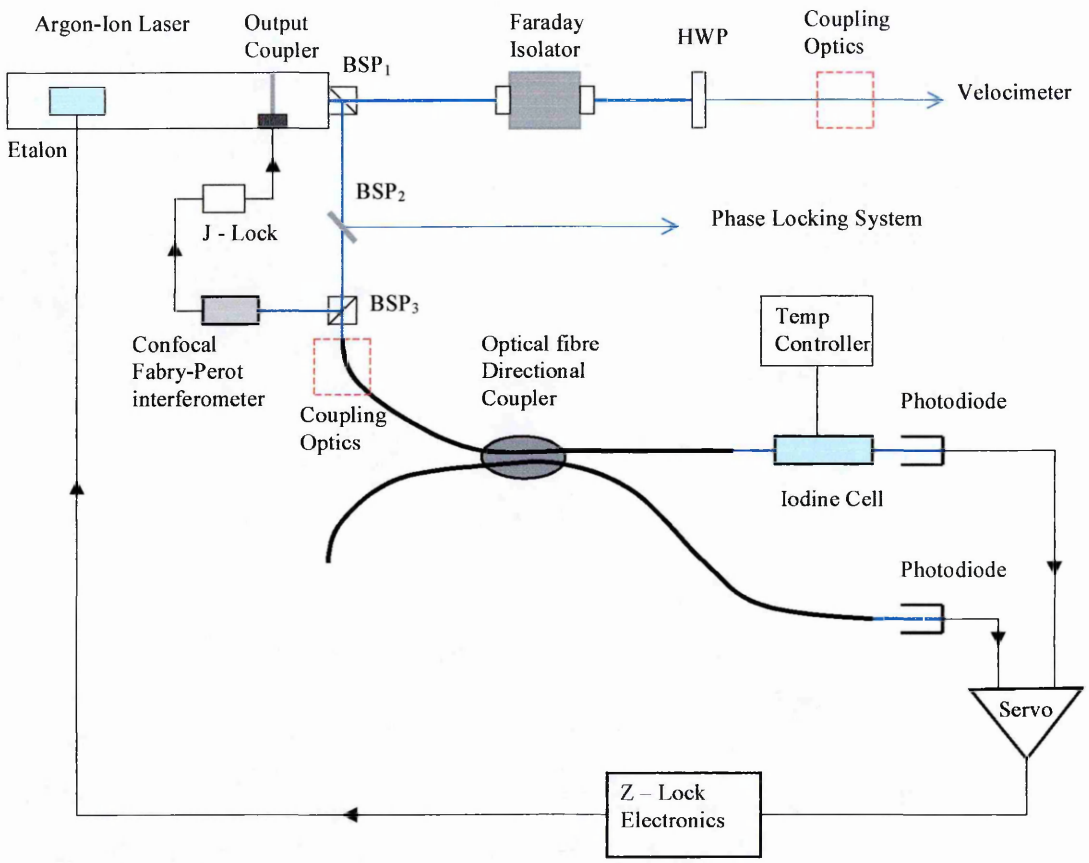

Figure 8. 4: Schematic of an active wavelength stabilisation system of the argon-ion laser.

HWP – half wave plate, BSP_1 (99:1), BSP_2 (50:50) & BSP_3 (50:50) – beam splitter cubes.

The outputs of the photodiodes were connected to a custom designed electronic controller. The first stage of this controller consisted of an analogue divider circuit that normalised the two detector signals to remove laser intensity fluctuations as well as dark noise with the remaining fluctuations accounting for the laser wavelength change. The next stage of the circuit generated an error voltage that was proportional to laser wavelength fluctuations or drift. Three other circuits acting as proportional, integral and derivative controllers were designed to act upon the generated error voltage, the result of which was fed-back to the laser via the existing Z-lok electronics of the laser. The Z-lok electronics generated a voltage that either heated or cooled the intra-cavity Fabry-Perot etalon thereby adjusting its cavity length. The details on the electronic circuit designs and components used are discussed in Appendix D.

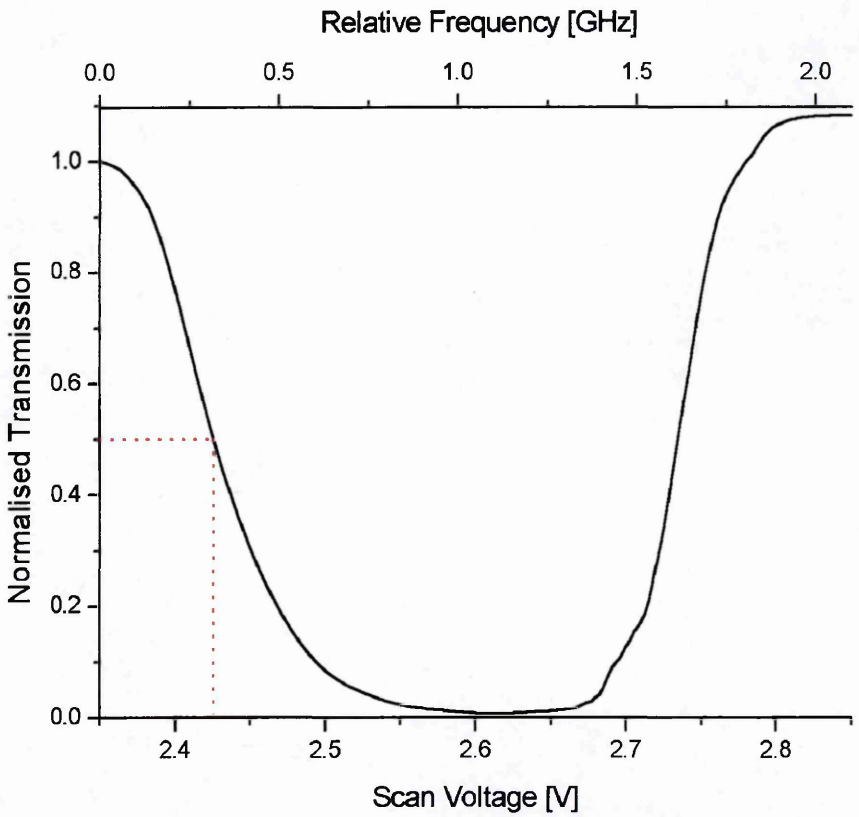

Figure 8. 5: The iodine absorption line showing the locking point at the intersection with the dotted lines.

8.3.2 Closed-Loop Response Curves

The control range required was 1 GHz i.e. ± 500 MHz of frequency corresponding to a voltage control of 0.24 V. The accuracy of control was required to be 0.72 mV which is equivalent to a frequency of 3 MHz. The ratio of iodine transmission to control voltage was determined to be 9.3 per volt (Figure 8.5) which converts to 0.002 change in transmission per 1 MHz change in frequency. Figures 8.6 and Figure 8.7 show examples of the various responses of the laser to different locking actions. The laser could be brought into lock mode in about 10 minutes but higher stability was achieved by increasing this time e.g. to 30 minutes as in Figure 8.7 (a). The laser could be locked to within 10 MHz for at least an hour.

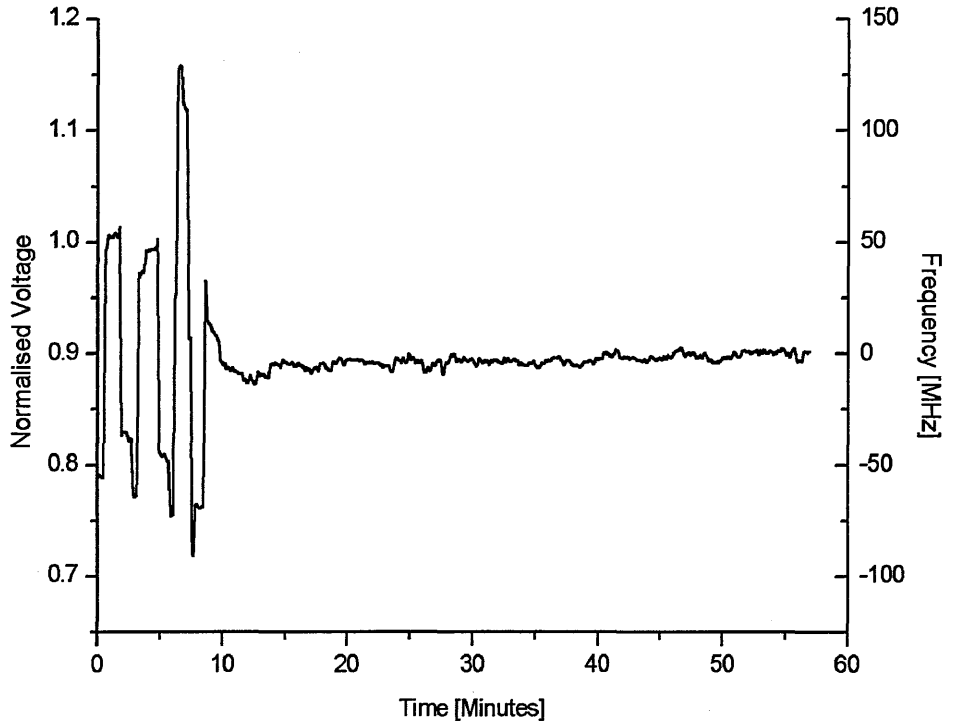

(a)

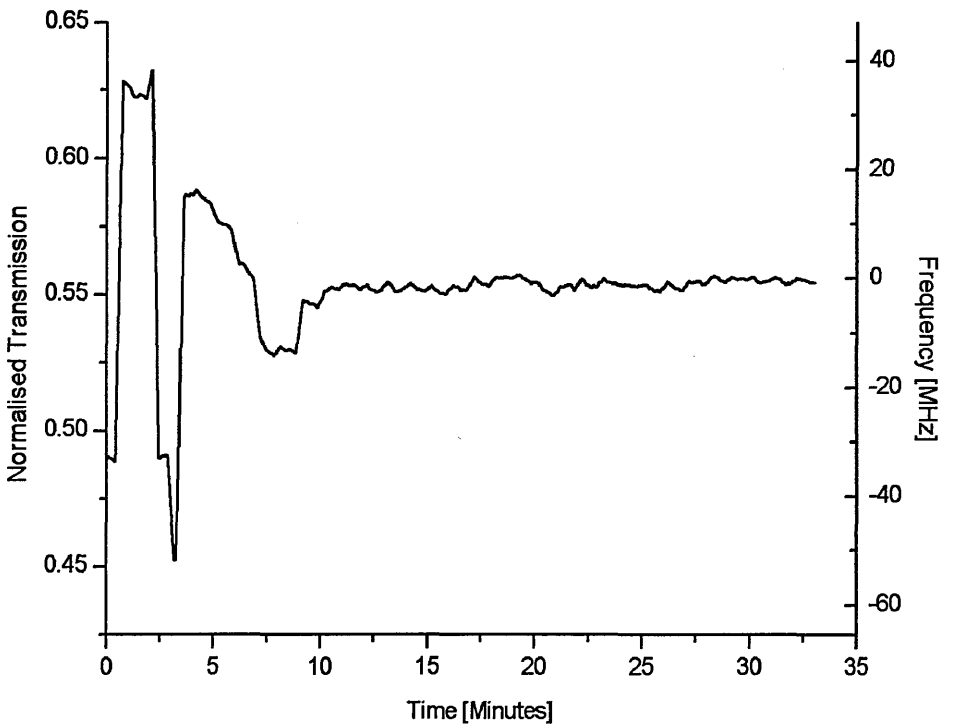

(b)

Figure 8. 6: Closed-loop feedback-control signal response given by the iodine cell transmission for the (a) Proportional and (b) integral control actions to the laser wavelength.

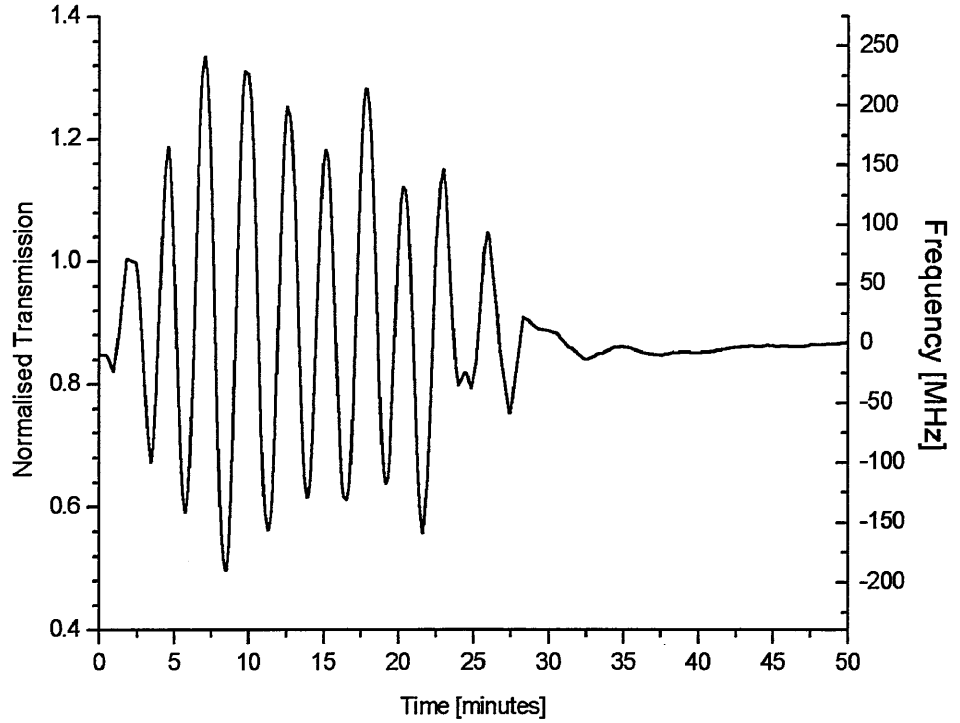

(a)

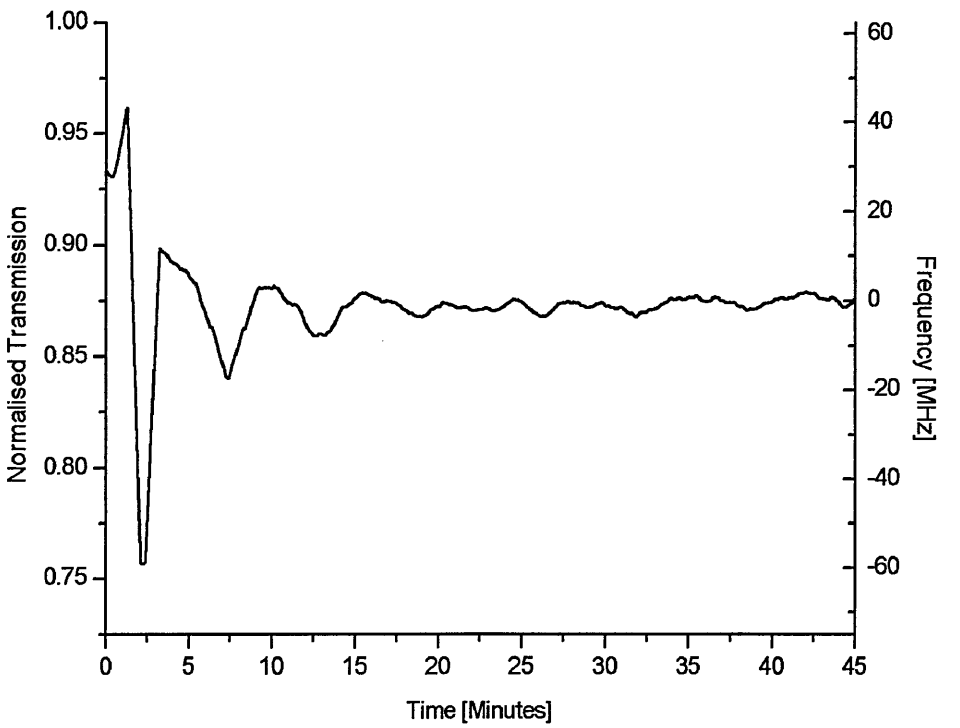

(b)

Figure 8. 7: Closed-loop feedback-control signal response given by the iodine cell transmission for the PID control action to the laser wavelength for (a) slow settling time (30 minutes) and (b) faster settling time (~ 10 minutes).

8.4 Interferometer Phase Control System

8.4.1 The Phase Drift

The output of the Fabry-Perot interferometer was found to fade with time, a consequence of phase drift. This drift was recorded even with the laser wavelength active stabilisation engaged. The drift could partly be removed by using a thermal shield made out of polystyrene placed around the interferometer. This drift was apparent even during the scan of the interferometer used to determine its transfer function. Figure 8.8 through to Figure 8.10 shows the recorded drift during a spectral scan of the interferometer that shows an overall drift of one free spectral range.

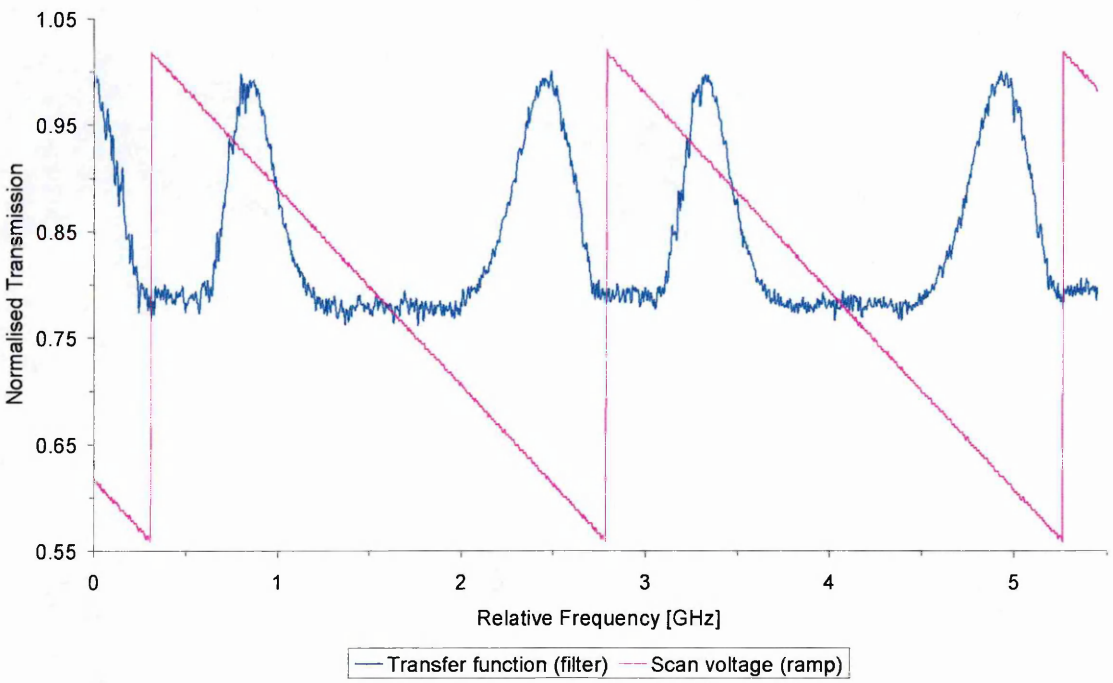

Figure 8. 8: Initial transfer function of a fibre-optic FP cavity under a strain scan.

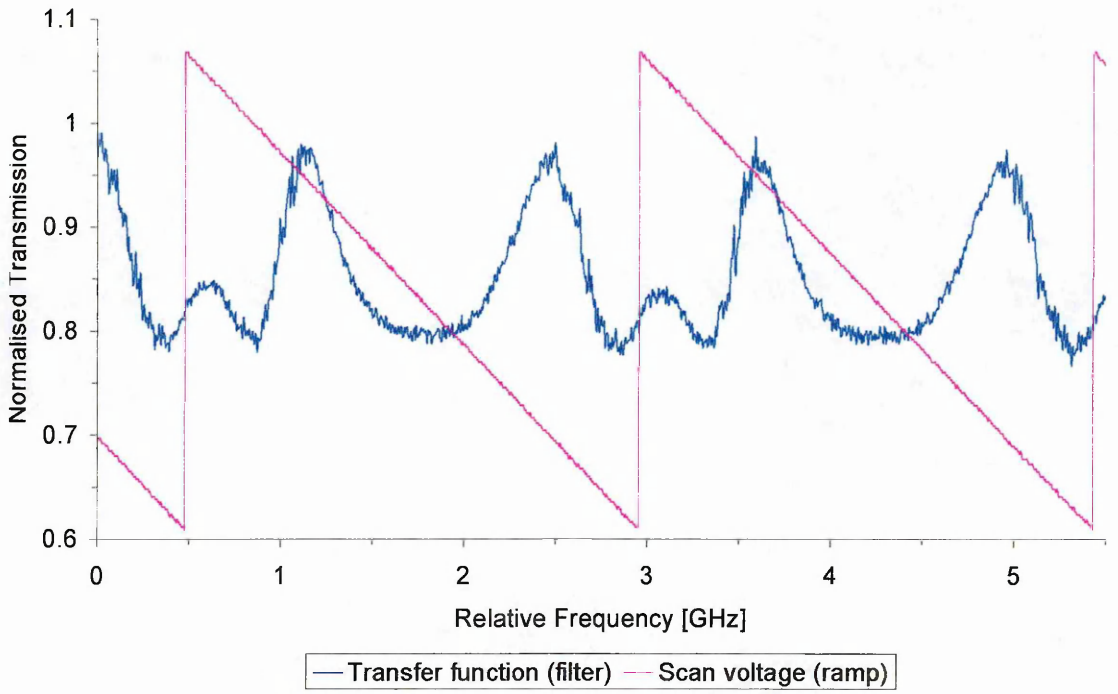

(a)

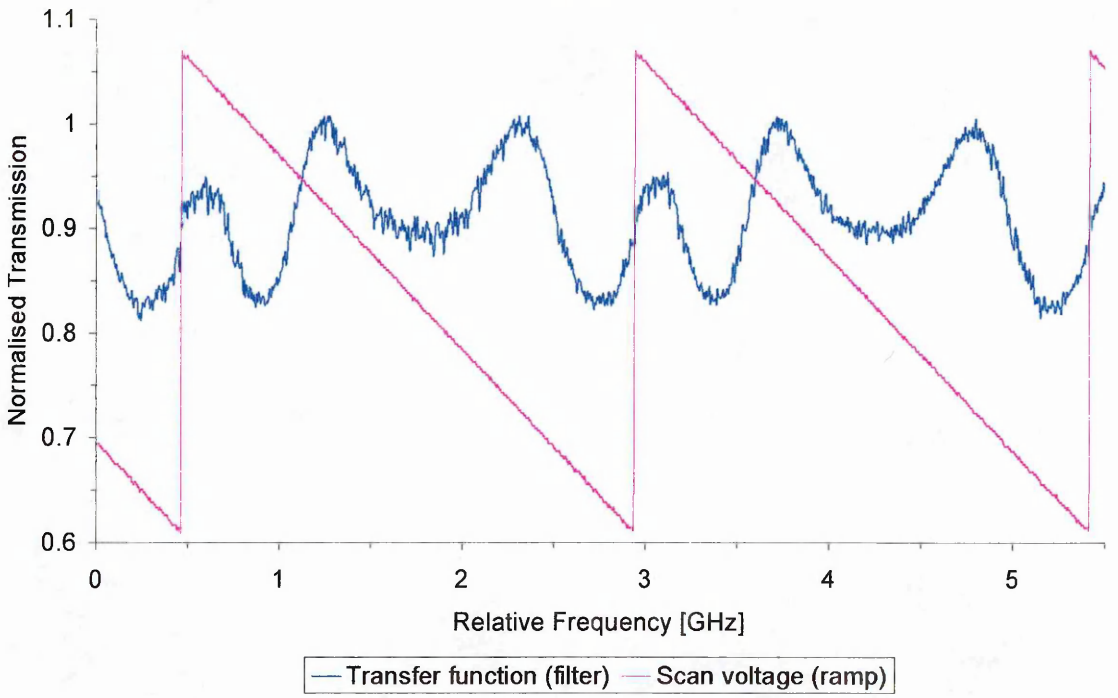

(b)

Figure 8. 9: The transfer function of a fibre-optic FP cavity (a) showing the onset of drift and (b) shows an increase in phase drift from that of (a).

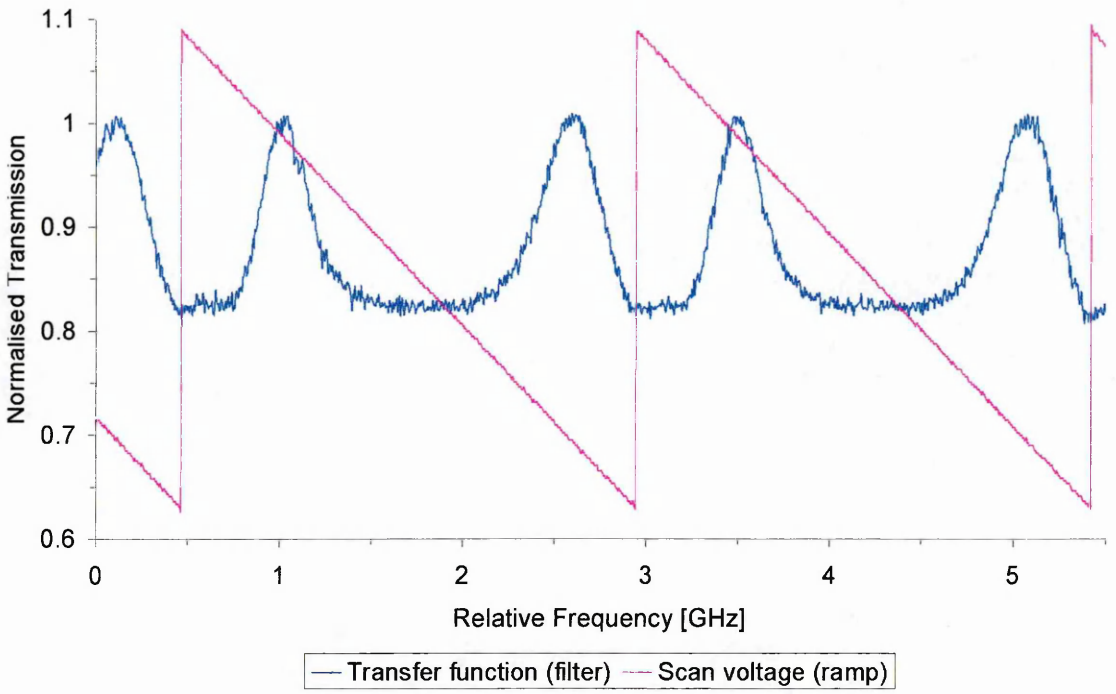

Figure 8. 10: The transfer function of a fibre-optic FP cavity that has gone through approximately 360 ^{0} phase drift and is nearly returned to that of Figure 8.8.

The filter transfer function was found to reset to its original form whenever a small offset strain was applied to one grating. The smallest step that could be obtained from a Stanford function generator was 0.01 V. A reset voltage of 0.01 V on the piezo-electric transducer controller changed the transfer function of Figure 8.9 (a) to that of Figure 8.10 nearly the same as the original function of Figure 8.8.

8.4.2 Closed-Loop Feedback Control

The ability to reset the transmission profile of the interferometer through small strain adjustments to one of the gratings of the FP interferometer whenever a phase drift occurred offered the possibility of an active control system. A simple feedback control system was therefore designed to lock the phase of the filter to the laser wavelength (Figure 8.11). This scheme, while compensating for phase changes due to temperature, relaxes the need to control the wavelength of the laser as the filter is automatically locked to track the laser wavelength. The scheme is based on phase detection with digital lock-in amplifiers (Stanford Research System model SR850) and custom

designed 3-term electronic controller for adjusting the strain level applied to the filter gratings.

A small amount of light from the argon-ion laser (< 1 μW) was effectively pulsed by passing it through an optical chopper at a frequency of 2 kHz (Stanford Research Systems model SR540) (Figure 8.11). The resulting pulse signal was coupled to one input arm of a single-mode fused fibre directional coupler (Fibrecore, type FSMC-514-50) at 514.5 nm wavelength having a split ratio of 50:50. The polarisation state controller, PSC_1 enabled the linear polarisation-state (vertical) of the input light to be matched to an eigenstate of the optical fibre by stress birefringence (Chapter 6). A polarisation beam splitter (PBS) placed at the output end of each arm of the coupler enabled the pulse signal to be detected by photomultiplier tubes, PMTsig and PMTref only (Figure 8.11). This automatically separated the pulse signal from the velocity signal that had been polarised orthogonally (horizontally) by use of PSC_2 in the second input arm of the coupler. The velocity signal from the flow was thus detected by photomultiplier tubes, PMT_1 and PMT_2.

The PMT signals were changed to voltage using current to voltage converters. The signals, PMTref and PMTsig were connected to two digital lock-in amplifiers, which were configured to lock the two signals in phase. The oscillator frequency that drives the chopper motor was connected to both lock-in amplifiers to provide a reference for locking purposes to cater for oscillator inconsistencies. The dynamic reserve of the lock-in amplifiers was set to maximum, the signal gain to 60 dB, and the time constant to either 100 ms or 300 ms. Any use of higher time constants produced a stable lock-in amplifier output but resulted in a feedback control system that was responding too slowly to the phase changes. The quality of phase detection was improved by using 24 dB/octave digital filters in the lock-in amplifiers. Digital filters occupy no space compared to analogue filters and hence more stages (4 or more) of low pass filtering can be used operating much faster than analogue filters that use a maximum of only 2 stages. Analogue filters provide only 12 dB/octave roll-off which is usually insufficient to isolate noise from the signal. The lock-in amplifiers voltage-output, proportional to

phase were divided using a software program set up in a personal computer (PC) consisting of a LabView data acquisition board (PCI-MIO-16E-4).

A proportional-integral-derivative (PID) electronic circuit was designed and set up to act upon the normalised lock-in amplifier signals that were output from the PC as an analogue signal (Appendix E). The circuit then generated an error signal that was fed-back to the piezoelectric driven translation stage of the second fibre Bragg grating, FBG_2 via a piezoelectric transducer (PZT) controller. A feedback voltage of 17.3 mV would move the FP interferometer through one free spectral range (FSR) and thus causing the translation stage to move by 0.173 μm.

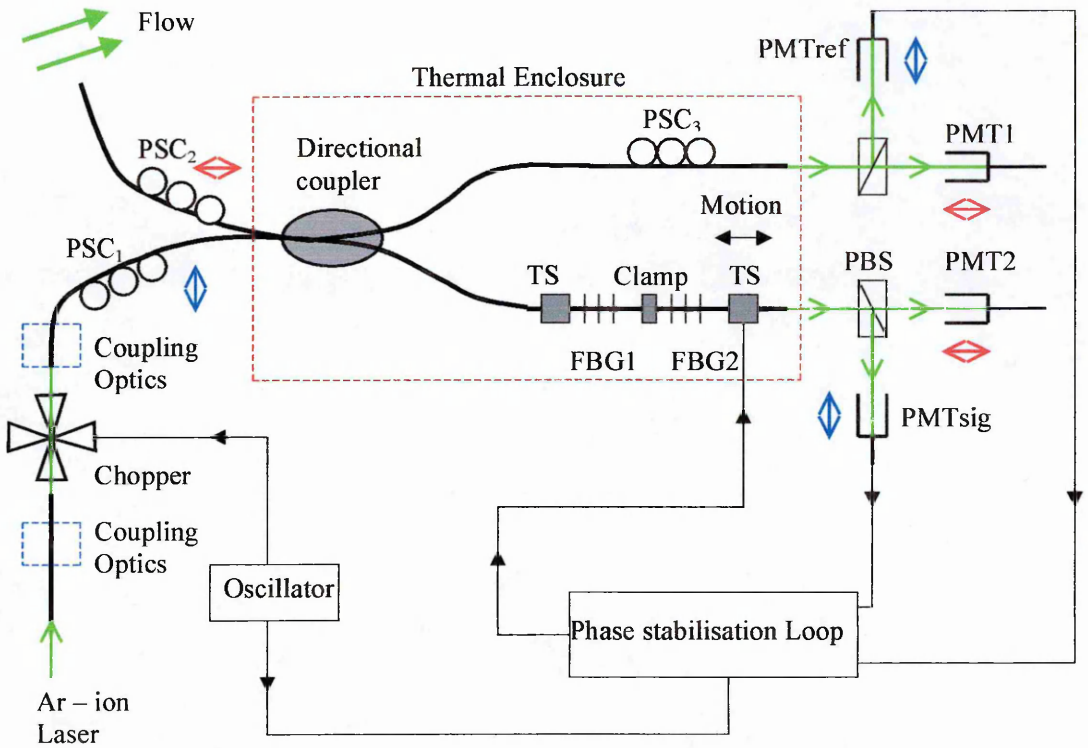

(a)

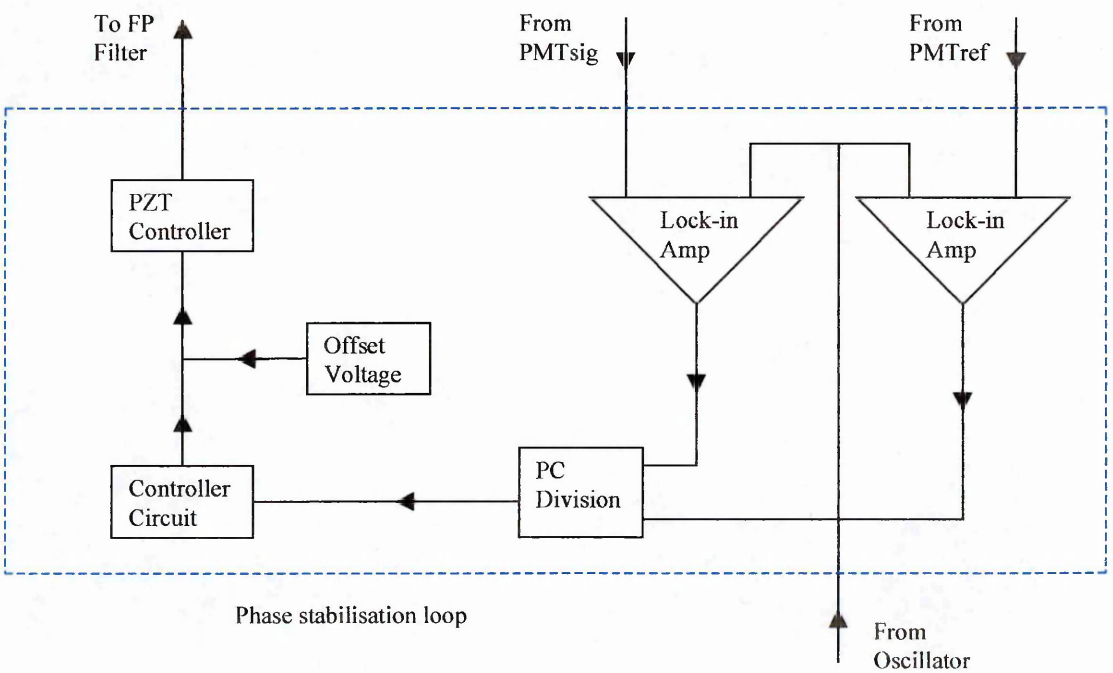

(b)

Figure 8. 11: (a) Schematic of an active phase stabilisation system for the fibre FP-filter and (b) the phase stabilisation loop for (a).

Mode hop-free locking for the FP filter was ensured by limiting the feedback voltage modulation to 5 mV, which corresponds to about 460 MHz of frequency span of the FP filter that corresponds to a traverse of 50 nm of the translation stage. An offset voltage on the PZT controller supplied by a function generator (Stanford Research Systems DS345) was required to tune the FP filter to 50 % transmission point of the transfer function, a requirement for directional discrimination in velocity.

8.4.3 The Circuit Time Constant

A reaction curve test of the phase-control system under open loop was adopted. This test, proposed by Cohen and Coon in 1953 [4] is one of many well-known tests in process control engineering that could be adopted. A step voltage of 0.05 V (ΔOP) (Figure 8.12) from the function generator was applied to the phase-loop system in open loop mode. This resulted in a change in the normalised lock-in amplifier signal or process variable (ΔPV) of about 0.12 V (Figure 8.13). A tangent is drawn to the process variable at the steepest point from which an apparent transit delay T_{delay} and apparent time constant T_c can be obtained. The controller settings for a full PID system are then given by [4]

$$PB = \frac{80 \cdot K_p \cdot T_{delay}}{T_c}\% \qquad (8.1)$$

$$T_{integral} = 2.5 \cdot T_{delay} \qquad (8.2)$$

$$T_{derivative} = 0.4 \cdot T_{delay} \qquad (8.3)$$

The parameters PB, $T_{integral}$, and $T_{derivative}$ are respectively the proportional band, the integral time constant and the derivative time constant. The process gain K_p is given by

$$K_p = \frac{\Delta PV}{\Delta OP} \qquad (8.4)$$

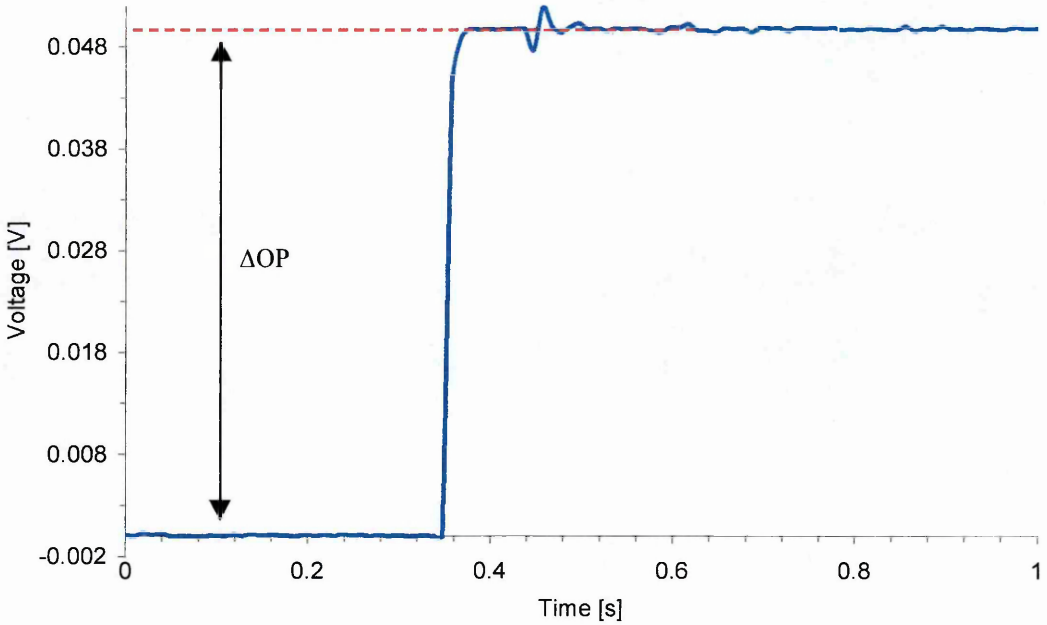

(a)

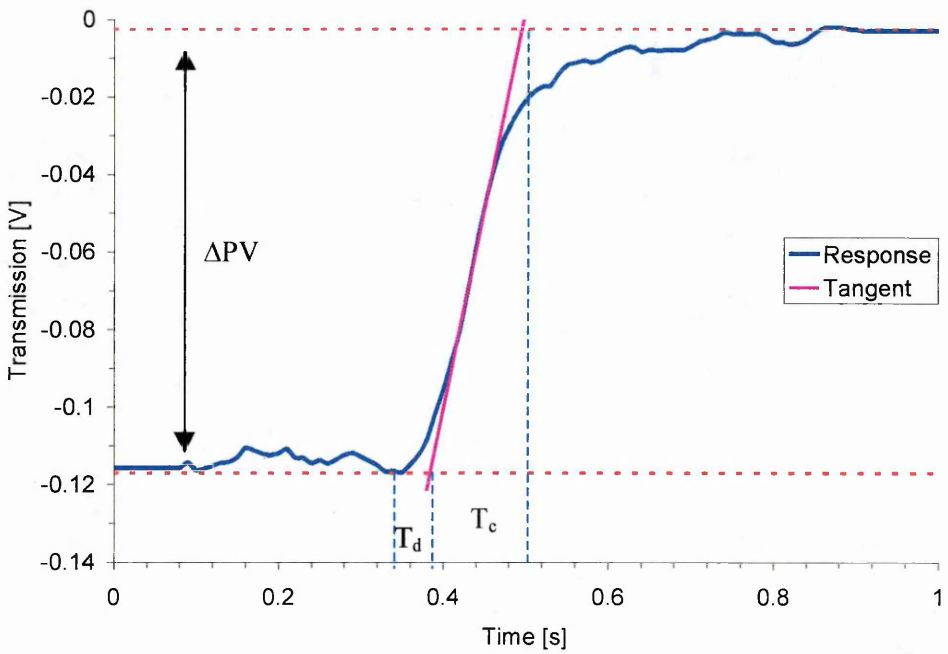

(b)

Figure 8. 12: Experimental results for (a) the step voltage used to drive the system in open loop mode and (b) the process variable showing the corresponding response of the control system in open loop mode subjected to this step forcing voltage.

The integral time-constant of the circuit was 0.22 s, derivative time-constant 0.04 s, and a proportional band of 77 %.

8.4.4 Closed-Loop Response Curves

The performance of the control loops depends on how well tuned the individual P and I actions are. The D action can only be tuned when used in conjunction with at least one other action. An integrated controller such as the PI, PD, ID or PID will still need further tuning if precision control is to be achieved and the tuning process may be time consuming. With the time constant of the integral action set to 0.22 s and 0.04 s for the derivative action as determined in section (8.4.3), it was left for the respective gain factors to be carefully tuned. The tuning process together with the electronic circuits are discussed in Appendix E. Figures (8.13) through to Figure (8.15) are respectively the examples of the proportional only, integral only, proportional-integral only, and proportional-integral-derivative control process variables when the system was in closed-loop feedback control mode. The system generally took about 0.5 s to stabilise to within 20 MHz and finally stabilise to within 5 MHz i.e. better than ± 3 MHz. These times and stability margins however depend on the amount of disturbance and the controller settings.

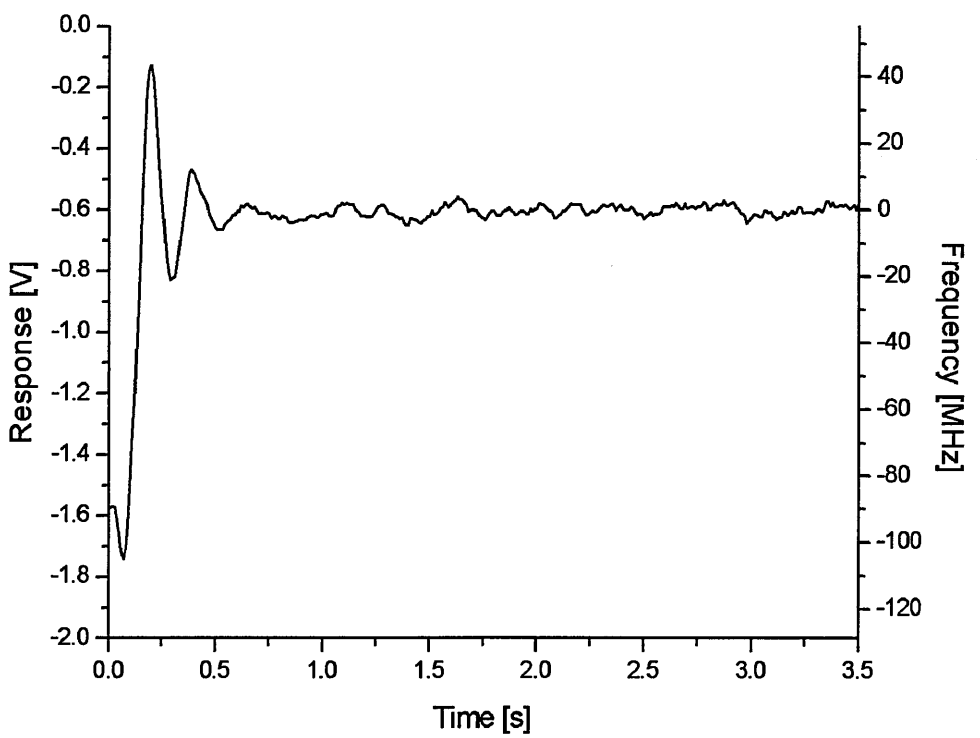

Figure 8. 13: Closed-loop feedback-control signal (response) of the PZT actuator for the Proportional only control action.

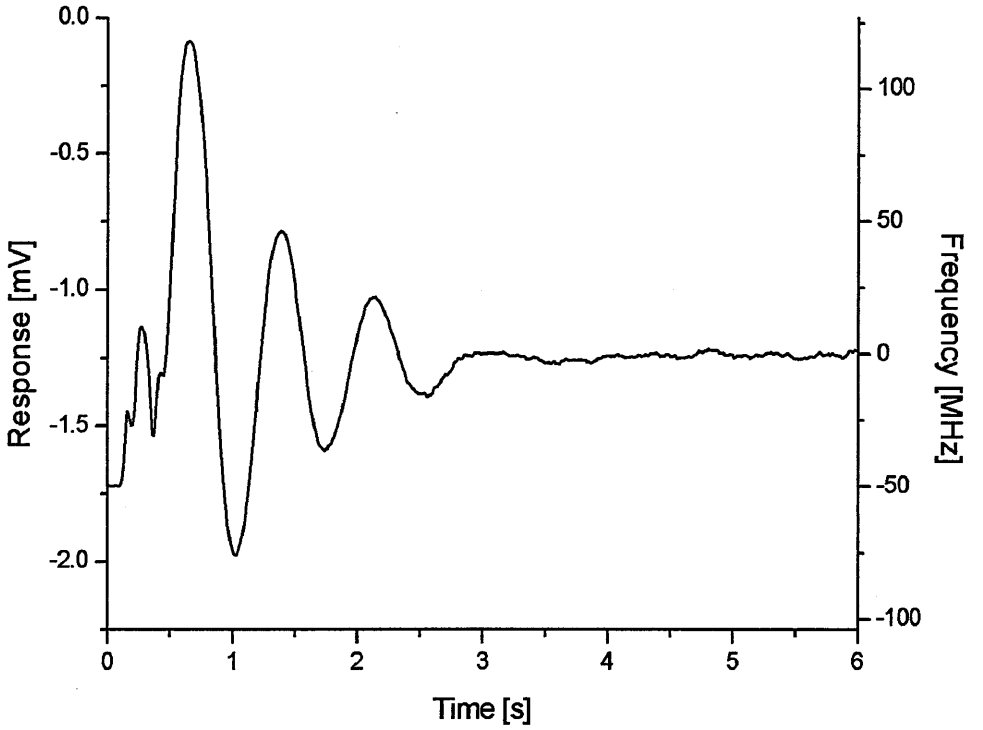

(a)

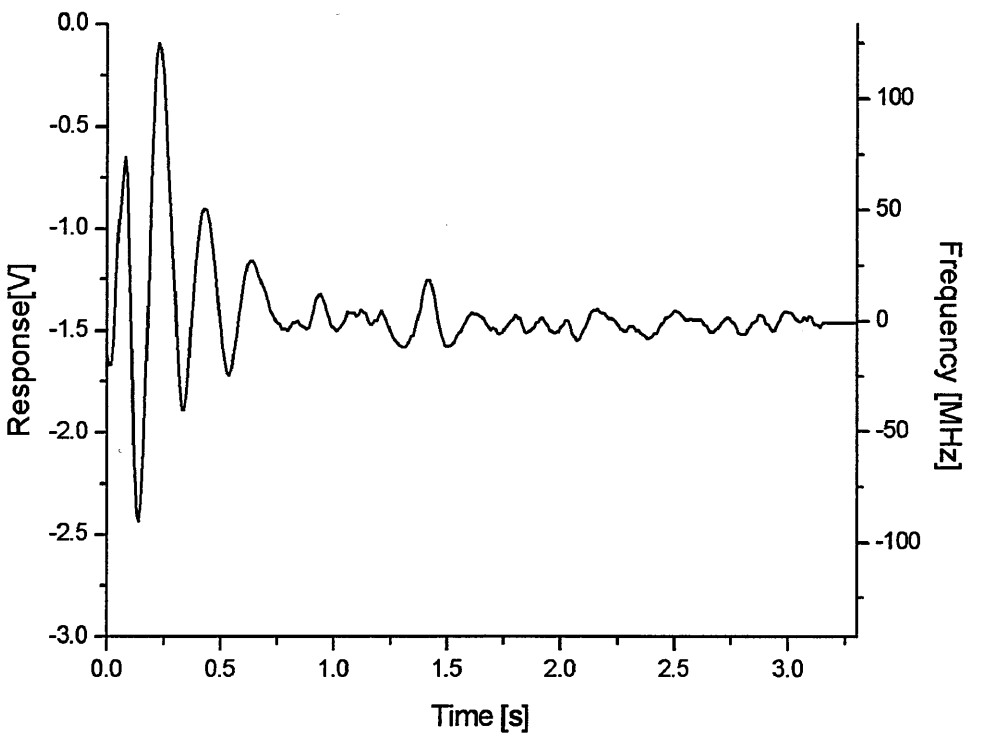

(b)

Figure 8. 14: Closed-loop feedback-control signal (response) of the PZT actuator for the (a) integral only (I) and (b) proportional-integral only (PI) control action.

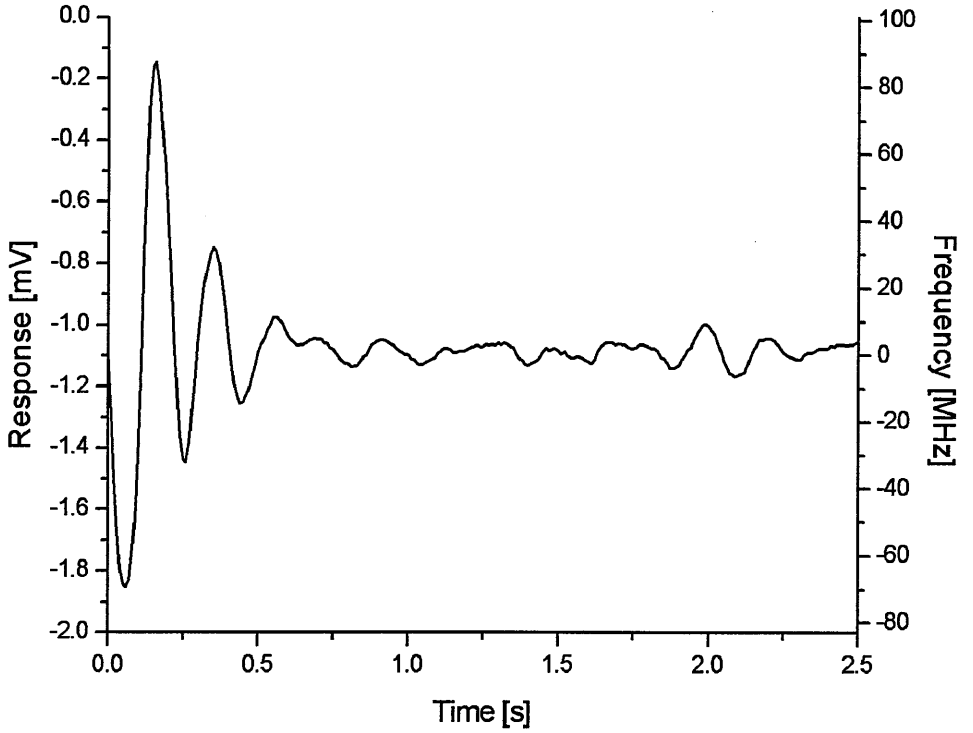

Figure 8. 15: Closed-loop feedback-control signal (response) of the PZT actuator for the PID control action.

8.5 Summary

The chapter discussed the implementation of two independent stabilisation systems that separately controlled the laser wavelength and the phase of a fibre Fabry-Perot interferometer. Both systems were based on custom designed PID electronic circuit controllers. The control stability achieved ±3 MHz short term and 10 MHz long term for the laser frequency and ± 3 MHz (an effective stability of 5 MHz) for the interferometer phase was sufficient for the intended application to flow measurement (Chapter 9). The achieved stability gives a minimum resolvable velocity of 0.2 ms^{-1}. Further discussion is presented in Appendices D and E.

References

[1] Y-J. Rao, "*In-fibre Bragg grating sensors*", Measurement Science and Technology, vol. 8, pp. 355-375, 1997.

[2] C. D. Johnson, "*Process Control Instrumentation Technology*", 6th edition, Prentice-Hall International, 2000.

[3] C. A. Smith and A. B. Corripio, "*Principles and Practices of Automatic Process Control*", John Wiley and Sons, NY, 1985.

[4] E. A. Parr, "*Control Engineering*", Butterworth Heinemann, 1996.

[5] R. Heilmann and J. Kuschel, "*Absolute frequency locking of diode-pimped Nd: YAG laser for application in free-space optical communication*", Electronics Letters, vol. 29, No. 9, 1993.

CHAPTER 9

In-Line Velocity Measurements

9.1 Introduction

A laser velocimeter is essentially made up of three main parts namely the laser source, the flow medium, and detection system. In addition a fibre transmission medium would be desirable for both easy instrument deployment as well as maintaining the polarisation of both the incident and light scattered from the flow. It is necessary to have a precise means of focussing laser light into the flow as well as the collection of the scattered light from the flow. The flow medium would be required to scatter enough light for detection purposes. An appropriately chosen detector is required to measure the Doppler shift in frequency of the scattered light collected through a spectroscopic filter. A signal processing system based on either a digital oscilloscope or computer based with the appropriate data acquisition board may be used and may be configured to provide real-time velocity data. These issues, including all component requirements for an all in-fibre based laser velocimeter have now been fully addressed in the preceding chapters. This chapter will focus on actual velocity measurements made from a rotating Perspex disc using the new technique. Three such experimental configurations will be discussed.

9.2 Simple Velocimeter Configuration

The initial experimental configuration for a single component laser Doppler velocimeter did not employ phase stabilisation on the FP filter [Figure 9.1]. The unused fibre ends were covered in index matching gel and all fibre ends were polished while those with FC/PC connectors were index matched before connected together, a precaution that prevented the formation of additional interferometers from fibre end reflections. A 63-mm cavity Bragg grating based Fabry-Perot filter was used to transduce the Doppler frequency shifts (a few MHz to several tens of MHz) to changes in intensity level of the

light scattered from the flow. A Faraday optical isolator was used to prevent feedback into the laser cavity that would otherwise destabilise the laser while a half wave plate was required to couple light into an eigen axis of a high birefringent fibre (Hi-Bi). Light was focussed onto the disc and coupled back into a single mode fibre using an LDV probe head constructed in our laboratory [1]. The light collected by the probe head was coupled to a single mode fibre coupler at 514.5 nm with a split ratio of 50:50 and one output arm was connected to the fibre Fabry-Perot filter to convert the Doppler shift in frequency to changes in the level of the intensity of the collected light (Chapter 2). The other arm formed the reference signal that was used to normalise the velocity signal and thus eliminated intensity fluctuations whose origin was not the velocity. Two-miniature Hamamatsu photomultiplier tube (PMT) detectors type H5783-1 with a rise time of 0.65 ns were used with signal processing done on a 300 MHz Lecroy 9450A digital storage oscilloscope. A clamp in the middle of the FP cavity enabled the individual Bragg gratings to be tuned via strain and thus position the laser wavelength at a known point on the transfer function of the FP filter. This point became the reference for the measurement of all the Doppler shift frequencies (Chapter 2). The Fabry-Perot etalon was used in a feedback system that eliminated jitter in the laser wavelength caused mainly by the water-hammer (Chapter 6), the water that cooled the laser head.

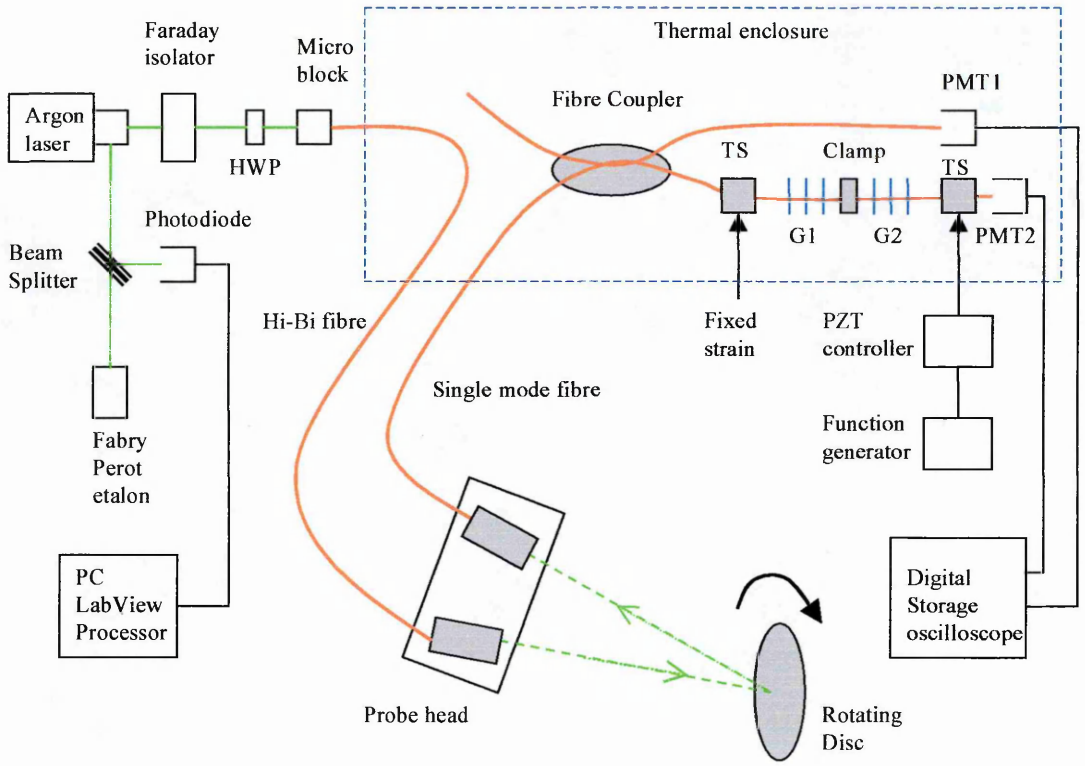

Figure 9. 1: Single component in-line fibre optic laser Doppler velocimeter.

The fibre FP filter, PMT detectors and directional coupler were placed in a thermal enclosure made out of polystyrene and shielded from stray light. A maximum power of 260 mW could be coupled into the measurement volume although this was reduced to 120 mW for the measurements taken. About 60 nW of power was collected from a stationary 15-cm diameter white-painted perspex disc. This power level required moderate gain settings of the PMT tubes (PMT1 – 0.57V and PMT2 – 0.40 V) and the use of an external amplifier was therefore not necessary. The perspex disc was used as a test surface to simulate the flow. The disc surface was not smooth and this caused the scattered light to fluctuate in intensity as is the case with a real flow where varying particle sizes in the flow and their number density would result in a similar effect. The disc was also useful for calibration purposes since its velocity could be accurately known e.g. by measuring its angular rotational frequency using an independent method as described in this section. The white reflective paint on the disc surface enhanced the light scattering which increased the amount of light collected by the detection system.

The measured velocity component was along the central axis of the probe head and the disc was aligned such that its plane made a small angle, ϕ (30 ^{0}) with this axis. The laser beam was focussed onto a point 4.6 cm from the centre of the disc and 4-mm to the left of a vertical line passing through the centre of the disc. The angle between the two heads, 2β was measured to be 20 ^{0} after calibration. The geometry of the disc set up is given in Figure 9.2. The measurement volume on the disc was 400 mm from the front lens of the probe head designed to have an f number of 8. Reversing the voltage applied to the motor reversed the disc velocity.

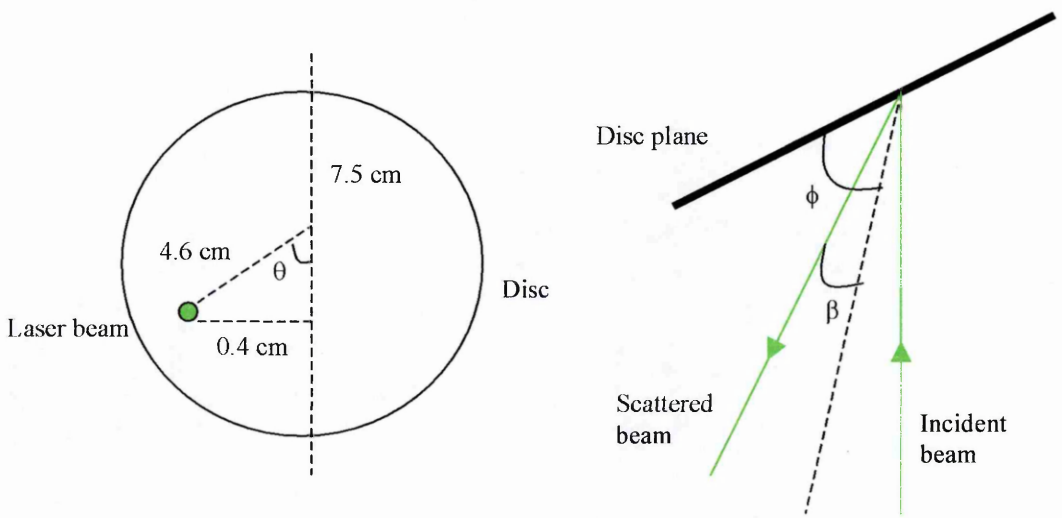

Figure 9. 2: Experimental geometry of the disc and angle definitions. ϕ = 30 ^{0} and 2β = 20 ^{0}.

The following equation relates together the Doppler shift in frequency $\Delta\nu$, the flow velocity V, laser wavelength λ, and the experimental geometry [2]. The unit vectors $\underline{i}$ and $\underline{o}$ are respectively the illumination and receiving directions.

$$\Delta\nu = \frac{1}{\lambda}\cdot(\underline{o}-\underline{i})\cdot\underline{V} \qquad (9.1)$$

The disc geometry of figure 8.2 simplifies this equation to the following

$$V = \frac{\lambda}{2\cdot\cos\beta\cdot\cos\theta\cdot\cos\phi}\cdot\Delta\nu \qquad (9.2)$$

Increasing the voltage applied to the disc motor from 0 to 30 V in either direction increased the velocity of the disc. Independent velocity measurements were made with a digital tachometer that measured the number of revolutions per minute (RPM) of the rotating disc. A stripe of reflective tape was stuck at the back of the disc and the digital tachometer light illuminated the tape and the RPM values could be read directly from the instrument. The reflective tape modulated the tachometer light at the angular frequency of rotation each time it passed through the light.

9.2.1 The Transfer Function

The accuracy of velocity measurements relies on the ability to accurately produce a true FP filter transfer function. The experimental details on the characterisation of the transfer function through strain scans of the filter cavity-length were discussed in Chapter 7. Figure 9.3 shows one such transfer function over one free spectral range having a visibility of about 20 %. This profile is neither Voigt nor sinusoidal but lies in between since the visibility is neither high nor low. The approximately linear region of the transfer function covers about 200 MHz of frequency corresponding to a velocity of about 61 ms^{-1} with the wheel geometry of Figure 9.2. The gradient of the linear region was measured to be 1.67 $[GHz]^{-1}$. A polynomial curve-fit of degree 8 to the graph of Figure 9.3 gave the graph of Figure 9.4 when fitted to one edge of the profile.

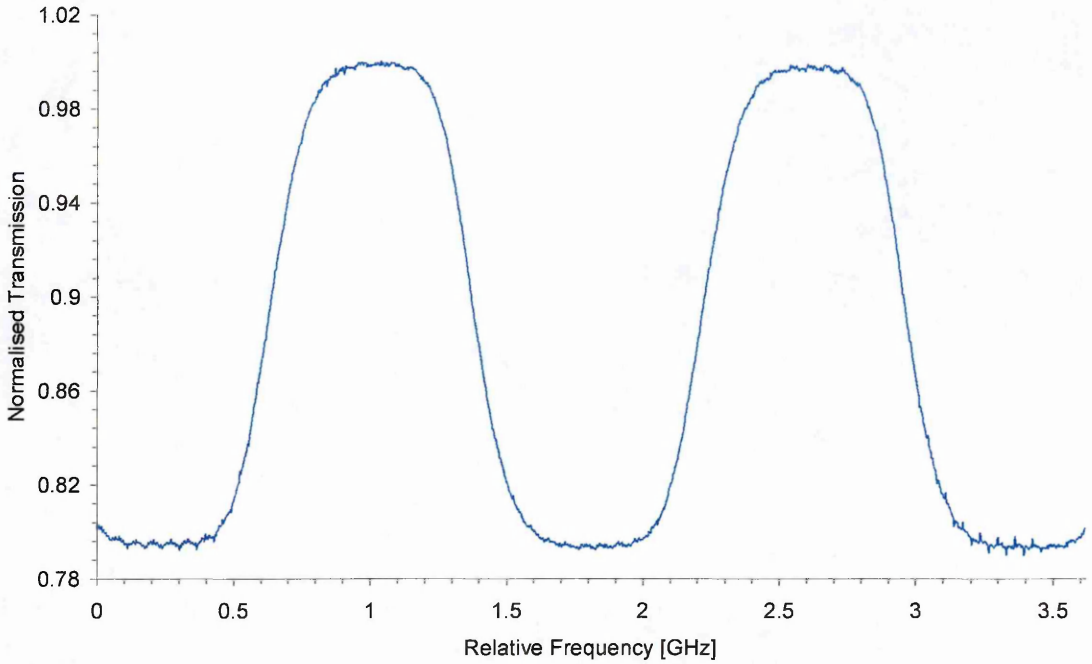

Figure 9. 3: The transfer function of a Bragg –grating based fibre Fabry-Perot interferometer obtained from a strain scan of the cavity (Chapter 7).

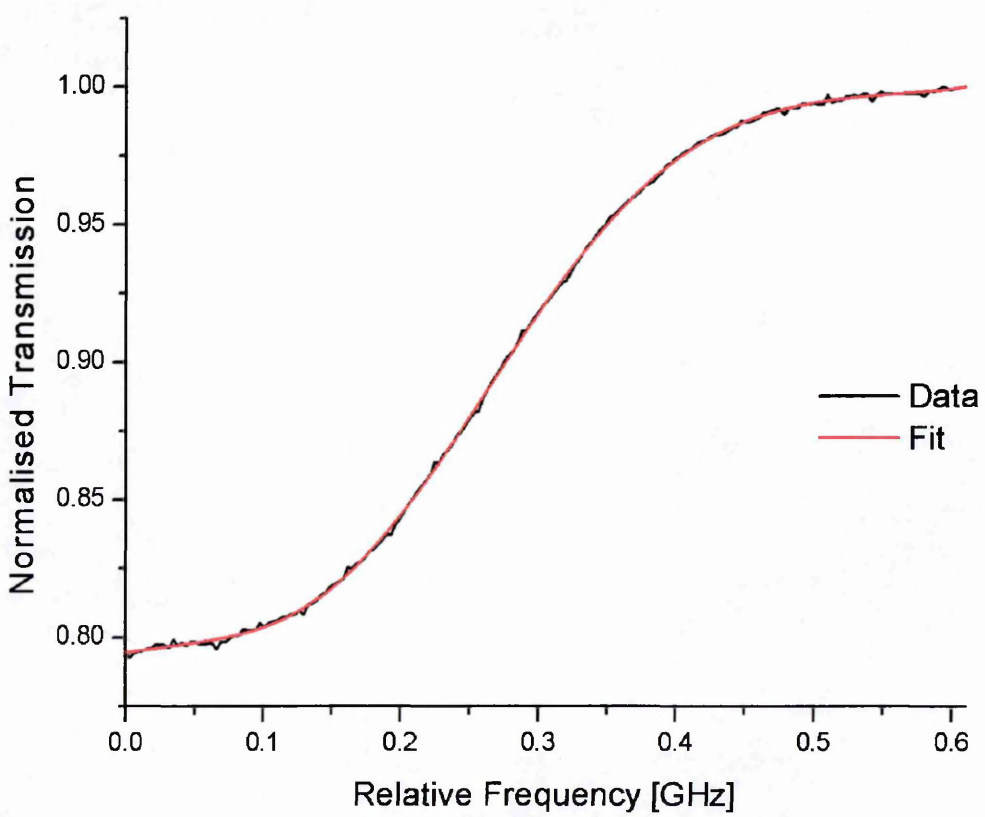

Figure 9. 4: Polynomial curve-fit of degree 8 to one edge of the profile of Figure 9.3.

9.2.2 Velocity Results

The velocity results could be analysed in two ways by either using the gradient of the transfer function of Figure 9.3 or by performing a curve fit to the transfer function as shown in Figure 9.4. Figure 9.5 shows the disc velocity over a velocity range of ± 20 ms^{-1} with the velocimeter resolution as 0.9 ms^{-1}. The velocity was calculated using the gradient of the transfer function of Figure 9.3 and the result is compared to independent measurements that were recorded using a digital tachometer. The frequency to velocity coefficient for the experimental configuration was 3.30 MHz/ms^{-1}. The graph of Figure 9.5 is seen to curve at both extreme ends while it is linear in the low velocity regime. The curving was attributed to drift in the transfer function of the FP filter and/or the laser wavelength drift. Figure 9.6 is for an experiment that was run over a small velocity range of about ± 10 ms^{-1} when the drift in the system had not become so apparent. The graph is linear thus showing the capability and potential of this new technique for flow velocity measurements. The standard deviation in the velocity over this range of velocity was found to be 0.2 ms^{-1} which can be improved by control of the interferometer drift (section 9.3).

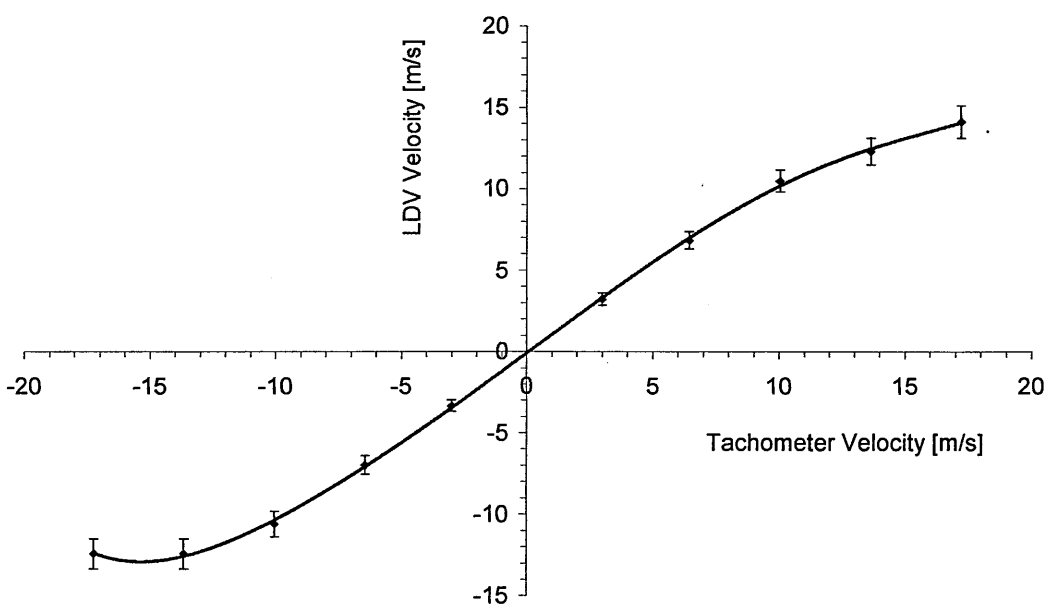

Figure 9. 5: Disc velocity measured by the fibre-optic laser Doppler velocimeter and the digital tachometer by using the gradient of Figure 9.3. The line is a polynomial fit of degree 6.

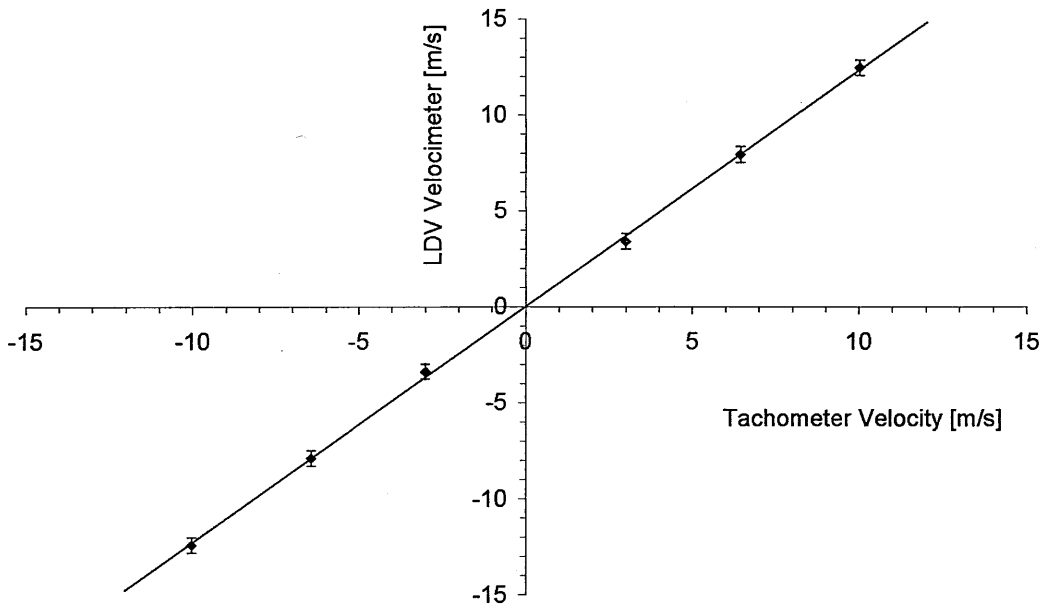

Figure 9. 6: Small velocity range of the disc measured by the fibre-optic laser Doppler velocimeter and the digital tachometer based on the gradient of Figure 9.3.

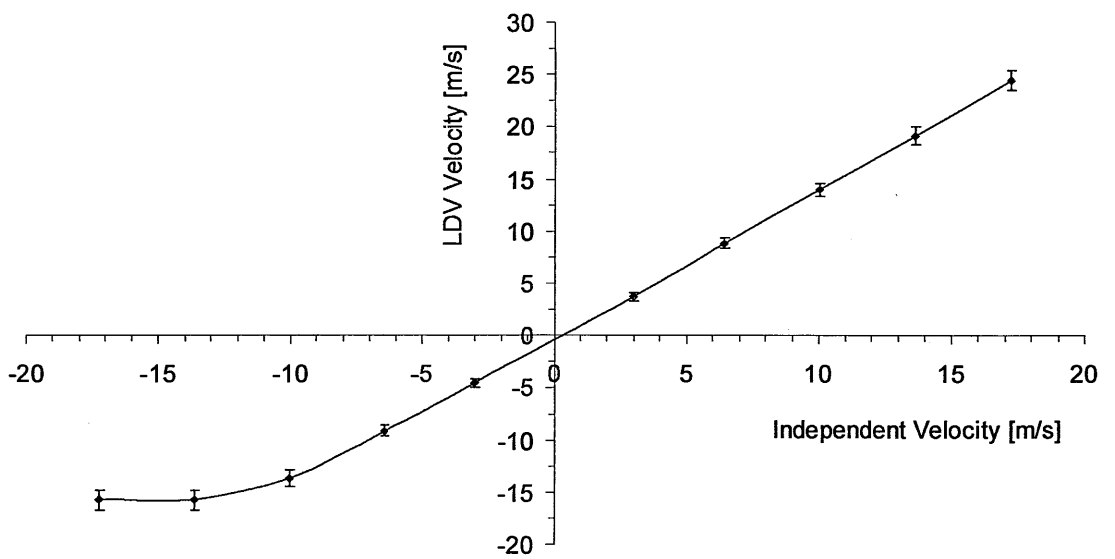

Figure 9. 7: Disc velocity measured by the fibre-optic laser Doppler velocimeter and the digital tachometer based on the curve-fit of Figure 9.4.

In Figure 9.7 are the results of Figure 9.5 that were analysed by using a polynomial curve-fit of Figure 9.4 and using Mathcad to extract the roots from a polynomial of degree 8. These results were expected to be more accurate as they took account of the shape of the transfer function. Indeed the results have improved, as the graph is now

more linear over a wider range except for the extreme negative velocity end but the values are not true, a consequence of the aforementioned phase drift or wavelength drift.

9.3 Drift Compensated Velocimeter

The results of section 9.2 suggested the need for an active control of the interferometer and laser drift by either one or both of the independent feedback systems for the fibre Bragg-grating Fabry-Perot interferometer phase and laser wavelength. The experimental details and results of the two control systems are fully covered in Chapter 8 while the electronic circuit designs and components are detailed in Appendix D and E. Here, only the integrated velocimeter and the results of measurements taken from a rotating perspex disc (21 cm in diameter) will be presented.

9.3.1 Velocimeter Configuration

Figure 9.8 shows the experimental configuration for the velocimeter, which is essentially all fibre-based. The velocimeter is an integrated system that incorporates two independent feedback loops that perform active control of the signal drift by way of compensating for the FP interferometer phase changes and laser wavelength variations. A light signal at the same wavelength as the tuned-wavelength of the fibre-optic FP filter is required concurrently with the flow signal in the velocimeter system to continuously monitor the interferometer phase changes and this is done using polarisation multiplexing of the signals. This signal was pulsed using an optical chopper at a frequency of 2 kHz to facilitate phase detection using digital lock-in amplifiers (Chapter 6 & 8). The vertical polarisation of this beam was matched to an eigenstate of the overall system consisting of the directional coupler and fibre filter using a stress birefringence based polarisation state controller (PSC_1). The coupler (Fibrecore, FSMC-514-50) was single-mode type and fused with an operational wavelength of 514.5 nm and 50:50 split ratio. Only photomultiplier tubes PMT_{sig} and PMT_{ref} thus detected the pulse signal through the aid of two polarisation beam-splitters (PBS). The two signals were used in a phase-locked loop consisting of 2 digital lock-in amplifiers (Stanford Research Systems model SR850), LabView data acquisition board (PCI-MIO-16E-4) in

a personal computer, a custom designed PID electronic circuit controller, function generator (Stanford Research Systems DS345), and a piezoelectric transducer controller (Photon Control, MD3-75C) unit that fed-back to a piezoelectric controlled translation stage (TS). The phase compensation is via translations of the TS that changes the cavity length of the FP interferometer. The locking system will drift and fail if the polarisation of the signal light drifts to be parallel to that of the locking signal. This is because the control loop would be trying to compensate for the Doppler frequency shift. Flare with fluctuating optical frequency and intensity would also drive the control loop out of lock. Experimental details on this system are discussed in Chapter 8 as well as in Appendix E.

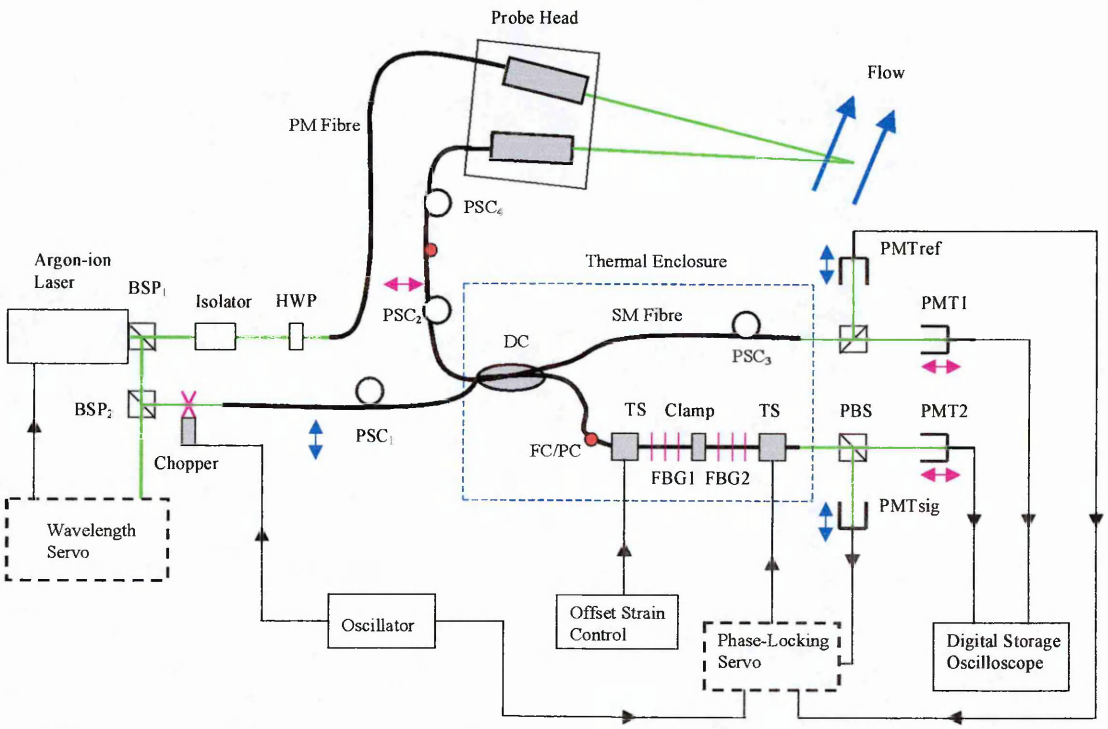

Figure 9. 8: Fibre-optic laser Doppler velocimeter integrated with two independent feedback loops for the active stabilisation of the laser wavelength as well as the phase control of the Bragg-grating based Fabry-Perot interferometer.

BSP_1 (99:1) & BSP_2 (50:50) - beam splitter cubes, HWP - half wave plate, PM - polarisation maintaining, PSC - polarisation state controller, DC - directional coupler, SM - single mode, TS - translation stage, FBG - fibre Bragg grating, PBS - polarisation beam splitter cube, PMT- photomultiplier tube.

About 5 % of the laser output power was split-off and a 50 % beam splitter cube further split this beam to supply the phase-lock loop as well as the wavelength servo. The wavelength servo consisted of a fibre directional-coupler, iodine cell and the associated

temperature controller, 2 photodiode detectors (BPX65), custom designed analogue divider electronic circuit and a PID electronic circuit controller, and the Z-lok electronics that fed-back to the intra-cavity laser etalon. The wavelength control is via adjustments of the etalon cavity length through heating or cooling. Details on the operational system are given in Chapter 9 as well as in Appendix D.

The scattered light from the flow constituting the velocity signal was coupled through the second input arm of the coupler and controlled by PSC_4 to be aligned othorgonal to the pulse signal and thus emerge horizontally polarised and was detected by PMT1 and PMT2. PSC_2 is pre-aligned to give a horizontal polarisation output to the detectors by coupling the laser light directly to this arm before the experiment. Originally a high birefringence (Hi-Bi) optical fibre was used from the probe head receiver to this input arm of the coupler but this required the rotation of the FC/PC connector that was connected to the coupler connector so that the eigen-axes of both fibres could be matched together. Coupling efficiency at the connector was poor, as the two fibres had different core sizes (Hi-Bi – 8 μm, SM – 4 μm). The coupler fibre was single-mode from Fibercore while the Hi-Bi fibre was Panda type (Fujikura, 480P). Also, the probe head receiver design comprised neither a polariser nor a half wave plate and thus the Hi-Bi fibre connector to the probe head had to be rotated in order to couple the scattered light down the eigen-axis of the Hi-Bi fibre. The rotation of this fibre end had serious consequences on the amount of light that could be collected as the two heads of the probe move out of alignment and would therefore need realignment, which is a rigorous process discussed in Chapter 6.

The polarisation of light through optical fibres is dependent on fibre deployment e.g. the presence of bends or twists will alter the polarisation of the light [3, 4]. PSC_3 was required to correct for the lost extinction ratio caused by fibre deployment in the two output arms of the coupler. The two signals were normalised and processed by a 300 MHz digital storage oscilloscope (Lecroy 9450A). The extinction ratio between the pulse signal and velocity signal was about 21 dB and this was recorded with the disc stationary. However, the scattered light collected from the disc was found to be completely depolarised no matter what orientation of the incident linear polarisation

was used. Mie scattering theory from small particles predicts that the polarisation of the scattered light is predominantly that of the incident beam and is dependent on the scattering angle among other things (Appendix C). The encountered depolarisation was therefore considered to be a consequence of the nature of the paint used on the disc particularly its particulate size.

A polariser in the form of a sheet was placed in front of the receiver head and was rotated until the polarisation of the signal was orthogonal to the pulse signal. While producing the desired extinction ratio, this resulted in the actual detected signal falling to about a third and thus causing a poor signal to noise ratio. Ideally a 50 % loss of power (equivalent to un-polarised light) is expected but light absorption and possibly dispersion in the polariser affected the light gathering power of the probe head whose alignment is critical (Chapter 6). The laser was operated at an optimum output power of 700 mW thus providing 100 nW of light power scattered from a stationary disc and about 30 – 50 nW for a rotating disc whose plane was set at an angle of about 35^{0} to the optical axis. This provided sufficient signal for operating the velocimeter with the 2-photomultiplier tube detectors set to medium gain values of 0.470 V and 0.410 V. The small residual cross talk from the pulse channel on the velocity channels was minimised by lowering the intensity level of the pulse signal. Also, the gain on the PMTsig and PMTref were sufficiently lowered to 0.08 V and 0.104 V respectively so that they did not record the small cross talk caused by the velocity signal on the pulse channels.

The velocity channels required 2 PMTs that had nearly identical responses such that the normalisation of the 2 signals remained accurate. The responses of the 4 PMTs were therefore investigated over a range of laser intensity. Figure 9.9 show that PMT1 and PMT2 have essentially identical responses and therefore were chosen as the detectors for the velocity signal. PMT_{sig} and PMT_{ref} were matched together at a laser power of 2 μW and were used for phase locking purposes.

Independent velocity measurements of the rotating disc were made from measurements of the angular frequency. A stripe of a reflective tape was placed at the back of the disc and a laser beam (632.8 nm wavelength) from a miniature laser (Spindler and Hoyer

SH650S) was directed onto the disc at the position of the tape with a photo-detector (Spindler and Hoyer E2V) positioned to receive the reflected light. The light reflected from the tape was modulated at the rotational frequency of the spinning disc that was measured on a dynamic signal analyser (Hewlett Packard 35660A). The recorded frequency was very stable with the error in a single measurement being less than 0.25 Hz, which was improved further by taking an average of 10 samples or more to give 0.02 Hz resolution. This technique was more accurate than the digital tachometer used in the original experiment (section 9.2). The rotational frequency was recorded simultaneously with the disc velocity as measured by the laser velocimeter. The angular frequency, ω, was converted to tangential velocity, V, of the disc using equation (9.3) in which r is the radius of the disc at the position of the laser beam.

$$V = r \cdot \omega \qquad (8.3)$$

The value of ω in this equation was calculated from

$$\omega = 2 \cdot \pi \cdot \nu \qquad (8.4)$$

where ν is the rotational frequency of the disc. The velocity along the probe head axis, considered to be the known velocity of the disc was obtained by resolving the tangential velocity V using the experimental geometry.

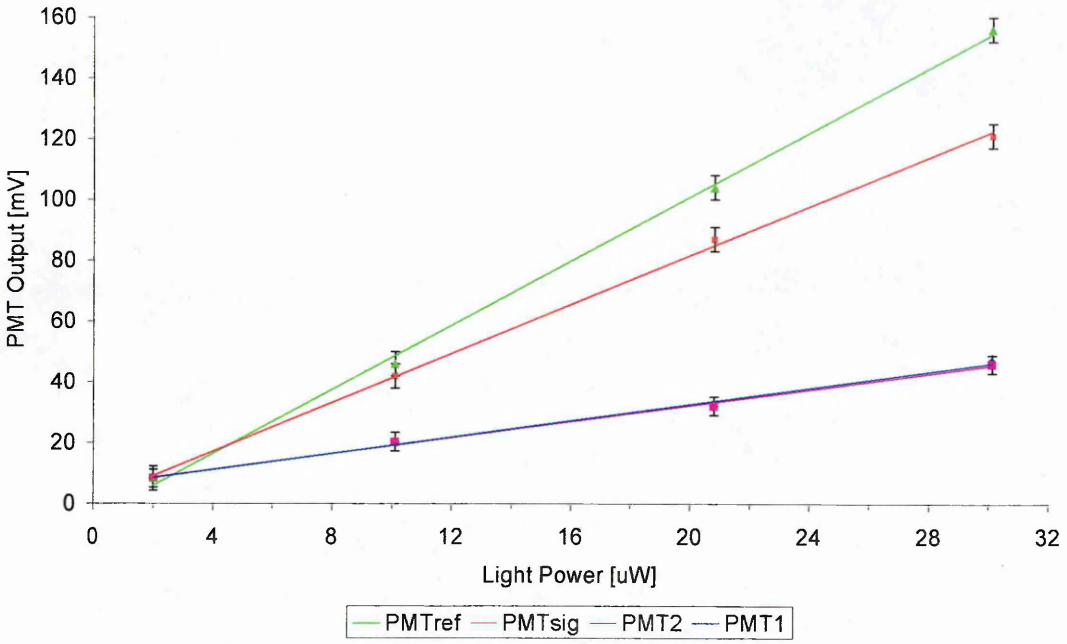

Figure 9. 9: Photomultiplier tube (PMT) detector response characteristics.

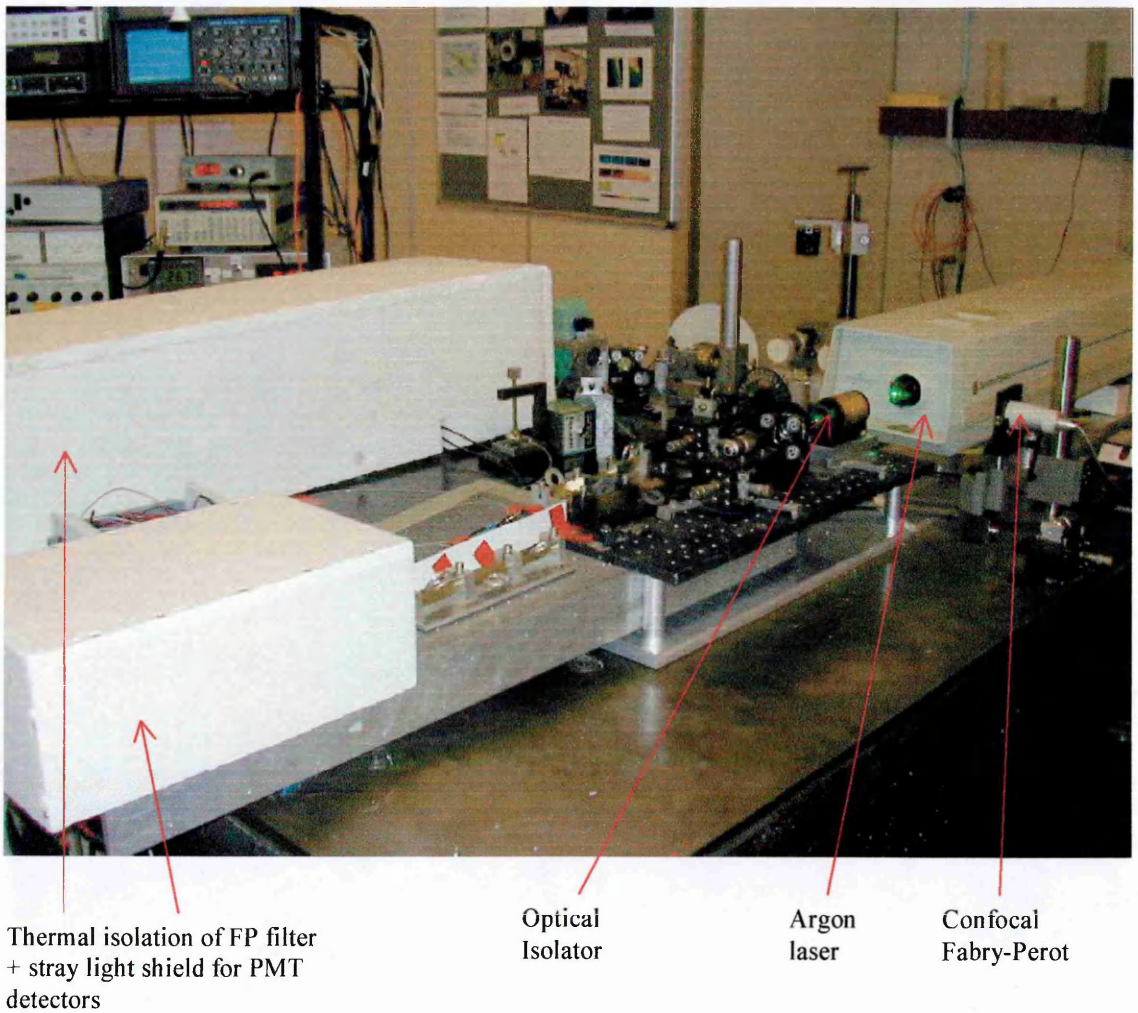

Photograph 9. 1: Part of the experimental set-up showing the polystyrene boxes used as thermal shields to the filter and also used for shielding back ground light onto the photomultiplier tube detectors.

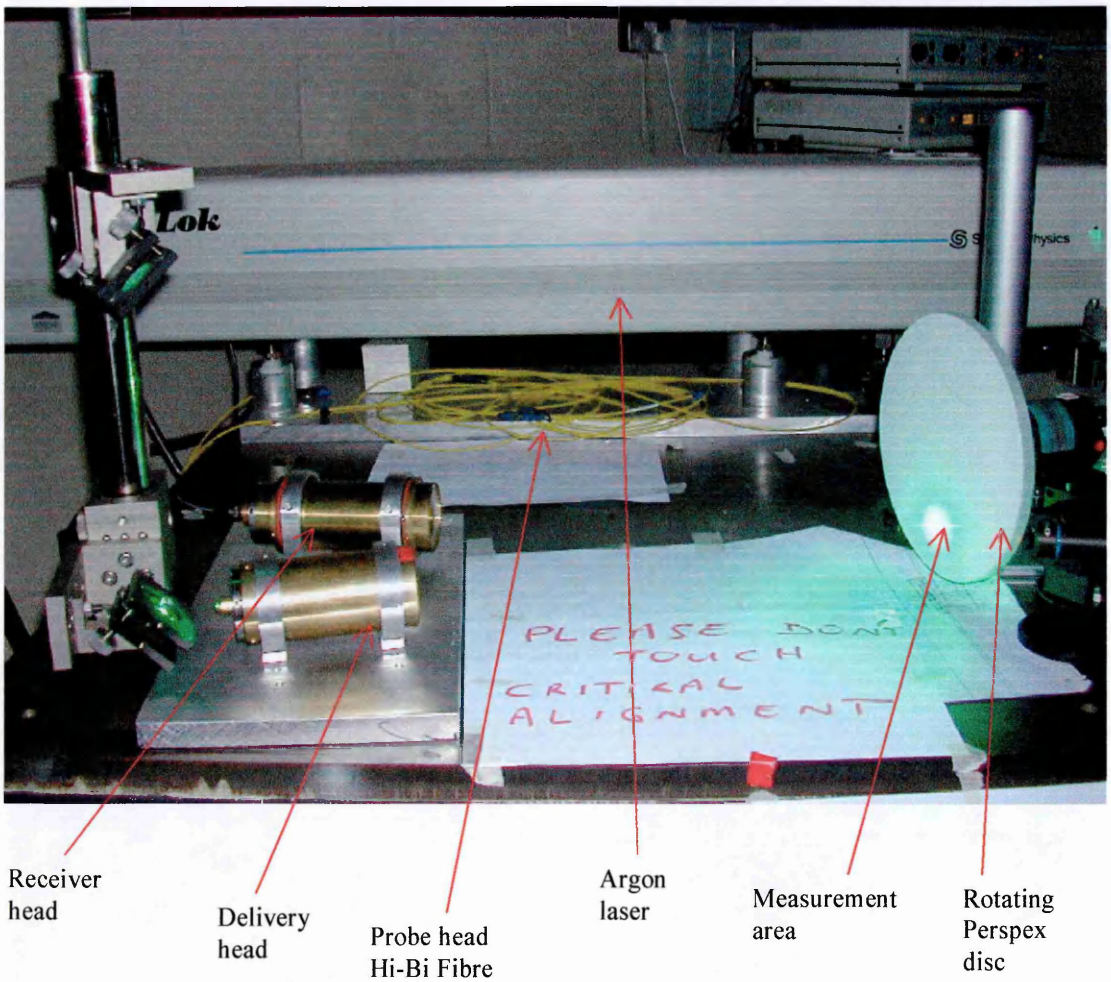

Photograph 9. 2: Experimental arrangement of the LDV probe head and the perspex disc. Behind the disc is a miniature HeNe laser and a photodiode detector for an independent measurement of the angular frequency of the disc. Also shown in the picture are Hi-Bi fibre delivery cables in yellow.

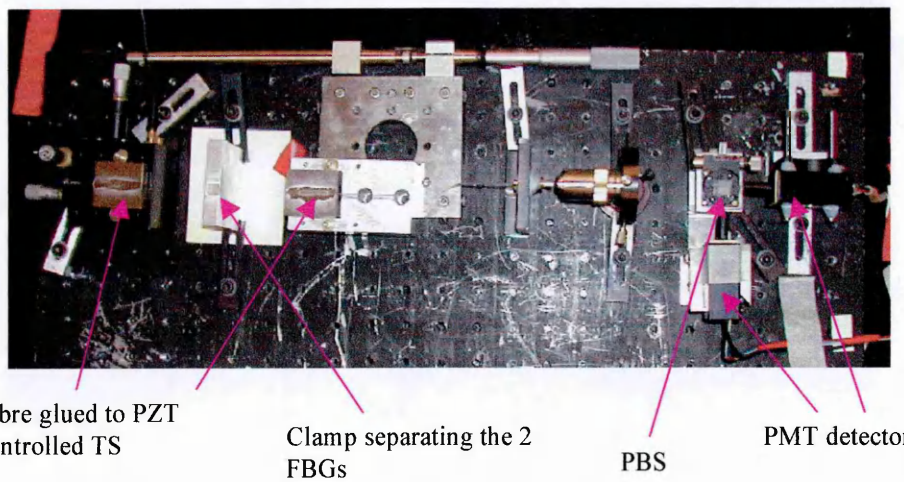

Photograph 9. 3: Picture showing the experimental arrangement of Fabry-Perot filter cavity and the photomultiplier tube (PMT) detectors. PZT-piezoelectric transducer, TS-translation stage, FBG-fibre Bragg grating, PBS-polarisation beam splitter.

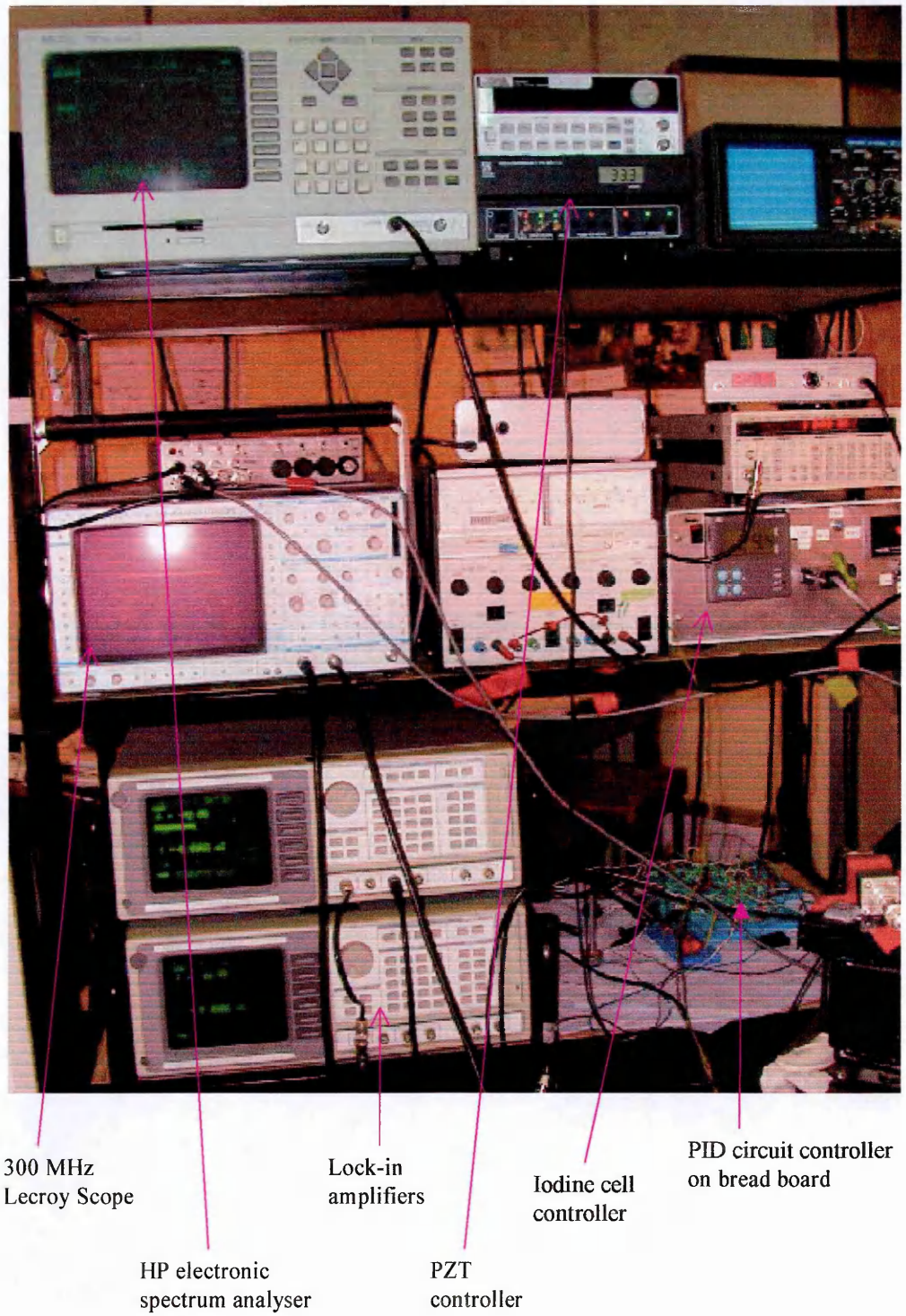

Photograph 9. 4: The picture shows part of the instrumentation bench used in the experiment.

9.3.2 The Transfer Function

Accurate transfer functions of the FP filter were obtained by limiting the scan bandwidth to cover only one free spectral range, that is, having 2 transmission peaks within one ramp as shown in Figure 9.10. When the interferometer was scanned over a larger bandwidth to obtain more transmission peaks, distortion of the filter profile was observed (Chapter 7) however the method gave accurate measurements of the visibility which was recorded as 22 %. In Figure 9.10 the second peak was not used because its shape was distorted as it is partly affected by the fly back of the scan. A polynomial curve fit of degree 6 was used on the transfer function to produce Figure 9.11.

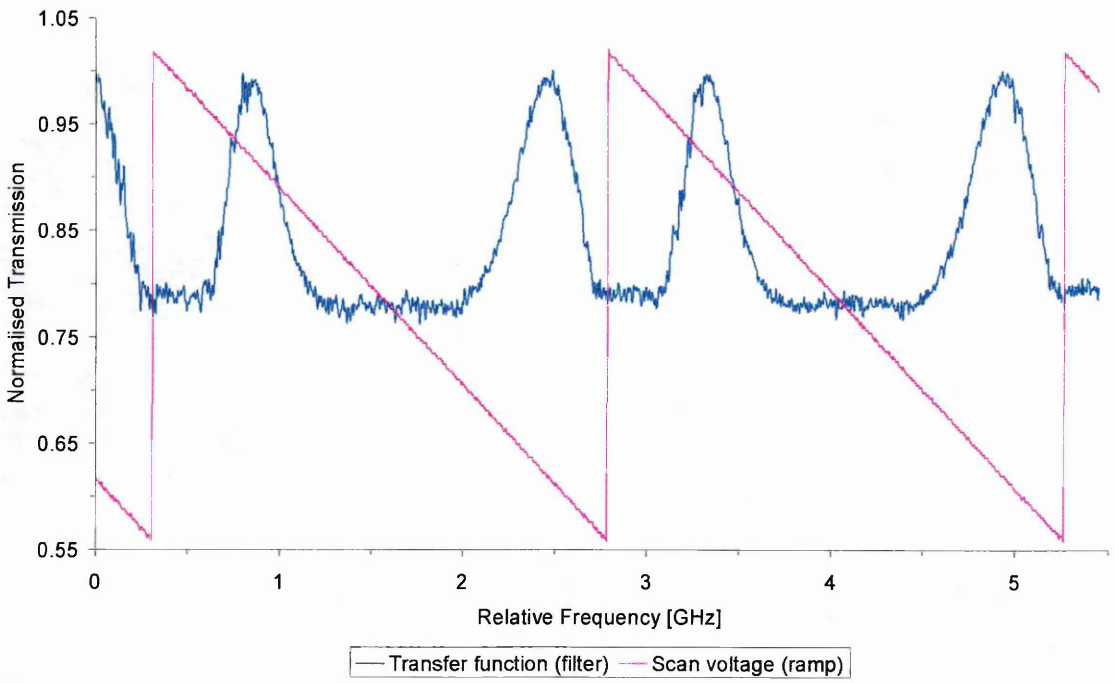

Figure 9. 10: Optical fibre Fabry-Perot filter transfer function scanned over one free spectral range using a ramp voltage (Chapter 7).

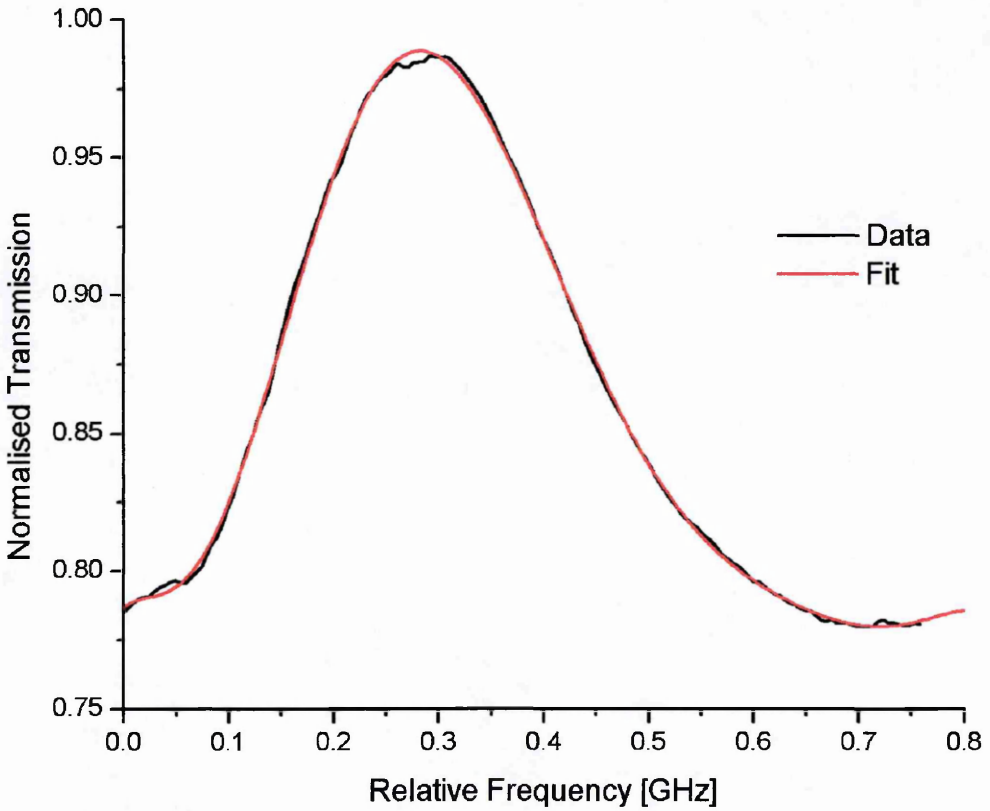

Figure 9. 11: Polynomial curve-fit of degree 6 to the FP transfer function of Figure 9.10.

9.3.3 Velocity Results

The measurement of the velocity of the disc was made with the geometry of Figure 9.12. This geometry gives a frequency to velocity coefficient of 2.23 MHz/ms^{-1}. The results were first calculated by using the gradient of the transfer function which was 1.29 [GHz]$^{-1}$ and the results are displayed in Figure 9.13. The measurements were made over a velocity range of ± 42 ms^{-1}. Figure 9.14 is the result when a polynomial curve-fit of degree 6 was made to the transfer function. The velocimeter resolution for the configuration was 0.4 ms^{-1}. The results demonstrate the ability of the drift compensated velocimeter to make accurate velocity measurements of the rotating wheel. The previous effects of phase and wavelength drift have been successfully overcome by engaging the two independent stabilisation schemes as described (section 9.3.1).

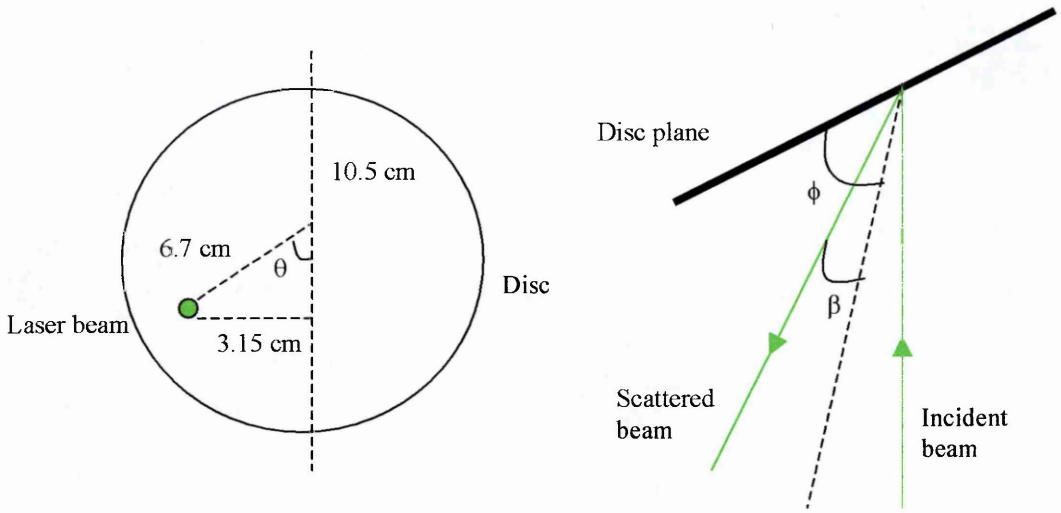

Figure 9. 12: Experimental geometry of the disc and angle definitions. $\phi = 48.5^0$ and $2\beta = 20^0$.

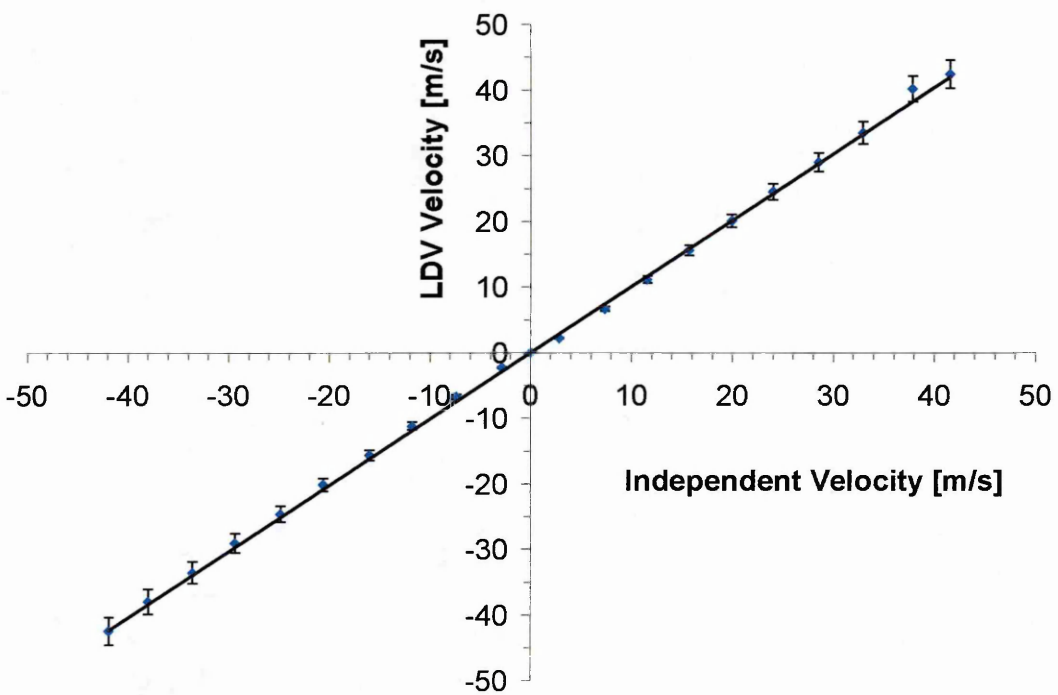

Figure 9. 13: Disc velocity measured by the drift compensated velocimeter. The results are calculated using the gradient of the transfer function and are compared to those measured from the rotational frequency of the disc. The gradient of the fitted line is 0.9976 i.e. 0.24% deviation from unity.

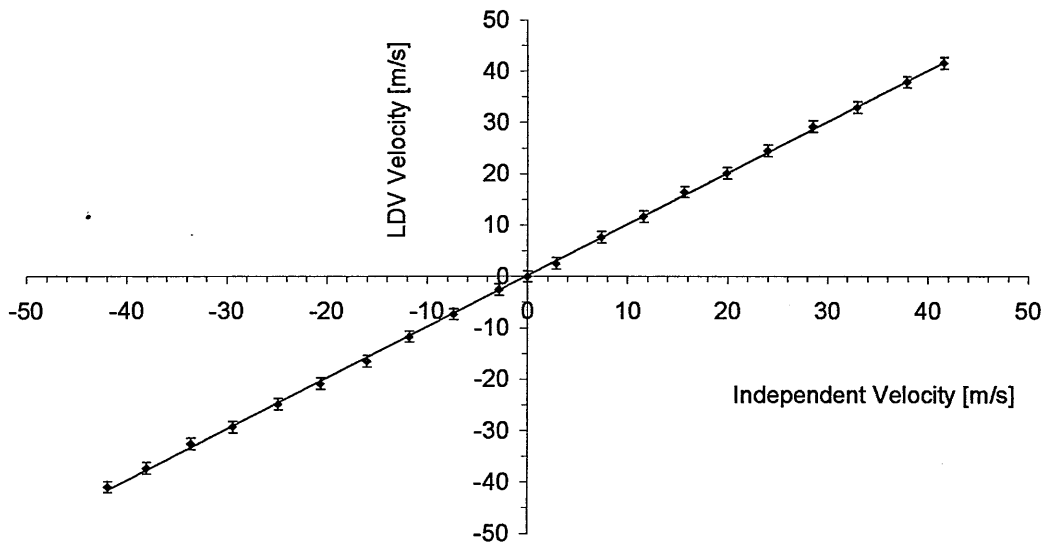

Figure 9. 14: Disc velocity measured by the drift compensated velocimeter. The results are calculated using a polynomial curve-fit (degree 6) to the transfer function and are compared to those measured from the rotational frequency of the disc. The gradient of the fitted line is 1.0054 i.e. 0.54% deviation from unity.

9.4 High Sensitivity Velocimeter

Quite often low regime velocities are required for example in low speed windtunnels and blood-flow measurements in a human body and it is therefore desirable to design an accurate instrument that can easily be adapted to measure low velocities while able to measure higher velocities. In all of the above configurations, variable sensitivity is obtainable by strain-tuning the shape of the FP-filter transfer function and thus changing its frequency to intensity conversion factor. The next section demonstrated yet another merit of the system that doubled the instrument sensitivity without any extra tuning to the FP filter thus allowing previously unresolved low velocities to be measurable. The technique could also be used in conjunction with filter tuning to increase the sensitivity even further.

9.4.1 Detection Principle

Figure 9.15 shows the principle of simultaneous detection of the velocity signals in reflection and transmission modes. The two signals are drawn superposed and if one

detector measures a transmission of T_1 then the other will measure a reflection of T_2. For a 50 % transmission both detectors will have an equal signal of $T_{50\%}$ and thus T_1 and T_2 are always equal and opposite as the two signals complement each other. If the change in transmission for one detector from $T_{50\%}$ to T_1 is $-\Delta T$ in a frequency change $\Delta\nu$, then the other will change by $+\Delta T$ from $T_{50\%}$ to T_2 over the same frequency change and the change between the 2 signals is therefore $2\Delta T$ over $\Delta\nu$. This shows that the intensity to frequency ratio doubles when using two complementary detector outputs. The filter will therefore give more sensitivity on the frequency to intensity conversion.

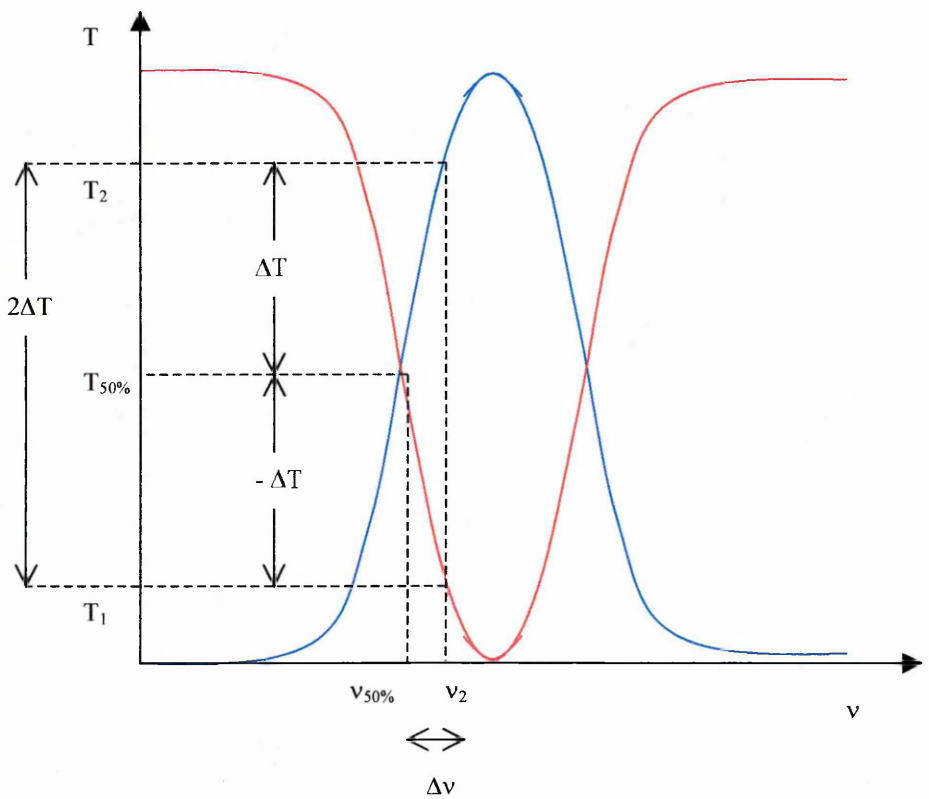

Figure 9. 15: The superposition of the transmission (red) and reflection (blue) signals illustrating the increase in sensitivity by the simultaneous use of detectors in both of these modes.

T - transmission or reflection, ΔT - change in transmission, ν - frequency, Δν - change in frequency.

The signal normalisation was based on the relation

$$T_N = \frac{T_1 - T_2}{|T_1| + |T_2|} \qquad (9.5)$$

The symbol T_N represents the normalised signal of the two detectors and is true for equal gain or matched detectors. The dynode voltage gain of photomultiplier tube PMT_1 was however increased from 0.470 V to 0.706 V, a signal gain of about 18. This was needed since the two detectors did not have equal signals. Equation (9.5) was therefore modified to

$$T_N = \frac{T_1 - m \cdot T_2}{|T_1| + m \cdot |T_2|} \qquad (9.6)$$

The parameter m represents the photomultiplier signal gain. Signal processing in LabView was configured to calculate T_N, and T_1 and m being known the true value of T_2 was calculated using

$$T_2 = \frac{(1 - T_N) \cdot T_1}{(1 + T_N) \cdot m} \qquad (9.7)$$

This value of T_2 together with the known value of T_1 was used in equation (9.5) for the required signal processing.

9.4.2 Simultaneous Reflection and Transmission Detection

The drift compensated velocimeter configuration of section 9.3 was reconfigured to increase the instrument sensitivity (Section 9.4.1), a unique attribute of the velocimeter presented in this thesis. Figure 9.16 shows the new experimental set up for the velocimeter reconfigured such that a reflected signal from the FP filter is detected by the photomultiplier tube detector PMT_1 that was originally placed in transmission. All other components were left unchanged. The flow and pulse signals, as in Figure 9.8 were

maintained orthogonal to each other using polarisation state controllers (PSC). The two fibre directional couplers were both of single mode type (Fibercore) at 514.5-nm wavelength and had a split ratio of 50:50. The light signal detected by PMT_1 was therefore 25 % of that reflected from the fibre FP interferometer. This signal was found to be so small, < 5·K mV, where K is the coupling efficiency between the FC/PC connectors, which at best could give 5 mV, a figure that approached the minimum detection sensitivity of the digital oscilloscope. A known gain could be applied to PMT_1 to increase the signal level but the signal to noise ratio was poor. The light gathering power of the receiver head could be maximised by alignment and increasing the laser power delivered to measurement volume. As before the polariser sheet in front of the receiver head caused signal attenuation to the collected signal.

A configuration that did not incorporate the second coupler was later adopted as in Figure 9.17. This configuration applied no phase stabilisation mechanism in order that the full 50 % of the reflected signal from the FP filter was utilised and also the polariser sheet was not in use. However the measurements took more than three days of waiting until stable laboratory conditions were obtained. The wheel geometry was also changed such that its plane made a large angle of 79^0 with the central axis of the probe head (Figure 9.18). This move increased the strength of the signal that was collected from the measurement volume on the wheel. The increase in the included angle between the plain of the wheel and the optical axis enabled the measurement of lower velocities to be accessible and measurable. The output power of the laser was increased to a maximum of 700 mW with a laser control current of 55 amperes i.e. 5 amperes below the maximum allowed current and the operating power range of the laser was set at 0 – 1 W. The PMT_1 signal recorded was in the range 60 – 100 mV on the digital oscilloscope that is before the gain of the detector was raised from 0.470 V to 0.706 V. The PMT_1 signal was made comparable in magnitude to that of PMT_2 by this increase in gain. The digital storage oscilloscope was replaced by a personal computer (PC) installed with a LabView data acquisition board (PCI-MIO-16E-4) having a 12-bit resolution and a bandwidth of 600 kHz. The use of a PC enabled more information to be captured and analysed so that using the known photomultiplier gain the true reflection and transmission signals were deduced. A thick polystyrene enclosure was used to shield the

FP filter system from environmental perturbations particularly ambient temperature variations. The system was left to stabilise before taking measurements.

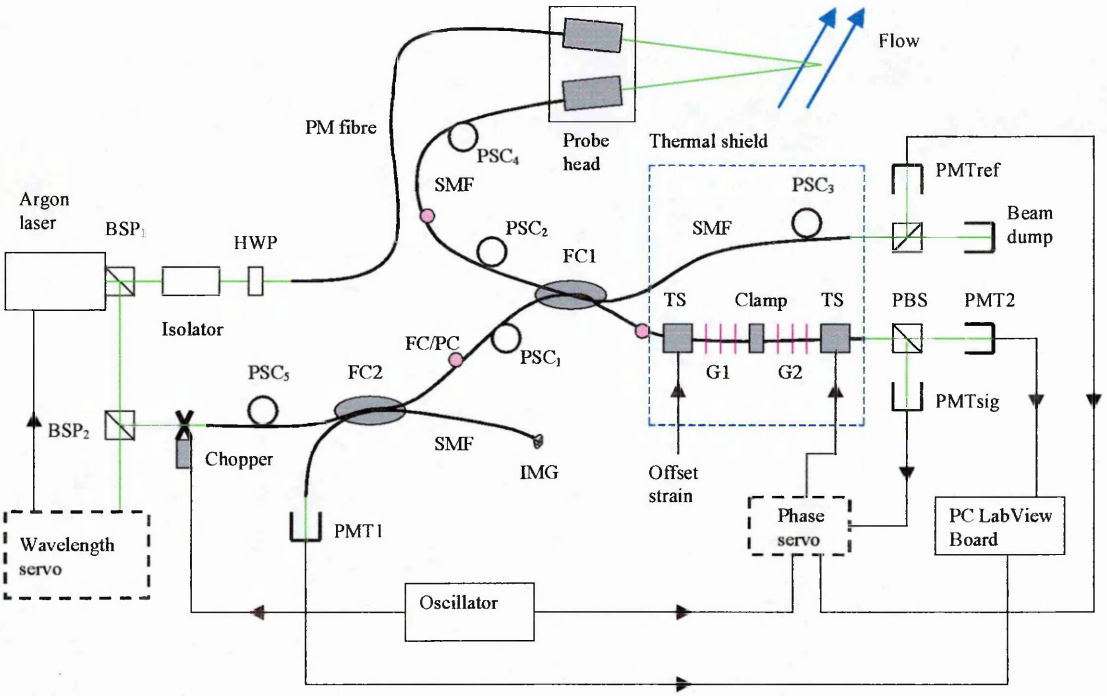

Figure 9. 16: Fibre-optic laser Doppler velocimeter configuration incorporating back-reflection mode and two independent feedback loops for the active stabilisation of the laser wavelength as well as the phase control of the Bragg-grating based Fabry-Perot interferometer.

BSP_1 (99:1) & BSP_2 (50:50) - beam splitter cubes, HWP - half wave plate, PM - polarisation maintaining, PSC - polarisation state controller, FC - directional coupler, SMF - single mode fibre, TS - translation stage, G - fibre Bragg grating, PBS - polarisation beam splitter cube, IMG - index matching gel, PMT- photomultiplier tube.

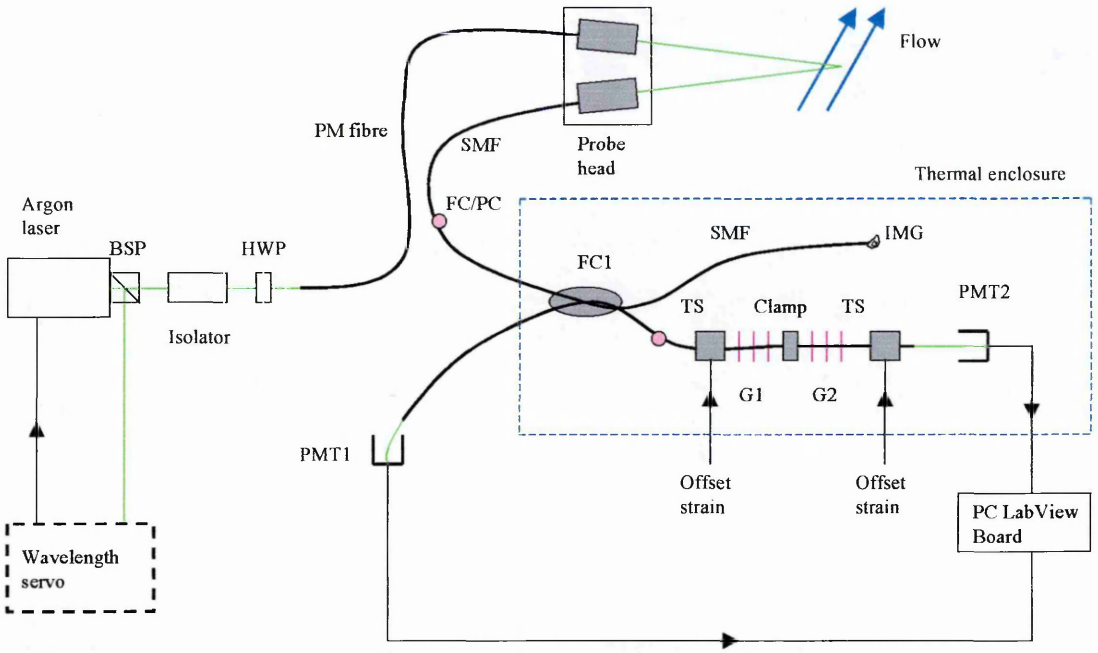

Figure 9. 17: Fibre-optic laser Doppler velocimeter configuration incorporating back-reflection mode and a feedback loop for the active stabilisation of the laser wavelength but no phase control of the Bragg-grating based Fabry-Perot interferometer.

BSP (50:50) - beam splitter cube, HWP - half wave plate, PM - polarisation maintaining, FC1 - directional coupler, SMF - single mode fibre, TS - translation stage, G - fibre Bragg grating, IMG - index matching gel, PMT- photomultiplier tube.

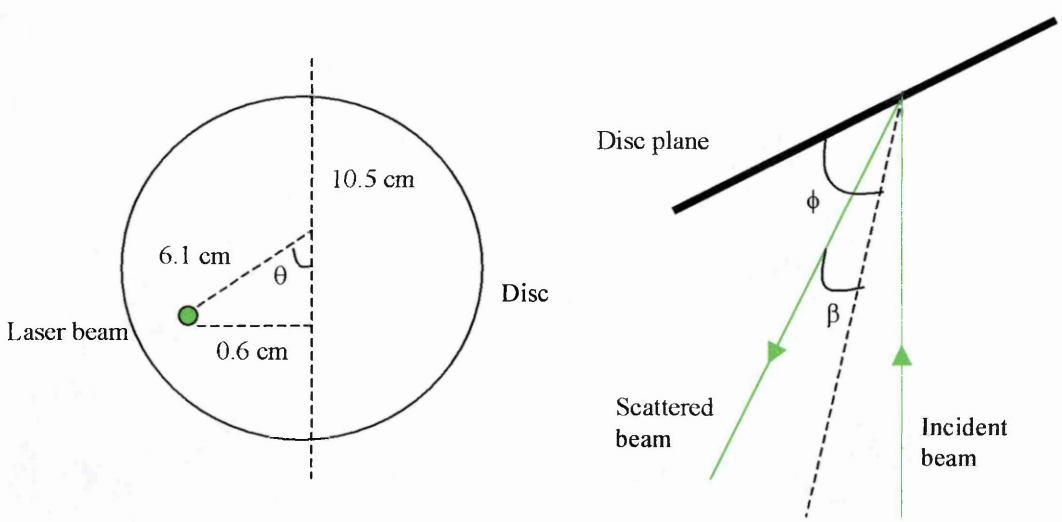

Figure 9. 18: Experimental geometry of the disc and angle definitions. $\phi = 79^0$ and $2\beta = 20^0$.

9.4.3 Velocity Results

The Doppler frequency to intensity conversion factor that was used for the calculation of velocity was 1.35 $[GHz]^{-1}$, which is the gradient of the filter transfer function. The velocity measurement range was ± 7 ms^{-1} while the velocimeter resolution was 0.2 ms^{-1} (Figure 9.19). The Doppler frequency-shift to velocity coefficient for the wheel configuration of Figure 9.18 was 0.73 MHz/ms^{-1}. There is a noticeable drift in the graph particularly in the positive velocity quadrant, which is a consequence of the signal drift of the velocimeter since the interferometer phase locking system was not used for the reasons discussed in section (9.4.2).

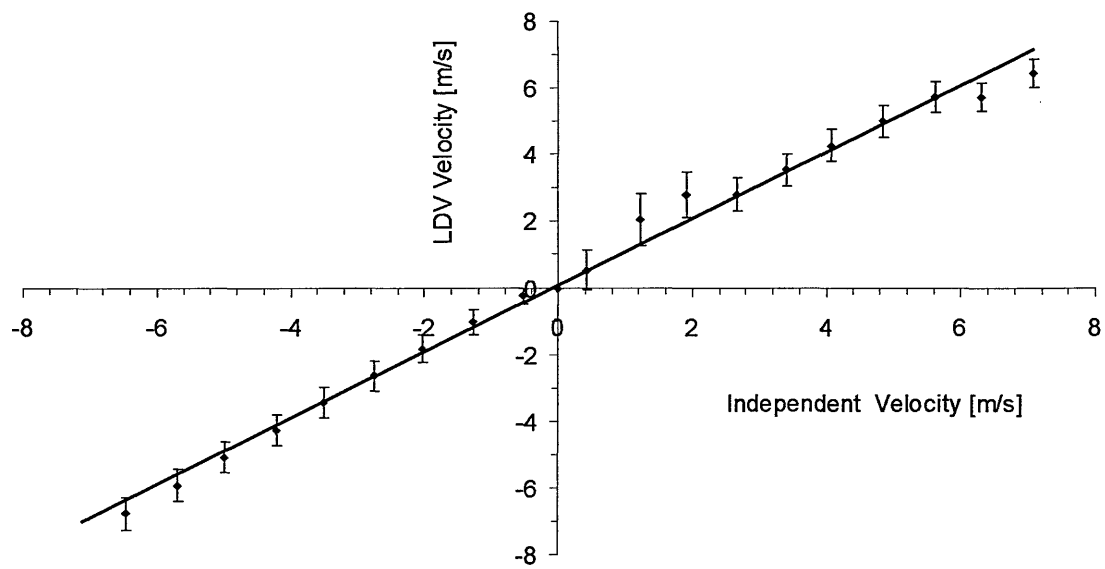

Figure 9. 19: Disc velocity measured by the experimental configuration of Figure 9.17 that incorporated signal detection in back reflection mode. The results were calculated using the gradient of the transfer function and are compared to those measured from the rotational frequency of the disc. The gradient of the fitted line is 0.9986 i.e. 0.14% deviation from unity.

A plot of the negative quadrant velocities alone (Figure 9.20) gave a linear graph with a standard deviation of 0.2 ms^{-1}, which is consistent with the phase drift of the filter since measurements were started from the negative end before this drift had taken effect. There is an offset of +0.3842 ms^{-1} in the velocimeter values which when subtracted would give an expected graph that passes through the origin. This zero error was due to the interpolation method used to obtain the zero value that was required as a reference

for calculation of the velocities. The interpolation had to be done on a data set with both positive and negative velocities. Figure 9.21 is the comparison of the Doppler frequency shift measured by the experiment and that calculated from the experimental geometry, the trend of which follows the velocity graph of Figure 9.19.

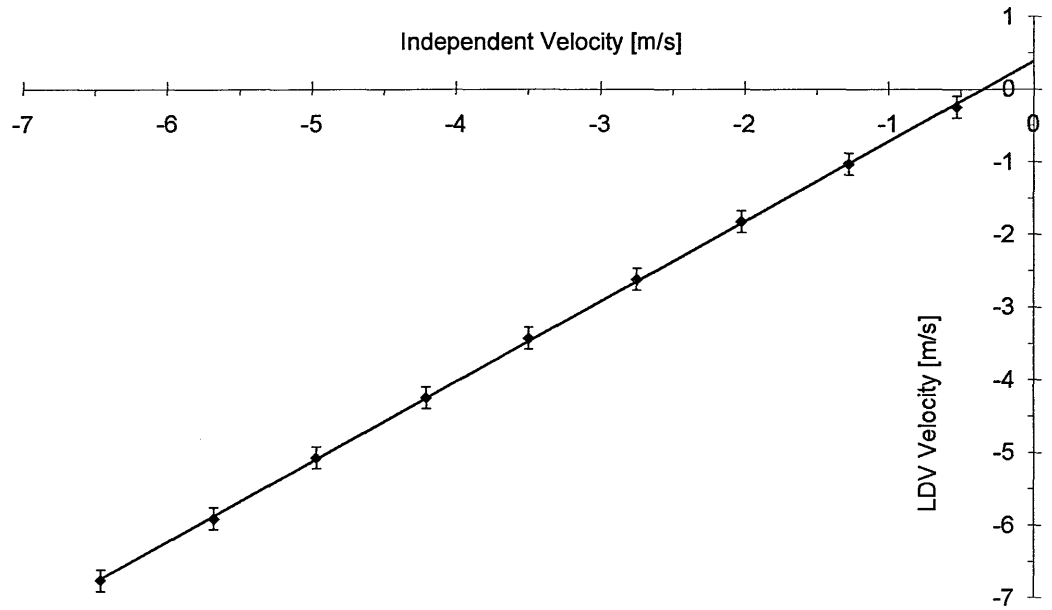

Figure 9. 20: A plot of negative velocity of Figure 9.19.

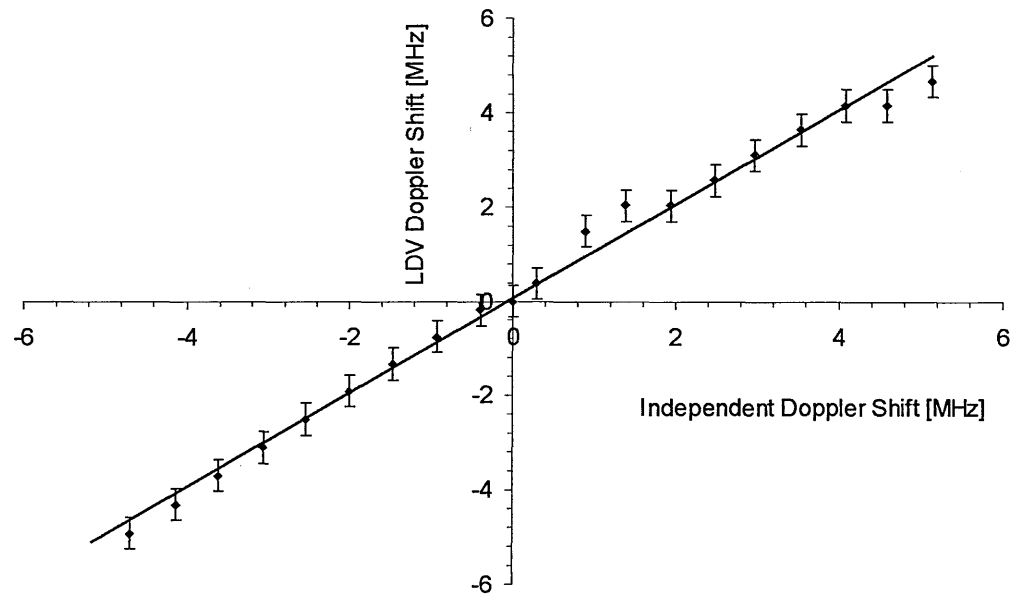

Figure 9. 21: Comparison of the Doppler frequency shift (LDV) from the velocimeter and experimental configuration (independent measurement).

9.5 Summary

This chapter presented three experimental configurations of a fibre-optic laser Doppler velocimeter based on a Bragg-grating Fabry-Perot interferometer as a frequency to intensity transducer. The initial configuration (Figure 9.1) revealed the presence of both interferometer phase drift and laser wavelength drift and the instrument could only be used over a limited velocity range, ±10 ms^{-1} with a standard deviation of 0.2 ms^{-1} i.e. before the drift had taken effect. The second configuration saw the implementation of drift compensation. This velocimeter configuration demonstrated the successful implementation of the new instrument in laboratory experimentation. Velocities of up to ± 42 ms^{-1} were measured from a rotating disc, the range of which was limited by the maximum speed of the motor used to drive the disc. The velocimeter resolution for the configuration was obtained as 0.4 ms^{-1}. The velocimeter demonstrated an advantage to obtain varying instrument sensitivities by strain-tuning the fibre FP filter e.g. the results presented in this chapter had the gradient of the transfer function separately tuned to 1.29, 1.35, and 1.67 $[GHz]^{-1}$. The final experimental configuration presented a unique attribute of this velocimeter that not only doubled the instrument sensitivity but also made low velocities accessible to measurement. The velocimeter resolution in stabilised mode was 0.2 ms^{-1} and the calculated standard deviation of the velocities was obtained as 0.2 ms^{-1}.

In all the measurements that were made it was the filter that was tuned to the laser wavelength such that directional velocity discrimination was achieved. This is a significant advantage when compared to planar Doppler velocimetry (PDV) where the iodine cell filter transfer function requires a tuneable laser source since the filter itself can not be tuned. Thus this thesis presents a system that offers yet another advantage with potentially large economic savings since it can be used with lasers that lack wavelength tuning. The velocimeter was designed around the use of an argon-ion laser but in principle any laser wavelength source could be used as Bragg grating Fabry-Perot interferometers or other interferometers as discussed in Chapter 4 could be fabricated at any preferred wavelength. Such versatility would be important particularly where

miniaturisation of instrument components may be paramount as miniature high power laser diode sources or solid state lasers are now available in the commercial market.

In conclusion, the new velocimeter was successfully designed and applied to velocity measurements over the full range that was available in the laboratory and the instrument could now be applied to measure flow velocities such as those in windtunnels and turbomachinery. The probe head may need slight modifications to include miniature polarisers in order to make it more efficient when using polarisation maintaining optical fibres.

References

[1] D. A. Egan, S. W. James, and R. P. Tatam, "*On-axis laser Doppler velocimetry for turbomachinery applications using optical fibre techniques*", Proceedings of SPIE: Optical Technology in Fluid, Thermal, and Combustion Flow 111, vol. 3172, pp. 17-26, 1997.

[2] H. Komine, S. J. Brosnan, A. B. Litton, and E. A. Stappaerts, "Real-*time Doppler global velocimetry*", 29th Aerospace Sciences Meeting, Paper AIAA-91-0337, Reno NV, 1991.

[3] I. P. Kaminow, "*Polarisation in optical fibres*", IEEE Journal of Quantum Electronics, QE17, pp. 15, 1981.

[4] R. Ulrich, S. C. Rashleigh and W. Eickhoff, "*Bending induced birefringence in single-mode fibre*", Optics Letters 5, pp. 173, 1980.

CHAPTER 10

Conclusions and Future Developments

The design, construction and application of the filter-based fibre-optic laser Doppler velocimeter have been described in the previous chapters of this thesis. The inclusion of this new instrument in laser Doppler velocimetry family has demonstrated a lot of potential and answers to some traditional problems.

10.1 In-line Velocimeter

10.1.1 Conclusions

An in-line laser Doppler velocimeter which utilised optical-fibre Bragg-grating Fabry-Perot interferometer was developed in a novel application to flow measurement. The motivation for such a design was triggered by the ever increasing industrial sophistication that impresses upon high accuracy in complex 3D flow measurements. There are many optical flow measurement techniques all of which have revealed some deficiency particularly in the in-line or on-axis component of velocity. Today's industry therefore presents a challenge to experimentalists to develop a 3D instrument capable of measuring all components with high resolution. It is desirable for the instrument to be capable of application to any given environment regardless of restriction on flow access, velocity range and nature of flow.

The market boasts of instruments such as the Doppler difference velocimeter and laser two focus anemometer that have acceptably high resolution for transverse velocity components but extremely low resolution for the on-axis component particularly in confined flows. The scanning FP interferometer, atomic or molecular absorption (iodine cell) filters and the reference beam laser Doppler velocimeter have been applied to the

measurement of the on-axis component with varying success. A bandwidth restriction on the reference beam technique has confined it to low velocities e.g. < 30 ms^{-1} for a processor of 120 MHz. Others measure high velocity with the FP interferometer measuring even higher velocities e.g. 600 ms^{-1} and higher. However the FP interferometer is susceptible to vibrations while the iodine absorption line has a finite bandwidth and resolution which impose an upper limit to the velocity range and resolution the instrument can measure. These short comings among many other traditional problems have set up the scene for the design and development for the velocimeter presented here which is essentially all fibre-based.

The system was implemented in three different configurations and was used to measure the velocity of a rotating disc in the velocity-range ± 20 ms^{-1}, ± 42 ms^{-1} and ± 7 ms^{-1}. The first configuration with a resolution of 0.9 ms^{-1} represented the original design of the instrument and it was from this set up that an experimental signal drift was observed. Such a configuration could only measure a small velocity range typically ± 12 ms^{-1} that gave a standard deviation of 0.2 ms^{-1}. This configuration was improved to cater for drift compensation and a full velocity range of ± 42 ms^{-1} was measured at a resolution of 0.4 ms^{-1}. This implementation saw the use of polarisation state controllers (PSC) to multiplex laser beams through the same singlemode fibre by polarisation, and 21 dB of cross-talk suppression was achieved. The light falling onto the rotating disc was of linear polarisation but the scattering was found to be completely depolarised. The scattered light had to be collected through a sheet of polariser, a process that reduced the signal strength due to the 50 % signal split between the 2 orthogonal polarisations and also material absorption. The laser had to be operated at maximum power.

The third experimental configuration was a unique set-up that automatically doubled the instrument resolution before any extra tuning to the filter was added. The disc geometry was adjusted for low velocity configuration, which the velocimeter measured as ± 7 ms^{-1} at resolution better than 0.2 ms^{-1}. This system was however implemented without drift compensation on the FP interferometer. This had to be done because detection in reflection mode with a pass through two directional couplers (split ratio 50 %) after the

sheet polariser reduced the signal intensity to only 12.5 % which resulted in poor signal to noise ratio (SNR). A single coupler was then used and with the polariser removed the detected signal was 50 % of the reflected signal. Also varied was the sensitivity, resolution and velocity range of the velocimeter by tuning the bandwidth of the FP filter in the range 400 – 800 MHz.

In the year 2001 my work won a bursary award from Bristol Industrial and Research Associates Limited (BIRAL, UK) and I was able to present a paper at the SPIE international conference on "Optical diagnostics for Fluids, Solids, and Combustion" in the USA.

10.1.2 Future Developments

i. The laser Doppler velocimeter has been fully developed for laboratory experiments and is considered ready for flow measurement applications with Cranfield University low and high speed turbomachinery test facilities. The test facilities pose turbulent environmental conditions in terms of temperature, draught and vibrations.

ii. There is a possibility of implementing the velocimeter in a simpler configuration that will not require polarisation multiplexing and demultiplexing. This means single mode fibres will be used without polarisation state controllers and polarisation beam splitters. Electronic filtering (Figure 10.1) could be used to separate the flow and pulse signals. The configuration reduces the use of PMTs from 4 to only 2, which has considerable implications on cost savings. Carefully designed band pass and high pass filters with appropriate roll-off and bandwidth characteristics will be required. The band stop filter will attenuate the pulse signal leaving the flow signal while the reverse is true with the high pass filter. Electronic filters however tend to introduce unwanted phase variations. The filters should therefore be designed around the Bessel filter that has excellent phase characteristics [1, 2].

iii. The current experimental configuration could be modified to constitute an all Hi-Bi fibre system. Polarisation maintaining (PM) directional couplers could be used while the fibre-optic Bragg grating filters could be fabricated in PM (Hi-Bi) optical fibre. Such a configuration enhances beam multiplexing using polarisation while signal drift that may be caused by thermal instabilities is minimised or eliminated.

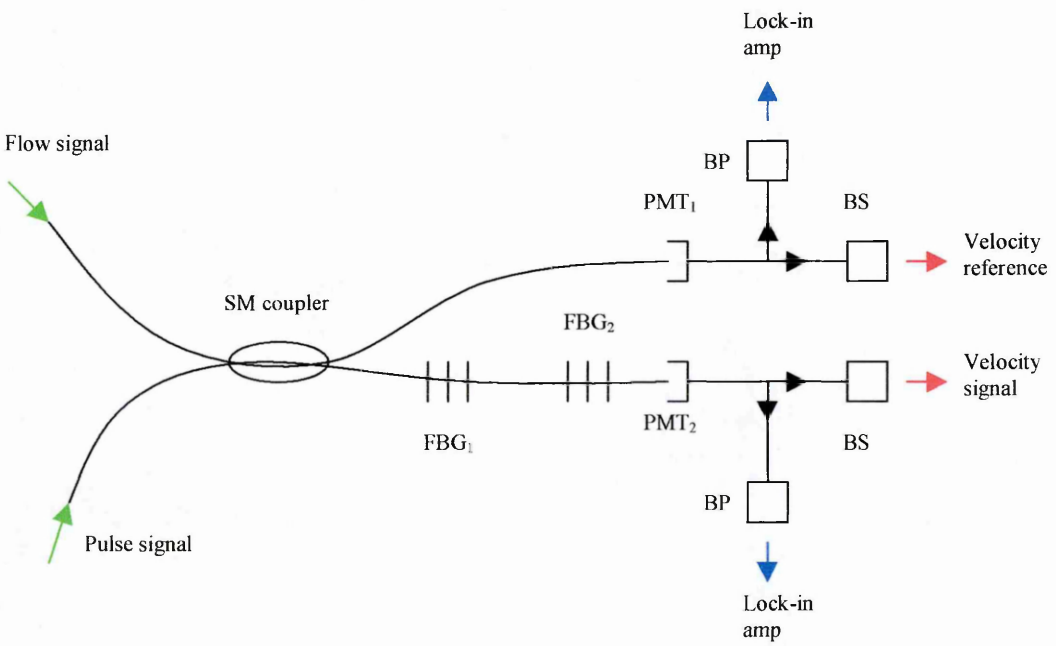

Figure 10. 1: Signal demultiplexing by electronic filtering.

SM – single mode, FBG – fibre Bragg grating, PMT – photomultiplier tube, BP – bandpass, BS – bandstop, amp – amplifier.

10.2 Experimental Drift

10.2.1 Conclusions

The experimental measurement technique involves transduction of Doppler frequency shifts into light intensity. This means any instability in light intensity and frequency from any part of the experiment may be falsely interpreted as a velocity changes. The instability could arise from the laser, FP interferometer and spurious signals from additional interferometers formed between fibre ends. Spurious signals have been

suppressed by using index matching gel at the fibre ends and by angle-polishing fibre ends at 8^0 where appropriate.

The argon-ion laser wavelength was locked at the 50 % transmission point on a corresponding Doppler broadened absorption line of molecular iodine vapour (514.5 nm). The system was implemented in an active closed-loop feedback format by actuating the optical path length of an intra-cavity FP etalon through heating and cooling mechanism. The laser that previously drifted by typically 600 MHz in about 2 hours could be stabilised to within 10 MHz over time duration of at least one hour that was sufficient for the velocimeter (Chapter 8). A custom designed 3-term PID electronic controller was used to provide the control signal over a control range of ± 500 MHz (Appendix D). The normalised signal through the iodine cell was expected to be constant for no wavelength jitter or drift.

An independent feedback control loop was set up to monitor and compensate for phase changes of the signal through the FP interferometer using digital lock-in amplifiers (Chapter 8). Another PID circuit controller provided the control signal that was fed-back to the FP interferometer to make tiny length adjustments using a piezoelectric actuator and a stability of within 5 MHz was achieved (Appendix E).

10.2.2 Future Developments

The current stabilisation system has proved sufficient for laboratory conditions but its performance in Cranfield university turbomachinery testing facilities which are expected to be harsh is not known. We suggest additional precautions that may be implemented to ensure sufficient stability under harsh environmental conditions.

i. I recommend that the laser be operated from temperature controlled cabinet to avoid drastic temperature fluctuations. Our laboratory has since installed successfully a similar cabinet to a Nd: YAG laser.

ii. There is scope for yet another active stabilisation scheme that could be applied to the velocimeter. The phase changes on the FP interferometer could be detected as before using lock-in amplifiers then feedback the control signal from the PID circuit controller to the laser instead of feeding back to the interferometer. Such a system will make the laser track the FP interferometer as it drifts. I note that this may not be the most favourable method as the laser has a limited tuning range. Considerations will also have to be taken concerning the response of the laser as this is governed by the expansion and contraction of the glass etalon.

iii. The signal drift from the Bragg-grating based FP interferometer is mainly from temperature fluctuations. We have compensated for this by actuating the length of the FP cavity. The feasibility of stabilising the temperature of the interferometer rather than compensate for it was also studied. I propose a simple system based on peltier elements and negative temperature coefficient (NTC) thermistors as sensors arranged in a Wheatstone bridge format. The greater the number of such sensors the higher the resolution e.g. 2 sensors give twice the sensitivity. More information on sensor arrangement and performance is given in Appendix F. The response of the optical fibre to temperature may be slower and the integrated temperature effect on the fibre needs to be measured.

iv. Fibre-optic telecommunications has introduced compact packaging systems for fibre-optic Bragg grating devices that feature strain and temperature compensation. Thermal drift better than 0.5 pm/^{0}C over a temperature range of -10 ^{0}C to 70 ^{0}C have been achieved [3, 4]. A similar design that could include an additional active temperature stabilisation using peltier elements and NTC thermistors could be used (Figure 10.2). The Bragg gratings forming the FP filter cavity could be athermalised and the package be fitted with strain relief boots for passive temperature and strain compensation. Additional active temperature control may be applied by fitting an external package that is fitted with Peltier temperature controller.

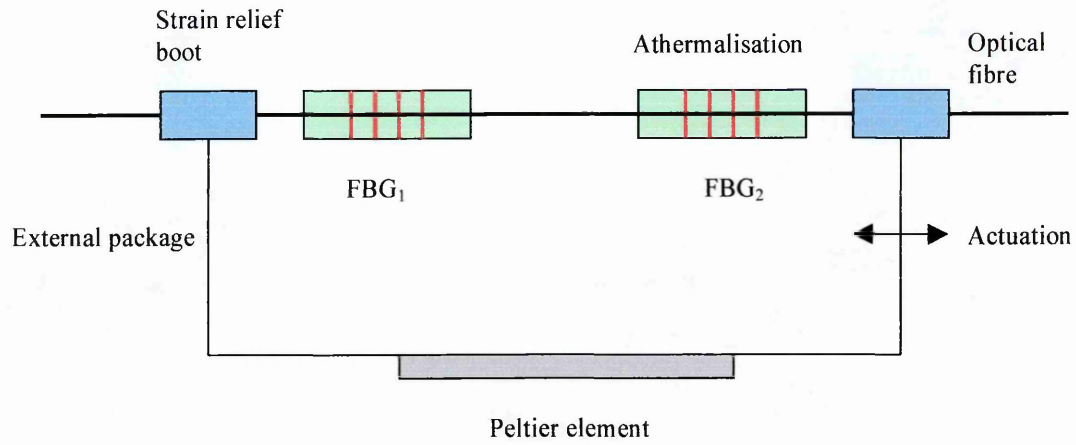

Figure 10. 2: Bragg grating packing with passive strain and temperature compensation as well as active temperature stabilisation.

10.3 Fibre-Optic Bragg-Grating Based Filters

10.3.1 Conclusions

Theoretical models were developed based on coupled-mode theory and transfer matrix approach to determine suitable Bragg grating filters to use as frequency to intensity transducers in a laser Doppler velocimeter system. The programming code in Fortran90 is given in Appendix B. The main requirement of the filters was to have narrow bandwidths of approximately 3 GHz and less.

End-pumped gratings were especially attractive due to their narrow bandwidth controlled by their length and their wavelength that forms at the exact laser wavelength. I could not however source the proper photosensitive fibre at 514.5 nm or 488 nm as the market is biased towards the longer telecommunications wavelengths and thus the fabricated gratings could only get to a maximum reflectivity of 12 %.

The FP filter models showed that high sensitivity for frequency to intensity conversion was obtainable from a combination of high finesse and small free spectral range (FSR). It was also shown that there is a cavity length corresponding to a thermally stable FP

filter and this could be considered for fabricating such filters. The filter fabrication technique adopted was easy to implement but could not guarantee the desired specifications. The velocimeter was operated with FP filters fabricated this way with FRS at 1.6 GHz and 3.2 GHz.

10.3.2 Future Developments

i. The FBGs of the FP filters that were fabricated did not have identical wavelength, bandwidth and reflectivity and furthermore these wavelengths did not match the laser wavelength. Also the FBGs had narrow bandwidths making it difficult to produce optimum cavity tuning to achieve high visibility for the interferometer. I therefore perceive that the working visibility of about 25 % was not the optimum. This therefore restricted the velocimeter sensitivity and velocity range. I propose future work to involve custom design of phase masks that would allow the fabrication of filters of the desired specifications. This will allow both FBGs to have same wavelength that is matched to that of the laser thus giving near optimised cavity. It will be desirable to chirp the phase mask so as to ease the FP cavity tuneability as the gratings will have wider wavelength bandwidths. There is the possibility also to implement passive strain and temperature compensation to the FP cavity by inscription of appropriate chirp in the phase mask.

ii. I have also investigated distributed feedback gratings (DFG) that are fabricated by incorporating a phase step in the grating. My models have shown that these form narrow bandwidths that make the filters suitable for our velocimetry application. Such gratings will be fabricated more easily by using properly designed phase masks. These filters being much smaller in size compared to FP filters will be more favourable particularly as it becomes easier to stabilise them. Compact packaging also incorporating athermalisation will be easier to implement.

iii. Moiré gratings were considered in the models and revealed that they can be as DFGs in almost all features. The inscription of these will however be a bit tricky as it involves fabricating 2 nearly identical gratings at the same place but slightly differing in wavelength. It is the control in the magnitude of the wavelength difference ~0.04 nm that will be difficult to make precisely. The same wavelength difference determines the shape and size of the bandpass of the filter.

iv. There is continual advancement in the development of high power lasers sources that could meet the demands of flow measurement instruments. Coherent, for example, have developed a high power solid state laser at 532 nm with output powers as high as 10 W [5]. Such a laser lacking wavelength tuning facility will not be compatible with iodine cells. We propose fabricating Bragg-grating based filters at wavelengths that correspond to high power laser sources and utilise the filter tuning facility.

Reference

[1] G. B. Clayton, "*Linear Integrated Circuit Applications*", Macmillan Press, 1997.

[2] R. G. Irvine, "*Operational Amplifier Characteristics and Applications*", Prentice Hall, 1981.

[3] Gould Fiber Optics Product Catalogue.

[4] D. L. Weidman, G. H. Beall, K. C. Chyung, G. L. Francis, R. A. Modavis, R. M. Morena, "*A novel negative expansion substrate material for athermalizing fiber Bragg gratings*", 22nd European Conference on Optical Communication, Oslo, 1996.

[5] Verdi V2/V5 and V8/V10 Data Sheet.

APPENDIX A

The Doppler Frequency Shift

The concept of the Doppler shift in frequency of electromagnetic radiation is well established and it takes place whenever there is relative motion between the source, observer, and intervening medium. Laser Doppler velocimetry considers the source and observer to be stationary relative to each other and the Doppler shift is caused by a moving particle in the medium. This interaction is illustrated in Figure A.1.

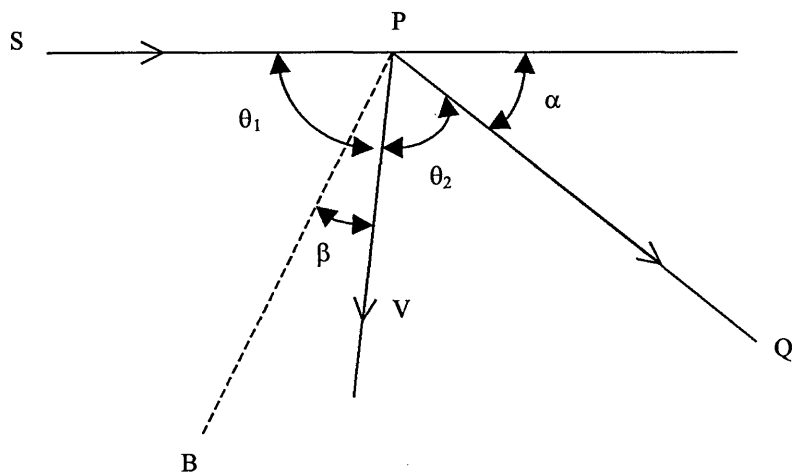

Figure A. 1: The Doppler shift from scattered light.

S – source, Q – observation direction, P – particle, B – bisector of angle SPQ, V – measured velocity component.

Consider light of frequency, ν from a source, S that is intercepted by a particle, P such that the scattered light is observed at position, Q. Suppose θ_1 and θ_2 are the angles made with PS and PQ by the direction of motion of the particle, then the frequency of light observed by P is given [1]

$$\nu' = \frac{\nu}{\left(1 - {}^{V^2}/_{C^2}\right)} \cdot \left(1 + \frac{V}{C} \cdot \cos\theta_1\right) \qquad \text{(A.1)}$$

The particle re-emits light of this frequency which is received by the observer at Q as ν'' where

$$\nu'' = \frac{\nu' \cdot \sqrt{\left(1 - {}^{V^2}/_{C^2}\right)}}{1 - \left({}^{V}/_{C}\right) \cdot \cos\theta_2} \qquad \text{(A.2)}$$

It can be shown that

$$\frac{\nu''}{\nu} = \frac{1 + \left({}^{V}/_{C}\right) \cdot \cos\theta_1}{1 - \left({}^{V}/_{C}\right) \cdot \cos\theta_2} \qquad \text{(A.3)}$$

Equation (A.3) is expanded to first order in (v/c) for $v << c$ to give

$$\Delta\nu = \nu'' - \nu = \frac{\nu V}{C} \cdot \left(\cos\theta_1 + \cos\theta_2\right) \qquad \text{(A.4)}$$

Equation (A.4) can be transformed to

$$\Delta\nu = \frac{2\nu V}{C} \cdot \cos\left(\frac{\theta_1 + \theta_2}{2}\right) \cdot \cos\left(\frac{\theta_1 - \theta_2}{2}\right) \qquad \text{(A.5)}$$

It is deduced from Figure A.1 that the scattering angle, α is given by

$$\alpha = \pi - \left(\theta_1 + \theta_2\right)$$

and

$$\sin\left(\frac{\alpha}{2}\right) = \cos\left(\frac{\theta_1 + \theta_2}{2}\right) \qquad \text{(A.6)}$$

In Figure A.1, β is an angle that defines the scattering vector and it also represents the momentum change of the radiation on scattering.

$$\beta = \frac{\theta_1 - \theta_2}{2} \qquad \text{(A.7)}$$

The Doppler shift from the scattered light is given by

$$\frac{\Delta\nu}{\nu} = \frac{2V}{C} \cdot \cos\beta \cdot \sin\left(\frac{\alpha}{2}\right)$$

or

$$\Delta\nu = \frac{2V}{\lambda} \cdot \cos\beta \cdot \sin\left(\frac{\alpha}{2}\right) \qquad \text{(A.8)}$$

Equation (A.8) shows that the Doppler shift depends on the bisector of the scattering angle and the component of the particle velocity in the direction of the scattering vector.

References

[1] L. E. Drain, "*The Laser Doppler Technique*", a Wiley-Interscience Publication, 1980.

APPENDIX B

Fortran90 Programs for Fibre Optic Filters

Computer programs were written in Fortran 90 based on the transfer matrix approach and coupled mode theory as described in chapter 5. The first program analyses the transfer function of normal Bragg gratings, chirped Bragg gratings, distributed feedback gratings and Fabry-Perot gratings including effects of strain and temperature perturbations using the transfer matrix approach (Figure A.1). The second program is a transfer matrix model of a Moiré grating while the third is a coupled mode theory model of a Fabry-Perot interferometer grating based on an analytical solution (Chapter 5). The program for the coupled mode theory is not given here for a normal Bragg grating because the theory is standard and analytical solutions are common elsewhere in the literature. Figure B.1 is the flow chart for the first program.

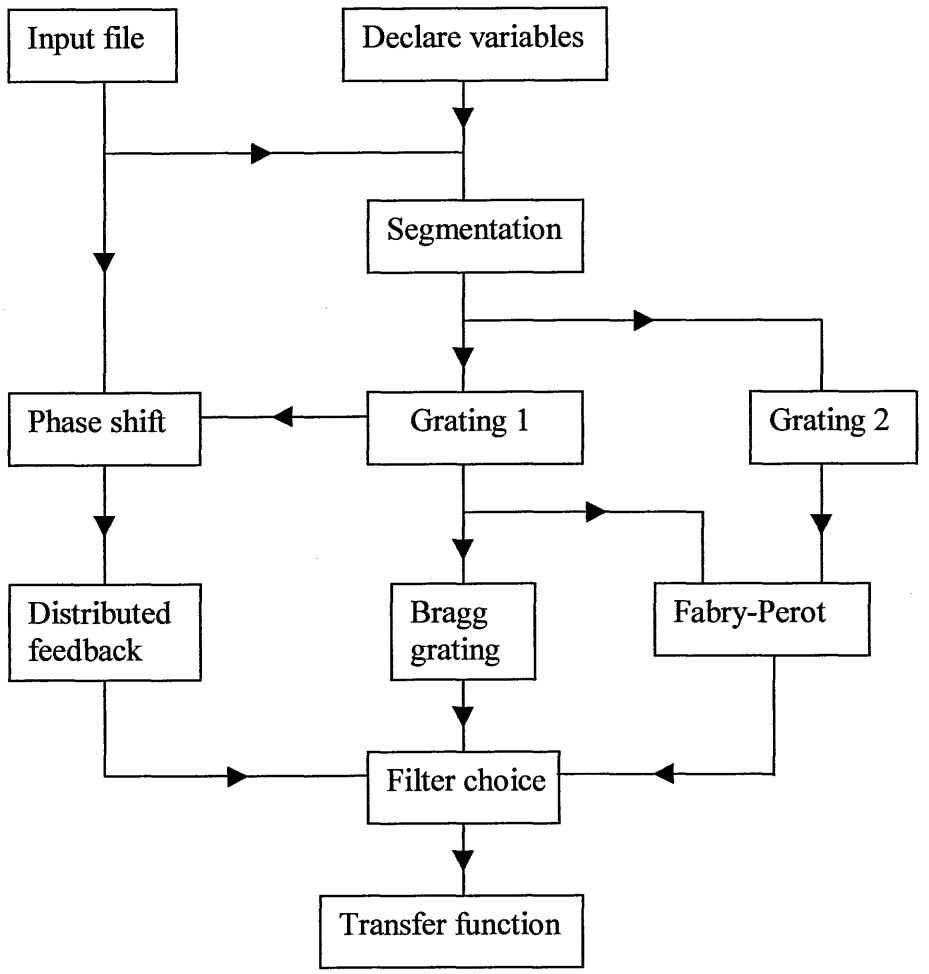

Figure B. 1: Transfer matrix model flow chart for Bragg grating, distributed feedback and Fabry-Perot filters.

```
PROGRAM MATRIX

!****************************************************************

! THIS PROGRAM DOES THE IN-FIBRE BRAGG GRATING, FABRY-PEROT, AND
! DISTRIBUTED FEED BACK GRATING CHARACTERISATION USING A
! TRANSFER MATRIX MODEL

!****************************************************************

! DEFINITION OF PARAMETERS USED

! L - grating length
! N - number of uniform sections into which the grating is
! divided
! n0 - unirradiated index of the fibre
! delta_ndc - average dc refractive index modulation
! V - fringe visibility constant
! chirpgrad - chirp gradient of the design wavelength (chirp per
! unit length of grating)
```

```
! Pa - apodisation period for garting 1
! Pa2 - apodisation period for grating 2
! delta_ndceff - effective dc index change as defined at centre
! of any given section and incorporates the modulation due to
! the Gaussian profile of the laser beam.
! neff - effective index of each grating section
! g - dc coupling coefficient
! lamdaBB - Bragg wavelength/nm
! lamda_B - bragg wavelength in nm
! k - ac coupling coeffient
! phasegrad - phase gradient due to chirp gradient in the bragg
! wavelength d - total detuning parameter for first grating
! gg - general dc self-coupling coeffiecient
! U - wavelength resolution for grating characterisation
! width - bandwidth in wavelength for which characterisation is
! carriedout about the bragg wavelength.
! lamdastart - wavelength at which characterisation starts.
! Po - nominal grating period
! Q - phase shift
! TP - phase-shift matrix
! POINT - position of the grating where phase-shift is inserted
! dTz - temperature gradient for first grating
! dt - temperature detuning for first grating
! ds - strain detuning for first grating
! de - strain gradient of first grating
! dt2 - temperature detuning for second grating
! dTT - temperature gradient for second grating
! ds2 - strain detuning for second grating
! dee - strain gradient of second grating
! d2 - total detuning parameter for second grating

! hc - cavity length for the Fabry-Perot
! Temp - temperature change around the cavity length
! x1 - unperturbed cavity length of the Fabry-Perot filter

!*************************************************************


! DECLARATION OF VARIABLES AND SETTING UP INPUT/OUTPUT FILES


IMPLICIT NONE

INTEGER:: N, I, J, U, POINT, x

INTEGER:: N2, I2, POINT2, control

PARAMETER NN = 100000

REAL:: lamdaB(NN), neff(NN), lamdaB2(NN), neff2(NN)

DOUBLE PRECISION:: L, pi, dL, n0, delta_ndc, chirpgrad, Pa, z
DOUBLE PRECISION:: delta_ndceff, Po, lamda, a1, b1, TRANS, V
DOUBLE PRECISION:: g, lamdaBB, lamda_B, k, phasegrad, d, gg,
DOUBLE PRECISION:: Y, A, B, C, width, lamdastart, lamda2, REF
DOUBLE PRECISION:: cs, ss, Q, m

DOUBLE PRECISION:: L2, dL2, z2, delta_ndceff2, delta_ndc2, Pa2
DOUBLE PRECISION:: lamda_B2, lamdaBBB, g2, k2, phasegrad2,
```

```
DOUBLE PRECISION:: chirpgrad2, d2, gg2, V2, Po2
DOUBLE PRECISION:: a2, b2, Y2, AA, BB, CC, Q2, m2, cs2, ss2

DOUBLE PRECISION:: cfp, sfp, x1, hc, Temp

DOUBLE PRECISION:: dd, dTz, dt, ds, de, dd2, dt2, dTT, ds2

COMPLEX:: F11, F21, F12, F22, E, H, T11, T22, T12, T21

COMPLEX:: FF11, FF12, FF21, FF22, TT11, TT12, TT21, TT22

COMPLEX:: FP11, FP12, FP21, FP22, E1, H1

COMPLEX, DIMENSION(2,2):: F, R, TP

COMPLEX, DIMENSION(2,2):: F2, R2, TP2

COMPLEX, DIMENSION(2,2):: FP, RF, RFR

OPEN (UNIT = 1, FILE = "Input.txt", STATUS = "Unknown")
OPEN (UNIT = 2, FILE = "Profile.dat", STATUS = "Unknown")

READ (1, *) L
READ (1, *) N
READ (1, *) n0
READ (1, *) delta_ndc
READ (1, *) V
READ (1, *) chirpgrad
READ (1, *) Pa
READ (1, *) lamdaBB
READ (1, *) U
READ (1, *) lamdastart
READ (1, *) width
READ (1, *) m
READ (1, *) POINT
READ (1, *) L2
READ (1, *) N2
READ (1, *) delta_ndc2
READ (1, *) v2
READ (1, *) chirpgrad2
READ (1, *) Pa2
READ (1, *) lamdaBBB
READ (1, *) m2
READ (1, *) POINT2
READ (1, *) x
READ (1, *) Temp
READ (1, *) dTz
READ (1, *) de
READ (1, *) dTT
READ (1, *) control

CLOSE (1)


!CALCULATION OF CONSTANT TERMS


pi = 4*DATAN(1.D0)
lamda_B = lamdaBB * 1.0D-9
```

```
Po = lamda_B/(2*n0)

dL = L/FLOAT(N)

Q = m * pi
cs = DCOS(Q/2)
ss = DSIN(Q/2)

T11 = CMPLX(cs, -1*ss)
T12 = CMPLX(0, 0)
T21 = CMPLX(0, 0)
T22 = CMPLX(cs, ss)

TP = RESHAPE((/T11, T21, T12, T22/), (/2,2/))

dL2 = L2/FLOAT(N2)

lamda_B2 = lamdaBBB * 1.0D-9
Po2 = lamda_B2/(2*n0)

Q2 = m2 * pi
cs2 = DCOS(Q2/2)
ss2 = DSIN(Q2/2)

TT11 = CMPLX(cs2, -1*ss2)
TT12 = CMPLX(0, 0)
TT21 = CMPLX(0, 0)
TT22 = CMPLX(cs2, ss2)

TP2 = RESHAPE((/TT11, TT21, TT12, TT22/), (/2,2/))

x1 = x * 0.2D-3


! CALCULATION OF THE REFLECTIVITY OF ONE BRAGG GRATING,
! INCORPORATING CHIRP, STRAIN AND TEMPERATURE DETUNING ON THE
! GRATING THAT IS DIVIDED INTO SECTIONS OF EQUAL WIDTH


DO J = 0, U

 WRITE (*, *) J

 lamda2 = lamdastart + (width * FLOAT(J)/FLOAT(U))
 lamda = lamda2 * 1.0D-9

   DO I = 1, N

    z = (FLOAT(I) - 1/2)*dL

    delta_ndceff = delta_ndc * DEXP(-1*(N*z/Pa) **2)

    neff(I) = n0 + delta_ndceff * (1+(V*DCOS(2*pi*z/Po)))

      IF (I==1) THEN

      lamdaB(I) = lamda_B

      ELSE
```

```
    lamdaB(I) = 2 * neff(I) * Po

    END IF

  g = 2 * pi * delta_ndceff/lamdaB(I)

  k = pi * V * delta_ndceff/lamdaB(I)

  phasegrad = -4 * pi * neff(I) * (z-(L-dL)/2) * chirpgrad/\
    (lamdaB(I) **2)

    dd = 2 * pi * neff(I) * ((1/lamda) - (1/lamdaB(I)))

    dt = ((9.15D-6)*2*pi*n0/lamdaB(I))*1*dTz              !

    ds = (1.42*pi*n0/lamdaB(I))*1*de                      !

    d = dd + dt + ds


    gg = d + g - phasegrad

    a1 = k * k
    b1 = gg * gg

    IF (a1>b1) THEN

  Y = DSQRT(a1-b1)
    A =   DCOSH(Y * dL)
    B = -1 * gg * DSINH(Y * dL)/Y
    C = k * DSINH(Y * dL)/Y

    ELSE IF (a1<b1) THEN

  Y = DSQRT(b1-a1)
    A = DCOS(Y * dL)
    B = -1 * gg * DSIN(Y * dL)/Y
    C = k * DSIN(Y * dL)/Y

    END IF

    F11 = CMPLX(A, B)
    F21 = CMPLX(0, C)
    F12 = CONJG(F21)
    F22 = CONJG(F11)

    F = RESHAPE((/F11, F21, F12, F22/), (/2,2/))

    IF (I==1) THEN

    R = F

    ELSE IF (I/=1 .AND. I/=POINT) THEN

    R = MATMUL(R, F)

    ELSE IF (I==POINT) THEN

    R = MATMUL(R, TP)
```

```
      END IF

  END DO


! CALCULATION OF THE REFLECTIVITY OF A SECOND BRAGG GRATING,
! INCORPORATING CHIRP, STRAIN AND TEMPERATURE DETUNING ON THE
! GRATING THAT IS DIVIDED INTO SECTIONS OF EQUAL WIDTH



  DO I2 = 1, N2

    z2 = hc + L2 + (FLOAT(I2) - 1/2)*dL2

    delta_ndceff2 = delta_ndc2 * DEXP(-1*(N2*z2/Pa2) **2)

    neff2(I2) = n0 + delta_ndceff2 * (1+(V2*DCOS(2*pi*z2/Po2)))

      IF (I2==1) THEN

      lamdaB2(I2) = lamda_B2

      ELSE

      lamdaB2(I2) = 2 * neff2(I2) * Po2

      END IF

    g2 = 2 * pi * delta_ndceff2/lamdaB2(I2)

    k2 = pi * V2 * delta_ndceff2/lamdaB2(I2)

    phasegrad2 = -4 * pi * neff2(I2) * (z2-(L2-dL2)/2) * \
      chirpgrad2/(lamdaB2(I2) **2)


      dd2 = 2 * pi * neff2(I2) * ((1/lamda) - (1/lamdaB2(I2)))

      dt2 = ((9.15D-6)*2*pi*n0/lamdaB2(I2))*1*dTT      !

      ds2 = (1.42*pi*n0/lamdaB2(I2))*1*de              !

      d2 = dd2 + dt2 + ds2


      gg2 = d2 + g2 - phasegrad2

      a2 = k2 * k2
      b2 = gg2 * gg2

      IF (a2>b2) THEN

    Y2 = DSQRT(a2-b2)
      AA =  DCOSH(Y2 * dL2)
      BB = -1 * gg2 * DSINH(Y2 * dL2)/Y2
      CC = k2 * DSINH(Y2 * dL2)/Y2

      ELSE IF (a2<b2) THEN
```

```
      Y2 = DSQRT(b2-a2)
      AA = DCOS(Y2 * dL2)
      BB = -1 * gg2 * DSIN(Y2 * dL2)/Y2
      CC = k2 * DSIN(Y2 * dL2)/Y2

      END IF

      FF11 = CMPLX(AA, BB)
      FF21 = CMPLX(0, CC)
      FF12 = CONJG(FF21)
      FF22 = CONJG(FF11)

      F2 = RESHAPE((/FF11, FF21, FF12, FF22/), (/2,2/))

      IF (I2==1) THEN

      R2 = F2

      ELSE IF (I2/=1 .AND. I2/=POINT2) THEN

      R2 = MATMUL(R2, F2)

      ELSE IF (I2==POINT2) THEN

      R2 = MATMUL(R2, TP2)

      END IF

  END DO

! CALCULATION OF THE PHASE SHIFT RESULTING FROM TEMPERATURE
! PERTURBATIONS AROUND THE UNPERTUBED CAVITY LENGTH OF THE
! FABRY-PEROT FILTER

  IF (control==1) THEN

      hc = (2+de)*x1/2

      ELSE IF(control==2) THEN

      hc = (1+de)*x1

      ELSE

      hc = x1

  END IF

  cfp = DCOS(2*pi*n0*hc/lamda + (100*x1*Temp))
  sfp = DSIN(2*pi*n0*hc/lamda + (100*x1*Temp))

  FP11 = CMPLX(cfp, -1*sfp)
  FP12 = CMPLX(0, 0)
  FP21 = CMPLX(0, 0)
  FP22 = CMPLX(cfp, sfp)

  FP = RESHAPE((/FP11, FP21, FP12, FP22/), (/2,2/))
```

```
! SELECTION OF FILTER TYPE AND EVALUATION OF THE REFLECTIVITY
! AND TRANSMISSION

  SELECT CASE (x)

  CASE (0)

  E = R(1,1)
  H = R(2,1)

  IF (E/=0) THEN

  REF = (ABS(H/E)) **2
  TRANS = 1 - REF

  ELSE

  REF = 1
  TRANS = 0

  END IF

  CASE DEFAULT

  RF = MATMUL(R, FP)
  RFR = MATMUL(RF, R2)

  E1 = RFR(1,1)
  H1 = RFR(2,1)

  IF (E1/=0) THEN

  REF = (ABS(H1/E1)) **2
  TRANS = 1 - REF

  ELSE

  REF = 1
  TRANS = 0

  END IF

  END SELECT

  WRITE (2, *) lamda2, TRANS, REF

END DO

CLOSE (2)

END PROGRAM MATRIX
PROGRAM MOIREGRATING

!*************************************************************

! THIS PROGRAM DOES THE IN-FIBRE MOIRE GRATING CHARACTERISATION
! USING THE TRANSFER MATRIX METHOD

!*************************************************************
```

```
! DEFINITIONS OF PARAMETERS USED

! L - length of grating
! N - number of uniform subdivisions of the grating
! n0 - unirradiated index of the fibre
! delta_nac - ac index modulation of each grating
! chirpgrad - chirp gradient of the design wavelength of the
! grating
! lamdaBB1 - Bragg wavelength/nm for one grating
! lamdaBB2 - Bragg wavelength/nm for the second grating
! P1 and P2 are respectively the periods of the two gratings
! dL - length of each uniform section of the grating
! lamdastart - wavelength at which characterisation starts
! width - bandwidth in wavelength for which characterisation is
! carriedout about the grating centre-wavelength.
! Ps - rapidly varying grating component
! Pc - slowly varying component of the grating
! neff - effective beat index of the two gratings forming the
! moire grating
! g - term that acts like a dc coupling coefficient
! k - ac coupling coefficient
! chirpgrad - chirpgradient of the design wavelength
! phasegrad - phase gradient due to chirpgradient in the
! wavelength
! d - detuning parameter

!*************************************************************

! DECLARATION OF VARIABLES AND SETTING UP INPUT/OUTPUT FILES


IMPLICIT NONE

INTEGER:: N, J, U, I

DOUBLE PRECISION:: L, n0, delta_nac, pi, lamdaBB1, lamdaB1
DOUBLE PRECISION:: lamdaBB2, lamda2, d, phasegrad
DOUBLE PRECISION:: lamdaB2, P1, P2, dL, lamdastart, width
DOUBLE PRECISION:: lamda, z, Ps, Pc, neff, g, k, chirpgrad
DOUBLE PRECISION:: gg, a1, b1, Y, A, B, C, REF, TRANS

COMPLEX:: F11, F12, F21, F22, E, H

COMPLEX, DIMENSION(2,2):: F, R

OPEN (UNIT = 1, FILE = "Input.txt", STATUS = "Unknown")
OPEN (UNIT = 2, FILE = "Profile.dat", STATUS = "Unknown")

READ (1, *) L
READ (1, *) N
READ (1, *) n0
READ (1, *) delta_nac
READ (1, *) lamdaBB1
READ (1, *) lamdaBB2
READ (1, *) U
READ (1, *) lamdastart
READ (1, *) width
READ (1, *) chirpgrad
```

```
CLOSE (1)

! CALCULATION OF CONSTANT TERMS

pi = 4 * DTAN(1.D0)

lamdaB1 = lamdaBB1 * 1.0D-9
lamdaB2 = lamdaBB2 * 1.0D-9
P1 = lamdaB1/(2*n0)
P2 = lamdaB2/(2*n0)
dL = L/FLOAT(N)

! CALCULATION OF THE TRANSFER FUNCTION INCORPORATING
! CHIRP

DO J = 0, U

  WRITE (*,*) J

  lamda2 = lamdastart + (width * FLOAT(J)/FLOAT(U))
  lamda = lamda2 * 1.0D-9

  DO I = 1, N

    z = (FLOAT(I) - (1/2)) * dL

      Ps = 2*P1*P2/(P1 + P2)
      Pc = 2*P1*P2/(P1 - P2)

      neff = n0 + 2 * delta_nac * (1 + (DCOS(2*pi*z/Pc) * \
      DCOS(2*pi*z/Ps)))
      g = 4*pi*delta_nac/(2*n0*Ps)
      k = 2*pi*delta_nac*DCOS(2*pi*z/Pc)/(2*n0*Ps)
      phasegrad = -4*pi*neff*(z-(L-dL)/2)*chirpgrad/\
      ((2*n0*Ps)**2)
      d = 2*pi*neff*((1/lamda) - (1/(2*n0*Ps)))

      gg = d + g - phasegrad
      a1 = k*k
      b1 = gg*gg

      IF (a1>b1) THEN

      Y = DSQRT(a1 - b1)
      A = DCOSH(Y * dL)
      B = -1*gg*DSINH(Y*dL)/Y
      C = k*DSINH(Y*dL)/Y

      ELSE IF (a1<b1) THEN

    Y = DSQRT(b1-a1)
      A = DCOS(Y*dL)
      B = -1*gg*DSIN(Y*dL)/Y
      C = k*DSIN(Y*dL)/Y

      END IF

      F11 = CMPLX(A, B)
      F21 = CMPLX(0, C)
```

```
      F12 = CONJG(F21)
      F22 = CONJG(F11)

      F = RESHAPE ((/F11, F21, F12, F22/), (/2,2/))

      IF (I==1) THEN

      R = F

      ELSE

      R = MATMUL(R, F)

      END IF

  END DO

  E = R(1,1)
  H = R(2,1)

  IF (E/=0) THEN

  REF = (ABS(H/E))**2
  TRANS = 1 - REF

  ELSE

  REF = 0
  TRANS = 1

  END IF

  WRITE (2, *) lamda2, TRANS, REF

END DO

CLOSE (2)

END PROGRAM MOIREGRATING



PROGRAM coupledmode_FP

!*****************************************************************

! THIS PROGRAM DOES AN ANALYTICAL CHARACTERISATION OF FIBRE-OPTIC
! FABRY-PEROT TRANSMISSION SPECTRUM USING COUPLED MODE THEORY.

!*****************************************************************

! lamdaB is the grating central wavelength
! delta_n is the index modulation
! x is the field overlap integral in the core
! K is the coupling constant between the two opposite modes
! neff is the effective index of the fundamental mode
! L is the grating length
! h unpeturbed length between the two gratings
```

```
! var is the wavelength resolution for plotting
! lamdastart is the wavelength at which iterations start
! step is the bandwidth over which the model is evaluated
! lamda is the wavelength
! delta_beta is the phase matching parameter
! Beta is the propagation constant of the fundamental mode
! Rg is the grating reflectivity
! Rfp is the reflectivity of the fibre-optic Fabry-Perot
! Rbg is the variable reflectivity of the Bragg grating
! N is the resolution in characterising the FP reflectivity


! DECLARATION OF VARIABLES AND SETTING UP INPUT/OUTPUT FILES


IMPLICIT NONE

INTEGER:: I, var, J, N

DOUBLE PRECISION:: pi, K, delta_n, x, lamdaB, neff, L, h
DOUBLE PRECISION:: lamda1, lamdastart, step, lamda, S1, S
DOUBLE PRECISION:: delta_beta, Beta, A, B, Q, C, D, E, T
DOUBLE PRECISION:: A2, B2, Q2, C2, D2, E2, Rg, Rb
DOUBLE PRECISION:: U, V, Rfp, Rbg

OPEN (UNIT = 1, FILE = "Spectrum.dat", STATUS = "UNKNOWN")
OPEN (UNIT = 2, FILE = "Input.txt", STATUS = "UNKNOWN")
OPEN (UNIT = 3, FILE = "Reflect.dat", STATUS = "UNKNOWN")

READ (2, *) lamdaB
READ (2, *) Rg
READ (2, *) x
READ (2, *) L
READ (2, *) h
READ (2, *) var
READ (2, *) lamdastart
READ (2, *) step
READ (2, *) neff
READ (2, *) N

CLOSE (2)

! CALCULATION OF CONSTANT TERMS

pi = 4 * DTAN (1.D0)

Rb = DSQRT (Rg)

IF (Rb/=1) THEN

K = (DLOG ((1 + Rb)/(1 - Rb)))/(2 * L)

ELSE

K = 0

END IF

delta_n = K * lamdaB/(pi * x)
```

```
WRITE (6, *) "delta_n =", delta_n, "  K =", K

!neff = lamdaB/(2 * (L + h))

DO I = 0, var

   lamda1 = lamdastart + (step * (FLOAT (I)/FLOAT (var)))

   lamda = lamda1 * 1.0D-9

   delta_beta = 2 * pi * neff * ((1/lamda) - (1/lamdaB))

   Beta = 2 * pi * neff/lamda

   S1 = (K * K) - (delta_beta ** 2)

   IF (S1>0) THEN

      S = DSQRT (S1)

        A = 2 * S * delta_beta * DSINH (S * L) * DCOSH (S * L)

        B = (S * DCOSH (S * L)) ** 2 - (delta_beta * \
        DSINH (S * L)) ** 2

        Q = DATAN (A/B)

        C = (DCOS ((delta_beta * L) - (Beta * (L + h)) - (Q/2)))\
         ** 2  !

        D = (K * DCOSH (S * L)) ** 2 - delta_beta ** 2

        E = ((K * DSINH (S * L)) ** 2)/(S ** 4)

        T = 1/(1 + (4 * E *D * C))

        ELSE IF (S1<0) THEN

        S = DSQRT (ABS (S1))

        A2 = 2 * S * delta_beta * DSIN (S * L) * DCOS (S * L)

        B2 = (S * DCOS (S * L)) ** 2 - (delta_beta * \
        DSIN (S * L)) ** 2

        Q2 = DTAN (A2/B2)

        C2 = (DCOS ((delta_beta * L) - (Beta * (L + h)) - \
        (Q2/2))) ** 2 !

        D2 = (K * DCOS (S * L)) ** 2 - delta_beta ** 2

        E2 = ((K * DSIN (S * L)) ** 2)/(S ** 4)

        T = 1/(1 - (4 * E2 * D2 * C2))

       ! ELSE
```

```
        ! T = 1

         END IF

        ! WRITE (6, *) delta_beta, lamda1, T
         WRITE (1, *) delta_beta, lamda1, T

END DO

! THIS SUBPROGRAM ANALYSES THE VARIATION OF THE FP REFLECTIVITY
! WITH THE BRAGG GRATING REFLECTIVITY

DO J = 0, N

   Rbg = FLOAT (J)/FLOAT (N)

   IF (Rbg/=1) THEN

   U = 4 * Rbg/((1 - Rbg) ** 2)

   V = (1 + (2 * Rbg/(1 - Rbg))) ** 2

   Rfp = U/V

   ELSE

   Rfp = 1

   END IF

   WRITE (3, *) Rbg, Rfp

END DO

CLOSE (1)
CLOSE (3)

END PROGRAM coupledmode_FP
```

APPENDIX C

Light Scattering by Small Particles

The laser Doppler velocimetry measurement technique depends on the presence of suitable particles in the flow to produce enough scattered light. The particles are required to be able to follow the flow sufficiently close and to provide sufficient light for an acceptable signal to noise ratio. The magnitude and directional distribution of light scattered from a particle depends on its size, shape and refractive index.

The formal rigorous solution is attributed to Gustav Mie (1908). The mathematical derivations given here follow those developed by Van de Hulst [1] and further analysis that was given by Martin [2] for laser Doppler anemometry. The mathematical derivation is considerably simplified by considering the scattering particles to be homogenous spheres and the incident radiation linearly polarised. The solution begins with the macroscopic Maxwell equations

$$\begin{aligned} \nabla \cdot E &= 0 \\ \nabla \cdot H &= 0 \\ \nabla \times E &= i\omega\mu H \\ \nabla \times H &= -i\omega\varepsilon E \end{aligned} \qquad \text{(C.1)}$$

where ω is the circular frequency, ε is the dielectric constant and μ (assumed to be 1) is the magnetic permeability. The electric field and magnetic field strength $\boldsymbol{E}$ and $\boldsymbol{H}$ are represented in complex notation by

$$\begin{aligned} E &= a_x e^{-ikz+i\omega t} \\ H &= a_y e^{-ikz+i\omega t} \end{aligned} \qquad \text{(C.2)}$$

where k is the propagation constant, $\boldsymbol{a}_x$ and $\boldsymbol{a}_y$ are unit vectors along the x and y axis (Figure C.1). The field amplitudes and the refractive index of the medium outside the particle have been assumed to be unity. The vector wave equations become

$$\nabla^2 E + k^2 E = 0$$
$$\nabla^2 H + k^2 H = 0 \qquad \text{(C.3)}$$

It is more straightforward to solve a scalar wave equation than the vector wave equation. A scalar function ψ satisfying a scalar wave equation is defined from which two vector functions $\boldsymbol{M}$ and $\boldsymbol{N}$ are constructed using appropriate vector derivatives such that they all satisfy the same vector wave equation. $\boldsymbol{M}$ and $\boldsymbol{N}$ also satisfy the requirement for electromagnetic fields and are vector spherical harmonics. The solution to a scalar wave equation is therefore followed in which a spherical coordinate system is used (r, θ, Φ) in direct correspondence to Cartesian coordinates (x, y, z). The origin is considered to be at the centre of the sphere with the positive z-axis along the direction of propagation of the incident wave and the x-axis in the plane of the electric field vibration of the incident wave.

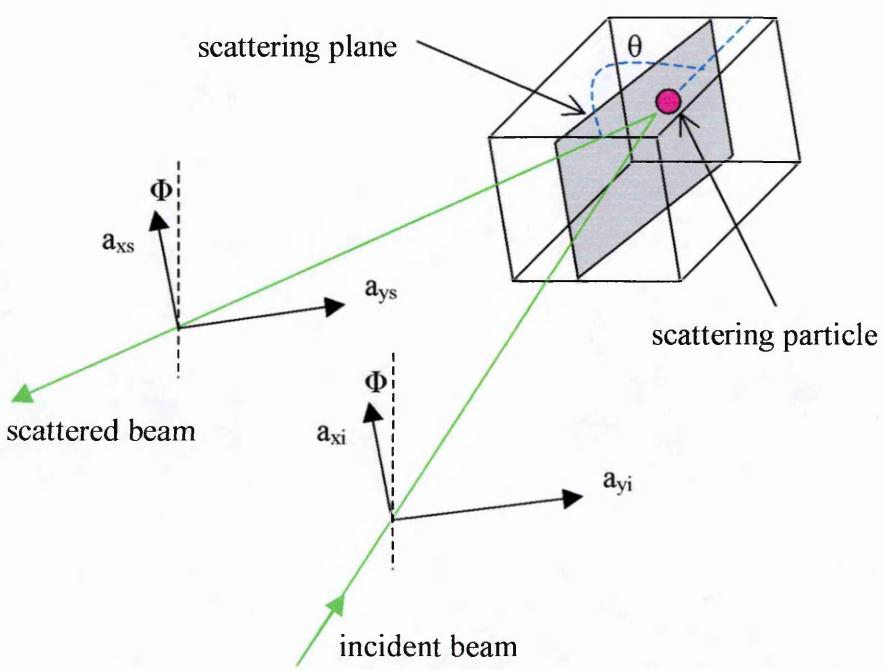

Figure C. 1: Electric and magnetic vectors for the incident and scattered waves.

The solution of the scalar wave equation in the spherical coordinates is variable separable consisting of three parts namely the harmonic (sine or cosine), Legendre polynomial, and the spherical Bessel function. The elementary solutions are therefore of the type

$$\psi_{\ln} = \cos(l\phi)\cdot P_n^l(\cos\theta)\cdot z_n(mkr)$$

or

$$\psi_{\ln} = \sin(l\phi)\cdot P_n^l(\cos\theta)\cdot z_n(mkr) \qquad \text{(C.4)}$$

The first term is the harmonic, the second is the associated Legendre polynomial while the third term is the spherical Bessel function and n and l are integers related by $n \geq l \geq 0$.

These solutions set the form of the fields outside and inside the sphere. The general solution of the scalar wave equation is a linear combination of these elementary solutions. The normal and tangential electromagnetic fields inside the sphere are correspondingly equal to those outside at the interface of the two media (boundary condition) while the out going field is required to behave asymptotically at infinity. The scalar functions for the scattered fields outside the sphere are thus given by

$$\psi_u = -\frac{i}{kr}\cdot e^{-ikr+i\omega t}\cdot\cos\phi\cdot\sum_{n=1}^{\infty} a_n\cdot\frac{2n+1}{n(n+1)}\cdot P_n^1(\cos\theta)$$

$$\psi_v = -\frac{i}{kr}\cdot e^{-ikr+i\omega t}\cdot\sin\phi\cdot\sum_{n=1}^{\infty} b_n\cdot\frac{2n+1}{n(n+1)}\cdot P_n^1(\cos\theta) \qquad \text{(C.5)}$$

where ψ_u and ψ_v are the scalar fields and a_n and b_n are coefficients to be determined and l is set to unity for elementary solutions. The vector functions for the scattered fields outside the sphere are obtainable from these by deriving the tangential field components. The resulting out going field components may therefore be written in the form

$$E_\theta = H_\phi = -\frac{i}{kr}\cdot e^{-ikr+i\omega t}\cdot\cos\phi\cdot S_2(\theta)$$

$$-E_\phi = H_\theta = -\frac{i}{kr}\cdot e^{-ikr+i\omega t}\cdot\sin\phi\cdot S_1(\theta) \qquad \text{(C.6)}$$

where $S_1(\theta)$ perpendicular to the scattering plane and $S_2(\theta)$ in the scattering plane are amplitude functions and they are given by

$$S_1(\theta)=\sum_{n=1}^{\infty}\frac{2n+1}{n(n+1)}\cdot[a_n\cdot\Pi_n(\cos\theta)+b_n\cdot\mathrm{T}_n(\cos\theta)]$$

$$S_2(\theta)=\sum_{n=1}^{\infty}\frac{2n+1}{n(n+1)}\cdot[b_n\cdot\Pi_n(\cos\theta)+a_n\cdot\mathrm{T}_n(\cos\theta)] \qquad \text{(C.7)}$$

The parameters Π_n and T_n are functions of the scattering angle that appear when deriving tangential field components equation (C.6) from the scalar functions equation (C.5) and they are given by

$$\Pi_n(\cos\theta)=\frac{1}{\sin\theta}\cdot P_n^1(\cos\theta)$$

$$\mathrm{T}_n(\cos\theta)=\frac{d}{d\theta}P_n^1(\cos\theta) \qquad \text{(C.8)}$$

The coefficients of the out going fields are given by

$$a_n=\frac{\psi_n'(y)\cdot\psi_n(x)-m\psi_n(y)\cdot\psi_n'(x)}{\psi_n'(y)\cdot\zeta_n(x)-m\psi_n(y)\cdot\zeta_n'(x)}$$

$$b_n=\frac{m\psi_n'(y)\cdot\psi_n(x)-\psi_n(y)\cdot\psi_n'(x)}{m\psi_n'(y)\cdot\zeta_n(x)-\psi_n(y)\cdot\zeta_n'(x)} \qquad \text{(C.9)}$$

where Ψ_n, ζ_n and χ_n are the Riccati-Bessel functions defined by

$$\psi_n(z)=z\cdot j_n(z)=S_n(z)$$

$$\chi_n(z)=-z\cdot n_n(z)=C_n(z)$$

$$\zeta_n(z) = z \cdot h_n^{(2)}(z) \qquad \text{(C.10)}$$

The argument z represents x or y which are defined by

$$x = ka = \frac{2\pi a}{\lambda}$$

$$y = mka \qquad \text{(C.11)}$$

where m is the refractive index and a is the radius of the sphere.

Programming Procedure

The first computation is that of the coefficients a_n and b_n. This requires the initialisation of the Riccati-Bessel functions as well as determining their recursive relations (equations C.12 - C.14).

$$\psi_0(z) = \sin z$$

$$\psi_1(z) = \frac{\sin z}{z} - \cos z$$

$$\psi_{n+1}(z) = \frac{2n+1}{z} \cdot \psi_n(z) - \psi_{n-1}(z)$$

$$\psi_n'(z) = -\frac{n}{z} \cdot \psi_n(z) + \psi_{n-1}(z) \qquad \text{(C.12)}$$

$$\chi_0(z) = \cos z$$

$$\chi_1(z) = \frac{\cos z}{z} + \sin z$$

$$\chi_{n+1}(z) = \frac{2n+1}{z} \cdot \chi_n(z) - \chi_{n-1}(z)$$

$$\chi_n'(z) = -\frac{n}{z} \cdot \chi_n(z) + \chi_{n-1}(z) \qquad \text{(C.13)}$$

The Riccati-Bessel functions are related together through

$$\zeta_n(z) = \psi_n(z) + i\chi_n(z)$$
$$\zeta_n'(z) = \psi_n'(z) + i\chi_n'(z) \qquad \text{(C.14)}$$

The argument z is given by x or y in equations (C.11) where m is the complex refractive index given by

$$m = m_{real} - jm_{imag} \qquad \text{(C.15)}$$

The computed Riccati-Bessel functions are substituted in equations (C.9) to evaluate the required coefficients. The next stage involves the computation of the amplitude functions or specific intensity $S_1(\theta)$ and $S_2(\theta)$. The first step requires the initialisation of the Legendre polynomial functions and establishment of their recursive relations (equations C.16).

$$\Pi_0(\cos\theta) = 0$$
$$\Pi_1(\cos\theta) = 1$$
$$\Pi_2(\cos\theta) = 3\cos\theta$$
$$\Pi_n(\cos\theta) = \cos\theta \cdot \frac{2n-1}{n-1} \cdot \Pi_{n-1}(\cos\theta) - \frac{n}{n-1} \cdot \Pi_{n-2}(\cos\theta)$$
$$T_n(\cos\theta) = n \cdot \Pi_n(\cos\theta) \cdot \cos\theta - (n+1) \cdot \Pi_{n-1}(\cos\theta) \qquad \text{(C.16)}$$

These results are substituted in equations (C.7) to compute the required specific intensity for the two orthogonal polarisations. The total scattering efficiency Q_{sca} is also calculated from

$$Q_{sca} = \frac{2}{x^2} \cdot \sum_{n=1}^{\infty} (2n+1) \cdot \left[|a_n|^2 + |b_n|^2 \right] \qquad \text{(C.17)}$$

If the area of the detector is denoted by A and input laser beam power as P_{in} then the power scattered by the particle P_{sca} as a function of scattering angle and state of polarisation is computed from

$$P_{sca} = P_{in} \cdot \frac{A}{\pi x^2 r^2} \cdot \left[|S_1(\theta)|^2 \cdot \sin^2 \phi + |S_2(\theta)|^2 \cdot \cos^2 \phi \right] \qquad \text{(C.18)}$$

This relation is used to deduce several aspects of the scattering medium. The scattered light may be analysed as a function of the scattering angle or as a function of wavelength. Also the variation of the scattered light with particle radius, refractive index or state of polarisation of the incident radiation may be inferred from this equation. Some examples are given in Figures C.2 to C.7.

Results

The results of the model were obtained from a program that was set up in MathCAD™. The results presented in graphical form are in most cases complex and show that there are no trends or general behaviour that can be inferred. However important information can be deduced that will be vital for successful flow measurements. Figure C.2 – C.4 show that the directional distribution of the scattered light is dependent on the polarisation of the illuminating light beam. Figure C.2 for example shows that the scattered light exhibit a minimum around 100^{0} for the beam polarised parallel to the scattering plane. Also an increase in particle diameter results in more ripples or oscillations in the scattered light thus making particles of diameter ≤ 1 μm suitable at 514.5 nm wavelength. Figure C.5 gives a comparison of these at perpendicular polarisation only.

It is shown in Figure C.6 that no trend can be established from light scattered by particles of various refractive indices but having same diameter and illuminated by the same wavelength. The same is true for Figure C.7 where everything else was made constant except for the wavelength of illumination that was varied. This figure shows that the lower the wavelength of illumination, the higher the scattered intensity that can be collected in any given direction.

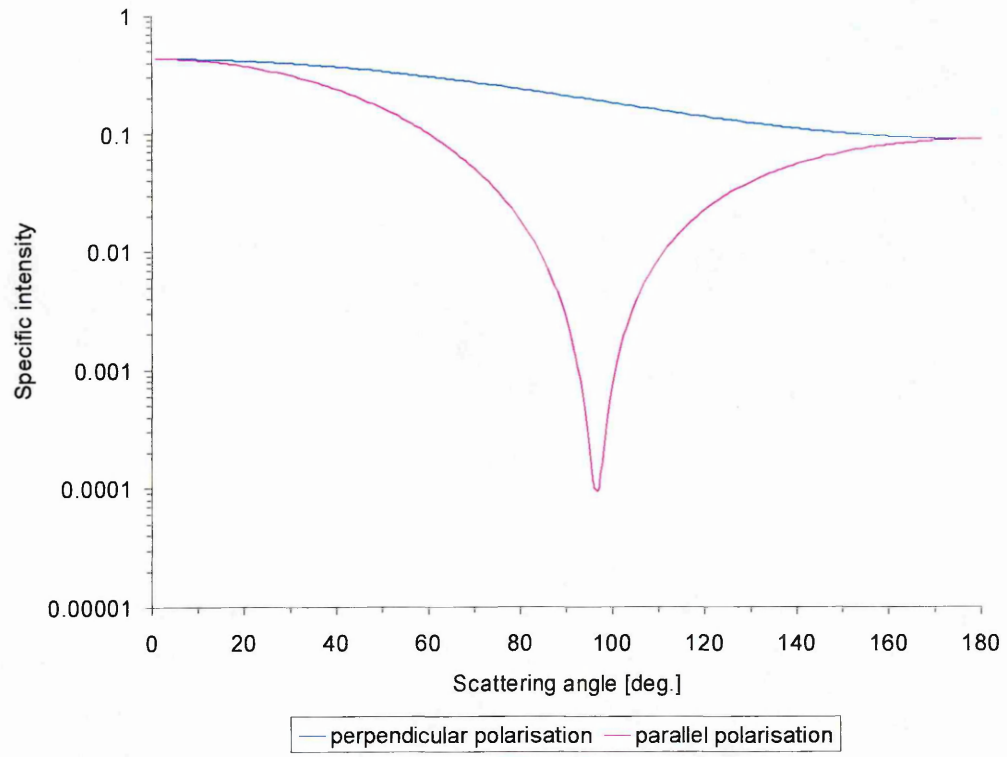

Figure C. 2: Scattered specific intensity for a 0.2 μm diameter particle illuminated by light of 514.5 nm wavelength with a refractive index of 1.5 (x = 1.221).

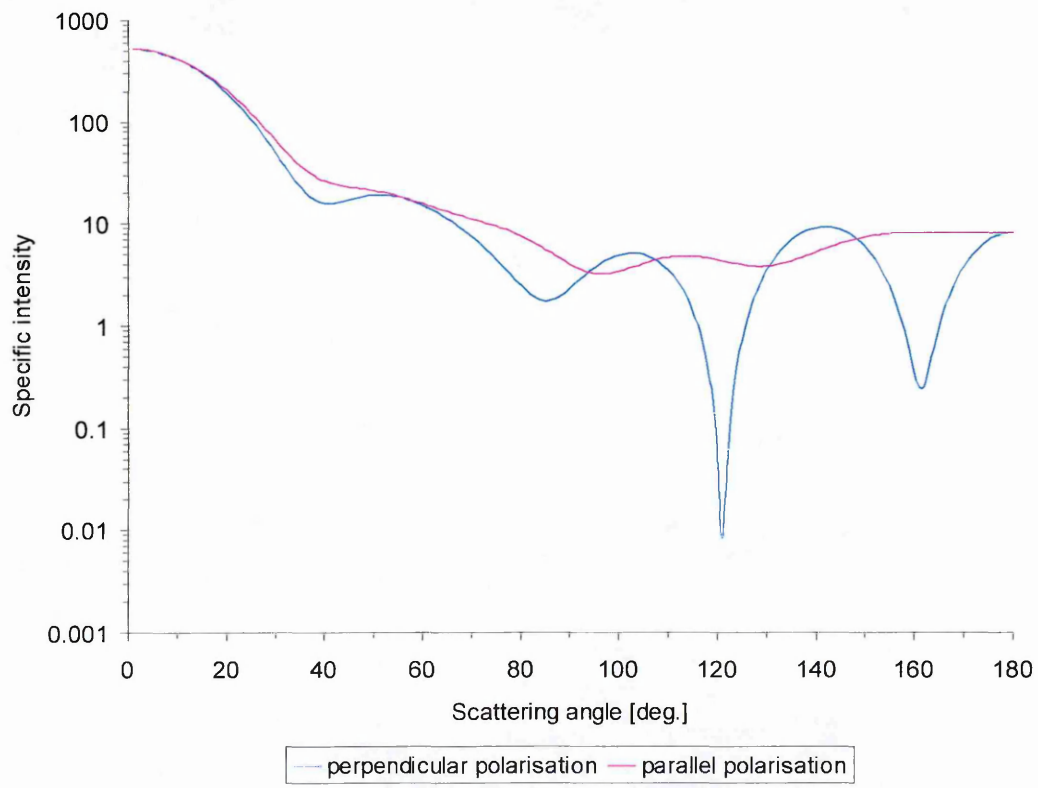

Figure C. 3: Scattered specific intensity for a 0.8 μm diameter particle illuminated by light of 514.5 nm wavelength for a refractive index of 1.5 (x = 4.885).

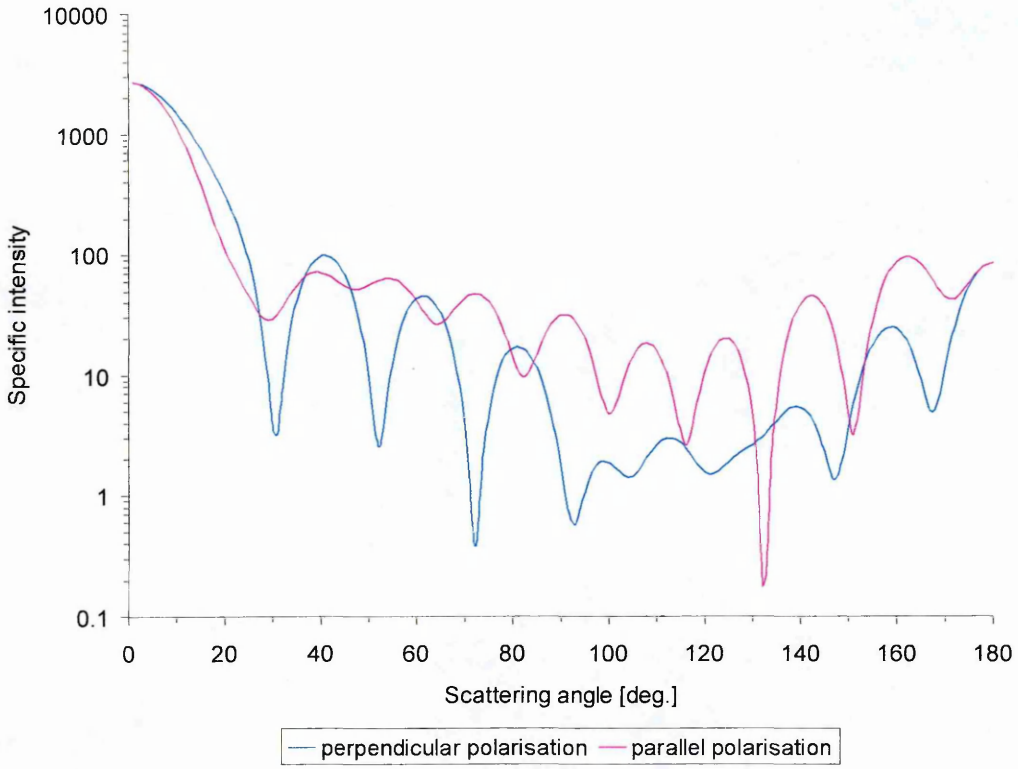

Figure C. 4: Scattered specific intensity for a 1.5 μm diameter particle illuminated by light of 514.5 nm wavelength for an index of 1.5 (x = 9.159).

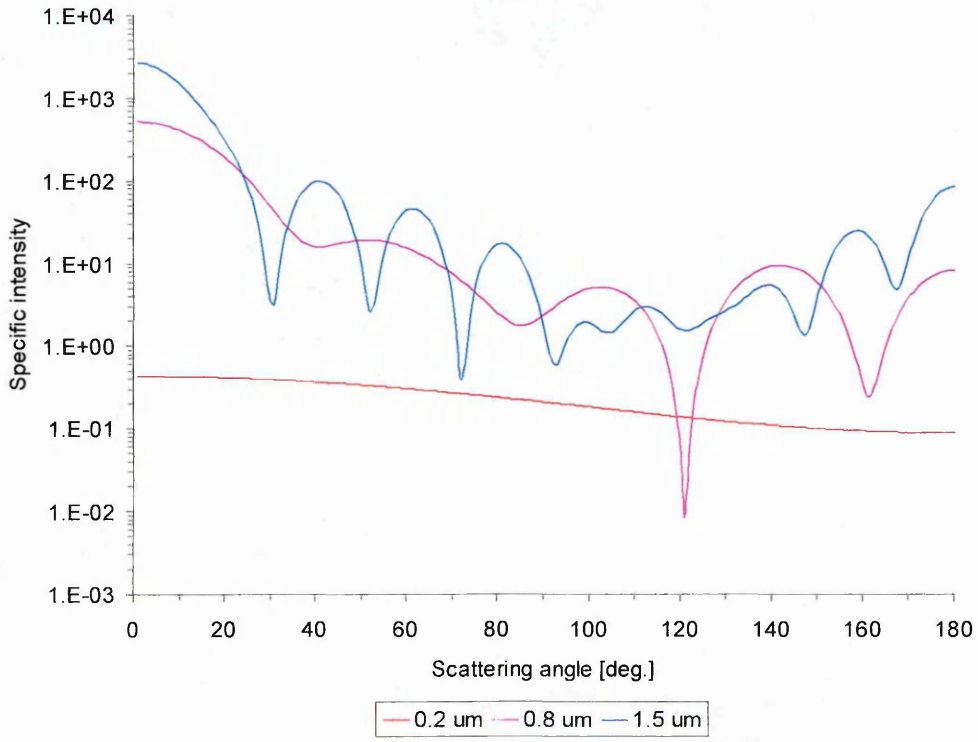

Figure C. 5: Scattered specific intensity for various particle diameters illuminated by light at 514.5 nm (perpendicular polarisation) for a refractive index of 1.5.

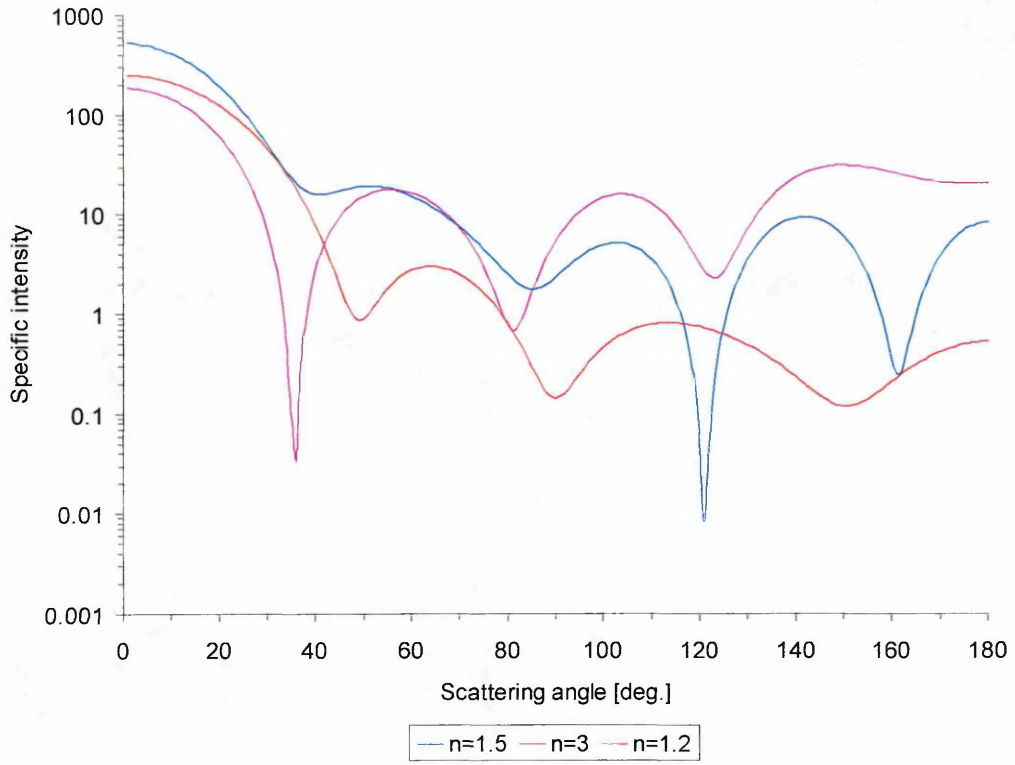

Figure C. 6: Scattered specific intensity for particles of 0.8 μm diameter (x = 4.885) of various refractive indices that are illuminated by light of 514.5 nm wavelength.

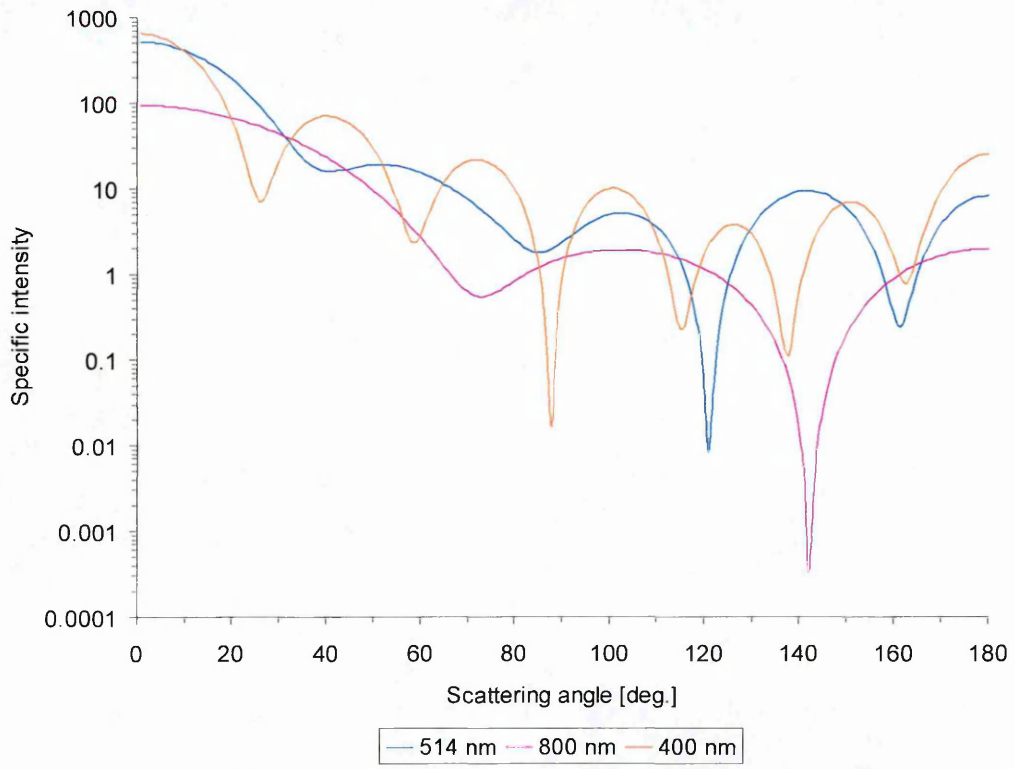

Figure C. 7: Scattered specific intensity for a particle of 0.8 μm diameter with a refractive index of 1.5 that is illuminated by light of various wavelength.

References

[1] H. C. Van de Hulst, "*Light scattering by small particles*", John Wiley & Sons, NY, 1957.

[2] R. J. Martin, "*Full-Field Optical Doppler Anemometry*", MPhil Thesis, Cranfield University, 1993.

APPENDIX D

Electronic Control Circuits for Laser Servo

This appendix discusses the electronic circuits that were designed to perform active control of the laser wavelength as required in Chapter 8. The automatic control process was implemented in closed loop feedback format incorporating a full PID system custom designed to offer individual adjustments to the P and I actions with D action only adjustable when used in conjunction with at least one other action. The circuits were designed around the use of operational amplifiers, resistors and capacitors, all chosen to offer minimum drift or noise. The required task of the circuit is summarised in the block diagram of Figure D.1.

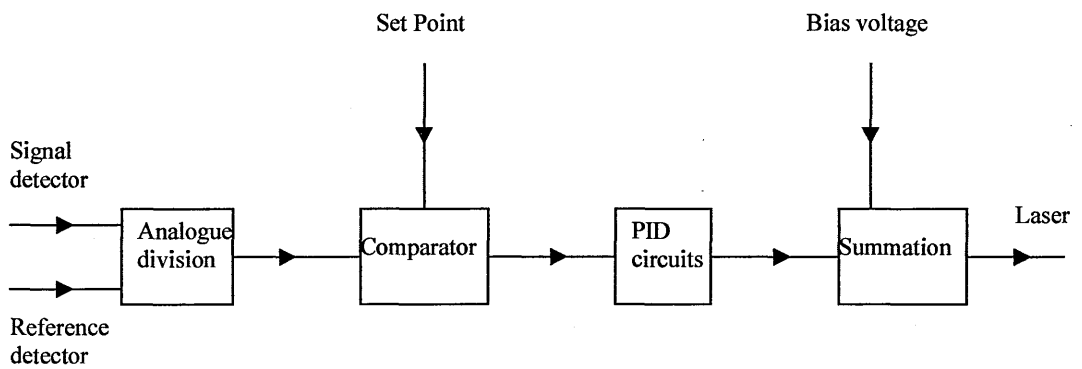

Figure D. 1: The tasks of the control circuit.

The analogue division circuit performs a division of the photodiode signal from the iodine cell by the reference photodiode signal. The resulting signal is compared to a set point value in the comparator that generates an error signal. Three different circuits that together provide a PID control signal act upon the error signal. The summation amplifier adds the control signal to a constant bias voltage with the resulting signal being fed-back to the laser.

The operational amplifier used was type OP-177 manufactured by Analog Devices and some of its parameters are listed in the table below [1].

offset voltage	4 μV
offset voltage drift	0.03 μV/^{0} C
common mode rejection ratio (CMRR)	140 dB
power supply rejection ratio (PSRR)	125 dB
input offset current	0.5 nA
input bias current	2.4 nA
input bias current drift	8 pA/^{0} C

Table D. 1: Analog Devices OP-177 characteristics.

All the resistors used were metallic ohmic resistors with very low drift. Analogue voltage division was performed using an AD734 chip from Analog Devices [2]. The operation of this chip is based on the equation

$$W = \frac{X \cdot Y}{U} \qquad \text{(D.1)}$$

The voltages X and Y may both be positive or negative while U is positive and W is the result of the analogue division. The chip requires that U be positive and in the range + 10 mV to + 10 V while input voltage X must have a magnitude of less than 1.25 U. Y is a scaling voltage that was supplied from a function generator and was kept constant.

Only a brief account of the circuit characteristics is given and readers are referred to electronics texts for more details [3, 4]. In the circuit of Figure D.2, the photodetector signals and the set-point constant-voltage source are input to instrumentation amplifiers. This type of amplifier configuration offers several advantages, which include the increase in the input impedance of the circuit, very low common mode gain, relaxed resistor matching, and offset voltage trimming can be on only one input operational amplifier (op-amp).

Figure D.2 shows the signal detection and analogue division circuits. The result of this circuit was fed to the circuit of Figure D.3 for the generation of the error voltage from which the control signal was derived. The control signal was fed to the Z-lok electronics of the laser that further modifies this signal to perform heating and cooling on the intra-cavity etalon acting as the actuator for wavelength control.

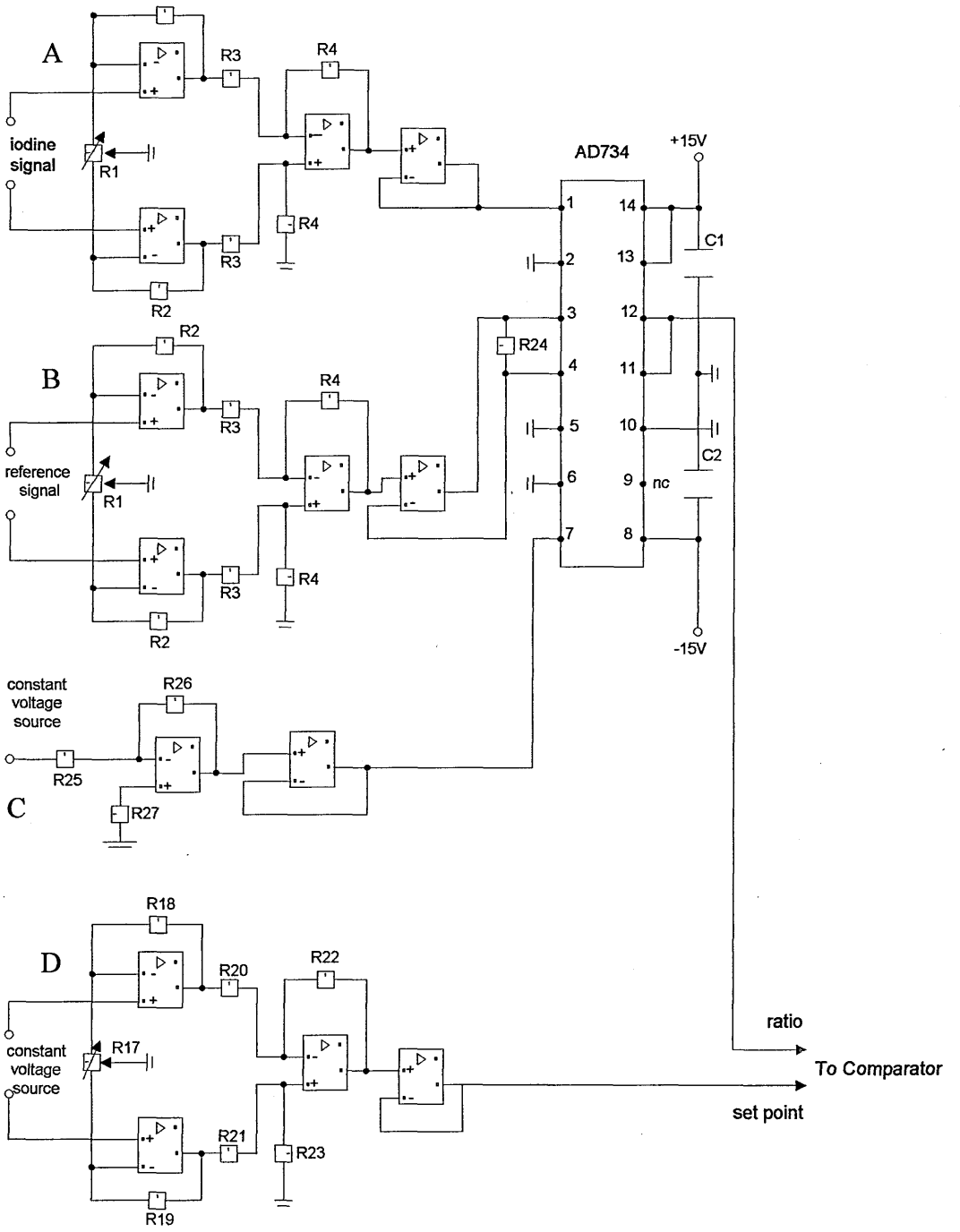

Figure D. 2: Signal detection, conditioning and analogue division circuits.

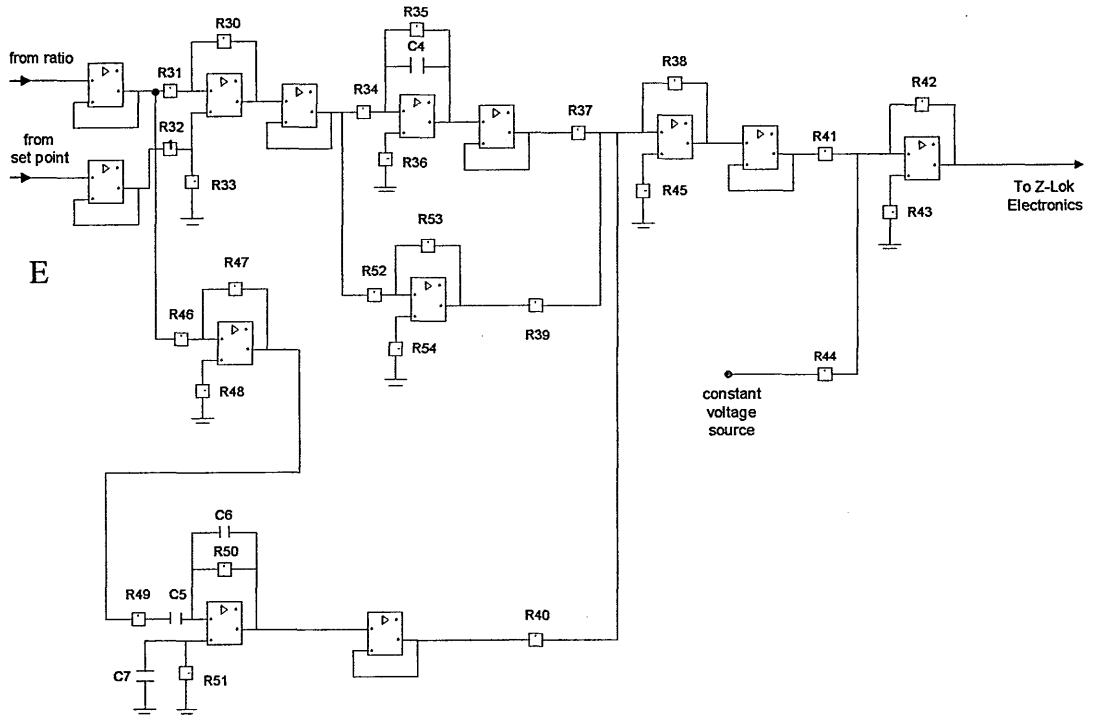

Figure D. 3: Generation of error voltage and PID control signal for feedback to laser.

The signal gain for the instrumentation amplifiers A and B of Figure D.2 is given by equations D.3 while that of D by equation D.4. The constant voltage source to an inverter amplifier C that supplies to pin 7 of the AD734 chip was from a Stanford Research Systems function generator.

$$Signal-gain=\left(1+\frac{2\cdot R_2}{R_1}\right)\cdot\frac{R_4}{R_3} \qquad \text{(D.3)}$$

$$Signal-gain=\left(1+\frac{2\cdot R_{18}}{R_{17}}\right)\cdot\frac{R_{22}}{R_{20}} \qquad \text{(D.4)}$$

The differential amplifier E was used to amplify the difference between two voltages i.e. the normalised signal (ratio) from Figure D.2 and a constant voltage source from a function generator used as the set point for the control system. This amplifier therefore

acted as a comparator and its result was the required error voltage, which is given by equation D.5.

$$V_{error} = \frac{R_{33}}{R_{32}} \cdot V_{ratio} - \frac{R_{30}}{R_{31}} \cdot V_{set-point} \qquad \text{(D.5)}$$

Amplifiers F, K and J are respectively the integral, proportional and derivative actions with F and K operating on the error signal V_{error} while J acts on the ratio signal V_{ratio} better known as the process variable. The algorithms for K, F and J are respectively given by equations D.6, D.7 and D.8.

$$V_{proportional} = -\frac{R_{53}}{R_{52}} \cdot V_{error} \qquad \text{(D.6)}$$

$$V_{integral} = -\frac{1}{C_4 \cdot R_4} \cdot \frac{\omega \cdot C_4 \cdot R_{35}}{\left(1 + \omega^2 \cdot {C_4}^2 \cdot {R_{35}}^2\right)^{\frac{1}{2}}} \cdot \int V_{error} \cdot dt \qquad \text{(D.7)}$$

$$V_{derivative} \approx R_{50} \cdot C_5 \cdot \frac{R_{47}}{R_{46}} \cdot \frac{dV_{ratio}}{dt} \qquad \text{(D.8)}$$

The parameter ω represents the frequency. R_{50} and C_5 are the actual differentiator parameters while C_6, R_{49} and C_7 were added to limit the high frequency gain. The differentiator parameters were chosen such that equation D.9 and D.10 are satisfied [3].

$$R_{50} \cdot C_6 = R_{49} \cdot C_5 \qquad \text{(D.9)}$$

$$f = \frac{1}{2 \cdot \pi \cdot R_{50} \cdot C_6} \qquad \text{(D.10)}$$

The response of the differentiator exhibited up to a maximum frequency f after which the gain falls. G_{max} below gives the maximum gain at frequency f.

$$G_{\max} = \frac{R_{50}}{R_{49}} \qquad \text{(D.11)}$$

The P, I and D action signals are added together in a summation amplifier G that has an adjustable gain for each action and this gain is set by the resistors R_{39}, R_{37} and R_{40} for the respective actions. The PID signal V_{pid} was added to a laser bias voltage (constant voltage) V_{bias} in the summation amplifier H to provide the control voltage $V_{control}$ that was fed-back to the laser through the Z-lok electronics that performed heating and cooling of the intra-cavity etalon. Equation (D.12) and (D.13) respectively give the PID and the control voltages.

$$V_{pid} = -\left[\frac{R_{38}}{R_{39}} \cdot V_{proportional} + \frac{R_{38}}{R_{37}} \cdot V_{integral} + \frac{R_{38}}{R_{40}} \cdot V_{derivative}\right] \qquad \text{(D.12)}$$

$$V_{control} = -\left[\frac{R_{42}}{R_{41}} \cdot V_{pid} + \frac{R_{42}}{R_{44}} \cdot V_{bias}\right] \qquad \text{(D.13)}$$

Extra tuning to the control signal was provided by the adjustment of resistor R_{41} and also R_{46} and R_{47} for the derivative action.

The integral time constant was set at 1.12 s and 0.2 s for the derivative action while the proportional factor gain of 25 % was used for the proportional action. The list of the components used and their values are in Table D.2 and D.3.

4k64	5k	10k	16k2	20k	51k1	61k9	100k	200k	511k
R_{27}	R_1	R_2	R_{39}	R_{38}	R_{25}	R_{46}	R_{31}	R_{50}	R_{34}
R_{43}	R_3	R_{18}	R_{37}		R_{30}	R_{47}	R_{32}	R_{51}	R_{36}
R_{49}	R_4	R_{19}	R_{40}		R_{33}		R_{41}		R_{52}
	R_{20}	R_{42}					R_{53}		
	R_{22}	R_{44}							
	R_{21}								
	R_{23}								
	R_{17}								

Table D. 2: Resistance values for the circuits.

Component	Value
C_1	0.2 µF
C_4	2.2 µF
C_5	1.0 µF
C_6	22 nF
R_{24}	2 M
R_{26}	6 k
R_{35}	5.6 M
R_{54}	9.8 k
R_{45}	4.25 k
R_{48}	31 k

Table D. 3: Capacitor and resistance values for the circuits.

References

[1] Analog Devices, "*Amplifier Reference Manual*", 1992.

[2] Analog Devices, "*Special Linear Reference Manual*", 1992.

[3] R. G. Irvine, "*Operational Amplifier: characteristics and applications*", Prentice-Hall, NJ, 1981.

[4] Horowitz Hill, "*The Art of Electronics*", Cambridge University Press, NY, 1980.

APPENDIX E

Electronic Control Circuits for Filter Servo

This appendix discusses the electronic circuits that were designed to perform active control of the Bragg-grating based fibre Fabry-Perot (FP) interferometer phase which was implemented in the closed loop feedback control system discussed in Chapter 8. The automatic control process included a full proportional-integral-derivative (PID) system custom designed to offer individual adjustments to the P and I actions with D action only adjustable when used in conjunction with at least one other action. The circuits were designed around the use of lock-in amplifiers, operational amplifiers, resistors and capacitors, all chosen to offer minimum drift or noise. The required task of the circuit is summarised in the block diagram of Figure E.1.

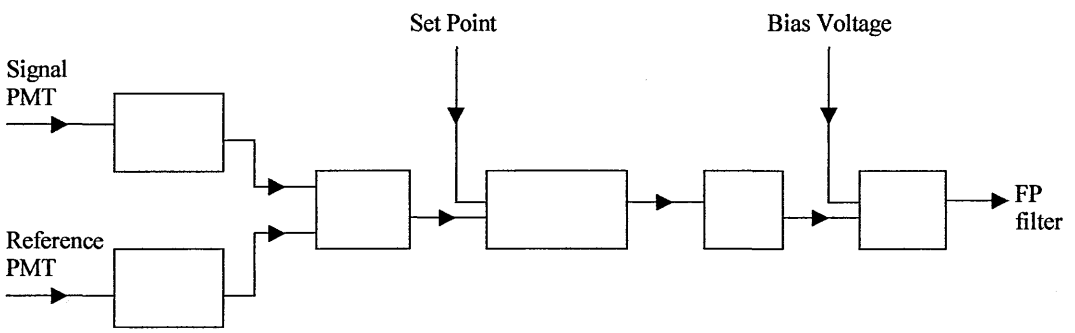

Figure E. 1: The tasks of the control loop.

The PMT signal from the fibre FP interferometer and the reference PMT signal were locked in phase to the pulse frequency (produced by a mechanical chopper) of the laser using digital lock-in amplifiers. Signal normalisation was done in a personal computer (PC) using a program set up in LabView. The result was output form the PC using an analogue output channel and was compared to a constant voltage from a function generator (Stanford Research Systems DS345) which represented the set point. Three circuits performing PID action acted upon the error voltage from the comparator. The

result was combined with a bias voltage (function generator) using a summation amplifier to generate the control voltage that was fed-back to the FP filter via a piezoelectric controller to a piezoelectric driven translation stage to which the FP filter was attached. The bias voltage takes the FP filter to 50 % of its transmission as required in Chapter 9. All circuit component characteristics were as described in Appendix D. Details on the working principles of key circuits such as the proportional, integral, and derivative actions, the signal comparator and the summation amplifiers will not be discussed here as they are related to those of Appendix D. Only the control equations of the circuit are given.

The ratio signal V_{ratio} from the software-based normalisation in the PC is the normalised voltage proportional to the phase changes in fibre FP interferometer. This signal becomes the process variable, which was generated by two digital lock-in amplifiers that were locked in phase. The control set point value $V_{set\text{-}point}$ was a constant voltage source from a function generator. The output from the comparator is the error voltage V_{error} given by equation E.1.

$$V_{error} = \frac{R_3}{R_1} \cdot V_{ratio} - \frac{R_4}{R_2} \cdot V_{set-point} \qquad \text{(E.1)}$$

The following relation gives the proportional signal $V_{proportional}$

$$V_{proportional} = \frac{R_6 \cdot R_{13}}{R_5 \cdot R_{12}} \cdot V_{error} \qquad \text{(E.2)}$$

If R_x is considered being the resistance at the potentiometer with total resistance R_8 then the integral signal $V_{integral}$ is given by equation E.3 below.

$$V_{integral} = \frac{R_6 \cdot R_x}{R_5 \cdot R_8 \cdot R_9 \cdot C_1} \cdot \frac{\omega \cdot C_1 \cdot R_{10}}{\left(1 + \omega^2 \cdot C_1^{\,2} \cdot R_{10}^{\,2}\right)^{\frac{1}{2}}} \cdot \int V_{error} \cdot dt \qquad \text{(E.3)}$$

Also, if R_y were considered being the resistance at the potentiometer with total resistance R_{16} then the relation below would give $V_{derivative}$ the derivative signal.

$$V_{derivative} \approx \frac{R_6 \cdot R_y \cdot R_{18} \cdot C_2}{R_5 \cdot R_{16}} \cdot \frac{dV_{error}}{dt} \qquad \text{(E.4)}$$

The maximum frequency f for the derivative action was determined from equation E.5 with the corresponding maximum gain G_{max} calculated from equation E.6.

$$f = \frac{1}{2 \cdot \pi \cdot R_{18} \cdot C_3} \qquad \text{(E.5)}$$

$$G_{\max} = \frac{R_{18}}{R_{17}} \qquad \text{(E.6)}$$

The PID action signal V_{pid} was calculated from equation E.7.

$$V_{pid} = -\left[\frac{R_{21}}{R_{15}} \cdot V_{proportional} + \frac{R_{21}}{R_{11}} \cdot V_{integral} + \frac{R_{21}}{R_{20}} \cdot V_{derivative}\right] \qquad \text{(E.7)}$$

The control signal $V_{control}$ was the sum of V_{pid} and V_{bias}, which was the bias voltage, adjusted on the piezoelectric controller and was fed-back to the piezoelectric translation stage to which the fibre FP filter was attached. The translation stage is therefore the actuator with $V_{control}$ being the actuator signal (equation E.8).

$$V_{control} = V_{pid} + V_{bias} \qquad \text{(E.8)}$$

The gains $G_{proportional}$, $G_{integral}$ and $G_{derivative}$ on P, I and D actions respectively were set according to the following relations.

$$G_{proportional} = \frac{R_6 \cdot R_{13} \cdot R_{21}}{R_5 \cdot R_{12} \cdot R_{15}} \qquad \text{(E.9)}$$

$$G_{integral} = \frac{R_6 \cdot R_x \cdot R_{21}}{R_5 \cdot R_8 \cdot R_{11}} \qquad \text{(E.10)}$$

$$G_{derivative} = \frac{R_6 \cdot R_y \cdot R_{21}}{R_5 \cdot R_{16} \cdot R_{20}} \qquad \text{(E.11)}$$

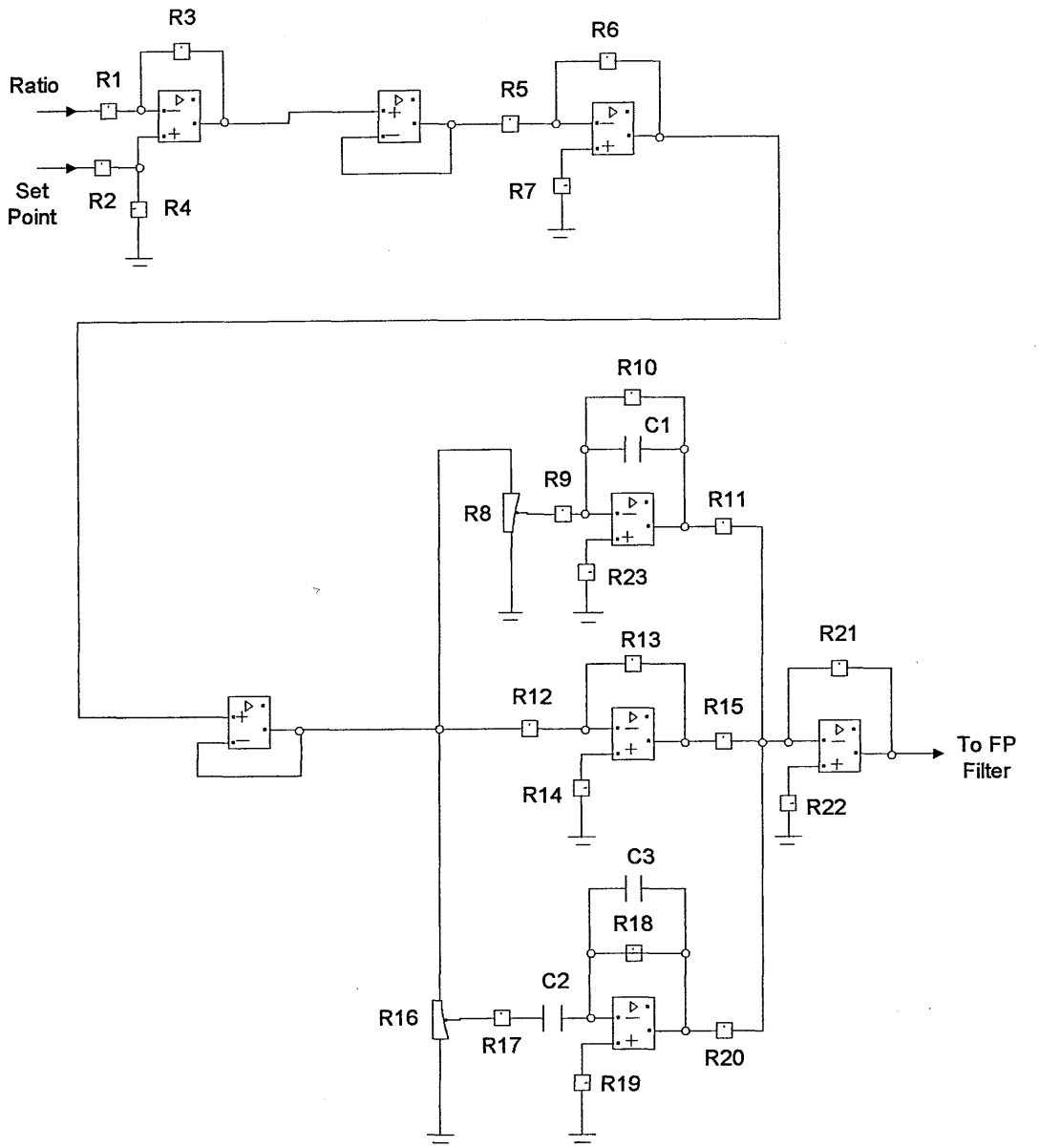

Figure E. 2: Generation of error voltage and PID control signal for feedback to piezoelectric translation stage attached to fibre FP filter.

The integral time constant was set at 0.22 s and 0.04 s for the derivative action while the proportional band was 77 % was used for the proportional action. The list of the components used and their values are in Table E.1.

2.2 μF	2nF	0.4 μF	1M	50k	2k	1.6k	60.4 k	37.7 k	100 k	20k	4.64 k	10k
C_1	C_3	C_2	R_{10}	R_{14}	R_{17}	R_{22}	R_6	R_7	R_1	R_8	R_{15}	R_{20}
									R_2	R_{16}	R_{21}	R_{11}
									R_3			
									R_4			
									R_9			
									R_{23}			
									R_{12}			
									R_{13}			
									R_5			
									R_{18}			
									R_{19}			

Table E. 1: Component values for the circuit.

APPENDIX F

Thermistors for Temperature Control

The success of any control system will depend on the accuracy of the sensor used. Negative temperature coefficient (NTC) thermistors have quick response and very high sensitivity to temperature changes, typically -4.5 % change in resistance for every 1 ^{0}C change in temperature at 25 ^{0}C. The temperature range of a thermistor is typically -50 ^{0}C to 300 ^{0}C. The current through the device is required to be kept small i.e. of the order of μA in order to avoid self-heating effects.

A simple sensor arrangement will have one thermistor in one leg of a Wheatstone bridge circuit but more sensors could be used in other legs for higher measurement resolution. Figure F.1 shows the set up of a 2 sensor bridge that is twice as sensitive as a single sensor. The inherent voltage divider of the bridge tends to linearise the output voltage as a function of temperature. The use of more than one sensor and a short temperature span reduces the linearity error.

The reference temperature of the system may be defined as corresponding to all resistors having an equal value R. Fixed resistors are denoted by R_1 and R_2 while R_{T1} and R_{T2} are resistance values for the two thermistors. The reference point sets the balance condition of the bridge. A change in temperature, ΔT, would cause a change in resistance, ΔR, in each of the thermistors (identical) (equation F.1 and F.2).

$$R_1 = R_2 = R \qquad \text{(F.1)}$$

$$R_{T1} = R_{T2} = R - \Delta R \qquad \text{(F.2)}$$

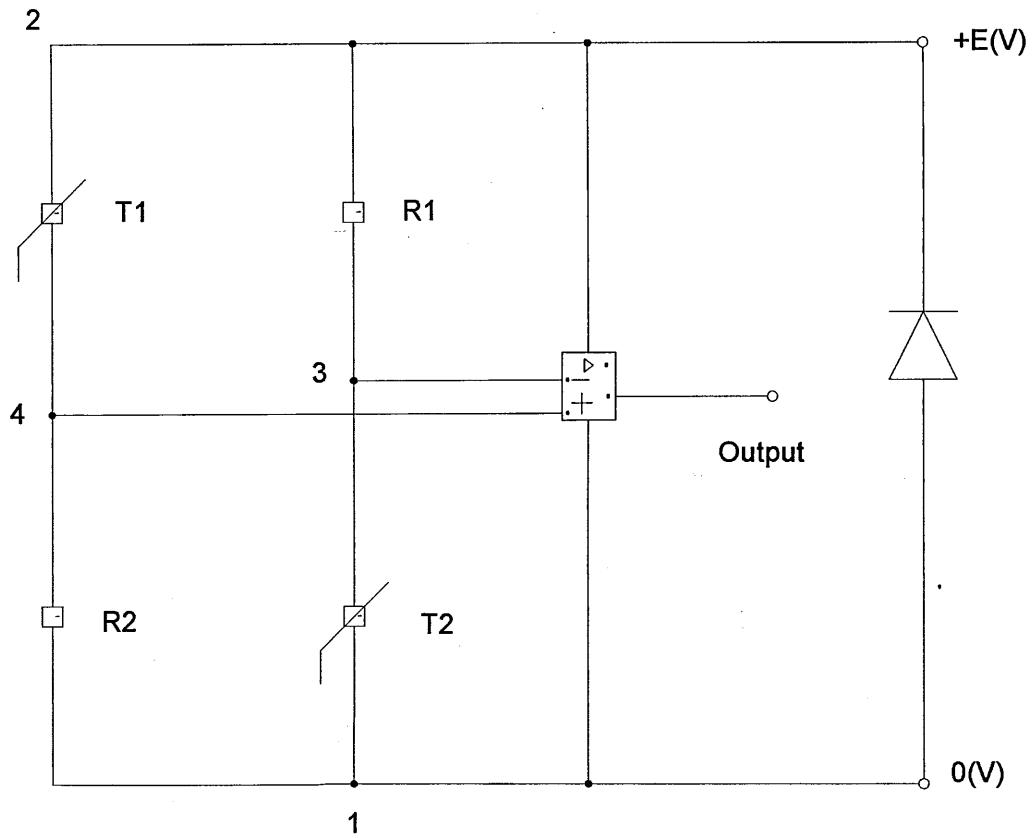

Figure F. 1: Thermistor sensor arrangement for a temperature controller.
T1 and T2 are Thermistors.

The bridge goes out of balance and thus delivers an output voltage. The current along the branch 241 and 231 is respectively given by I_{241} and I_{231}.

$$I_{241} = \frac{E}{R_{T1} + R_2} \qquad \text{(F.3)}$$

The equation leads to (F.4) upon substitution of (F.1) and (F.2) into equation (F.3).

$$I_{241} = \frac{E}{2R - \Delta R} \qquad \text{(F.4)}$$

The potential difference, V_{41} across R_2 is given by

$$V_{41} = I_{241} \cdot R_2 \qquad \text{(F.5)}$$

Equation (F.5) leads to

$$V_{41} = \frac{E \cdot R}{2R - \Delta R} \qquad \text{(F.6)}$$

Similarly

$$I_{231} = \frac{E}{2R - \Delta R} \qquad \text{(F.7)}$$

The potential difference, V_{31} across thermistor T_2 ids given by

$$V_{31} = I_{231} \cdot R_{T2} \qquad \text{(F.8)}$$

Equations (F.2) and (F.7) yield (F.9) when substituted into equation (F.8).

$$V_{31} = \frac{ER - E\Delta R}{2R - \Delta R} \qquad \text{(F.9)}$$

The out of balance potential ΔV is given by equation (F.10) and (F.11).

$$\Delta V = V_{41} - V_{31} \qquad \text{(F.10)}$$

$$\Delta V = \frac{E\Delta R}{2R - \Delta R} \qquad \text{(F.11)}$$

If it is now assumed that ΔT and therefore ΔR is small then $R >> \Delta R$ then

$$\Delta V = \frac{E\Delta R}{2R} \qquad \text{(F.12)}$$

Equation (F.12) shows that for small deviations in temperature from the set point, the output voltage is linear in the unbalance condition. The inclusion of a high gain

operational amplifier is essential for very small changes about the set point to be detectable and thus further improves the sensor resolution. The balance condition is ratiometric and therefore the null condition does not shift with variations in supply voltage. A reference diode is included in the circuit to ensure absolute voltage reference.

The temperature and resistance characteristics of a thermistor are given by

$$R = R_0 \cdot e^{\left(\frac{\beta}{T} - \frac{\beta}{T_0}\right)} \qquad \text{(F.13)}$$

Parameter β is the characteristic temperature constant and is governed by the material composition of the thermistor, R_0 is the resistance of the thermistor at T_0, R is the resistance at temperature T, and α is the temperature coefficient.

$$\alpha = -\frac{\beta}{T^2} \qquad \text{(F.14)}$$

Publications from the project

1. E. Chehura, C. C. Ye, and R. P. Tatam, "*In-line laser Doppler velocimetry*", Proceedings of SPIE, Optical Diagnostics for Fluids, Solids, and Combustion, vol. 4448, pp. 72-83, 2001.

2. E. Chehura, C. C. Ye, and R. P. Tatam, "*In-line fibre optic laser Doppler velocimeter using a Bragg grating based Fabry-Perot interferometer*", Institute of Physics Optical Group Annual Meeting, London, 2001.

3. E. Chehura, C. C. Ye, and R. P. Tatam, "*Optical Fibre Bragg Grating based Fabry-Perot Interferometer for In-Line Laser Doppler Velocimetry*", 15th Optical Fiber Sensors Conference Technical Digest, pp. 515-518, Portland, USA, 2002.

4. E. Chehura, and R. P. Tatam, "*In-Line Laser Doppler Velocimeter using Fibre Optic Bragg Grating Interferometric Filters*", submitted to Measurement Science and Technology.